HARNESSING OPTOCHEMICAL WAVES IN POLYMERS: FROM BEAM INTERACTIONS TO INSCRIPTION OF PRISMATIC ELEMENTS

By

Derek R. Morim, B.Sc.

A Thesis

Submitted to the School of Graduate Studies

In Partial Fulfilment of the Requirements

For the Degree

Doctor of Philosophy

McMaster University

DOCTOR OF PHILIOSOPHY (2019) McMaster University

(Department of Chemistry and Chemical Biology) Hamilton, Ontario

TITLE: HARNESSING OPTOCHEMICAL WAVES IN POLYMERS: FROM BEAM INTERACTIONS TO INSCRIPTION OF PRISMATIC ELEMENTS

AUTHOR: Derek R. Morim, B.Sc.

SUPERVISORS: Dr. Kalaichelvi Saravanamuttu, Dr. Ignacio Vargas-Baca

NUMBER OF PAGES: XXX, 259

Abstract

The nonlinear propagation of a visible, continuous wave laser beam was studied in three types of polymer systems that harness photochemical reactions: (i) a photopolymerization to create permanent self-written structures, (ii) a photo-oxidation hosted within a polymer matrix and (iii) a reversible photoisomerization that triggers the contraction of a photoresponsive hydrogel. The process of self-trapping was characterized by monitoring the spatial intensity profiles over time. The mechanism of each material was determined with a series of control experiments in order to confirm the nature of the nonlinear response, including their reversibility and intensity-dependence.

These observations led to the study of interactions between self-trapped beams. Two beams under linear conditions will pass through one another, but two beams travelling in a nonlinear medium will interact and influence one another. The interactions of two beams introduced into the aforementioned photochemical systems were investigated and revealed a rich diversity of phenomena including: (i) the attraction between beams, (ii) merging of beams into a single waveguide, (iii) nonlocal attraction between beams, (iv) orbiting of beams, (v) switching of beam positions, and (vi) inhibition of the self-trapping of a neighbouring beam. Each observation is dependent on a detailed understanding of the underlying mechanism of refractive index change. Numerical simulations supplement some of these experiments and provide further evidence for the nonlinear mechanisms.

The formation of permanent self-written structures with these nonlinear waves offers the opportunity to create seamless 3D printed materials with prismatic geometries. Several macroscopic objects were constructed using nonlinear waves from incoherent

LEDs and amplitude masks. Decomposition of 3D objects into prismatic elements was carried out using an algorithm that breaks an object into individual pieces. Using a multi-step printing process, several prismatic elements can be combined to form a target object.

The results of these experimental and theoretical studies improve upon the current understanding of the dynamics of nonlinear light propagation in photochemical systems. These insights may allow us to harness other nonlinear effects and develop new materials for applications such as optical communication, computing and 3D printing.

Acknowledgements

I would like to thank my supervisors, Dr. Kalaichelvi Saravanamuttu and Dr. Ignacio Vargas-Baca, for their guidance and support throughout my doctoral studies. I thank them for the opportunity to work under their direction alongside their enthusiasm, their constant willingness to help with problems and the enjoyable discussions that have inspired new ideas.

I would like to thank my supervisory committee members, Dr. Alex Adronov and Dr. Emily Cranston, for always being supportive and for their helpful suggestions.

I thank professors, researchers and technicians who have granted access to equipment or assisted with a technique or problem over the years including: Dr. Alex Adronov, Dr. Michael Brook, Dr. Harald Stöver, Dr. Adam Hitchcock, Dr. David Emslie, Dr. Gillian Goward, Dr. William J. Leigh, Dr. Andrea Armstrong, Dr. Bob Berno, Dr. Hilary Jenkins, Dr. James (Jim) Britten, Dr. Steve Kornic, Dr. Greg Bahun, and Ms. Karen Neumann.

I express my gratitude to Dr. Liqun Qiu, who assisted with the initial calibration of the single beam optical setup, and Dr. Ana Villafranca and Jonathan Lannan for the code of an external subroutine that was adapted for simulations in the collinear study. I thank all collaborators and co-authors in the publications that serve as chapters in this thesis. A special thanks to Dr. Ankita Shastri, Amos Meeks and Dr. Anna Shneidmann who visited from the Aizenberg group to carry out research and further our collaboration.

I also thank past and present lab members and undergraduate students including: Dr. Lucia Lee, Dr. Alex Hudson, Chris Gendy, Peter Ho, Fariha Mahmood, Kathryn

Benincasa, Matthew Ponte, Dr. Hao Lin, Dr. Dinesh Basker, Andy Tran, Damian Bevern, Natalie Blanchard, Amy Pan, Steven Chen, Alberto Cevallos, Jin Wang, Dr. Ian Hosein, Dr. Phil Elder and Oscar Alejandro Herrera Cortes.

I would also like to thank the funding sources that made my research possible: Natural Sciences and Engineering Research Council (NSERC), Ontario Graduate Scholarship (OGS), James A. Morrison Memorial Scholarship in Chemistry, Canadian Foundation for Innovation, Ontario Innovation Trust, and McMaster University.

I thank the friends I have made during my time at McMaster University including: Dr. Alex Hudson, Dr. Lucia Lee, Fariha Mahmood, Kathryn Benincasa, Stuart McNelles, Chris Gendy, Peter Ho, Sam Ros, Dr. Blossom Yan, Urooj Gill, Jeffrey Price, Novan Gray, Sonny Vasanthakumar, Katia Paskaruk, Sheilan Sinjari, Meghan Stearns and Dr. Greg Bahun.

I would like to thank all of my friends and family for their unconditional support, especially my parents Adriana and Manuel, my sister Brittany, and my grandmother Maria (Nivea) Vaz.

Table of Contents

List of Figures

List of Tables

LIST OF ABBREVIATIONS AND SYMBOLS

α	attenuation coefficient (cm^{-1})
γ	growth rate of MI (s^{-1})
$\Delta\psi$	transverse phase shift
Δn	refractive index difference
Δn_s	maximum change in refractive index at saturation
Δs	separation between two beams under linear conditions (μm)
Δs_{min}	minimum separation between 2 beam vectors (linear cond.; μm)
Δx	distance between two beams along the x direction (μm)
ε_0	permittivity in vacuum (F m^{-1})
θ	angle or angular separation (°)
λ	wavelength (nm)
λ_{max}	wavelength of maximum absorbance (nm)
ν	frequency of light (Hz)
ρ	density (g cm^{-3})
τ	delay time (μs)
ϕ	volume fraction of polymer in SP gels
$\chi^{(n)}$	susceptibility tensor
ψ	relative variation in gel volume fraction
ω	angular velocity (rad s^{-1})

$1/e^2$	width of beam at waist with intensity ~0.135 relative to centre (μm)
2D	two-dimensional
3D	three-dimensional
A	material dependent index growth rate ($cm^2\ mW^{-1}\ s^{-1}$)
AAc	acrylic acid
AAm	acrylamide
AM	amplitude mask
APS	ammonium persulfate
C	polarizing beamsplitter cube
c.w.	continuous wave
CAL	computed axial lithography
CCD	charge coupled device
CLIP	continuous liquid interface production
DI	deionized
DLP	digital light processing
DMPA	2,2-dimethyl-2-phenylacetophenone
DMSO	dimethyl sulfoxide
E	electric field (V/m)
E_0	initial electric field (V/m)
EAP	electroactive polymer
F	filter
f.l.	focal length (cm)

FRAP	fluorescence recovery after photobleaching
h	Planck's constant = 6.626×10^{-34} m^2 kg s^{-1}
HEMA	hydroxyethyl methacrylate
I	intensity (W cm^{-2})
J_ψ	polymer flux (s^{-1})
k	chemical rate constant (s^{-1}, M^{-1} s^{-1})
k_0	Wavenumber (cm^{-1})
L	length of sample (mm)
LCST	lower critical solution temperature (°C)
LED	light-emitting diode
LP	linearly polarized modes of optical fibres
M	mirror
MAPTMS	3-(trimethoxysilyl)propyl methacrylate photopolymer system
MC	merocyanine
MI	modulation instability
MLCT	metal-to-ligand charge transfer
n_0	initial refractive index
P	Polarization (D cm^{-3})
p	value indicate whether single (p = 1) /multi-photon process (p > 1)
PAG	photoacid generator
PI	photoinitiator
PMMA	poly(methyl methacrylate)

PPO	poly(propylene oxide)
PQ	phenanthrenequinone
PVA	poly(vinyl alcohol)
QTH	quartz tungsten halogen lamp
ROI	region of interest
SLA	stereolithography apparatus
SP	spiropyran
SR	swelling ratio
TEA	triethanolamine
TEMED	tetramethylethylenediamine
TFA	trifluoroacetic acid
THF	tetrahydrofuran
U_0	critical exposure (W cm^{-2})
UV	ultraviolet
V	applied voltage (V)
v	linear velocity (mm s^{-1})
W	molecular weight (g mol^{-1})
W	λ/2 waveplate
WEL	waveguide-encoded lattice
z	propagation direction

1 Introduction

Optical waves that alter the properties of the medium in which they travel can lead to self-action effects – nonlinear waves that are reinforced as they propagate.[1–4] These nonlinear phenomena are the result of feedback between the medium and the propagating wave. One example of these nonlinear waveforms is the self-trapped beam or spatial optical soliton, which is formed when the divergence of a beam is suppressed by light-induced changes in refractive index within the medium that the light is travelling through.[1–4]

The principal requirement for these optical self-action effects is a photoresponse that results in a refractive index change. Originally, these changes were studied in Kerr media with high laser intensities[5–7], but other media have been employed, such as photorefractives,[8–11] liquid crystals[12–15] and photochemical systems.[16–19] Photochemical reactions offer the ability to dynamically change a material in response to light by creating new chemical species with different refractive indices – an intensity-dependent process that allows the observation of the same types of self-action effects as other nonlinear materials but often at lower intensities.[4,20–22] The mechanism of each medium's photoresponse is critical to the dynamics of these processes. Depending on the reversibility of these materials, we may be able harness nonlinear waves to reversibly control the properties of an optical beam[24–26] or fabricate 3D permanent functional structures.[4,27–29]

This Chapter introduces some of the different self-action phenomena that can occur in nonlinear materials, including optical self-trapping and spatial solitons, diffraction rings

from spatial self-phase modulation, filamentation due to modulation instability, and self-defocusing effects. This Chapter also highlights the origins of the responses that different materials exhibit and the different types of interactions that are possible between self-trapped beams. The underlying chemistry for some of these photoresponsive systems are described with a focus on polymers and their applications, including 3D printing. Finally, the research objectives surrounding this thesis will be highlighted.

1.1 Optically-induced nonlinear phenomena in photoresponsive media

The field of nonlinear optics has existed since the advent of the laser in the fifties and investigates the mutual responses between light and light-responsive materials.[3,30] These light-matter interactions often rely on high intensities in order to elicit nonlinear responses in materials that exploit higher order susceptibilities when exposed to light, but other types of responses also exist.[2–4] The spatial distribution of light evolves and creates different nonlinear waveforms within materials including Kerr media,[5–7,23,31,32] photorefractives,[8,9,11,33,34] liquid crystals[12] and materials that rely on photochemical reactions[16,35–41] such as photopolymers[18–20,42–46].

1.1.1 Optical self-trapping and spatial solitons

Light beams naturally broaden in space as they propagate in dispersive linear media.[3] When introduced into a nonlinear medium, the light can produce an increase in refractive index, which causes the beam to self-focus and bend towards the regions of higher refractive index. This self-focusing effect counters the natural diffraction of light and

creates a self-trapped beam when the two processes are balanced (Figure 1-1).[47,48] A self-trapped optical beam maintains its shape as it propagates through a medium.

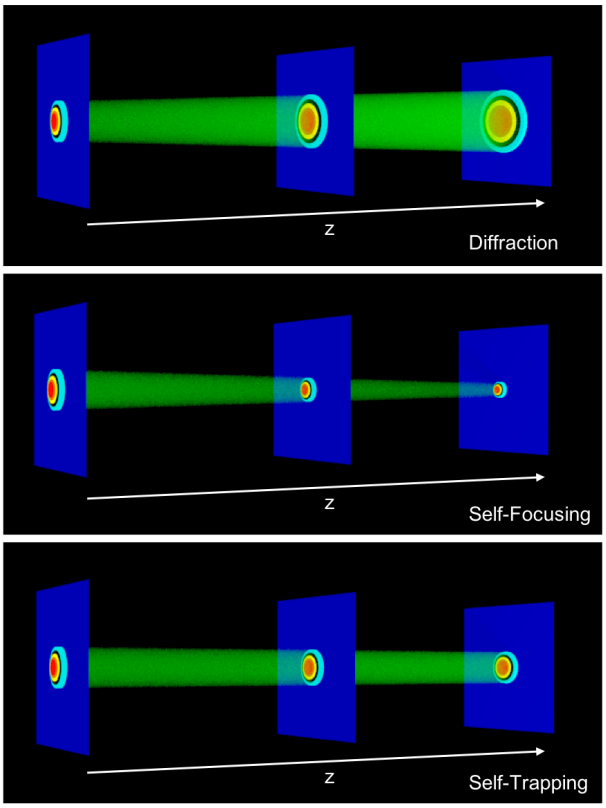

Figure 1-1 Scheme illustrating changes to a near-Gaussian beam from diffraction under linear conditions, self-focusing or lensing, and self-trapping that occurs when diffraction is suppressed in nonlinear media allowing a beam to maintain its profile as it propagates.

The paraxial wave equation (eq 1.1) (nonlinear Schrödinger equation) describes this effect where ε is the electric field vector of the incident electromagnetic wave propagating along z, n_0 is the initial refractive index of the medium and k_0 is the free space wave vector.[2,25] The equation shows that the natural diffraction of the beam along its transverse axes described by $\nabla_t^2 = \left(\frac{\partial^2}{\partial x^2}\right) + \left(\frac{\partial^2}{\partial y^2}\right)$ is counterbalanced by self-induced

changes in the refractive index (Δn) of the medium along its propagation path (z). The equation also considers the attenuation coefficient (α) of the medium.[2–4]

$$ik_0 n_0 \frac{\partial \varepsilon}{\partial z} + \frac{1}{2}\nabla_t^2 \varepsilon + k_0^2 n_0 \Delta n \varepsilon + \frac{i}{2} k_0 n_0 \alpha \varepsilon = 0 \quad (1.1)$$

Different responses can be observed depending on whether the refractive index changes are positive or negative, local or nonlocal, or if they are permanent or reversible. These additional effects are described in the subsequent chapters. This phenomenon has been demonstrated in materials including Kerr media[1], photorefractive crystals[11], liquid crystals[12], photosensitive glasses[37] and photopolymers.[49]

Self-trapping in media that increase refractive index through photopolymerization leaves permanent structures inscribed in the material – these self-written waveguides are capable of guiding light through total internal reflection and can be used as passive devices once they are generated (Figure 1-2).[18,20,28,37,49–51]

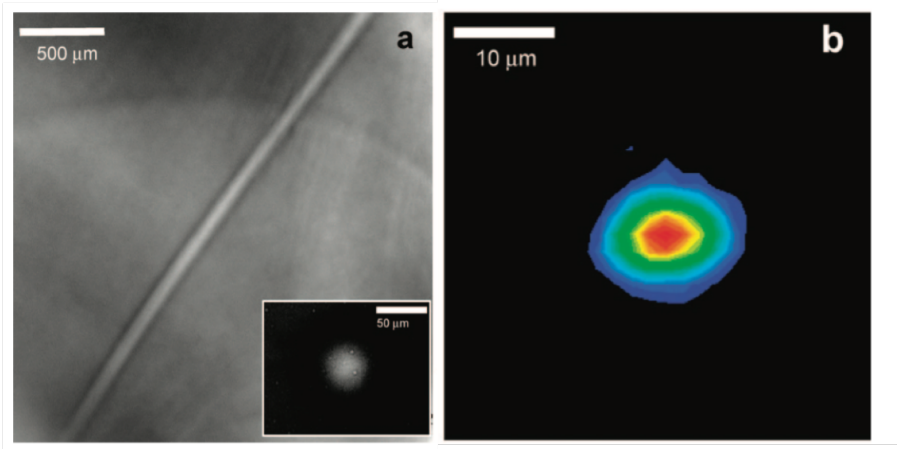

Figure 1-2. Transmission optical micrograph of a) a self-written waveguide in an organosiloxane from self-trapping and b) the 2D intensity profile at the output of the waveguide (z = 6.0 mm). Reprinted (adapted) with permission from Villafranca, A. B.; Saravanamuttu, K. An Experimental Study of the Dynamics and Temporal Evolution of Self-Trapped Laser Beams in a Photopolymerizable Organosiloxane. *J. Phys. Chem. C* **2008**, *112*, 17388–17396. Copyright 2008 American Chemical Society.[20]

1.1.2 Modulation instability, self-phase modulation and self-defocusing

Filamentation of optical beams due to modulation instability (MI) is considered a universal process that occurs in a variety of nonlinear systems.[27,52–55] A high-intensity beam of light introduced into a nonlinear material can filament into several individual self-guided beams with random order. The breakup of a broad beam (E_0) into filaments from MI originates from small and normally negligible perturbations (e) in the optical field ($|e|<<E_0$).[52] This noise becomes amplified when introduced into a nonlinear medium, and the beam stabilizes by breaking up (eq 1.2).

$$E = (E_0 + e)\exp(-i\gamma z) \tag{1.2}$$

The growth rate of the medium (γ) also affects the resulting breakup of the beam. MI arises from the same nonlinearity as self-trapping, with each filament corresponding to a self-trapped beam, allowing arrays of self-trapped beams to be created using a single broad beam.[27] This phenomenon has been observed in materials including atomic vapor,[56] Kerr liquids,[57] nanoparticle colloids[58,59] polymer solutions,[60] photorefractive crystals,[53,61] photorefractive polymers,[62] liquid crystals,[63,64] and photopolymers (Figure 1-3).[27,44,51,54,65,66] MI has been achieved with both coherent sources and incoherent sources; one of the benefits of generating nonlinear waves with incoherent sources is the ability to use widely accessible, inexpensive and relatively low-energy incoherent sources such as QTH lamps and LEDs.[4,27,56,63] Modulation instability in photopolymers has been used to make microstructured polymer materials with light-guiding properties due to the self-inscribed waveguides that form.[44,51,67]

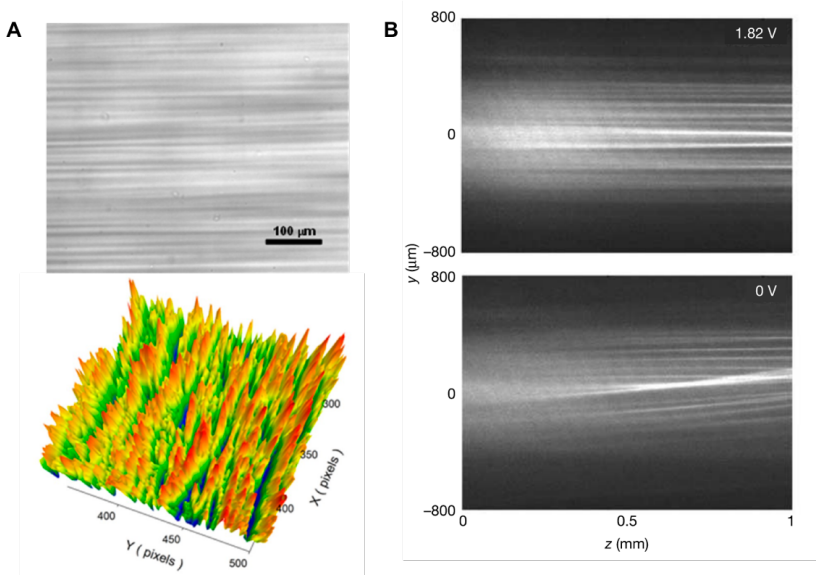

Figure 1-3 (A) Filamentation of a broad beam of light due to modulation instability in (A) a photopolymer and (B) a liquid crystal sample with and without an applied electric field. (A) Reprinted (adapted) with permission from Basker, D. K.; Brook, M. A.; Saravanamuttu, K. Spontaneous Emergence of Nonlinear Light Waves and Self-Inscribed Waveguide Microstructure during the Cationic Polymerization of Epoxides. *J. Phys. Chem. C* **2015**, *119*, 20606–20617. Copyright 2015 American Chemical Society.[44] (B) Reprinted by permission from Peccianti, M. et al. Routing of Anisotropic Spatial Solitons and Modulational Instability in Liquid Crystals. *Nature* **2004**, *432*, 733–737. Copyright 2004 Springer Nature.[63]

Another spatial effect that has been observed in nonlinear media is the formation of rings from spatial phase modulation.[21,22,68–73] As the refractive index changes, the transverse phase also changes, resulting in interference between different points on the beam (eq 1.3).[68] A coherent source that induces refractive index changes (Δn) in a nonlinear material produces a phase shift ($\Delta\psi$) described by (1.3):

$$\Delta\psi(r) = \frac{2\pi}{\lambda}\int_{z_0}^{z_0+d}\Delta n(r,z)dz \qquad (1.3)$$

where r is the radial direction transverse to the propagation direction (z), z_0 is the position at which the beam enters the sample, d is the sample thickness and λ is the wavelength of

light.[68] The formation of these rings can occur in materials with self-focusing and self-defocusing nonlinearities, as long as there is a refractive index change and corresponding transverse phase shift. When a beam is introduced into a saturable medium, intensities above the saturation threshold can generate a flat-top index profile, resulting in larger phase shifts near the periphery of the beam; the constructive and destructive interference between these regions of different phase result in rings which may also filament due to modulation instability, depending on the input and material parameters.[22,71] These effects have been observed in materials including photopolymers (Figure 1-4), [21,22,70] liquid crystals,[68] lead glass[74] and dispersions of graphene.[75]

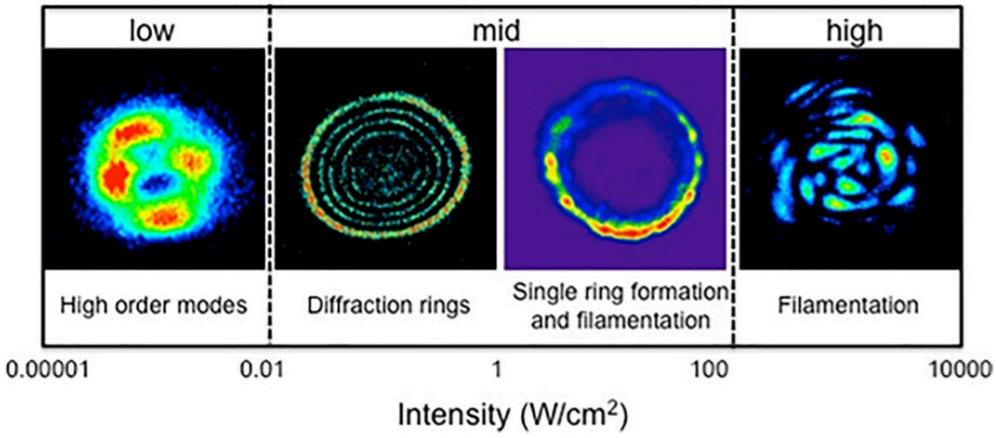

Figure 1-4 Spatial intensity profiles of the output of an organosiloxane photopolymer (3-(trimethyoxysilyl)propyl methacrylate/Irgacure® 784) illustrating the different phenomena observed due to the intensity-dependent photopolymerization response. Reprinted (adapted) with permission from Biria, S.; Morim, D. R.; An Tsao, F.; Saravanamuttu, K.; Hosein, I. D. Coupling Nonlinear Optical Waves to Photoreactive and Phase-Separating Soft Matter: Current Status and Perspectives. *Chaos* **2017**, *27*, 104611. Copyright 2017 AIP Publishing.[4]

Self-defocusing is an effect that occurs when the refractive index decreases within a medium when exposed to light.[3,23] A light-induced decrease in the refractive index tends

to cause light to bend away from the irradiated regions, leading to enhanced broadening of the beam. If the decrease occurs rapidly, dark regions can form in the centre resulting in dark beams that propagate through the medium. Dark beams have been demonstrated in various materials including Kerr media[76], photorefractives[77] and photopolymers.[78] Another method of fabricating dark beams in photopolymers with positive nonlinearities is through use of an amplitude mask.[79] By introducing a region that is dark into a sample that increases its index in the presence of light, it is possible for the dark region to propagate through the material. This effect occurs due to self-focusing in the surrounding regions away from the dark area.

1.2 Materials with different nonlinear mechanisms

The nonlinear response of most materials depends on the motion of electrons in response to an electric field. The bulk polarization (P) of a material therefore depends on the electric field (E) according to (eq 1.4):

$$P = \varepsilon_0(\chi^{(1)}E + \chi^{(2)}EE + \chi^{(3)}|E|^2E + \cdots) \quad (1.4)$$

where ε_0 is the vacuum permittivity and $\chi^{(n)}$ corresponds to the n^{th} order components of the susceptibility of the medium.[3] The first term in (1) involving $\chi^{(1)}$ represents the behaviour in linear media, where the polarization varies linearly with the electric field. The higher-order terms that contain tensors $\chi^{(2)}$ (e.g. photorefractive effect) and $\chi^{(3)}$ (e.g. Kerr effect[5–7,23,31,32]) represent the nonlinear responses related to a weak asymmetric ($\chi^{(2)}$) and symmetric ($\chi^{(3)}$) anharmonicity of the electron displacement. Some other mechanisms of changing the refractive index of a medium include movement or reorientation of

molecules (e.g. liquid crystals[12]), photothermally-induced structural changes (e.g. lead glass[80]) and photochemical reactions[16,35–41] (e.g. photopolymers[18–20,42–46]).

Some important properties of nonlinear materials include the saturability, reversibility and locality of the response. Materials that have a maximum attainable refractive index change are considered saturable media, and do not exhibit further changes once this value is reached.[3,4] Saturable media include photorefractive crystals and photochemical systems; the maximum changes are limited by the electric field strength and concentration of reagents, respectively.[41,49,81] Reversible nonlinear materials can revert back to their original state once the optical field is removed, sometimes requiring an external DC electric field such as with liquid crystals and photorefractive crystals. When the changes of refractive index occur in the irradiated region, the response is considered local; nonlocal refractive index changes extend outside of the optical field. Table 1 summarizes select nonlinear mechanisms and provides information about their properties with some examples.

Table 1-1 Select nonlinear mechanisms, examples, required intensities, timescales and properties of the refractive index change.

Type	**Mechanism of Δn**	**Select Examples**	**Intensities and Timescales**	**Properties of Δn**
Kerr Effect	Nonlinear polarization based on $\chi^{(3)}$ $(P_{NL} = \varepsilon_0 \chi^{(3)} \lvert E \rvert^2 E)$	atomic vapor[7,23] e.g. sodium liquids[6,31] e.g. carbon disulfide nanoparticle colloids[5,32] e.g. PS spheres/H_2O	MW cm^{-2} to GW cm^{-2} ~10^{-15} s	Δn ~10^{-4} to 10^{-8} Nonsaturable Reversible Local

Type	Mechanism of Δn	Select Examples	Intensities and Timescales	Properties of Δn
Photorefractive Effect	Nonlinear polarization based on $\chi^{(2)}$ $(P_{NL} = \varepsilon_0 \chi^{(2)} E_1 E_2)$	photorefractive crystals[11,33] e.g. potassium niobate photorefractive polymers[9,82,83] e.g.PVK:5CB	mW cm^{-2} to MW cm^{-2} 10^{-9} s to 10^{2} s	Δn ~10^{-2} to 10^{-4} Saturable Reversible with applied DC field Local or nonlocal
Reorientation Effect	Change orientation/structure relative to external electric field	liquid crystals[12,82] e.g. E7 LC photorefractive polymers with LCs[9,10] e.g. PVK: 7-DCST:CzEPA:TNF	mW cm^{-2} to kW cm^{-2} 10^{-3} s to 10^{-1} s	Δn ~10^{-1} to 10^{-3} Saturable Reversible with applied DC field Nonlocal
Photothermal Effect	Absorbed light generates heat that adjusts the structure of a material	photothermal glass[80] e.g. lead glass dye-doped thermotropic LCs e.g. 4-cyano-4'-pentylbiphenyl/1-(methylamino)-anthraquinone[84,85]	kW cm^{-2} to MW cm^{-2} 10^{-4} s to 10^{-1} s	Δn ~10^{-1} to 10^{-4} Nonsaturable Reversible Nonlocal
Photochemical Reactions	Conversion of one chemical compound results in a product with a different structure and refractive index	doped liquid crystals and polymers[12,16,35,36] e.g. E7 LC/azobenzene photoaddressable polymers e.g. azobenzene polymers[86,87] photosensitive glasses[37–41] e.g. germosilicate glass photopolymers e.g. organosiloxanes[19,20], acrylamides[42,43], epoxies[18,44] with photoinitator	10^{2} μW cm^{-2} to kW cm^{-2} 10^{-3} s to 10^{3} s	Δn ~10^{-1} to 10^{-4} Saturable Reversible or irreversible Local or nonlocal

1.2.1 Kerr effect

The Kerr effect arises due to the nonlinear polarization (1) that occurs in the presence of an electric field ($P_{NL} = \varepsilon_0 \chi^{(3)} |E|^2 E$) based on the symmetric ($\chi^{(3)}$) anharmonicity of the electron displacement. While all materials have a non-zero $\chi^{(3)}$, very high intensities are required (W to GW cm^{-1}) to observe small changes in refractive index (on the order of $\Delta n \sim 10^{-5}$).[1,2,88,89] The responses are essentially instantaneous (10^{-15} s) and local, but they are also nonsaturable, which often results in material damage during self-action effects at extremely large intensities.

1.2.2 Photorefractive effect

The nonlinear polarization (1) emerging from the photorefractive effect occurs due to the asymmetric ($\chi^{(2)}$) anharmonicity of the electron displacement with an electric field ($P_{NL} = \varepsilon_0 \chi^{(2)} E_1 E_2$). An externally applied DC field can result in the electro-optic (Pockels) effect if the field produces a polarization at a particular optical frequency. This effect is only possible in non-centrosymmetric media.[11,33,90] Photorefraction within doped electro-optic materials leads to charge transport and the migration of photo-excited electrons from bright regions to dark regions, creating a charge distribution that forms localized space-charge fields that modify the refractive index. By varying the intensity, the response time can be changed from nanoseconds at high intensities (MW/cm^2) to minutes at low intensities (mW/cm^2).[48,89] Refractive index changes tend to be on the order of 10^{-3} in photorefractive crystals. Photorefractive polymers – conductive polymers doped with photosensitizer – are also able to exhibit this type of effect due to the change in electron distribution, sometimes introducing liquid crystals to amplify the refractive

index modulation.[10,34]

1.2.3 Reorientational effect

Nematic liquid crystals are elongated molecules that can change their spatial orientation in response to an electric field (Figure 1-5).[91] Due to their shape, they are birefringent and show an orientation-dependent refractive index. A polarized beam can reorient liquid crystals differently relative to the bulk by inducing a torque between the liquid crystals and an applied electric field; this external DC electric field is used to pre-align the LCs.[12,15] The maximum change in refractive index is based on the magnitude of birefringence[14] and response times of these systems tend to be on the order of milliseconds to seconds, with refractive index changes on the order of $\sim 10^{-2}$ at intensities of mW to W cm^{-2}.[15] These systems can exhibit nonlocal changes in refractive index when the twisting LCs affect their neighbours, creating a bulk rotation that extends outside the optical field. The re-orientation of liquid crystal systems has also been achieved by adding photoswitchable chromophores, including LCs in photorefractive polymers[92] and adding absorbing dyes to LCs; these methods use a photoisomerization reaction, photorefractive effect and photothermal effects, respectively, to help reorient the liquid crystals. The trajectories of self-trapped beams in LCs (nematicons) have also been shown to interact with additional external electric[93] and magnetic fields,[94] which can alter the trajectories of self-trapped beams in targeted regions.

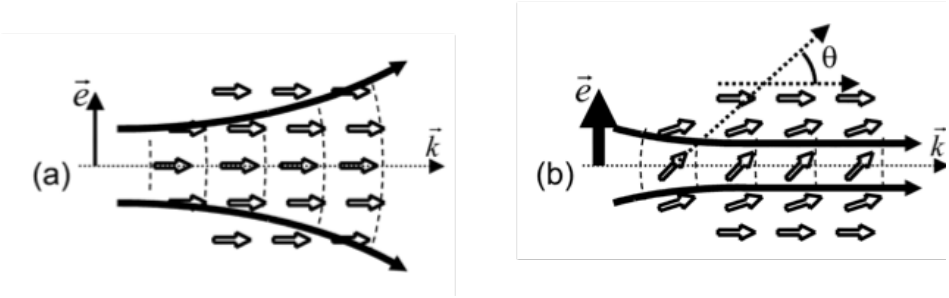

Figure 1-5 Reorientation of liquid crystals in the presence of light and an externally applied electric field can change a diffracting beam (a) to a self-trapped beam (b).[15] © [2003] IEEE. Reprinted, with permission, from Assanto, G.; Peccianti, M. Spatial Solitons in Nematic Liquid Crystals. *IEEE J. Quantum Electron.* **2003**, *39*, 13–21.

1.2.4 Photothermal effects

Photothermal effects are observed in materials where heat from the incident beam can influence the refractive index of the medium.[78,84,95,96] Thermal effects tend to decrease the refractive index due to decreases in the density of the material. Nonradiative dissipation of absorbed light in the form of heat can result in thermal defocusing in PQ-PMMA photopolymers[78] and waves of convection in photopolymers undergoing MI.[27,95] There exist some lead glasses that exhibit positive nonlinearities when exposed to light due to a thermal structural rearrangement that allows the glass to increase its refractive index.[80] Photothermal changes in refractive index are often nonlocal since heat can diffuse through a medium and influence the material outside of the optical field. Photothermal effects have also been applied to change the orientation of thermotropic liquid crystals.[84]

1.2.5 Photochemical reactions

Chemical reactions present another method of refractive index modulation. The absorption of a photon can lead to the formation of a new chemical species; the product of

the reaction will have a different refractive index than that of the starting reagents.[4] Photochemical reactions offer the ability to manipulate the kinetics of nonlinear wave formation, the reversibility of the system, and even the locality of the refractive index changes.[4,18] The formation of any new species within a matrix can also affect the different intermolecular interactions between functional groups and influence the structure, and thereby the refractive index[37].

Reversible photochemical reactions such as photoisomerization and photodimerization lead to changes in optical properties including absorbance and refractive index, but they will also influence the physical properties including hydrophobicity, structure and density. Photoswitchable molecules such as azobenzenes, spiropyrans, diarylethenes, and fulgides possess two chemical forms that can be photochemically converted from one form to another with light (Figure 1-6 A).[97] These photochromic compounds tend to possess one form that is more stable, causing the less stable form to thermally revert back to the stable form, even in the absence of light. Liquid crystals and polymers doped with these reversible photoswitches can change their orientation and structures with light.[12] Covalent attachment of these switches to liquid crystalline polymers (i.e. photoaddressable polymers) have been used to change refractive index in holographic data storage applications.[86] Photodimerization reactions, such as those exhibited by coumarins and cinnamic acid, are bimolecular cycloaddition reactions that have been used to cross-link polymers (Figure 1-6 B).[98] The photodimerized product can often remain in that form much longer than photoswitches, requiring a second wavelength to revert the dimer to its monomer units.

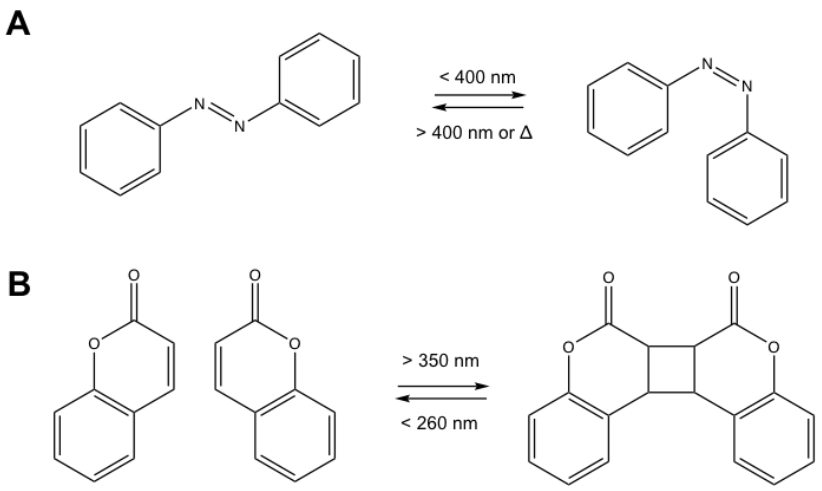

Figure 1-6 The reversible (A) photoisomerization of azobenzene and (B) photodimerization of coumarin.[97,98]

Irreversible photochemical reactions result in permanent patterning of materials such as those exhibited with photosensitive glasses and photopolymers. These reactions often harness photoredox chemistry to generate new chemical species through single electron transfer reactions. Molecular photoredox catalysts, such as octahedral ruthenium and iridium complexes, are ideal for these types of transformations due to the wide range of properties (e.g. absorbance ranges, redox potentials) that are possible by changing the ligands on the metal (Figure 1-7).[99] By tuning the relative redox potentials of the photocatalyst and the reagents, the catalyst can either oxidize or reduce the surrounding reagents. Photoredox reactions have been used in dye-sensitized solar cells with an iodide/triiodide redox couple used in the electrolyte[100] – light is absorbed and converted to electricity through a sequence of electron transfer processes.[101] A variation of the Belousov-Zhabotinsky reaction, a nonlinear chemical oscillator, exhibits a colorimetric perturbation that propagates from its source based on a photoredox reaction.[102,103] The

performance of these catalysts are affected in the presence of oxygen since the photoexcited states of these complexes can often react with oxygen to form singlet oxygen.[104]

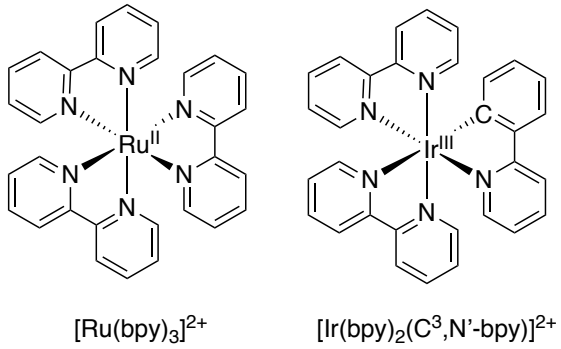

Figure 1-7 Structure of two complexes capable of photoredox chemistry.[99]

Photoredox reactions can also occur with metal ions doped within materials. The response of photosensitive glasses is attributed to metal ions within the glass that are capable of undergoing photoredox reactions upon exposure to light, leading to changes in the charge distribution within the glass and a corresponding change in the structure. These reactions form permanent self-written structures. For example, the reactions in chalcogenide glasses have resulted in different changes from processes including photocrystallization, photopolymerization, photodecomposition, photocontraction, and photoexpansion.[17,37–39,105,106] The associated changes in refractive index in photosensitive glasses tend to be lower than those obtained in photopolymer systems.[37]

Photopolymers are materials where light-induced reactions convert small monomer units into polymer chains, resulting in permanent self-written structures.[107,108] Initiation of a reactive species occurs through the absorption of a photon by a photosensitizer or photoinitiator. The reactive species, often a radical or cation, can react

with monomer to generate a new reactive species. These species continue to react during polymer chain growth (propagation) until a termination event occurs, resulting in polymer. Although the chain growth mechanism is the most commonly employed photopolymerization mechanism, photopolymers can also participate in crosslinking, functionalization, depolymerization, and step-growth reactions with light.[109–111] Photopolymerization reactions achieve refractive index changes often on the order of 10^{-1} to 10^{-3} with intensities ranging from μW-W/cm^2. The larger index contrast of photopolymers relative to photosensitive glasses is often due to the increase in density that occurs from the crosslinking of the polymer and the associated contraction of the polymerized regions.[20,42,43,49] Examples also exist where multiple nonlinear mechanisms were combined; liquid crystalline photopolymers[112] and electro-optic photopolymers[113] combine the changes from the reorientational and photorefractive effects, respectively, to change the refractive index and light distribution during photopolymerization. Photochemical materials all exhibit a saturable refractive index because the index change depends on conversion of one reagent to another and there will always be a finite concentration of reagents to photochemically convert.

Intensity-dependent saturable photochemical systems with irreversible responses can be described by (eq 1.5):

$$\frac{\partial \Delta \mathrm{n(x,y,z,t)}}{\partial t} = AI(x,y,z,t)^p \left(1 - \frac{\Delta n(x,y,z,t)}{\Delta n_s}\right) \tag{1.5}$$

where A is a material-dependent parameter, I is the intensity, p = 1 for single-photon reactions and Δn_s is the maximum achievable refractive index difference.[18,20,39,114,115] Self-trapping in these materials result in self-written waveguides – permanent structures that confine and guide light through total internal reflection.

1.3 Chemistry of photopolymers

Photopolymers are photosensitive polymer-based materials that respond to light through a chemical change. The majority of photopolymers are formed through chain growth of monomer into a polymer. The process begins by photoinitiation, whereupon light creates a reactive species such as a radical, that can react with monomer. The reaction of the active monomer can then propagate, reacting with additional monomer until a termination process ends the growth of the chain. Other types of photopolymers include those formed through light-induced step-growth polymerizations,[109] crosslinking reactions,[111] end-group modification[116] and photo-induced cleavage reactions or depolymerizations.[110] Each of these types of polymers will cause different changes to occur based on the kinetics of the system. The breaking of bonds, for example, can decrease the refractive index of a material upon exposure to light.[110] Inhibition by oxygen or inhibitors present within the monomer can also affect the growth of the polymer chains, slowing down or stopping the formation of polymer at the beginning of the irradiation.[117,118] Chain transfer reactions can end a growing chain and start the growth of a new chain, thereby affecting the spatial distribution of molecular weights and refractive index.[119] Some photopolymer systems that have been used to study nonlinear waves

include organosiloxanes,[19,20] acrylamides,[42,43] epoxies[18,44] and thiol-ene-based systems.[45,46]

One photopolymer that has been shown to exhibit self-trapping, modulation instability and self-phase modulation is 3-(trimethoxysilyl)propyl methacrylate (Figure 1-8).[19,20] 3-(Trimethoxysilyl)propyl methacrylate, Irgacure® 784 (a titanocene photoinitiator) and dilute acid are combined, and stirred for a set amount of time to allow for partial condensation of the siloxane network. This creates a more viscous, partially cross-linked structure containing -SiOSi- linkages as hydrolysis of the methoxy groups occurs. Irgacure® 784, a free-radical photoinitiator, generates radical species with UV or visible light (Figure 1-8), thereby starting the chain growth polymerization of the methacrylate groups and creating denser regions of higher refractive index in the irradiated regions.[120]

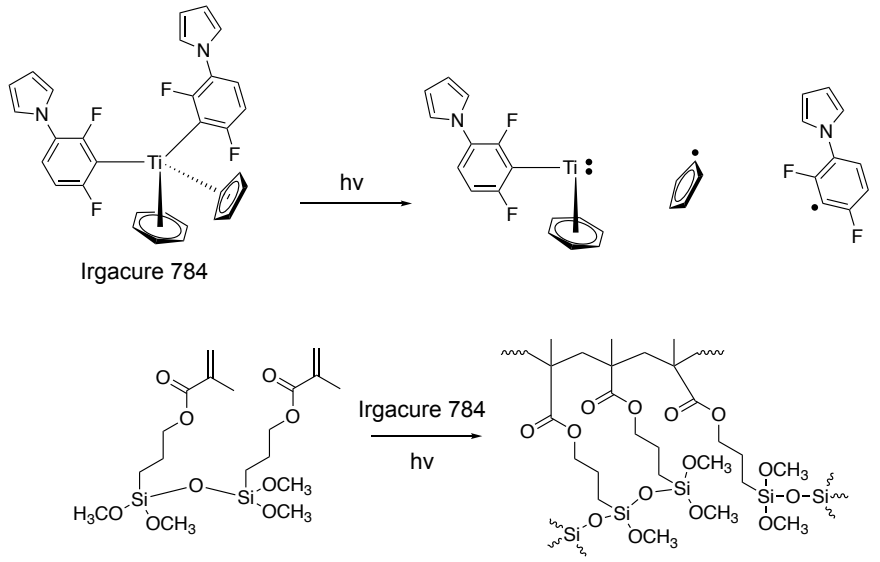

Figure 1-8 Free-radical photopolymerization of 3-(trimethoxysilyl)propyl methacrylate with Irgacure® 784.[120]

While many photoinitiation systems directly form the radicals that react with monomer, some systems use a co-initiator that gets consumed instead of the photosensitizer. One example of such a system is based on an acrylamide photopolymer (Figure 1-9) and has been used for holography and the formation of self-induced waveguides.[42,43] A dye or photosensitizer such as Methylene Blue, Eosin Y or Ploxine B is combined with a co-initiator such as triethanolamine.[42,43] The triethanolamine radical reacts with the acrylate monomers to initiate polymerization. This particular photopolymer formulation uses a poly(vinyl alcohol) (PVA) binder to hold the materials together.

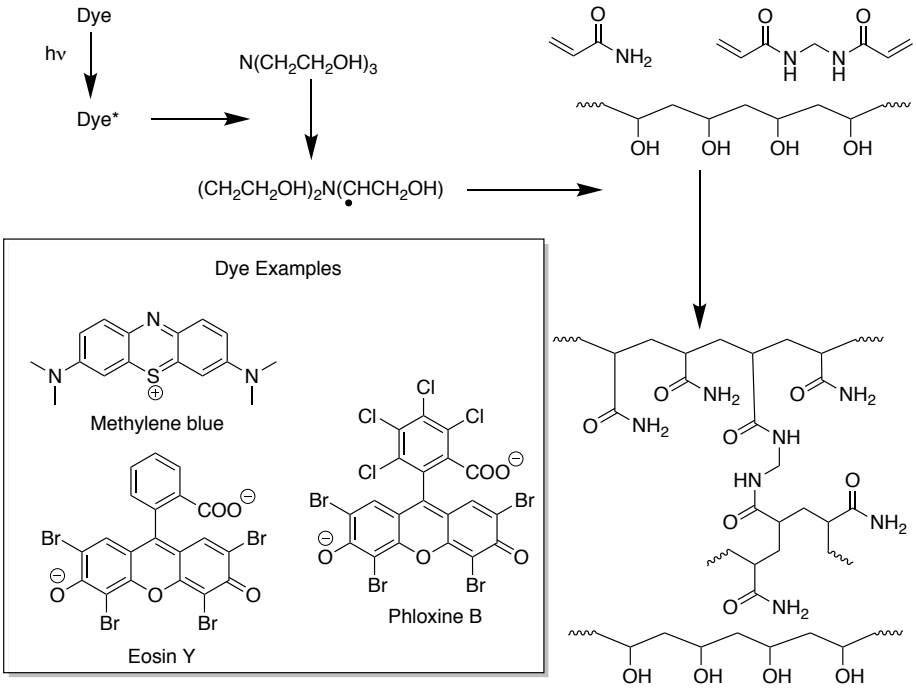

Figure 1-9 Free-radical photopolymerization of acrylamide using a triethanolamine co-initator within a poly(vinyl alcohol) (PVA) binder.[121–125]

Cationic polymerizations can also be utilized and require a cationic species to initiate the polymerization with the cation propagating during chain growth. Diaryliodonium salts are commonly used and can generate cationic species directly from

irradiation (often UV) or they can oxidize a photogenerated radical (formed by a photosensitizer) to create a reactive cation (Figure 1-10).[44,126,127]

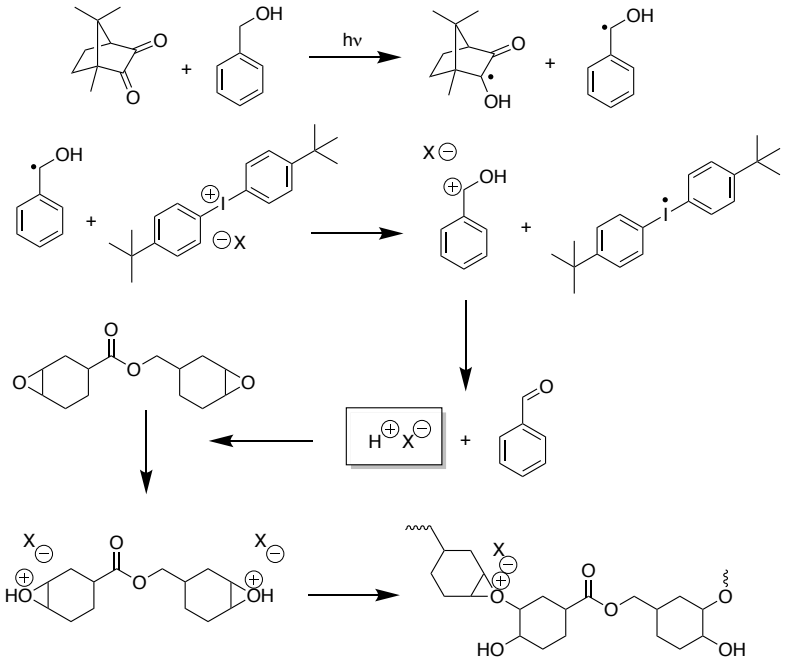

Figure 1-10 Cationic photopolymerization of an epoxide system using a diaryliodonium salt as co-initiator.[44,126,127]

Photopolymerizations that contain chain transfer agents can also enhance the spatial resolution of a polymerized region since they stop the growth of polymer chains. Figure 1-11 depicts a thiol-ene photopolymer that uses this technique in order to improve their structures.[128–131] A photoinitiator (e.g. 2,2-Dimethoxy-2-phenylacetophenone/DMPA), chain transfer agent (e.g. thiol) and monomer (e.g. acrylate) are part of this system. The radicals generated by DMPA react with the thiol to create a radical. During propagation, additional thiol present in the sample can cause further chain transfer reactions that stop the initial chain growth and create a new growing chain. Termination of these polymerizations tend to occur through coupling reactions.

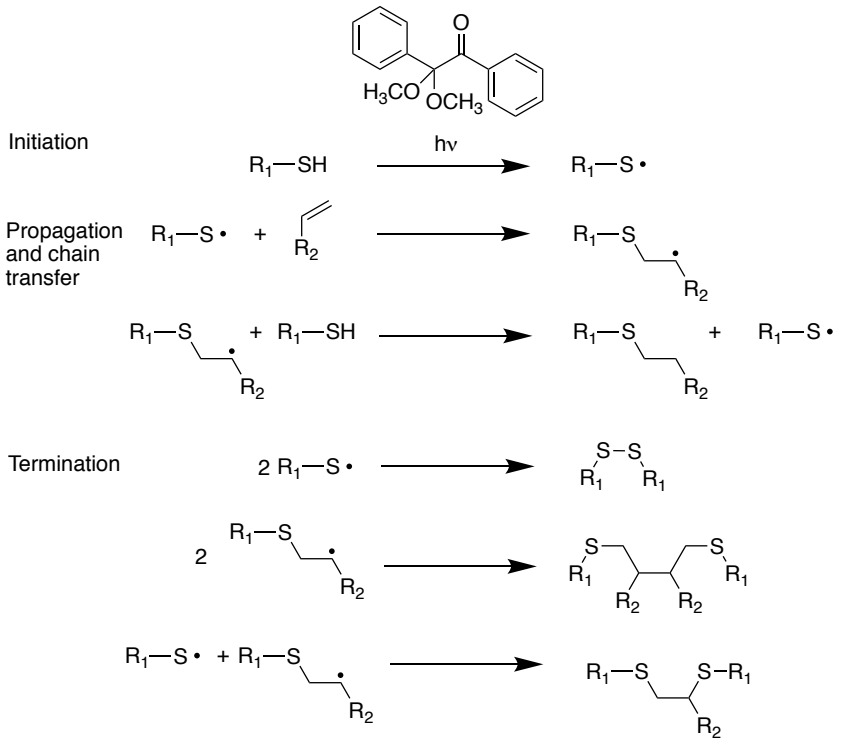

Figure 1-11 Free-radical photopolymerization of thiol-ene photopolymer using 2,2-dimethoxy-2-phenylacetophenone (DMPA).[128–131]

Another type of system that has been used for self-written waveguides is that of crosslinking reactions, where a chemical moiety is attached to an already formed polymer chain. One such example is that of the phenanthrenequinone-doped poly(methyl methacrylate) system (Figure 1-12). Photo-excited phenanthrenequinone can abstract a hydrogen from PMMA, resulting in a semiquinone radical and a polymer radical. These radicals can react with residual olefins in the sample or with one another, resulting in structural rearrangements that influence the refractive index of the sample.[111,132]

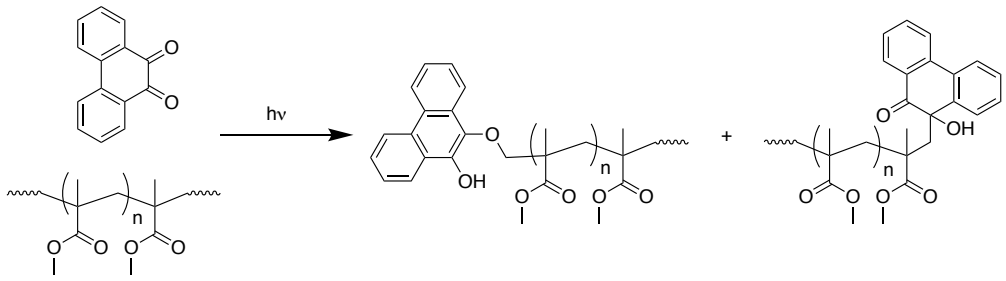

Figure 1-12 Photochemical crosslinking reaction involving phenanthrenequinone and poly(methyl methacrylate) (PQ-PMMA).[111,132]

Degradation reactions, such as the photolysis of poly(methyl methacrylate) with UV light or the deprotection by a photoacid generator (Figure 1-13), also yields a different refractive index, allowing for the formation of Bragg gratings.[133,134] Positive photoresists are known for these photo-induced cleavage reactions.[110]

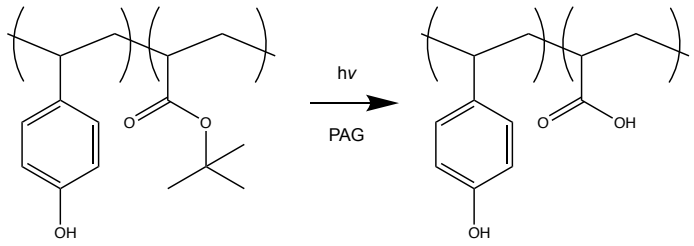

Figure 1-13 Example of a positive photoresist that breaks bonds upon exposure to light due to acid formation from a photoacid generator (PAG).[110]

The formation of nonlinear waveforms within photopolymers depends on the chemical kinetics of the given system and the polymer properties. For example, the sensitivity to visible light can be increased by changing the photoinitiator – different photoinitiators will have different efficiencies and absorbances at different wavelengths.[123–125,135] Two-photon photoinitiators can be used to enhance the spatial resolution of a pattern, since it requires absorption of two photons in order to generate a reactive species.[136–141] Photoinhibitors have also been developed and can prevent polymerization

from occurring in select regions with a second wavelength, by generating radicals that cannot initiate polymerization.[142,143] Refractive index contrast and diffraction efficiency can be increased by using non-active species with different refractive indices that can diffuse as the polymerization occurs, such as high-index nanoparticles.[144] The refractive index of a polymer can be approximated by a version of the Lorentz-Lorenz equation (eq 1.6):[145]

$$\frac{n^2-1}{n^2+2} = \frac{R}{M}\rho \tag{1.6}$$

that describes the refractive index of a polymer, *n*, in terms of molar refraction, R ($cm^3\ mol^{-1}$), molecular weight of a repeat unit, M ($g\ mol^{-1}$), and density, ρ ($g\ cm^{-3}$). The conversion of monomer to polymer in photopolymer systems is accompanied by an increase in density from a contraction, which contributes to the increase in refractive index.[49] Heavier atoms with more electrons tend to be more polarizable, which is why the incorporation of heavier elements is one method of increasing the refractive index of a polymer (larger molar refraction).

Photoinitiators can often react with oxygen, slowing down the polymerization reaction during the initial light exposure, and enhancing resolution by inhibiting polymerization outside the optical field.[104] The delay that occurs in chain growth photopolymers has been included in a model by Kewitsch and coworkers by equation (eq 1.7):

$$\Delta n'(x,y,z,t) = \Delta n' \left\{1 - exp\left[-\frac{1}{U_0}\int_0^{t-\tau} |E(x,y,z,t')|^2 dt'\right]\right\} \tag{1.7}$$

where the change in refractive index is dependent on a critical threshold (U_0) that must be reached in order for the index to grow exponentially.[49] A delay time (τ) is also introduced to account for the delay in growth that occurs in photopolymers due to inhibition. This equation is comparable to (eq 1.5) in that they are both exponential models used to describe saturable systems (Figure 1-14), and both have been utilized to characterize the refractive index development in photopolymers.

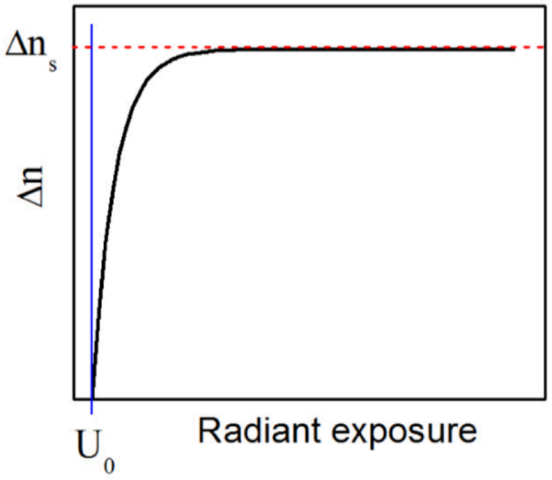

Figure 1-14 Refractive index changes with light exposure above the critical threshold (U_0) in photopolymers. Reprinted with permission from ref 49, The Optical Society.

Polymer properties including molecular weight, dispersity, crosslinking density, wettability, and mechanical properties can be controlled by tuning the chemical structure of the polymer. Larger molecular weight polymers with longer chain lengths tend to have higher refractive indices and are more likely to form solids.[146] The conversion of liquid monomer or oligomers into a solid polymer occurs more rapidly with the formation of larger chains or by the addition of more crosslinker. These more rigid structures tend to be harder with larger crosslinking densities but this is only true below approximately 20-

30% crosslinking density, as very large crosslinking densities can negatively impact the strength of polymers.[146] Monomers with different functional groups will interact with other chains differently once polymerized; these intermolecular polymer-polymer interactions can also act as crosslinks or may form different domains within the polymer, such as those obtained by phase-separated block copolymers.[147] Hydrogen bonding, for example, can be used to form gels within aqueous mixtures of Pluronic® F-127 based on hydrogen bonding between the polymer chains and the water.[148,149]

The dispersity of a polymer describes the distribution of different length chains in a polymer.[146] This property is difficult to measure when dealing with cross-linked structures such as those typically found in photopolymers. High molecular weights, large crosslinking density and nonpolar monomers can be used to control the hydrophobicity or wettability of the polymer. More hydrophilic polymers, such as hydrogels that are swollen with water, can also vary their structures depending on the amount of water they have absorbed. The swelling ratio, obtained by taking the ratio of the swollen and dried polymer, can be used to determine the amount of water that the polymer can support.[146]

Photopolymers are versatile as their physical and optical properties can be tailored by modifying their chemistry. By changing the chemical composition, the degree of polymerization, or the method of polymerization, the resulting physical and optical properties of the end product will change.[150,151] By incorporating different orthogonal functional groups into the polymer chain or side groups, it is possible to create different architectures or introduce post-processing techniques that can change or improve the function of the polymer.[108]

1.4 Interactions between self-trapped beams

Self-trapped beams or spatial solitons formed within nonlinear materials have the ability to interact with one another.[25,38,152,153] The light-guiding-light concept exploits photoinduced changes in a material to influence a second beam of light for the all-optical rerouting of light or optical signals. In this manner, two beams of light, which would ordinarily pass through one another under linear conditions, interact in a discrete way. Investigations into these processes may expand our ability to manipulate and transfer information between two optical signals.[24] The interactions of spatial solitons are very diverse and depend on launch trajectories, input geometries, relative intensities, coherence, relative phases and beam proximity, as well as the mechanism of their formation.[2,3,19,20,25,154] Copropagating beams, colliding beams and even well-separated beams have the potential to interact within nonlinear materials. The understanding of the underlying mechanism of refractive index change is critical to understanding the communicative effects from the resulting interaction. Some of the behaviours that have been observed include attraction between beams, fusion, repulsion, spiraling, annihilation, and birth of solitons. These interactions can even occur over long distances in non-local materials. The following sections describe some of these interactions further.

1.4.1 Interactions between collinear spatial solitons

Spatial solitons travelling parallel to one another have been shown to interact in materials including Kerr media,[155] photorefractive crystals[156], photopolymers,[157]

photothermal glasses[158], nanoparticle colloids[32] and liquid crystals.[14] The interaction has been shown to be highly dependent on the relative phase of the beams when coherent sources are used.[156] Coplanar beams have been shown to attract one another due to constructive interference in the overlapping region between the beams when in-phase and have been shown to repel one another due to destructive interference when out-of-phase (Figure 1-15). The interaction is also highly dependent on spatial proximity of the beams.[25] For example, two in-phase beams that are one beam width apart will interact and fuse into a single beam, but as the input beams are moved further apart, they begin to repel one another, eventually not interacting at all when the distance is too large.[158,159]

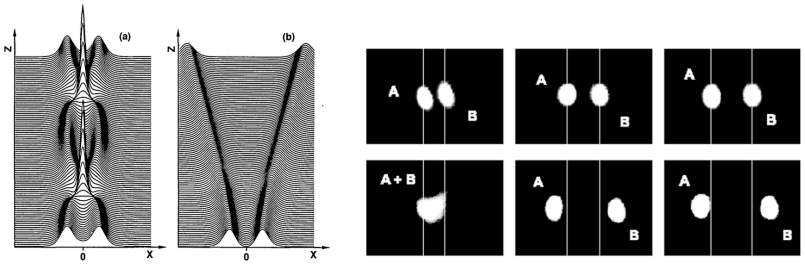

Figure 1-15 (left) Interaction between copropagating coparallel beams in Kerr media [simulation; coherent light in-phase (a) and out-of-phase (b)]. (right) Output of the interaction between copropagating coparallel beams in a photorefractive [different separations before (top) and after interaction (bottom)]. (left) Reprinted with permission from ref 158, The Optical Society. (right) Reprinted with permission from Królikowski, W. et al. Interaction of Two-Dimensional Spatial Incoherent Solitons in Photorefractive Medium. Appl. Phys. B **1999**, 68, 975-982. Copyright 1999 Springer Nature.[159]

This distance-dependent effect has also been observed in photopolymers, where two incoherent beams fused at close proximities and repelled when moved further away.[157] At a certain separation, there was no longer communication between the beams. Chapter 4 is centred primarily on these types of interactions in two photochemical systems.

Two counterpropagating self-trapped beams that are travelling towards one another, perfectly aligned, will often merge to form a single waveguide (Figure 1-16, left).[160] This technique is used for optical solders and interconnects by introducing light from two optical fibers in order to connect the two fibers. If there is any mismatch between trajectories of the counterpropagating waveguides, the growing solitons can experience a repulsion that diverts both beams from their path (Figure 1-16, right).[161]

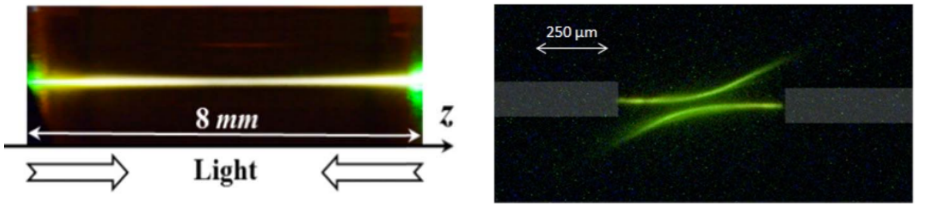

Figure 1-16 Interaction between counterpropagating self-trapped beams in photopolymers; aligned (left) vs. misaligned (right).[161,162] (left) Reprinted with permission from ref 162, The Optical Society. (right) Reprinted with permission from ref 161, The Optical Society.

1.4.2 Interactions between angled solitons

Collisions between solitons leads to several phenomena such as attraction, fusion, interlacing, bending, birth, annihilation and spiraling.[24,25,163,164] Coherent collisions, similar to observations with collinear beams, depends on the relative phase of the beams and can lead to attraction of in-phase beams and repulsion of out-of-phase beams. Incoherent collisions lead to attraction between beams under the same circumstances. When a collision between 2 incoherent beams occurs at a low angle, the beams tend to merge or fuse into a single beam, similar to what occurs with co-parallel beams (Figure 1-

17 A).[50] As this angle is increased, the beams can pass through one another if the beams are perfectly symmetric. These collisions tend to be studied as particle-like interactions; the symmetry of two beams colliding allows them to maintain their trajectories because momentum is conserved. Once this symmetry is broken by increasing the intensity of one of the beams, the collision results in light being guided along the trajectory of the more intense beam (Figure 1-17 B).[165]

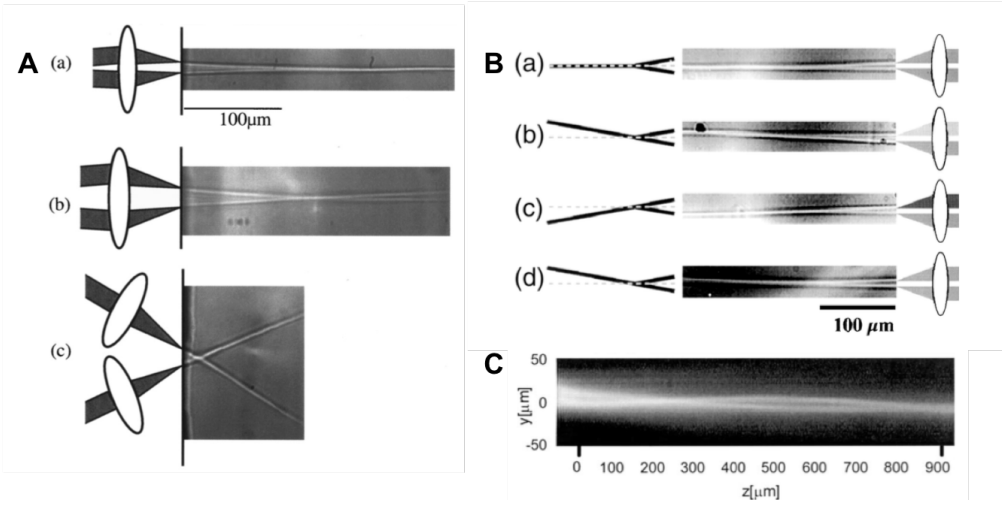

Figure 1-17 Interactions between beams that are angled towards one another with the same intensity (A) and different intensities (B) in photopolymer samples. (C) Interactions between beams in liquid crystals launched away from one another can interlace from an attractive interaction. (A) Reprinted (adapted) with permission from Shoji, S.; Kawata, S. Optically-Induced Growth of Fiber Patterns into a Photopolymerizable Resin. *Appl. Phys. Lett.* **1999**, *75*, 737–739. Copyright 1999 AIP Publishing.[50] (B) Reprinted with permission from ref 165, The Optical Society. (C) Reprinted with permission from ref 166, The Optical Society.

When two beams merge in a liquid crystal material, it is possible to observe an interlacing effect that occurs due to regions of higher refractive index (Figure 1-17 C).[166] A similar phenomenon can be observed in photopolymers, as will be discussed further in

Chapter 4. Collisions have also been used to modulate a passive signal beam with a control beam that elicits a response in a photorefractive crystal.[26,167] The collision causes a shift to the control beam that registers on the photodetector.

When using multiple angles, it is possible to achieve birth and annhilation of solitons. The collision of two solitons can give rise to a third soliton (birth).[164] When the angles and intensities of three incident beams are carefully selected, it is possible to collide three solitons to convert them into two through the annhilation of one of the solitons.[163] This reverse process is often difficult and can result in incomplete annhiliation.

When the collision between two solitons occurs out-of-plane, one of the most interesting effects is orbiting or spiraling of the beams.[80,168–171] Although each self-trapped beam alone possesses no angular momentum, the out-of-plane collision of a system of two beams can result in the rotation of the beams around one another (Figure 1-18). The criteria for this effect are dependent on many parameters such as their proximity to one another, their angular separation and the nonlinear mechanism of the material. Chapter 5 of this thesis explores the orbiting of two self-trapped beams within two different photochemical systems.

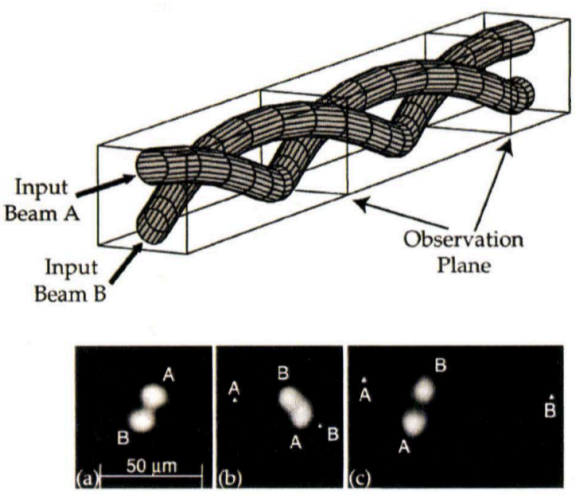

Figure 1-18 3D-Spiraling from an out-of-plane collision between self-trapped beams in a photorefractive crystal results in input beams (a) rotating as they propagate through the sample: (b) 6.5 mm and (c) 13 mm..[170] Reprinted figure with permission from [Shih, M.; Segev, M.; Salamo, G. *Phys. Rev. Lett.* **1997**, *78*, 2551–2554.] Copyright 1997 by the American Physical Society.

1.4.3 Interactions between nonlocal solitons

Two solitons can interact far apart within a medium when the nonlinearity is nonlocal.[80,166,172] Some systems that can exhibit nonlocal nonlinearities include thermal glasses[80] and liquid crystals.[166] In thermal glasses, the nonlocal nature of the nonlinearity is mediated by the thermal diffusion of heat that is photogenerated in the medium. The heat extends outside of the optical field, thereby influencing the refractive index outside of the optical field and allowing two beams to interact at far distances relative to one another (Figure 1-19, left).[80] Spiraling has also been observed in this system with well-separated beams and interactions have also been demonstrated in two separate materials connected by thermally conductive wire.

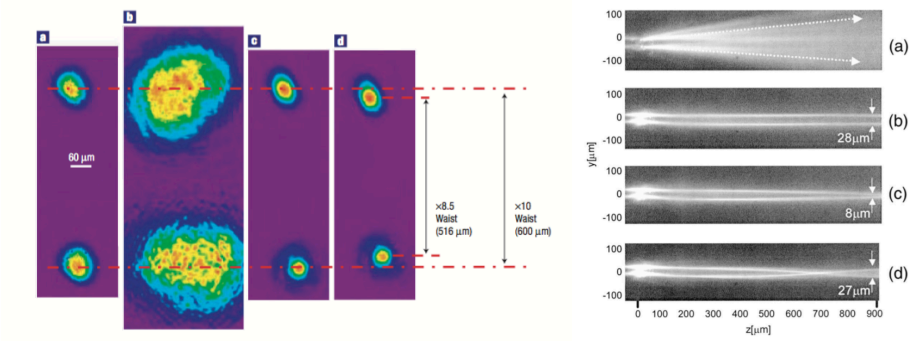

Figure 1-19 Nonlocal attraction in a photothermal glass (left) and in a liquid crystal sample with increasing intensity from top to bottom (right). [80,166] (left) Reprinted by permission from Rotschild, C.; Alfassi, B.; Cohen, O.; Segev, M. Long-Range Interactions between Optical Solitons. *Nature Physics*. **2006**, *2*, 769–774. Copyright 2006 Springer Nature.[80] (right) Reprinted with permission from ref 166, The Optical Society.

In liquid crystal materials, the change in orientation of the liquid crystals from the optical field causes the neighbouring liquid crystals to rotate as well – this torque extends beyond the optical field and can influence the refractive index in those areas.[166] One example of this occurs when two beams that are directed away from one another begin to attract one another across distances much greater than the beam width (Figure 1-19, right).[166] As the intensity of each beam is increased, the refractive index change increases causing a greater attraction to occur between the beams.

Within this thesis, multiple types of interactions are observed between self-trapped beams including the (i) attraction between beams, (ii) merging of beams into a single waveguide, (iii) nonlocal attraction between beams, (iv) orbiting of beams, (v) swapping of beam positions, and (vi) inhibition of the self-trapping of a neighbouring beam – each of these observations reveals a new aspect to these interactions within photochemical systems.

1.5 Applications of photopolymers

Nonlinear light propagation in photopolymers offers the ability to fabricate permanent, self-inscribed functional structures in materials. One consequence of using nonlinear waves of light to inscribe structures within polymers is that the resulting polymer structures will also possesses light-guiding properties. This method has been harnessed to create three-dimensional microstructured materials.[28,117,173–176] The self-inscription of macroscopic structures has also been achieved and used as a fast method of 3D printing.[28,177] Photopolymers have also been used in holography and data storage, recording information in the form of patterns within the photopolymer.[29,178] The ability to impart other functionalities to polymers allows us to make these light-guiding structures that are responsive to other stimuli such as heat,[179] pH[180] and electric fields.[181] Using these stimuli, it would be possible to modulate passive devices of different geometries after they have been printed.

1.5.1 Fabrication of three-dimensional microstructures and integrated optics

Optical self-trapping within photopolymers can lead to individual self-written waveguides that can be incorporated into devices for polymer-based optics.[182–189] One commonly discussed element is the optical interconnect or optical solder.[160,190–194] Optical interconnects can be used to connect two optical waveguides by submerging the two waveguides into a polymer resin until the two fibers are connected (Figure 1-20 A). Two slightly misaligned waveguides can still merge and connect within a certain tolerance.

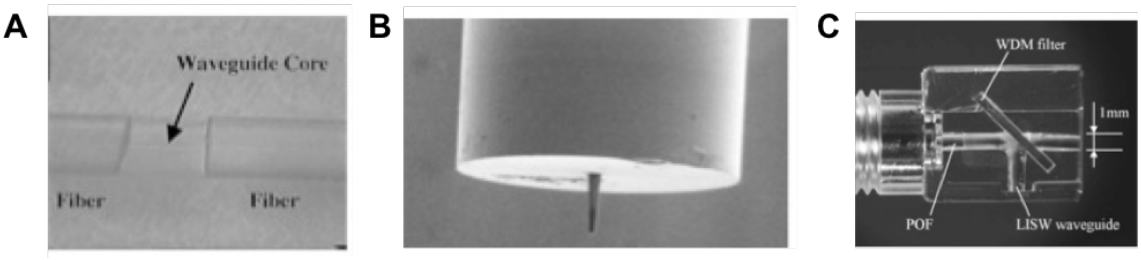

Figure 1-20 Optical self-inscribed waveguide devices including (A) an optical interconnect bridging two optical fibers, (B) a tipped fiber and (C) a visible wavelength multiplexing module. (A) © [2003] IEEE. Reprinted, with permission, from Sugihara, O.; Tsuchie, H.; Endo, H.; Okamoto, N.; Yamashita, T.; Kagami, M.; Kaino, T. Light-Induced Self-Written Polymeric Optical Waveguides for Single-Mode Propagation and for Optical Interconnections. *IEEE Photonics Technol. Lett.* **2004**, *16*, 804–806.[195] (B) Reprinted with permission from ref 196, The Optical Society. (C) Reprinted with permission from ref 197, The Optical Society.

Self-written waveguides with luminescent[174] and photochromic dyes[198] have been fabricated as well. Controlled growth of a self-written fiber can form different polymer fiber tips (Figure 1-20 B) that can be used to control the optical profile, including potential applications as microlenses.[196] A visible light multiplexing module was fabricated using self-written waveguides and allowed the transmission of green light and reflection of red light (Figure 1-20 C). This was achieved by incorporating a filter into the photopolymerizing resin prior to the self-writing process. This module could be incorporated within an optical circuit to divert particular wavelengths of light.[197]

Larger three-dimensional structures can also be created through the simultaneous generation of large populations of self-trapped beams, using masks to create several self-trapped filaments at once.[45,46,175,176,199–204] This process has also been demonstrated using the breakup of a beam due to modulation instability and relying on the noise of the system to generate self-trapped filaments.[27,51,65] Photolithographic techniques have been used to

create micropillar arrays[199–202] and conic structures.[175] Lattice structures such as micro-trusses[45,46,203], radial arrays[204] and other intersecting arrays[176] have been built using nonlinear waves. The application of nonlinear waves has also extended into polymer blends, taking advantage of the photo-induced polymerization in the presence of inactive polymers to instigate phase separation.[205–207]

Materials that are composed of large arrays of self-trapped filaments have been shown to enhance light collection, carry out lens-like operations and have large fields of view.[176,204] These waveguide-encoded lattices (WELs) contain different orientations of waveguides throughout the material, including five separate angled arrays of intersecting waveguides (Figure 1-21 A)[176] and WELs with a radial distribution of waveguides. (Figure 1-21 B).[204]

The physical properties of these self-written structures have also been modified. Micro-truss structures have been made flexible by selecting an appropriate photopolymer (Figure 1-21 C).[45,46,203] Compression tests were conducted on several of these micro-truss structures to optimize strength and stability, and their buckling behaviour has demonstrated a resistance to external stresses, making them ideal candidates for applications such as heat exchangers[208], metallic microlattices[209] and sacrificial templates.[210]

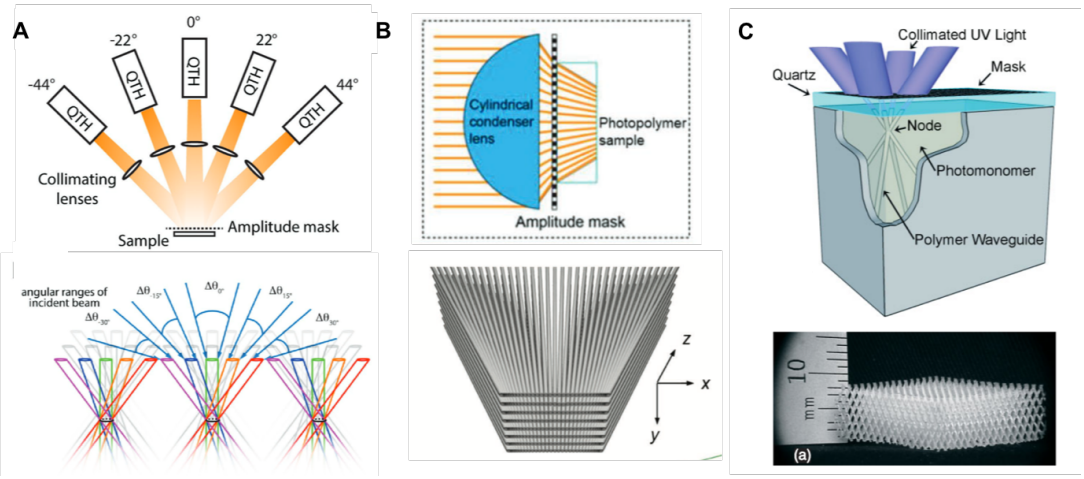

Figure 1-21 (A) Waveguide-encoded lattice (WEL) with 5 intersecting arrays of self-trapped filaments, each possessing its own angular acceptance range and a large cumulative field of view (B) WEL with a radial distribution of waveguides capable of lens-like operations and a continuous field of view (C) Micro-truss lattice composed of self-propagating waveguides with improved buckling behaviour. Reprinted with permission from (A) ref 176, (B) ref 204, and (C) ref 45, John Wiley and Sons.

Permanently inscribed self-written waveguides have an angular acceptance range that depends on the refractive index contrast between the core and the cladding (eq 1.8).[154]

$$\theta_A < \arcsin\left(\sqrt{n_{core}^2 - n_{clad}^2}\right) \quad (1.8)$$

Light contained within waveguides can be shared between adjacent waveguides depending on the distribution of refractive index. Waveguides can also be characterized by the modes that they can support. The majority of examples presented in this thesis focus on the TEM_{00} mode, but as the refractive index difference increases between a self-written waveguide and the background index, higher order modes can become supported. Small waveguides can be used to contain a single mode – the fundamental[211] – whereas

larger waveguides become multimodal. The modes within an optical fiber depend on the core size (a) and the refractive index contrast (eq 1.9).[212]

$$V = \frac{2\pi}{\lambda} a\sqrt{n_{core}^2 - n_{clad}^2} \quad (1.9)$$

When the V-number <2.405, only the fundamental mode can exist within the fiber, where k_0 is the wavenumber, a is the core radius and λ is the wavelength of interest. [212] Single mode self-trapped Gaussian beams can become multimodal as thickening of the waveguide core occurs over time. Saravanamuttu et al. created self-induced waveguides in a hybrid glass[213] and demonstrated that when the refractive index of the self-induced waveguide increases sufficiently, higher-order modes can be hosted and cause periodic intensity variations in the waveguide.[20] Waveguides and waveguide-encoded lattice structures offer many possibilities for passively manipulating light.

1.5.2 3D printing

Nonlinear waves can be extended to create macroscopic objects using 3D printing. 3D printing is a method of creating 3D materials by converting volumetric information on a computer to a physical three-dimensional object. A layer-by-layer method is often employed; some of these include inkjet printing, fused deposition modeling, selective laser sintering, and stereolithography.[214] The process of stereolithography also uses photopolymerization to spatially control the solidification of a monomer and photoinitiator mixture.[215] Light is projected onto a resin bath to create the first layer that adheres to the bottom of a stage (Figure 1-22A). The stage is then translated vertically, and the next layer is created in the same manner. This process is then repeated until the full object has been printed.

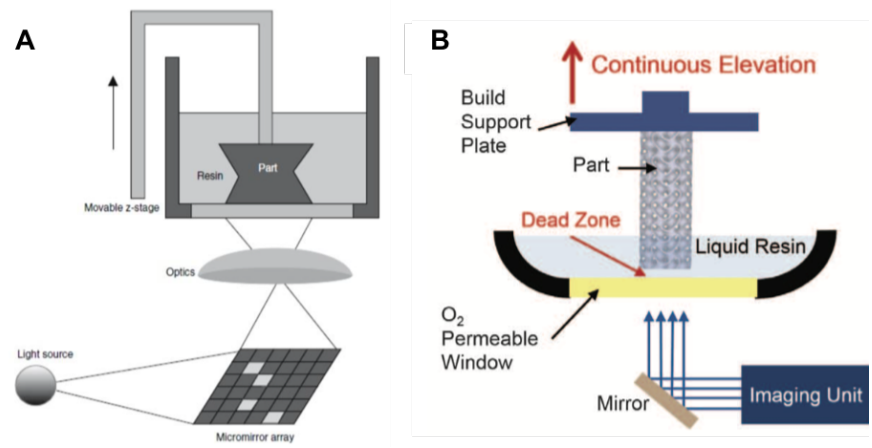

Figure 1-22 (A) Setup of a standard stereolithographic 3D printer and (B) setup of a continuous liquid interface production (CLIP) printer that utilizes an oxygen permeable window to allow for continuous printing. (A) Reprinted with permission from Liska, R. et al. Photopolymers for Rapid Prototyping. *J. Coatings Technol. Res.* **2007**, *4*, 505–510. Copyright 2007 Springer Nature.[215] (B) Reprinted with permission from ref 216, The American Association for the Advancement of Science.

There have been recent advances that move away from the layer-by-layer method of printing to methods that are continuous, allowing for seamless objects to be fabricated. One such technique is 3D NSCRIPT, a method for creating micro- and macroscopic dielectric and metallodielectric polymer structures with seamless depths using nonlinear waves of blue light.[177] This technique exploits the self-trapping of light during epoxide photopolymerization to inscribe 3D structures. It was also shown that the simultaneous reduction of gold salts could be carried out during photopolymerization, resulting in the formation of gold nanoparticles in the final structures. A working da Vinci catapult was printed using this method, which employs amplitude masks to selectively irradiate regions of the photopolymer sample – the pattern that is exposed to light propagates through the medium to inscribe the target structures. Some of the limitations of this technique are

described in Chapter 6, where we describe the geometric features that are required when implementing nonlinear waves for printing.

In Continuous Liquid Interface Production (CLIP), UV images are projected under the resin bath onto an oxygen-permeable window placed at the bottom of the bath, thus creating a dead zone in which no polymerization takes place (Figure 1-22 B)[216]. The printing process starts above the dead zone and as it proceeds, the object is pushed out of the resin bath, leaving a space that is occupied by new resin. This process is significantly faster (500 mm/hour) than conventional stereolithography (a few millimeters/hour) since the layers are continuously produced.

Spadaccini et al. developed two techniques that can fabricate 3D objects without a layer-by-layer process; one approach involves the formation of a hologram within the resin and the other involves launching images into the resin while it rotates. The holographic 3D approach uses patterned optical fields from a green laser and launches them orthogonally into a photopolymer resin bath, creating objects in a pure 3D unit operation.[13] This technique creates non-periodic objects with a high complexity in a time scale of seconds, but it requires lasers and sophisticated optical equipment to implement. The second approach – computed axial lithography (CAL) – is a technique where light patterns are launched from a DLP (Digital Light Processing) projector into a photoresin on a rotating stage[217,218]. As the stage rotates, the light patterns are changed based on computed images, creating objects with a constant cross-section in z (Figure 1-23).[14]

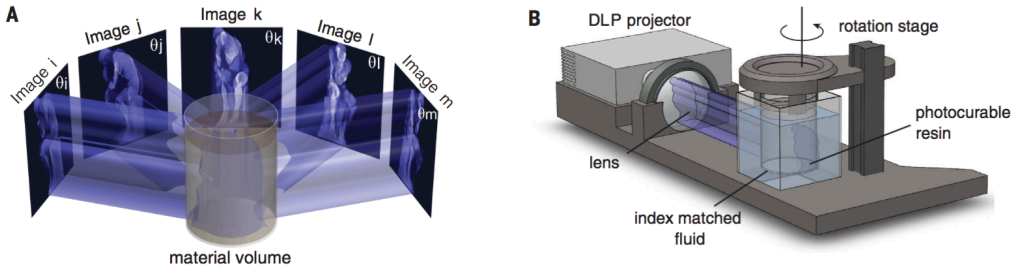

Figure 1-23 Computed axial lithography (CAL) setup uses multiple images from a DLP projector launched at a rotating sample to create 3D objects. Reprinted with permission from ref 219, The American Association for the Advancement of Science.

The resolution of light-based 3D printing techniques have been improved by using photoinhibitors,[142,143] two-photon photoinitators,[137,214] and photochromic dyes.[220,221] Use of photochromic dyes or large amounts of photoinitiator have also led to formation of conical structures.[220,221] Many of the tools for modifying photopolymers were discussed in Section 1.3; these additives and polymer properties can be controlled to enable faster printing speeds, better resolutions and more functionalities of the final printed structures.

1.6 Summary

A variety of self-action effects and beam interactions are possible in nonlinear media. The dynamics of these phenomena depend strongly on the type of nonlinearity and the underlying mechanism. Although self-trapping and other nonlinear effects have been studied in photopolymers, less research has occurred on self-trapping in other photochemical materials.

In this thesis, we demonstrate (i) the ability to develop new photochemical systems capable of hosting nonlinear waves, (ii) the capacity of these nonlinear waves to interact

with one another when they are launched into these systems, and (iii) the capability of harnessing these nonlinear waves to 3D print seamless prismatic elements.

Chapters 2 and 3 describe two such photochemical systems that are capable of generating self-trapped beams. The interactions of these self-trapped beams are described in Chapters 3, 4 and 5 and demonstrate the ability to merge, spiral or even cause inhibition of self-trapping for its co-parallel propagating partner. Chapter 6 describes how a 3D object can be broken down into prismatic elements that can be subsequently printed using nonlinear waves in a photopolymer.

This thesis expands on the previous self-trapping knowledge in photochemical systems in a significant way and will hopefully inspire further advancements of coupling light-induced waves with chemistry. Chapter 7 also contains select additional experimental data that may inspire future projects, including work on electroactive polymer waveguides that can be used to bend light with application of electric fields.

1.7 Published contributions to the field of nonlinear light propagation in polymers

Contributions to the field of nonlinear light propagation in polymers within this thesis includes studies into new photochemical polymer-based materials, investigations into interactions between self-trapped beams using these systems and the use of propagating photochemical waves to 3D printing.

The thesis consists of 5 articles which have been accepted or submitted to scientific journals and 2 reviews with select information included within the introduction.

Articles:

(1) Morim, D. R.; Vargas-Baca, I. Saravanamuttu, K. Reversibly Trapping Visible Laser Light through the Catalytic Photo-oxidation of I^- by $Ru(bpy)_3^{2+}$. *J. Phys. Chem. Lett.* **2016***, 7*, 1585-1589.
(2) Morim, D. R.; Meeks, A.; Shastri, A.; Tran, A. Shneidman, A. V.; Mahmood, F. Aizenberg, J.; Saravanamuttu, K. Opto-chemo-mechanical transduction in photoresponsive gels: switchable self-trapped beams and their remote interactions. *Submitted 2019.*
(3) Morim, D. R.; Shastri, A.; Aizenberg, J.; Vargas-Baca, I.; Saravanamuttu, K. Interactions Between Collinear Photochemically-Formed Self-Trapped Beams. *In Preparation.*
(4) Morim, D. R.; Bevern, D.; Vargas-Baca, I.; Saravanamuttu, K. 3D Spiraling Self-Trapped Light Beams in Polymers. *Submitted 2019.*
(5) Cortes, O. A. H.; Morim, D. R.; Colin, D.; Martinez Hernandez, E. A.; Arora, R.; Saravanamuttu, K. Prismatic 3D Printing: Rapid Photopolymerization of Seamless Elements and Construction of 3D Objects. *In Preparation.*

Reviews:

(1) Biria, S.; Morim, D. R.; Tsao, F. A.; Saravanamuttu, K.; Hosein, I. D. Coupling nonlinear optical waves to photoreactive and phase-separating soft matter: Current status and perspectives. *Chaos* **2017**, *27*, 104611.
(2) Morim, D. R.; Tsao, F. A.; Hosein, I. D.; Saravanamuttu, K. 3-D Printing Functional Polymer Architectures with Nonlinear Waves of Light: Progress and Opportunities. *In Preparation.*

1.8 Author contributions

Chapter 2 (Article 1): DRM performed experimental work. DRM, IVB, KS conceived experiments, analyzed data and wrote the manuscript.

Chapter 3 (Article 2): DRM, AM and AS contributed equally to this manuscript. DRM, AS, AT, FM, KS designed, carried out and analysed data from experimental studies. AM developed and wrote the numerical model used in simulations. DRM, AS, AM, AVS, JA, KS wrote and edited the manuscript.

Chapter 4 (Article 3): DRM and AS performed experimental work. DRM, AS, JA, IVB, KS wrote and edited the manuscript.

Chapter 5 (Article 4): DRM and DB performed experimental work. DRM, IVB, KS conceived experiments, analyzed data and wrote the manuscript.

Chapter 6 (Article 5): OAHC and DRM contributed equally to this manuscript. OAH, DRM, DC, EAMH, RA performed experimental work. DRM was responsible for the decomposition of objects into prisms. DRM, KS, IVB, and OAH wrote and edited the manuscript.

Chapter 7 (Outlook): Figure 7-5 contains data obtained by DRM, NB and OAHC based on prismatic printing of electroactive polymers.

1.9 References

(1) Chiao, R. Y.; Garmire, E.; Townes, C. H. Self-Trapping of Optical Beams. *Phys. Rev. Lett.* **1964**, *13*, 479–482.

(2) Trillo, S.; Torruellas, W. *Spatial Solitons*; Springer: New York, 2001.

(3) Boyd, R. W. *Nonlinear Optics*, 2nd ed.; Academic press: San, 2003.

(4) Biria, S.; Morim, D. R.; An Tsao, F.; Saravanamuttu, K.; Hosein, I. D. Coupling Nonlinear Optical Waves to Photoreactive and Phase-Separating Soft Matter: Current Status and Perspectives. *Chaos* **2017**, *27*, 104611.

(5) Ashkin, A.; Dziedzic, J. M.; Smith, P. W. Continuous-Wave Self-Focusing and Self-Trapping of Light in Artificial Kerr Media. *Opt. Lett.* **1982**, *7*, 276–278.

(6) Ganeev, R. A.; Ryasnyansky, A. I.; Baba, M.; Suzuki, M.; Ishizawa, N.; Turu, M.; Sakakibara, S.; Kuroda, H. Nonlinear Refraction in CS2 . *Appl. Phys. B* **2004**, *78*, 433–438.

(7) Ackemann, T.; Scholz, T.; Vorgerd, C.; Nalik, J.; Hoffer, L. M.; Lippi, G. L. Self-Lensing in Sodium Vapor: Influence of Saturation, Atomic Diffusion and Radiation Trapping. *Opt. Commun.* **1998**, *147*, 411–428.

(8) Shih, M. F.; Leach, P.; Segev, M.; Garrett, M. H.; Salamo, G.; Valley, G. C. Two-Dimensional Steady-State Photorefractive Screening Solitons. *Opt. Lett.* **1996**, *21*, 324–326.

(9) Sutter, K.; Hulliger, J.; Günter, P. Photorefractive Effects Observed in the Organic Crystal 2-Cyclooctylamino-5-Nitropyridine Doped with 7,7,8,8-Tetracyanoquinodimethane. *Solid State Commun.* **1990**, *74*, 867–870.

(10) Chen, Z.; Asaro, M.; Ostroverkhova, O.; Moerner, W. E.; He, M.; Twieg, R. J. Self-Trapping of Light in an Organic Photorefractive Glass. *Opt. Lett.* **2003**, *28*, 2509–2511.

(11) Lan, S.; Shih, M.; Segev, M. Self-Trapping of One-Dimensional and Two-Dimensional Optical Beams and Induced Waveguides in Photorefractive KNbO3. *Opt. Lett.* **1997**, *22*, 1467–1469.
(12) Peccianti, M.; Assanto, G. Signal Readdressing by Steering of Spatial Solitons in Bulk Nematic Liquid Crystals. *Opt. Lett.* **2001**, *26*, 1690–1692.
(13) Karpierz, M. A.; Assanto, G. Light Self-Trapping in Nematic Liquid Crystals. In *Localized States in Physics: Solitons and Patterns*; Springer, 2011; pp 3–16.
(14) Assanto, G.; Karpierz, M. A. Nematicons: Self-Localised Beams in Nematic Liquid Crystals. *Liq. Cryst.* **2009**, *36*, 1161–1172.
(15) Assanto, G.; Peccianti, M. Spatial Solitons in Nematic Liquid Crystals. *IEEE J. Quantum Electron.* **2003**, *39*, 13–21.
(16) Serak, S. V.; Tabiryan, N. V.; Assanto, G. Nematicons in Azobenzene Liquid Crystals. *Molecular Crystals and Liquid Crystals*. 2012, pp 202–213.
(17) Aitchison, J. S.; Silberberg, Y.; Weiner, A. M.; Leaird, D. E.; Oliver, M. K.; Jackel, J. L.; Vogel, E. M.; Smith, P. W. E. Spatial Optical Solitons in Planar Glass Waveguides. *J. Opt. Soc. Am. B* **1991**, *8*, 1290–1297.
(18) Frisken, S. J. Light-Induced Optical Waveguide Uptapers. *Opt. Lett.* **1993**, *18*, 1035.
(19) Zhang, J.; Kasala, K.; Rewari, A.; Saravanamuttu, K. Self-Trapping of Spatially and Temporally Incoherent White Light in a Photochemical Medium. *J. Am. Chem. Soc.* **2006**, *128*, 406–407.
(20) Villafranca, A. B.; Saravanamuttu, K. An Experimental Study of the Dynamics and Temporal Evolution of Self-Trapped Laser Beams in a Photopolymerizable Organosiloxane. *J. Phys. Chem. C* **2008**, *112*, 17388–17396.
(21) Villafranca, A. B.; Saravanamuttu, K. Diffraction Rings Due to Spatial Self-Phase Modulation in a Photopolymerizable Medium. *J. Opt. A Pure Appl. Opt.* **2009**, *11*, 125202.
(22) Villafranca, Ana; Saravanamuttu, K. Spontaneous and Sequential Transitions of a Gaussian Beam into Diffraction Rings, Single Ring and Circular Array of Filaments in a Photopolymer. *Opt. Express* **2011**, *19*, 15560–15573.
(23) Zerom, P.; Boyd, R. W. Self-Focusing, Conical Emission, and Other Self-Action Effects in Atomic Vapors BT - Self-Focusing: Past and Present: Fundamentals and Prospects; Boyd, R. W., Lukishova, S. G., Shen, Y. R., Eds.; Springer New York: New York, NY, 2009; pp 231–251.
(24) Snyder, A. W.; Sheppard, A. P. Collisions, Steering, and Guidance with Spatial Solitons. *Opt. Lett.* **1993**, *18*, 482–484.
(25) Stegeman, G. I.; Segev, M. Optical Spatial Solitons and Their Interactions: Universality and Diversity. *Science* **1999**, *286*, 1518–1523.
(26) Andrade-Lucio, J. A.; Alvarado-Mendez, B.; Rojas-Laguna, R.; Ibarra-Manzano, O. G.; Torres-Cisneros, M.; Jaime-Rivas, R.; Kuzin, E. A. Optical Switching by Coherent Collision of Spatial Solitons. *Electron. Lett.* **2000**, *36*, 1403–1405.
(27) Burgess, I. B.; Shimmell, W. E.; Saravanamuttu, K. Spontaneous Pattern Formation Due to Modulation Instability of Incoherent White Light in a Photopolymerizable Medium. *J. Am. Chem. Soc.* **2007**, *129*, 4738–4746.

(28) Kewitsch, A. S.; Yariv, A. Nonlinear Optical Properties of Photoresists for Projection Lithography. *Appl. Phys. Lett.* **1996**, *68*, 455–457.
(29) Malallah, R.; Li, H.; Kelly, P. D.; Healy, J. J.; Sheridan, T. J. A Review of Hologram Storage and Self-Written Waveguides Formation in Photopolymer Media. *Polymers*. 2017, p 337.
(30) Schawlow, A. L.; Townes, C. H. Infrared and Optical Masers. *Phys. Rev.* **1958**, *112*, 1940–1949.
(31) Shen, Y. R. Self-Focusing: Experimental. *Prog. Quantum Electron.* **1975**, *4*, 1–34.
(32) Fardad, S.; Mills, M. S.; Zhang, P.; Man, W.; Chen, Z.; Christodoulides, D. N. Interactions between Self-Channeled Optical Beams in Soft-Matter Systems with Artificial Nonlinearities. *Opt. Lett.* **2013**, *38*, 3585–3587.
(33) Pismennaya, K.; Kashin, O.; Matusevich, V.; Kiessling, A.; Kowarschik, R. Beam Self-Trapping and Self-Bending Dynamics in a Strontium Barium Niobate Crystal. *J. Opt. Soc. Am. B* **2008**, *25*, 136–139.
(34) Moerner, W. E.; Grunnet-Jepsen, A.; Thompson, C. L. PHOTOREFRACTIVE POLYMERS. *Annu. Rev. Mater. Sci.* **1997**, *27*, 585.
(35) Yang, X.; Qi, S.; Zhang, C.; Chen, K.; Liang, X.; Yang, G.; Xu, T.; Han, Y.; Tian, J. The Study of Self-Diffraction of Mercury Dithizonate in Polymer Film. *Opt. Commun.* **2005**, *256*, 414–421.
(36) Morim, D. R.; Vargas-Baca, I.; Saravanamuttu, K. Reversibly Trapping Visible Laser Light through the Catalytic Photo-Oxidation of I-by Ru (Bpy) 32+. *J. Phys. Chem. Lett.* **2016**.
(37) Monro, T. M.; Moss, D.; Bazylenko, M.; Martijn de Sterke, C.; Poladian, L. Observation of Self-Trapping of Light in a Self-Written Channel in a Photosensitive Glass. *Phys. Rev. Lett.* **1998**, *80*, 4072–4075.
(38) Monro, T. M.; De Sterke, C. M.; Poladian, L. Catching Light in Its Own Trap. *J. Mod. Opt.* **2001**, *48*, 191–238.
(39) Monro, T. M.; Martijn de Sterke, C.; Poladian, L. Self-Writing a Waveguide in Glass Using Photosensitivity. *Opt. Commun.* **1995**, *119*, 523–526.
(40) Monro, T. M.; Sterke, C. M. De; Poladian, L. Investigation of Waveguide Growth in Photosensitive Germanosilicate Glass. **2006**, *13*, 2824–2832.
(41) Monro, T. M.; de Sterke, C. M.; Poladian, L. Analysis of Self-Written Waveguide Experiments. *J. Opt. Soc. Am. B* **1999**, *16*, 1680–1685.
(42) Li, H.; Qi, Y.; Ryle, J. P.; Sheridan, J. T. Self-Written Waveguides in a Dry Acrylamide/Polyvinyl Alcohol Photopolymer Material. *Appl. Opt.* **2014**, *53*, 8086–8094.
(43) Jisha, C. P.; Kishore, V. C.; John, B. M.; Kuriakose, V. C.; Porsezian, K.; Kartha, C. S. Self-Written Waveguide in Methylene Blue Sensitized Poly(Vinyl Alcohol)/Acrylamide Photopolymer Material. *Appl. Opt.* **2008**, *47*, 6502–6507.
(44) Basker, D. K.; Brook, M. A.; Saravanamuttu, K. Spontaneous Emergence of Nonlinear Light Waves and Self-Inscribed Waveguide Microstructure during the Cationic Polymerization of Epoxides. *J. Phys. Chem. C* **2015**, *119*, 20606–20617.
(45) Jacobsen, A. J.; Barvosa-Carter, W.; Nutt, S. Micro-Scale Truss Structures Formed from Self-Propagating Photopolymer Waveguides. *Adv. Mater.* **2007**, *19*, 3892–

3896.
(46) Jacobsen, A. J.; Barvosa-Carter, W.; Nutt, S. Micro-Scale Truss Structures with Three-Fold and Six-Fold Symmetry Formed from Self-Propagating Polymer Waveguides. *Acta Mater.* **2008**, *56*, 2540–2548.
(47) Stegeman, G. I. A.; Christodoulides, D. N.; Segev, M. Optical Spatial Solitons: Historical Perspectives. *IEEE J. Sel. Top. Quantum Electron.* **2000**, *6*, 1419–1427.
(48) Kivshar, Y. S.; Agrawal, G. P. *Optical Solitons*; Academic Press, 2003.
(49) Kewitsch, a S.; Yariv, a. Self-Focusing and Self-Trapping of Optical Beams upon Photopolymerization. *Opt. Lett.* **1996**, *21*, 24–26.
(50) Shoji, S.; Kawata, S. Optically-Induced Growth of Fiber Patterns into a Photopolymerizable Resin. *Appl. Phys. Lett.* **1999**, *75*, 737–739.
(51) Burgess, I. B.; Ponte, M. R.; Saravanamuttu, K. Spontaneous Formation of 3-D Optical and Structural Lattices from Two Orthogonal and Mutually Incoherent Beams of White Light Propagating in a Photopolymerisable Material. *J. Mater. Chem.* **2008**, *18*, 4133.
(52) Bespalov, V. I.; Talanov, V. I. Filamentary Structure of Light Beams in Nonlinear Liquids. *JETP Lett.* **1966**, *3*, 307–310.
(53) Kip, D.; Soljacic, M.; Segev, M.; Eugenieva, E.; Christodoulides, D. N. Modulation Instability and Pattern Formation in Spatially Incoherent Light Beams. *Science* **2000**, *290*, 495–498.
(54) Streppel, U.; Michaelis, D.; Kowarschik, R.; Bräuer, A. Modulational Instability in Systems with Integrating Nonlinearity. *Phys. Rev. Lett.* **2005**, *95*, 073901.
(55) Zakharov, V. E.; Ostrovsky, L. A. Modulation Instability: The Beginning. *Phys. D Nonlinear Phenom.* **2009**, *238*, 540–548.
(56) Giusfredi, G.; Valley, J. F.; Pon, R.; Khitrova, G.; Gibbs, H. M. Optical Instabilities in Sodium Vapor. *J. Opt. Soc. Am. B* **1988**, *5*, 1181–1192.
(57) Centurion, M.; Pu, Y.; Tsang, M.; Psaltis, D. Dynamics of Filament Formation in a Kerr Medium. *Phys. Rev. A* **2005**, *71*, 63811.
(58) Reece, P. J.; Wright, E. M.; Dholakia, K. Experimental Observation of Modulation Instability and Optical Spatial Soliton Arrays in Soft Condensed Matter. *Phys. Rev. Lett.* **2007**, *98*.
(59) Matuszewski, M.; Krolikowski, W.; Kivshar, Y. S. Spatial Solitons and Light-Induced Instabilities in Colloidal Media. *Opt. Express* **2008**, *16*, 1371–1376.
(60) Anyfantakis, M.; Loppinet, B.; Fytas, G.; Pispas, S. Optical Spatial Solitons and Modulation Instabilities in Transparent Entangled Polymer Solutions. *Opt. Lett.* **2008**, *33*, 2839.
(61) Liu, Z.; Liu, S.; Guo, R.; Gao, Y.; Qi, X.; Zhou, L.; Li, Y. Modulation Instability with Incoherent White Light in Self-Defocusing Photorefractive Crystal. *Opt. Commun.* **2008**, *281*, 3171–3176.
(62) Jisha, C. P.; Kuriakose, V. C.; Porsezian, K. Modulational Instability and Beam Propagation in Photorefractive Polymer. *J. Opt. Soc. Am. B* **2008**, *25*, 674.
(63) Peccianti, M.; Conti, C.; Assanto, G.; De Luca, A.; Umeton, C. Routing of Anisotropic Spatial Solitons and Modulational Instability in Liquid Crystals. *Nature* **2004**, *432*, 733–737.

(64) Braun, E.; Faucheux, L. P.; Libchaber, A.; McLaughlin, D. W.; Muraki, D. J.; Shelley, M. J. Filamentation and Undulation of Self-Focused Laser Beams in Liquid Crystals. *EPL Europhysics Lett.* **1993**, *23*, 239–244.
(65) Kasala, K.; Saravanamuttu, K. Optochemical Self-Organisation of White Light in a Photopolymerisable Gel: A Single-Step Route to Intersecting and Interleaving 3-D Optical and Waveguide Lattices. *J. Mater. Chem.* **2012**, *22*, 12281.
(66) Qiu, L.; Saravanamuttu, K. Modulation Instability of Incandescent Light in a Photopolymer Doped with Ag Nanoparticles. *Journal of Optics*. 2012, p 125202.
(67) Ponte, M. R.; Welch, R.; Saravanamuttu, K. An Optochemically Organized Nonlinear Waveguide Lattice with Primitive Cubic Symmetry. *Opt. Express* **2013**, *21*, 4205–4214.
(68) Durbin, S. D.; Arakelian, S. M.; Shen, Y. R. Laser-Induced Diffraction Rings from a Nematic-Liquid-Crystal Film. *Opt. Lett.* **1981**, *6*, 411–413.
(69) Meyer, Y. H.; Photophysique, L. De; Paris-sud, U. MULTIPLE CONICAL EMISSIONS FROM NEAR RESONANT LASER PROPAGATION IN DENSE SODIUM VAPOR. **1980**, *34*.
(70) Villafranca, A. B.; Saravanamuttu, K. Diversity and Slow Dynamics of Diffraction Rings: A Comprehensive Study of Spatial Self-Phase Modulation in a Photopolymer. *J. Opt. Soc. Am. B* **2012**, *29*, 2357.
(71) Grow, T. D.; Ishaaya, A. a; Vuong, L. T.; Gaeta, A. L.; Gavish, N.; Fibich, G. Collapse Dynamics of Super-Gaussian Beams. *Opt. Express* **2006**, *14*, 5468–5475.
(72) Maioli, P.; Salamé, R.; Lascoux, N.; Salmon, E.; Béjot, P.; Kasparian, J.; Wolf, J.-P. Ultraviolet-Visible Conical Emission by Multiple Laser Filaments. *Opt. Express* **2009**, *17*, 4726–4731.
(73) Santamato, E.; Shen, Y. R. Field-Curvature Effect on the Diffraction Ring Pattern of a Laser Beam Dressed by Spatial Self-Phase Modulation in a Nematic Film. *Opt. Lett.* **1984**, *9*, 564–566.
(74) Dabby, F. W.; Gustafson, T. K.; Whinnery, J. R.; Kohanzadeh, Y.; Kelley, P. L. THERMALLY SELF-INDUCED PHASE MODULATION OF LASER BEAMS. *Appl. Phys. Lett.* **1970**, *16*, 362–365.
(75) Wu, R.; Zhang, Y.; Yan, S.; Bian, F.; Wang, W.; Bai, X.; Lu, X.; Zhao, J.; Wang, E. Purely Coherent Nonlinear Optical Response in Solution Dispersions of Graphene Sheets. *Nano Lett.* **2011**, *11*, 5159–5164.
(76) Luther-Davies, B.; Yang, X. Steerable Optical Waveguides Formed in Self-Defocusing Media by Using Dark Spatial Solitons. *Opt. Lett.* **1992**, *17*, 1755–1757.
(77) Chen, Z.; Mitchell, M.; Segev, M.; Coskun, T. H.; Christodoulides, D. N. Self-Trapping of Dark Incoherent Light Beams. *Science* **1998**, *280*, 889–892.
(78) Tolstik, E.; Kashin, O.; Matusevich, V.; Kowarschik, R. Broadening of the Light Self-Trapping Due to Thermal Defocusing in PQ-PMMA Polymeric Layers. *Opt. Express* **2011**, *19*, 2739–2747.
(79) Kasala, K.; Saravanamuttu, K. A Black Beam Borne by an Incandescent Field Self-Traps in a Photopolymerizing Medium. *J. Am. Chem. Soc.* **2012**, *134*, 14195–14200.
(80) Rotschild, C.; Alfassi, B.; Cohen, O.; Segev, M. Long-Range Interactions between

Optical Solitons. *Nature Physics*. 2006, pp 769–774.
(81) Tikhonenko, V.; Christou, J.; Luther-Davies, B. Three Dimensional Bright Spatial Soliton Collision and Fusion in a Saturable Nonlinear Medium. *Phys. Rev. Lett.* **1996**, *76*, 2698–2701.
(82) Shih, M. F.; Sheu, F. W. Photorefractive Polymeric Optical Spatial Solitons. *Opt. Lett.* **1999**, *24*, 1853–1855.
(83) Lynn, B.; Blanche, P.-A.; Peyghambarian, N. Photorefractive Polymers for Holography. *J. Polym. Sci. Part B Polym. Phys.* **2014**, *52*, 193–231.
(84) Derrien, F.; Henninot, J. F.; Warenghem, M.; Abbate, G. A Thermal (2D+1) Spatial Optical Soliton in a Dye Doped Liquid Crystal. *J. Opt. A Pure Appl. Opt.* **2000**, *2*, 332–337.
(85) Sasaki, T.; Miura, K.; Ono, H.; Hanaizumi, O. Optically Controlled Light Propagation in Dye-Doped Nematic Liquid Crystals with Homogeneous Alignment. *Key Eng. Mater.* **2012**, *497*, 142–146.
(86) Liquid Crystalline Siloxanes Containing Spiropyran Chromophores as Reversible Optical Data Storage Materials. *Adv. Mater. Opt. Electron.* **1992**, *1*, 293–297.
(87) Yesodha, S. K.; Sadashiva Pillai, C. K.; Tsutsumi, N. Stable Polymeric Materials for Nonlinear Optics: A Review Based on Azobenzene Systems. *Prog. Polym. Sci.* **2004**, *29*, 45–74.
(88) Garmire, E.; Chiao, R. Y.; Townes, C. H. Dynamics and Characteristics of the Self-Trapping of Intense Light Beams. *Phys. Rev. Lett.* **1966**, *16*, 347–349.
(89) Lederer, F.; Stegeman, G. I.; Christodoulides, D. N.; Assanto, G.; Segev, M.; Silberberg, Y. Discrete Solitons in Optics. *Phys. Rep.* **2008**, *463*, 1–126.
(90) Segev, M. Optical Spatial Solitons. *Opt. Quantum Electron.* **1998**, *30*, 503–533.
(91) Peccianti, M.; De Rossi, A.; Assanto, G.; De Luca, A.; Umeton, C.; Khoo, I. C. Electrically Assisted Self-Confinement and Waveguiding in Planar Nematic Liquid Crystal Cells. *Appl. Phys. Lett.* **2000**, *77*, 7–9.
(92) Moerner, W. E.; Grunnet-Jepsen, a.; Thompson, C. L. Photorefractive Polymers. *Annu. Rev. Mater. Sci.* **1997**, *27*, 585–623.
(93) Peccianti, M.; Dyadyusha, A.; Kaczmarek, M.; Assanto, G. Tunable Refraction and Reflection of Self-Confined Light Beams. *Nat. Phys.* **2006**, *2*, 737–742.
(94) Izdebskaya, Y.; Shvedov, V.; Assanto, G.; Krolikowski, W. Magnetic Routing of Light-Induced Waveguides. *Nat. Commun.* **2017**, *8*, 14452.
(95) Hennessy, M. G.; Vitale, A.; Cabral, J. T.; Matar, O. K. Role of Heat Generation and Thermal Diffusion during Frontal Photopolymerization. *Phys. Rev. E Stat. Nonlinear, Soft Matter Phys.* **2015**, *92*, 022403/1-022403/15.
(96) Bentley, S. J.; Boyd, R. W.; Butler, W. E.; Melissinos, A. C. Spatial Patterns Induced in a Laser Beam by Thermal Nonlinearities. *Opt. Lett.* **2001**, *26*, 1084–1086.
(97) Russew, M.-M.; Hecht, S. Photoswitches: From Molecules to Materials. *Adv. Mater.* **2010**, *22*, 3348–3360.
(98) Kaur, G.; Johnston, P.; Saito, K. Photo-Reversible Dimerisation Reactions and Their Applications in Polymeric Systems. *Polym. Chem.* **2014**, *5*, 2171–2186.
(99) Yoon, T. P.; Ischay, M. a; Du, J. Visible Light Photocatalysis as a Greener

Approach to Photochemical Synthesis. *Nat. Chem.* **2010**, *2*, 527–532.
(100) Troian-Gautier, L.; Turlington, M. D.; Wehlin, S. A. M.; Maurer, A. B.; Brady, M. D.; Swords, W. B.; Meyer, G. J. Halide Photoredox Chemistry. *Chem. Rev.* **2019**, *119*, 4628–4683.
(101) Boschloo, G.; Hagfeldt, A.; Spectus, C. O. N. Characteristics of the Iodide / Triiodide Redox Mediator in Dye-Sensitized Solar Cells. **2009**, *42*, 1819–1826.
(102) Kuksenok, O.; Dayal, P.; Bhattacharya, A.; Yashin, V. V; Deb, D.; Chen, I. C.; Van Vliet, K. J.; Balazs, A. C. Chemo-Responsive, Self-Oscillating Gels That Undergo Biomimetic Communication. *Chem. Soc. Rev.* **2013**, *42*, 7257–7277.
(103) Masuda, T.; Hidaka, M.; Murase, Y.; Akimoto, A. M.; Nagase, K.; Okano, T.; Yoshida, R. Self-Oscillating Polymer Brushes. *Angew. Chemie Int. Ed.* **2013**, *52*, 7468–7471.
(104) Derosa, M. C.; Crutchley, R. J. Photosensitized Singlet Oxygen and Its Applications. **2002**, *234*.
(105) Zakery, A.; Elliott, S. R. Optical Properties and Applications of Chalcogenide Glasses: A Review. *Journal of Non-Crystalline Solids*. 2003, pp 1–12.
(106) Aitchison, J. S.; Weiner, A. M.; Silberberg, Y.; Leaird, D. E.; Oliver, M. K.; Jackel, J. L.; Smith, P. W. E. Experimental Observation of Spatial Soliton Interactions. *Opt. Lett.* **1991**, *16*, 15–17.
(107) Gio, Jinxin; Gleeson, Michael R.; Sheridan, J. T. A Review of the Optimisation of Photopolymer Materials for Holographic Data Storage. *Phys. Res. Int.* **2012**, *2012*.
(108) Crivello, J. V; Reichmanis, E. Photopolymer Materials and Processes for Advanced Technologies. *Chem. Mater.* **2014**, *26*, 533–548.
(109) Sari, E.; Yilmaz, G.; Koyuncu, S.; Yagci, Y. Photoinduced Step-Growth Polymerization of N-Ethylcarbazole. *J. Am. Chem. Soc.* **2018**, *140*, 12728–12731.
(110) MacDonald, S. A.; Willson, C. G.; Frechet, J. M. J. Chemical Amplification in High-Resolution Imaging Systems. *Acc. Chem. Res.* **1994**, *27*, 151–158.
(111) Tolstik, E.; Romanov, O.; Matusevich, V.; Tolstik, A.; Kowarschik, R. Formation of Self-Trapping Waveguides in Bulk PMMA Media Doped with Phenanthrenequinone. *Opt. Express* **2014**, *22*, 3228–3233.
(112) Jisha, C. P.; Hsu, K.-C.; Lin, Y.; Lin, J.-H.; Jeng, C.-C.; Lee, R.-K. Tunable Pattern Transitions in a Liquid-Crystal-Monomer Mixture Using Two-Photon Polymerization. *Opt. Lett.* **2012**, *37*, 4931–4933.
(113) Jemal, A.; Ben Belgacem, M.; Kamoun, S.; Gargouri, M.; (Honorat) Dorkenoo, K. D.; Barsella, A.; Mager, L. Electro-Optic Phase Modulation in Light Induced Self-Written Waveguides Propagated in a 5CB Doped Photopolymer. *Opt. Express* **2013**, *21*, 1541–1546.
(114) Monro, T. M.; Miller, P. D.; Poladian, L.; Martijn de Sterke, C. Self-Similar Evolution of Self-Written Waveguides. *Opt. Lett.* **1998**, *23*, 268–270.
(115) Kewitsch, A. S.; Yariv, A. Self-Focusing and Self-Trapping of Optical Beams upon Photopolymerization. *Opt. Lett.* **1996**, *21*, 24–26.
(116) Arumugam, S.; Popik, V. V. Patterned Surface Derivatization Using Diels–Alder Photoclick Reaction. *J. Am. Chem. Soc.* **2011**, *133*, 15730–15736.
(117) Chen, F. H.; Pathreeker, S.; Biria, S.; Hosein, I. D. Synthesis of Micropillar Arrays

via Photopolymerization: An in Situ Study of Light-Induced Formation, Growth Kinetics, and the Influence of Oxygen Inhibition. *Macromolecules* **2017**, *50*, 5767–5778.

(118) O'Brien, A. K.; Bowman, C. N. Modeling the Effect of Oxygen on Photopolymerization Kinetics. *Macromol. Theory Simulations* **2006**, *15*, 176–182.

(119) Sheridan, J. G. and M. R. G. and S. L. and J. T. Non-Local Spatial Frequency Response of Photopolymer Materials Containing Chain Transfer Agents: II. Experimental Results. *J. Opt.* **2011**, *13*, 95602.

(120) Tehfe, M. A.; Lalevée, J.; Allonas, X.; Fouassier, J. P. Long Wavelength Cationic Photopolymerization in Aerated Media: A Remarkable Titanocene/Tris(Trimethylsilyl)Silane/Onium Salt Photoinitiating System. *Macromolecules* **2009**, *42*, 8669–8674.

(121) Gómez, M. L.; Avila, V.; Montejano, H. A.; Previtali, C. M. A Mechanistic and Laser Flash Photolysis Investigation of Acrylamide Polymerization Photoinitiated by the Three Component System Safranine-T/Triethanolamine/Diphenyliodonium Chloride. *Polymer (Guildf).* **2003**, *44*, 2875–2881.

(122) Blaya, S.; Carretero, L.; Madrigal, R. F.; Ulibarrena, M.; Acebal, P.; Fimia, A. Photopolymerization Model for Holographic Gratings Formation in Photopolymers. *Appl. Phys. B* **2003**, *77*, 639–662.

(123) Kızılel, S.; Pérez-Luna, V. H.; Teymour, F. Photopolymerization of Poly(Ethylene Glycol) Diacrylate on Eosin-Functionalized Surfaces. *Langmuir* **2004**, *20*, 8652–8658.

(124) Lin, S.-H.; Hsiao, Y.-N.; Hsu, K. Y.; Whang, W.-T. Eosin Y Spirit Soluble/Triethanolamine Doped Poly (Methyl Methacrylate-Co-Hydroxyethyl Methacrylate) Photopolymer for Holographic Data Storage. *Opt. Mem. Neural Networks* **2008**, *17*, 119.

(125) Qi, Y.; Gleeson, M. R.; Guo, J.; Gallego, S.; Sheridan, J. T. Quantitative Comparison of Five Different Photosensitizers for Use in a Photopolymer. *Phys. Res. Int.* **2012**.

(126) Crivello, J. V. The Discovery and Development of Onium Salt Cationic Photoinitiators. *J. Polym. Sci. Part A Polym. Chem.* **1999**, *37*, 4241–4254.

(127) Crivello, J. V. A New Visible Light Sensitive Photoinitiator System for the Cationic Polymerization of Epoxides. *J. Polym. Sci. Part A Polym. Chem.* **2009**, *47*, 866–875.

(128) Hoyle, C. E.; Lee, T. Y.; Roper, T. Thiol–Enes: Chemistry of the Past with Promise for the Future. *J. Polym. Sci. Part A Polym. Chem.* **2004**, *42*, 5301–5338.

(129) Ortiz, R. A.; Garcia Valdéz, A. E.; Martinez Aguilar, M. G.; Berlanga Duarte, M. L. An Effective Method to Prepare Sucrose Polymers by Thiol-Ene Photopolymerization. *Carbohydr. Polym.* **2009**, *78*, 282–286.

(130) Hoyle, C. E.; Bowman, C. N. Thiol–Ene Click Chemistry. *Angew. Chemie Int. Ed.* **2010**, *49*, 1540–1573.

(131) Mucci, V.; Vallo, C. Efficiency of 2,2-Dimethoxy-2-Phenylacetophenone for the Photopolymerization of Methacrylate Monomers in Thick Sections. *J. Appl. Polym. Sci.* **2012**, *123*, 418–425.

(132) Hsiao, Y. N.; Whang, W. T.; Lin, S. H. Analyses on Physical Mechanism of Holographic Recording in Phenanthrenequinone-Doped Poly(Methyl Methacrylate) Hybrid Materials. *Opt. Eng.* **2004**, *43*, 1993–2002.
(133) Liu, C.; Cardoso, M. R.; Zhang, W.; Chen, X. Characterization of Polymer Fiber Bragg Grating with Ultrafast Laser Micromachining. **2016**.
(134) Wochnowski, C.; Shams Eldin, M. A.; Metev, S. UV-Laser-Assisted Degradation of Poly(Methyl Methacrylate). *Polym. Degrad. Stab.* **2005**, *89*, 252–264.
(135) Yagci, Y.; Jockusch, S.; Turro, N. J. Photoinitiated Polymerization: Advances, Challenges, and Opportunities. *Macromolecules* **2010**, *43*, 6245–6260.
(136) Strickler, J. H.; Webb, W. W. Three-Dimensional Optical Data Storage in Refractive Media Bytwo-Photon Point Excitation. *Opt. Lett.* **1991**, *16*, 1780–1782.
(137) Schafer, K. J.; Hales, J. M.; Balu, M.; Belfield, K. D.; Van Stryland, E. W.; Hagan, D. J. Two-Photon Absorption Cross-Sections of Common Photoinitiators. *J. Photochem. Photobiol. A Chem.* **2004**, *162*, 497–502.
(138) Barsella, A.; Dorkenoo, H.; Mager, L. Near Infrared Two-Photon Self-Confinement in Photopolymers for Light Induced Self-Written Waveguides Fabrication. *Appl. Phys. Lett.* **2012**, *100*, 221102.
(139) Woods, R.; Feldbacher, S.; Langer, G.; Satzinger, V.; Schmidt, V.; Kern, W. Epoxy Silicone Based Matrix Materials for Two-Photon Patterning of Optical Waveguides. *Polymer (Guildf).* **2011**, *52*, 3031–3037.
(140) Hidai, H.; Hwang, D. J.; Grigoropoulos, C. P. Self-Grown Fiber Fabrication by Two-Photon Photopolymerization. *Appl. Phys. A* **2008**, *93*, 443.
(141) Cai, B.; Komatsu, K.; Sugihara, O.; Kagami, M.; Tsuchimori, M.; Matsui, T.; Kaino, T. A Three-Dimensional Polymeric Optical Circuit Fabrication Using a Femtosecond Laser-Assisted Self-Written Waveguide Technique. *Appl. Phys. Lett.* **2008**, *92*, 253302.
(142) Forman, D. L.; Cole, M. C.; McLeod, R. R. Radical Diffusion Limits to Photoinhibited Superresolution Lithography. *Phys. Chem. Chem. Phys.* **2013**, *15*, 14862–14867.
(143) de Beer, M. P.; van der Laan, H. L.; Cole, M. A.; Whelan, R. J.; Burns, M. A.; Scott, T. F. Rapid, Continuous Additive Manufacturing by Volumetric Polymerization Inhibition Patterning. *Sci. Adv.* **2019**, *5*, eaau8723.
(144) Liu, J.; Ueda, M. High Refractive Index Polymers: Fundamental Research and Practical Applications. *J. Mater. Chem.* **2009**, *19*, 8907–8919.
(145) Huang, Y.; Paul, D. R. Physical Aging of Thin Glassy Polymer Films Monitored by Optical Properties. *Macromolecules* **2006**, *39*, 1554–1559.
(146) Stevens, M. P. *Polymer Chemistry: An Introduction.*, 3rd ed.; Oxford University Press: New York, 2000; Vol. 5.
(147) Bates, F. S.; Fredrickson, G. H. Block Copolymers-Designer Soft Materials. *Phys. Today* **1999**, *52*, 32–38.
(148) Quarton, M.; Couvreur, P. Temperature-Dependent Rheological Behavior of Pluronic F-127 Aqueous Solutions. **1987**, *39*, 121–127.
(149) Pina, F.; Hatton, T. A. Photochromic Soft Materials: Flavylium Compounds Incorporated into Pluronic F-127 Hydrogel Matrixes. *Langmuir* **2008**, *24*, 2356–

2364.
(150) Rumi, M.; Bunning, T. J. Polymers in Photonics: Controlling Information by Manipulating Light. *J. Polym. Sci. Part B Polym. Phys.* **2014**, *52*, 157.
(151) Hasegawa, M.; Horie, K. Photophysics, Photochemistry, and Optical Properties of Polyimides. *Prog. Polym. Sci.* **2001**, *26*, 259–335.
(152) Królikowski, W.; Denz, C.; Stepken, A.; Saffman, M.; Luther-Davies, B. Interaction of Spatial Photorefractive Solitons. *J. Opt. B Quantum Semiclassical Opt.* **1998**, *10*, 823–837.
(153) Snyder, A. W.; Ladouceur, F. Light Guiding Light: Letting Light Be the Master of Its Own Destiny. *Opt. Photonics News* **1999**, *10*, 35.
(154) Hecht, E. *Optics*, 4th ed.; Addison-Wesley, 2002.
(155) Anderson, D.; Lisak, M. Bandwidth Limits Due to Incoherent Soliton Interaction in Optical-Fiber Communication Systems. *Phys. Rev. A* **1985**, *32*, 2270.
(156) Ku, T.-S. Sen; Shih, M.-F. F.; Sukhorukov, A. A.; Kivshar, Y. S. Coherence Controlled Soliton Interactions. *Phys. Rev. Lett.* **2005**, *94*, 063904.
(157) Kasala, K.; Saravanamuttu, K. An Experimental Study of the Interactions of Self-Trapped White Light Beams in a Photopolymer. *Appl. Phys. Lett.* **2008**, *93*, 051111.
(158) Aitchison, J. S.; Weiner, a M.; Silberberg, Y.; Leaird, D. E.; Oliver, M. K.; Jackel, J. L.; Smith, P. W. Experimental Observation of Spatial Soliton Interactions. *Opt. Lett.* **1991**, *16*, 15–17.
(159) Królikowski, W.; Luther-Davies, B.; Denz, C.; Petter, J.; Weilnau, C.; Stepken, A.; Belić, M. Interaction of Two-Dimensional Spatial Incoherent Solitons in Photorefractive Medium. *Appl. Phys. B* **1999**, *68*, 975–982.
(160) Kagami, T. M. and T. Y. and M. Improvement in Positioning Accuracy of Light-Induced Self-Written Polymeric Optical Waveguide Using an "Optical Solder" Effect. *Jpn. J. Appl. Phys.* **2006**, *45*, L1033.
(161) Ben Belgacem, M.; Kamoun, S.; Gargouri, M.; Honorat Dorkenoo, K. D.; Barsella, A.; Mager, L. Light Induced Self-Written Waveguides Interactions in Photopolymer Media. *Opt. Express* **2015**, *23*, 20841–20848.
(162) Malallah, R.; Cassidy, D.; Muniraj, I.; Ryle, J. P.; Healy, J. J.; Sheridan, J. T. Self-Written Waveguides in Photopolymer. *Appl. Opt.* **2018**, *57*, E80–E88.
(163) Królikowski, W.; Luther-Davies, B.; Denz, C.; Tschudi, T. Annihilation of Photorefractive Solitons. *Opt. Lett.* **1998**, *23*, 97–99.
(164) Królikowski, W.; Holmstrom, S. a. Fusion and Birth of Spatial Solitons upon Collision. *Opt. Lett.* **1997**, *22*, 369–371.
(165) Shoji, S.; Kawata, S.; Sukhorukov, A. A.; Kivshar, Y. S. Self-Written Waveguides in Photopolymerizable Resins. *Opt. Lett.* **2002**, *27*, 185–187.
(166) Peccianti, M.; Brzdkiewicz, K. A.; Assanto, G. Nonlocal Spatial Soliton Interactions in Nematic Liquid Crystals. *Opt. Lett.* **2002**, *27*, 1460–1462.
(167) Shi, T.-T.; Chi, S. Nonlinear Photonic Switching by Using the Spatial Soliton Collision. *Opt. Lett.* **1990**, *15*, 1123–1125.
(168) Fratalocchi, A.; Piccardi, A.; Peccianti, M.; Assanto, G. Nonlinearly Controlled Angular Momentum of Soliton Clusters. *Opt. Lett.* **2007**, *32*, 1447–1449.

(169) Stegeman, G. I. Optical Spatial Solitons and Their Interactions: Universality and Diversity. *Science* **1999**, *19*, 1518–1523.
(170) Shih, M.; Segev, M.; Salamo, G. Three-Dimensional Spiraling of Interacting Spatial Solitons. *Phys. Rev. Lett.* **1997**, *78*, 2551–2554.
(171) Poladian, L.; Snyder, A. W.; Mitchell, D. J. Spiralling Spatial Solitons. *Opt. Commun.* **1991**, *85*, 59–62.
(172) Hu, W.; Zhang, T.; Guo, Q.; Xuan, L.; Lan, S. Nonlocality-Controlled Interaction of Spatial Solitons in Nematic Liquid Crystals. *Appl. Phys. Lett.* **2006**, *89*.
(173) Baharudin, N. A.; Fujikawa, C.; Mitomi, O.; Suzuki, A.; Taguchi, S.; Mikami, O.; Ambran, S. Tapered Spot Size Converter by Mask-Transfer Self-Written Technology for Optical Interconnection. *IEEE Photonics Technology Letters*. 2017, pp 949–951.
(174) Sugimoto, S.; Kawaguchi, T.; Yamashita, K. Integrated Light Sources Based on Self-Formed Polymer Waveguide Doped with Active Medium; 2012; Vol. 8435, p 84351O–8435–8.
(175) Streppel, U.; Dannberg, P.; Wächter, C.; Bräuer, A.; Kowarschik, R. Formation of Micro-Optical Structures by Self-Writing Processes in Photosensitive Polymers. *Appl. Opt.* **2003**, *42*, 3570–3579.
(176) Hosein, I. D.; Lin, H.; Ponte, M. R.; Basker, D. K.; Brook, M. A.; Saravanamuttu, K. Waveguide Encoded Lattices (WELs): Slim Polymer Films with Panoramic Fields of View (FOV) and Multiple Imaging Functionality. *Adv. Funct. Mater.* 1702242–n/a.
(177) Basker, D. K.; Cortes, O. A. H.; Brook, M. A.; Saravanamuttu, K. 3D Nonlinear Inscription of Complex Microcomponents (3D NSCRIPT): Printing Functional Dielectric and Metallodielectric Polymer Structures with Nonlinear Waves of Blue LED Light. *Adv. Mater. Technol.* **2017**, *2*, 1600236–n/a.
(178) Hudson, A. D.; Ponte, M. R.; Mahmood, F.; Pena Ventura, T.; Saravanamuttu, K. A Soft Photopolymer Cuboid That Computes with Binary Strings of White Light. *Nat. Commun.* **2019**, *10*, 2310.
(179) No Title. *Program. Finite Elem. Method* **2004**.
(180) Dai, S.; Ravi, P.; Tam, K. C. PH-Responsive Polymers: Synthesis, Properties and Applications. *Soft Matter* **2008**, *4*, 435–449.
(181) Han, D.; Farino, C.; Yang, C.; Scott, T.; Browe, D.; Choi, W.; Freeman, J. W.; Lee, H. Soft Robotic Manipulation and Locomotion with a 3D Printed Electroactive Hydrogel. *ACS Appl. Mater. Interfaces* **2018**, *10*, 17512–17518.
(182) Ma, H.; Jen, A. K.-Y.; Dalton, L. R. Polymer-Based Optical Waveguides: Materials, Processing, and Devices. *Adv. Mater.* **2002**, *14*, 1339–1365.
(183) Eldada, L.; Shacklette, L. W. Advances in Polymer Integrated Optics. *IEEE Journal of Selected Topics in Quantum Electronics*. 2000, pp 54–68.
(184) Ozawa, H.; Obata, Y.; Mimura, Y.; Mikami, O.; Shioda, T. Self-Written Waveguide Connection across Diced Waveguide Gaps. *IEEE Photonics Technol. Lett.* **2006**, *18*, 880–882.
(185) Ozawa, H.; Obata, Y.; Mimura, Y.; Mikami, O.; Shioda, T. Self-Written Waveguide Connection between VCSEL and Optical Fiber with 45/Spl Deg/

Mirror Using Green Laser. *IEEE Photonics Technology Letters*. 2006, pp 532–534.
(186) Yamashita, K.; Ito, M.; Fukuzawa, E.; Okada, H.; Oe, K. Device Parameter Analyses of Solid-State Organic Laser Made by Self-Written Active Waveguide Technique. *J. Light. Technol.* **2009**, *27*, 4570–4574.
(187) Yamashita, K.; Kitanobou, A.; Ito, M.; Fukuzawa, E.; Oe, K. Solid-State Organic Laser Using Self-Written Active Waveguide with in-Line Fabry–Pérot Cavity. *Appl. Phys. Lett.* **2008**, *92*, 143305.
(188) Yamashita, K.; Fukuzawa, E.; Kitanobou, A.; Oe, K. Self-Written Active Waveguide for Integrated Optical Amplifiers. *Appl. Phys. Lett.* **2008**, *92*, 51102.
(189) Jisha, C. P.; Kuriakose, V. C.; Porsezian, K. Dynamics of a Light Induced Self-Written Waveguide Directional Coupler in a Photopolymer. *Opt. Commun.* **2008**, *281*, 1093–1098.
(190) Hirose, N.; Yoshimura, T.; Ibaragi, O. Optical Component Coupling Using Self-Written Waveguides. *Proceedings 27th European Conference on Optical Communication (Cat. No.01TH8551)* **2003**, 2, 140–141.
(191) Ozawa, H.; Obata, Y.; Mimura, Y.; Mikami, O.; Shioda, T. High Efficient Self-Written Connection between V-Slot Optical Waveguide. *Proc. SPIE* **2005**, 6014, 601418–601419.
(192) Yoshimura, T.; Nawata, H. Micro/Nanoscale Self-Aligned Optical Couplings of the Self-Organized Lightwave Network (SOLNET) Formed by Excitation Lights from Outside. *Opt. Commun.* **2017**, *383*, 119–131.
(193) Günther, A.; Petermann, A. B.; Gleissner, U.; Hanemann, T.; Reithmeier, E.; Rahlves, M.; Meinhardt-Wollweber, M.; Morgner, U.; Roth, B. Cladded Self-Written Multimode Step-Index Waveguides Using a One-Polymer Approach. *Opt. Lett.* **2015**, *40*, 1830–1833.
(194) Jradi, S.; Soppera, O.; Lougnot, D. J. Fabrication of Polymer Waveguides between Two Optical Fibers Using Spatially Controlled Light-Induced Polymerization. *Appl. Opt.* **2008**, *47*, 3987–3993.
(195) Sugihara, O.; Tsuchie, H.; Endo, H.; Okamoto, N.; Yamashita, T.; Kagami, M.; Kaino, T. Light-Induced Self-Written Polymeric Optical Waveguides for Single-Mode Propagation and for Optical Interconnections. *IEEE Photonics Technol. Lett.* **2004**, *16*, 804–806.
(196) Bachelot, R.; Ecoffet, C.; Deloeil, D.; Royer, P.; Lougnot, D.-J. Integration of Micrometer-Sized Polymer Elements at the End of Optical Fibers by Free-Radical Photopolymerization. *Appl. Opt.* **2001**, *40*, 5860–5871.
(197) Yonemura, M.; Kawasaki, A.; Kato, S.; Kagami, M.; Inui, Y. Polymer Waveguide Module for Visible Wavelength Division Multiplexing Plastic Optical Fiber Communication. *Opt. Lett.* **2005**, *30*, 2206–2208.
(198) Sugihara, O.; Yasuda, S.; Cai, B.; Komatsu, K.; Kaino, T. Serially Grafted Polymer Optical Waveguides Fabricated by Light-Induced Self-Written Waveguide Technique. *Opt. Lett.* **2008**, *33*, 294–296.
(199) Chou, S. Y.; Zhuang, L. Lithographically Induced Self-Assembly of Periodic Polymer Micropillar Arrays. *J. Vac. Sci. Technol. B Microelectron. Nanom. Struct. Process. Meas. Phenom.* **1999**, *17*, 3197–3202.

(200) Brusatin, G.; Della Giustina, G.; Guglielmi, M.; Casalboni, M.; Prosposito, P.; Schutzmann, S.; Roma, G. Direct Pattern of Photocurable Glycidoxypropyltrimethoxysilane Based Sol–Gel Hybrid Waveguides for Photonic Applications. *Mater. Sci. Eng. C* **2007**, *27*, 1022–1025.
(201) Uematsu, T.; Watanabe, A.; Yamaguchi, Y. Self-Organization of Striped Pattern of Refractive Indices in Photopolymer Film. *J. Polym. Sci. Part B Polym. Phys.* **2004**, *42*, 3351–3358.
(202) US5462700-Process for Making an Array of Tapered Photopolymerized Waveguides, 1995.
(203) Jacobsen, A. J.; Barvosa-Carter, W.; Nutt, S. Compression Behavior of Micro-Scale Truss Structures Formed from Self-Propagating Polymer Waveguides. *Acta Mater.* **2007**, *55*, 6724–6733.
(204) Lin, H.; Hosein, I. D.; Benincasa, K. A.; Saravanamuttu, K. A Slim Polymer Film with a Seamless Panoramic Field of View: The Radially Distributed Waveguide Encoded Lattice (RDWEL). *Adv. Opt. Mater.* **2019**, *7*, 1801091.
(205) Biria, S.; Malley, P. P. A.; Kahan, T. F.; Hosein, I. D. Tunable Nonlinear Optical Pattern Formation and Microstructure in Cross-Linking Acrylate Systems during Free-Radical Polymerization. *J. Phys. Chem. C* **2016**, *120*, 4517–4528.
(206) Biria, S.; Malley, P. P. A.; Kahan, T. F.; Hosein, I. D. Optical Autocatalysis Establishes Novel Spatial Dynamics in Phase Separation of Polymer Blends during Photocuring. *ACS Macro Lett.* **2016**, *5*, 1237–1241.
(207) Tredici, A.; Pecchini, R.; Sliepcevich, A.; Morbidelli, M. Polymer Blends by Self-Propagating Frontal Polymerization. *J. Appl. Polym. Sci.* **1998**, *70*, 2695–2702.
(208) Roper, C. S.; Schubert, R. C.; Maloney, K. J.; Page, D.; Ro, C. J.; Yang, S. S.; Jacobsen, A. J. Scalable 3D Bicontinuous Fluid Networks: Polymer Heat Exchangers Toward Artificial Organs. *Adv. Mater.* **2015**, *27*, 2479–2484.
(209) Schaedler, T. A.; Jacobsen, A. J.; Torrents, A.; Sorensen, A. E.; Lian, J.; Greer, J. R.; Valdevit, L.; Carter, W. B. Ultralight Metallic Microlattices. *Science* **2011**, *334*, 962 LP-965.
(210) Jacobsen, A. J.; Mahoney, S.; Carter, W. B.; Nutt, S. Vitreous Carbon Micro-Lattice Structures. *Carbon N. Y.* **2011**, *49*, 1025–1032.
(211) Yamashita, K.; Kuro, T.; Oe, K.; Mune, K.; Hikita, T.; Mochizuki, A. Propagation-Mode-Controlled Fabrication of Self-Written Waveguide in Photosensitive Polyimide for Single-Mode Operation. *IEEE Photonics Technology Letters*. 2005, pp 786–788.
(212) Fischer-Hirchert, U. H. P. Optical Waveguides BT - Photonic Packaging Sourcebook: Fiber-Chip Coupling for Optical Components, Basic Calculations, Modules; Fischer-Hirchert, U. H. P., Ed.; Springer Berlin Heidelberg: Berlin, Heidelberg, 2015; pp 23–55.
(213) Saravanamuttu, K.; Andrews, M. P. Visible Laser Self-Focusing in Hybrid Glass Planar Waveguides. *Opt. Lett.* **2002**, *27*, 1342–1344.
(214) Ngo, T. D.; Kashani, A.; Imbalzano, G.; Nguyen, K. T. Q.; Hui, D. Additive Manufacturing (3D Printing): A Review of Materials, Methods, Applications and Challenges. *Compos. Part B Eng.* **2018**, *143*, 172–196.

(215) Liska, R.; Schuster, M.; Inführ, R.; Turecek, C.; Fritscher, C.; Seidl, B.; Schmidt, V.; Kuna, L.; Haase, A.; Varga, F.; et al. Photopolymers for Rapid Prototyping. *J. Coatings Technol. Res.* **2007**, *4*, 505–510.
(216) Tumbleston, J. R.; Shirvanyants, D.; Ermoshkin, N.; Janusziewicz, R.; Johnson, A. R.; Kelly, D.; Chen, K.; Pinschmidt, R.; Rolland, J. P.; Ermoshkin, A.; et al. Continuous Liquid Interface Production of 3D Objects. *Science* **2015**, *347*, 1349–1352.
(217) Shusteff, M.; Browar, A. E. M.; Kelly, B. E.; Henriksson, J.; Weisgraber, T. H.; Panas, R. M.; Fang, N. X.; Spadaccini, C. M. One-Step Volumetric Additive Manufacturing of Complex Polymer Structures. *Sci. Adv.* **2017**, *3*, eaao5496.
(218) Kelly, B. E.; Bhattacharya, I.; Shusteff, M.; Panas, R. M.; Taylor, H. K.; Spadaccini, C. M. Computed Axial Lithography (CAL): Toward Single Step 3D Printing of Arbitrary Geometries; 2017.
(219) Kelly, B. E.; Bhattacharya, I.; Heidari, H.; Shusteff, M.; Spadaccini, C. M.; Taylor, H. K. Volumetric Additive Manufacturing via Tomographic Reconstruction. *Science* **2019**, *363*, 1075 LP-1079.
(220) Dolinski, N. D.; Page, Z. A.; Callaway, E. B.; Eisenreich, F.; Garcia, R. V; Chavez, R.; Bothman, D. P.; Hecht, S.; Zok, F. W.; Hawker, C. J. Solution Mask Liquid Lithography (SMaLL) for One-Step, Multimaterial 3D Printing. *Adv. Mater. (Weinheim, Ger.* **2018**, *30*, n/a.
(221) Soppera, O.; Jradi, S.; Lougnot, D. J. Photopolymerization with Microscale Resolution: Influence of the Physico-Chemical and Photonic Parameters. *J. Polym. Sci. Part A Polym. Chem.* **2008**, *46*, 3783–3794.

2 Reversibly trapping visible laser light through the catalytic photo-oxidation of I^- by $Ru(bpy)_3^{2+}$ †

2.1 Abstract

A Gaussian, visible laser beam travelling in a hydrogel doped with NaI and $Ru(bpy)_3Cl_2$ spontaneously transforms into a localized, self-trapped beam, which propagates without diverging through the medium. The catalytic, laser-light induced oxidation of I^- by $[Ru(bpy)_3]^{2+}$ generates I_3^- species, which creates a refractive index increase along the beam path. The result is a cylindrical waveguide, which traps the optical field as bound modes and suppresses natural diffraction. When the beam is switched off, Grotthuss-type diffusion of I_3^- erases the waveguide within minutes and the system reverts to its original composition, enabling regeneration of the self-trapped beam. Our findings demonstrate reversible self-trapping for the first time in a precisely controllable, molecular-level photoreaction and could open routes to circuitry-free photonics devices powered by the interactions of switchable self-trapped beams.

---

* Reprinted (adapted) with permission from Morim, D. R.; Vargas-Baca, I.; Saravanamuttu, K. Reversibly Trapping Visible Laser Light through the Catalytic Photo-oxidation of I^- by $Ru(bpy)_3^{2+}$. *J. Phys. Chem. Lett.* **2016**, *7*, 1585-1589.
 Contribution: Morim was responsible for all experimental work. All co-authors were involved in analysis and writing of the manuscript.

2.2 Manuscript

The overarching goals of photonics research are to gain precise 3-D control over the propagation of light beams, manipulate and manage their diffraction and spatially confine and concentrate optical fields within microstructures. Spatially self-trapped bright beams or solitons, which are generated under nonlinear conditions, propagate over long distances (>> Rayleigh range) without suffering divergence, thus preserving their spatial intensity profiles.[1, 2] They form the basis of the light-guiding-light concept,[3] which is a powerful vision of circuitry-free, switchable, interconnected and multi-layered photonics systems driven entirely by the solitonic interactions of spatially self-trapped beams; such reconfigurable systems require self-trapped beams to be reversibly and rapidly generated in the medium. Although studied in several systems with reversible optical nonlinearities including liquid crystals[4], photorefractive crystals[5] and Kerr media[6], there have, to our knowledge, been no systematic studies of the reversible generation – the switching *on* and *off* - of self-trapped beams.

Self-trapped beams are mathematically described by:

$$ik_0 n_0 \frac{\delta\varepsilon}{\delta z} + \frac{1}{2}\nabla_t^2 \varepsilon + \frac{i}{2} k_0^2 n_0 \Delta n \varepsilon + \frac{i}{2} k_0 n_0 \alpha \varepsilon = 0 \qquad (2.1)$$

where ε is the electric field amplitude and k_0, the free-space wavenumber of the optical field and α is the attenuation coefficient of the medium.[7] Eq 2.1 shows that self-trapping occurs when the natural diffraction of the beam (∇_t^2) is countered by the beam-induced change in refractive index (Δn). Here we show that self-trapped laser beams can be reversibly generated during the laser-induced oxidation of I^- by $Ru(bpy)_3^{2+}$, which due to

its catalytic nature produces a Δn that can be deliberately erased by switching off the optical field:

$$[Ru(bpy)_3]^{2+} \xrightarrow{h\nu} [Ru(bpy)_3]^{2+*} \quad (2.2)$$

$$[Ru(bpy)_3]^{2+*} + I^- \longrightarrow [Ru(bpy)_3]^{+} + I^{\bullet} \quad (2.3)$$

$$I^{\bullet} + I^- \longrightarrow I_2^{\bullet -} \quad (2.4)$$

$$I_2^{\bullet -} + I_2^{\bullet -} \longrightarrow I^- + I_3^- \quad (2.5)$$

$$I_2^{\bullet -} + [Ru(bpy)_3]^{+} \longrightarrow [Ru(bpy)_3]^{2+} + 2I^- \quad (2.6)$$

Tris(bipyridine)ruthenium(II) absorbs light in the blue-green region (λ_{max} of 460 nm), exciting a metal-to-ligand charge transfer (MLCT) that results in a triplet species (eq 2.2), which depending on its environment, reacts by accepting or donating an electron, or relaxes to the ground state by releasing light or heat.[8,9,10] In the presence of iodide, the triplet accepts an electron and generates an iodide radical (eq 2.3), which reacts with excess iodide to form other species including triiodide (eqs 2.4, 2.5) or recombines to regenerate $Ru(bpy)_3Cl_2$ (eq 2.6). The photocatalytic reaction sequence[11,12,13,14] in eqs 2.2-2.6 has been elegantly exploited to design solar cells where a photo-excited ruthenium dye transfers an electron into the conduction band of titanium dioxide.[15] The oxidized dye is reduced by iodide, leading to diiodide radicals, which disproportionate into iodide and triiodide (eqs 2.4-2.5).

We reason that the *same* visible-light induced catalytic sequence in eqs 2.2-2.6 produces the *intensity-dependent*, *spatially localized* and *positive change in refractive index* (Δn) required for optical self-trapping. Specifically, Δn originates from photo-

generated I_3^- (eqs 2.4-2.5), which can be expected to be significantly more polarizable, and based on the Lorentz-Lorenz relationship, contributes to a larger *n* relative to its precursors[16]. The magnitude of Δn within a given volume in a specific time period is proportional to the quantum yield of I_2 and I_3^- and thereby determined by optical field intensity (photons per unit area per unit time). To suppress rapid diffusion of photoproducts and ensure that Δn is spatially localized, the reaction is hosted in a hydrogel (Pluronic® F-127) consisting of polyethylene and polypropylene oxide triblock copolymer micelles[17,18]. Above the lower critical solution temperature (≈ 10°C), dehydration of poly(propylene oxide) segments together with the interleaving of poly(ethylene oxide) segments triggers gelation.[19,20] In this diffusion-limited system, I_3^- (and Δn) accumulates strictly along the propagation path of a continuous wave, laser beam. Because of its intensity-dependence, the spatial profile of Δn mirrors the Gaussian beam shape - maximizing and then decaying with radial symmetry about the most-intense, axial region; the resulting lens-like Δn profile is a key prerequisite of self-trapping.[21,22] Importantly, once the laser is switched off, photoproducts diffuse away, restoring the original profile of the medium along the beam path and erasing all traces of self-trapping.

In a typical experiment, we launched a continuous wave, visible laser beam (λ = 532 nm) into an optically transparent sample cell containing the hydrogel doped with $Ru(bpy)_3Cl_2$ (1.3 mM) and NaI (0.2 M) (Supplementary 2.4.1). At the sample entrance face, the beam had a width of 20 μm ($1/e^2$) and intensity of 8 W cm^{-2}. In the hydrogel without the photocatalyst (*i.e.*, under linear conditions), the beam diverged from its focal

width of 20 μm at the sample entrance face to 120 μm (0.015°) at the exit face (pathlength = 6.0 mm), exactly the same as the theoretical divergence in this system.

Results collected in Figure 2-1 show that the beam's natural divergence was strongly suppressed in hydrogels containing $Ru(bpy)_3Cl_2$ and NaI. Temporal variations in the spatial intensity profile of the beam, at the sample exit face, reveal that within the first 45 s, the beam undergoes a four-fold decrease in width ($1/e^2$) from 120 μm to 30 μm with a complementary increase in relative intensity from 10% to 70% (Figure 2-1a); select 2-D and 3-D profiles trace the striking, rapid transformation (Figure 2-1b-i). The results confirmed that the beam self-traps and propagates through the medium with minimal divergence. By contrast, the beam remained diverged and diffuse in a control experiment carried out in a hydrogel sample without $Ru(bpy)_3Cl_2$ and NaI, confirming that Δn required for self-trapping originated from reactions in eqs 2.2-2.6 (Figure 2-16).

The apparent decrease in intensity and slight increase in effective beam width observed after t = 45 s (Figure 2-1a) signifies the excitation of high order optical modes of the self-trapped beam (Figure 2-1f-i).

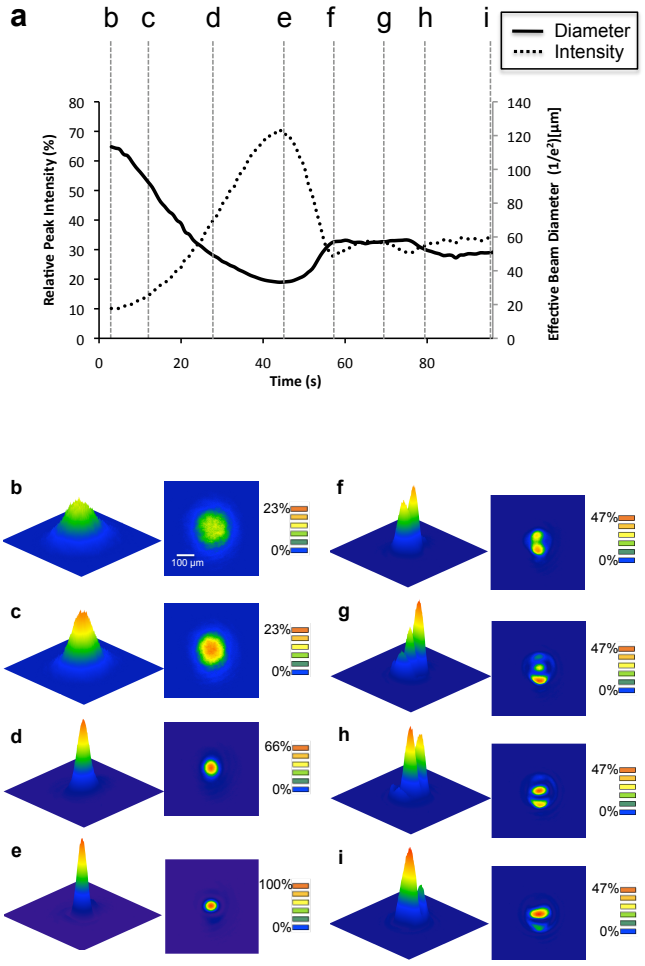

Figure 2-1 (a) Temporal evolution of peak intensity and beam diameter of 532 nm, cw laser beam (8.0 W cm^{-2}) propagating through a Pluronic® F-127 gel containing 1.3 mM $Ru(bpy)_3Cl_2$ and 0.2 M NaI. 2-D, 3-D Spatial intensity profiles at (b) 3 s, (c) 12 s, (d) 28 s, (e) 45 s, (f) 58 s, (g) 70 s, (h) 80 s, and (i) 96 s are included with colour intensity scales. (Also see Movie_S1).

The self-trapped beam propagates in a region of enhanced index – a narrow cylindrical region defined by an increased concentration of I_3^- (eqs 2.4-2.5) – that is in fact a cylindrical waveguide. Initially, the beam propagates as the fundamental waveguide mode but as the concentration of photoproducts (and Δn) increases further, high order modes are excited: the approximately Gaussian profile of the fundamental mode (LP_{00})

(Figure 2-1d, e) transforms into the anisotropic profiles characteristic of LP_{11} (Figure 2-1f) and LP_{01}+LP_{00} (Figure 2-1g-i) modes of cylindrical waveguides.[23]

We confirmed laser-induced generation of I_3^- by acquiring a UV-Vis absorbance spectrum of a hydrogel doped with NaI and $Ru(bpy)_3Cl_2$, which had been exhaustively irradiated with 532 nm laser light (20 mW, 10 h). Comparison with a non-irradiated sample showed the emergence of absorbance bands attributed to I_3^- (Figure 2-2a: A = 290 nm, B = 360 nm)[12,13,14] and decrease in absorbance bands attributed to the metal-to-ligand charge transfer transition of $Ru(bpy)_3^{2+}$ (Figure 2-2a: C = 455 nm).

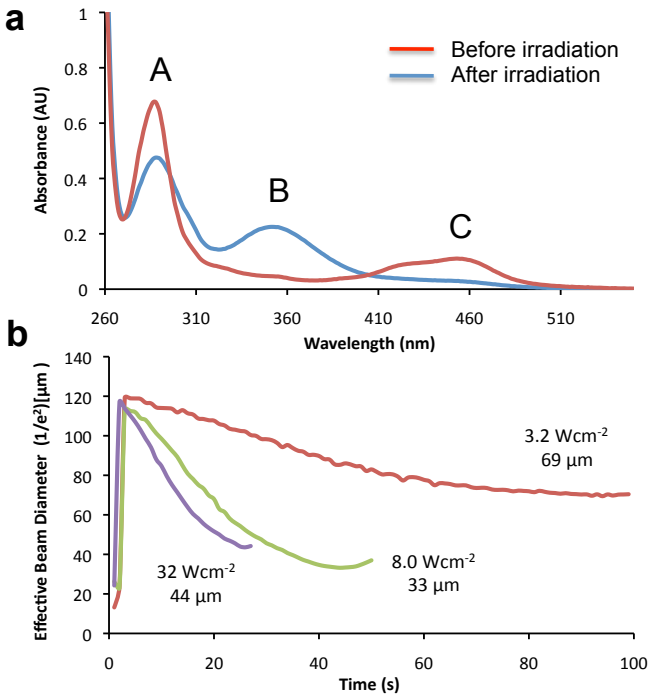

Figure 2-2 (a) Absorbance spectra of a gel with $Ru(bpy)_3Cl_2$ and NaI before and after irradiation (20 mW, 10 h). (b) Evolution of beam diameter during self-trapping at different incident intensities; minimum diameters are indicated.

The dynamics of self-trapping can be tuned through the rate of formation of I_3^-, which in turn is determined by the concentration of reactants and optical intensity. We first examined the intensity-dependence of self-trapping in hydrogels containing the greatest amount of precursors (1.3 mM $Ru(bpy)_3Cl_2$, 0.2 M NaI). In this system, self-trapping was not elicited at intensities < 3.2 W cm^{-2} because a sufficiently large population of I_3^- (and Δn) could not be generated. At 3.2 W cm^{-2}, the beam self-trapped to a minimum width of ~70 μm (Figure 2-2b) over a period of 100 s. With increasing intensity and corresponding rise in the rate and magnitude of laser-induced Δn, the rate of self-trapping increased significantly. For e.g. a minimum self-trapped beam width of 33 μm was achieved at 45 s at 8.0 Wcm^{-2} while a width of 44 μm was achieved within only 25 s at 32 W cm^{-2} (Figure 2-2b; Section 2.4.2) Prolonged, high-intensity irradiation also caused photodecomposition of $Ru(bpy)_3Cl_2$; depletion of the MLCT absorbance band (Figure 2-3a) indicated > 50% of the photocatalyst decomposed when irradiated for 3 h at 6 kW cm^{-2}. Self-trapping in systems containing smaller concentrations of NaI (<0.02 M) or $Ru(bpy)_3Cl_2$ (0.1 mM) could not be achieved at any of the previously employed intensities. In these cases, the concentration of photogenerated I_3^- was not large enough to induce the required Δn. Even greater concentrations of NaI (0.4 M) suppressed gelation of the hydrogel and could not be employed.[24]

Self-trapping and waveguide-inscription in the Ru(II) system is reversible. Figure 2-3a traces the beam diameter during the switching *on-off-on* sequence of a self-trapped beam. After initial self-trapping, which occurs during the first two minutes, the beam is

switched off. When the same beam, now at a low-intensity incapable of inducing Δn, was launched into the system, it reverts to its diverged form after 30 min. This *off* or "dark" period corresponds to the erasure or relaxation of the waveguide inscribed by the self-trapped beam. Once the beam intensity was switched back "on", the self-trapped beam (with minimum diameter = 30 μm) is regenerated within 2 min. The mechanism underlying reversibility is illustrated in Figure 2-3b; once the optical field is removed, I_3^- species that populated the beam path and formed the cylindrical waveguide diffuse away. This mass transport occurs through the Grotthuss-type exchange equilibria[25,26]:

$$I^- + I_2 \rightleftharpoons I_3^- \qquad (2.8)$$

$$\mathbf{I}^- + [I\text{-}I\text{-}I]^- \rightleftharpoons [\mathbf{I}\text{-}I\text{-}I]^- + I^- \qquad (2.9)$$

Re-equilibration of the system ranges from 30 min to 8 h and was related to the concentration of photogenerated I_3^-; greater intensities and longer irradiation times result in longer relaxation times. To confirm this transport mechanism, a drop of a concentrated solution of NaI and I_2 was injected into hydrogels with and without NaI distributed throughout the sample. In the latter, the injected droplet remained fixed in the medium while in the former, the droplet diffused throughout the gel over the course of 1 h and appeared homogeneously distributed.

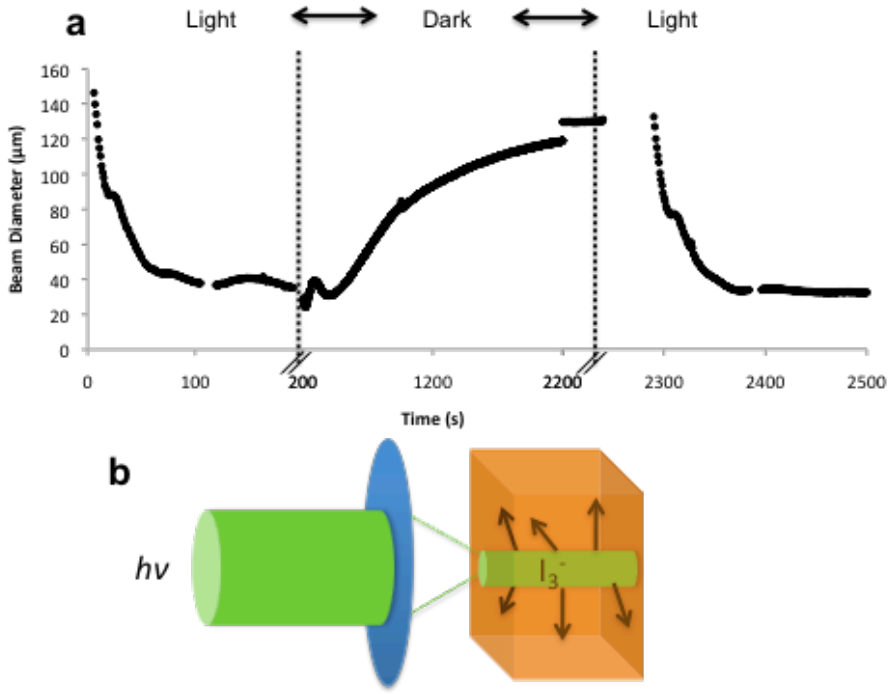

Figure 2-3 (a) Reversible self-trapping demonstrated through changes in the beam diameter during the presence (light) and after the absence (dark) of the optical field. (b) Scheme of triiodide diffusion away from the original propagation path of the beam.

We observed a significantly slower, *irreversible* form of self-trapping in hydrogels containing $Ru(bpy)_3Cl_2$ alone (*i.e.* in the absence of NaI); self-induced waveguides were permanently inscribed in this system, persisting under dark conditions for > 24 h (Section 2.4.3). Self-trapping occurred over timescales at two orders of magnitude greater than and at intensities, at least an order of magnitude greater compared to systems with NaI, implying that a much smaller Δn governed this secondary process; for e.g. self-trapping occurred in 4000 s (159 W cm^{-2}) versus the 45 s (at only 8 W cm^{-2}) in samples with NaI. Detailed control experiments (Section 2.4.3) suggest that Δn originates from crosslinking of the Pluronic® F-127 hydrogel due to photogenerated singlet oxygen. In the presence of

NaI however, secondary self-trapping is negligible and self-trapped beams formed quickly and reversibly.

In summary, we demonstrated the reversible generation of multimoded self-trapped beams of c. w., visible laser light in a hydrogel. Self-trapping originates from I_3^- species and corresponding Δn generated along the beam propagation path due to photocatalytic oxidation of NaI by $Ru(bpy)Cl_2$. By exploiting Grotthuss-type diffusion of I_3^- in the absence of the optical field, self-trapped beams could be switched *on* and *off* at timescales of 2000 s at typical intensities of 8 W cm^{-2}. Moreover, by controlling reaction kinetics through reagent concentration and/or optical intensity, it is possible to control self-trapping dynamics.

These findings highlight the significant potential of reversible photochemical reactions in eliciting and precisely controlling reversible self-trapped beams. Although in the past half-century, self-trapped beams have predominantly been studied in systems where Δn originates from photophysical mechanisms (e.g. Kerr media, photorefractive and liquid crystals), the reversibility of these processes has not been examined in detail. Furthermore, photophysical systems such as Kerr media, while possessing fast, reversible responses (ns to ps), require extremely high intensities (GW cm^{-2}) to generate the necessary Δn[6] and moreover only support self-trapped beams within planar waveguides (and not bulk media). Liquid crystals and photorefractive crystals, while hosting self-trapped beams in the bulk, typically require electric fields, which can complicate experimental set-ups.[4, 5]

2.3 Acknowledgements

Financial support was provided by the Natural Sciences and Engineering Research Council of Canada, the Canada Foundation for Innovation, and the Ontario Innovation Trust. D. R. M. is grateful for the Ontario Graduate Scholarship.

2.4 Supporting information

2.4.1 Experimental methods

2.4.1.1 Materials

Methyl orange (Fisher Scientific Co.), fluorescein sodium salt (Aldrich), rhodamine B (Aldrich), methyl violet (Aldrich), tris(bipyridine)ruthenium(II) chloride hexahydrate (Strem Chemicals Inc.), Pluronic® F-127 polymer (Sigma-Aldrich), methyl viologen dichloride hydrate (Aldrich), and tetramethylorthosilicate (Aldrich) used without further purification. Furfuryl alcohol (Aldrich) was distilled under reduced pressure.

2.4.1.2 Preparation of Pluronic® F-127 gels for optical self-trapping

Gels were made by preparing a 25 wt. by wt.% solution of Pluronic® F-127 polymer below its lower critical solution temperature (LCST) by dissolving the polymer with a glass rod in deionized H_2O (Milli-Q®, 18.2 MΩcm) surrounded by an ice bath. Equilibration to room temperature results in the formation of a gel due to the dehydration of the PPO segments of the triblock copolymer.

Doped gels were prepared by substituting deionized water with an aqueous solution of the desired dopant(s) in deionized water. Different concentrations were utilized, but optimal self-trapping was achieved for 1.3 mM $Ru(bpy)_3Cl_2$ and 0.2 M NaI. Samples

without iodide contained 80 μM tris(bipyridine)ruthenium(II) chloride hexahydrate.

Samples for optical experiments were prepared by transferring the solutions below their LCST into cylindrical cells (diameter = 12 mm, pathlength = 6 mm) with optically flat, transparent windows.

2.4.1.3 Optical assembly

Self-trapping experiments were carried out on an optical assembly adapted from previous studies.[21] The excitation source was the TEM_{00} mode (Gaussian beam, M2 < 1.1) of c,w. visible (532 nm) light emitted by a diode-pumped solid-state laser (Verdi V2, Coherent, Inc., California, USA). The output beam, which had a diameter 2.25 mm and power of 500 mW, was passed through a λ/2 waveplate, polarizing beam splitter cube and neutral density filter. The λ/2 waveplate orientation was adjusted to obtain the required intensity and the attenuated beam was guided by a pair of 45° elliptical mirrors onto a planoconvex lens [focal length = 75.6 mm], which focused the beam to a diameter of 20 μm onto the entrance window of the sample cell containing the sample.

The spatial intensity profile of the beam at the exit face of the cell was imaged by a pair of planoconvex lenses (f. l. = 75.6 mm and f. l. = 300.0 mm) onto a high-resolution charge-coupled device (CCD) camera [736 horizontal × 484 vertical pixels; pixel size = 4.80 μm horizontal × 5.58 μm vertical; LaserCam IIID 1⁄400, Coherent, Inc., California, USA]. Combinations of neutral density filters (F) mounted on three separate rotatable wheels (VARM, Coherent, Inc.) were placed between imaging lenses to prevent saturation of the CCD camera. All imaging optical components could be translated along the *z* direction with a resolution of 0.25 mm. Images were collected every second for the

first 256 s and then every 20 s afterwards. The camera used BeamView Analyzer software (Version 3.2), which calculates beam diameter ($1/e^2$) and relative peak intensity, generates two-dimensional (2D) and three-dimensional (3D) intensity profiles and corrects for image magnification by the lenses (×4.0). The effective beam diameter corresponds to the circular area of all pixels with relative intensity > 13.5% ($1/e^2$) of the maximum (peak) intensity. The relative peak intensity is the ratio between the greatest intensity on one or more pixels in an image and the saturation intensity of the camera.

Intensities ranging from 6.4 W cm^{-2} to 318.0 W cm^{-2} were employed for experiments of self-trapping. For experiments probing the reversibility of self-trapping in samples without NaI, the laser beam was blocked after self-trapping had begun and then unblocked after a specific amount of time had lapsed. For samples containing NaI, the beam intensity was decreased by 100-fold in order to passively monitor the beam size.

Plots of spatial intensity profiles of the beam were generated with SigmaPlot™ software.

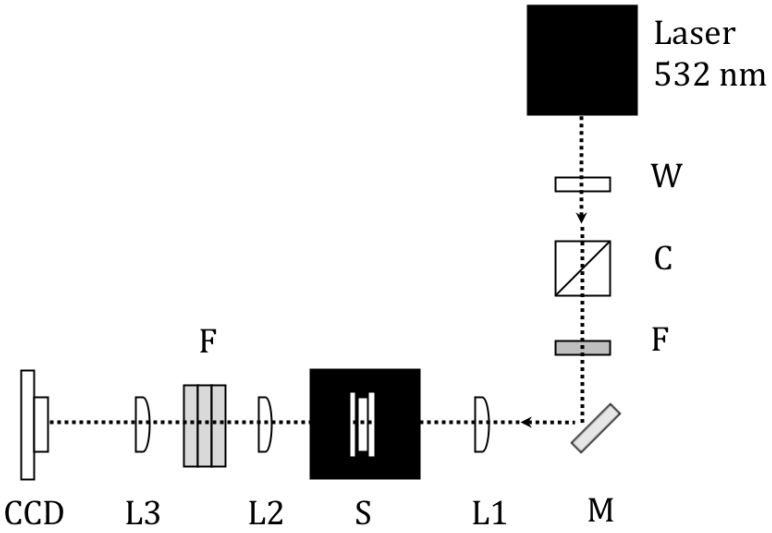

Figure 2-4 Optical assembly for self-trapping.[21]

2.4.1.4 Instrumental techniques

UV-Visible spectroscopy

Absorbance spectra were acquired by a Cary 50 spectrophotometer (Agilent Technologies). Fluorescence measurements were carried out on a Cary 50 Eclipse spectrophotometer (Agilent Technologies).

An aqueous solution and separately, a Pluronic® F-127 gel of tris(bipyridine)ruthenium(II) chloride with and without NaI was irradiated in a quartz cuvette for 10 h with a 532 nm (20 mW) beam. Absorbance spectra were acquired before and after irradiation to identify photoproducts and photodecomposition. Fluorescence spectroscopy was used for the Stern-Volmer study (Section 2.4.1.6).

Differential scanning calorimetry was carried out on a Q20 Differential Scanning Calorimeter (TA Instruments). Measurements were made of the 25 wt. by wt.%

Pluronic® F-127 gels with and without $Ru(bpy)_3Cl_2$; scans of each sample were acquired before and after irradiation (3 h, 532 nm, 40 mW cm^{-2}). Samples were prepared and weighed in Tzero™ hermetic sample cells; an empty hermetic sample cell served as the reference. A heating/cooling rate of 0.2 °C min^{-1} was employed.

2.4.1.5 Control experiments

Pluronic® F-127 gels were prepared from solutions of tris(bipyridine)ruthenium (II) chloride (80 μM). A sample was made with a solution of 100 mM of methyl orange to determine if optical self-trapping originates through a thermal mechanism.

Pluronic® F-127 gels doped with different luminescent chromophores, fluorescein sodium salt (400 μM), rhodamine B (400 μM), and methyl violet (5 mM), were prepared to probe whether luminescence and excitation to a triplet state is a requirement for self-trapping.

To determine the effect of singlet oxygen scavengers on the rate of self-trapping, furfuryl alcohol (0.17 M) was added to a gel containing 80 μM $Ru(bpy)_3Cl_2$.

To probe the role of the Pluronic® F-127 gel matrix on self-trapping, samples were also prepared from a siloxane glass (0.54 M tetramethylorthosilicate; 12 μM $Ru(bpy)_3Cl_2$ in water).

2.4.1.6 Quenching studies with methyl viologen

Aqueous solutions of tris(bipyridine)ruthenium(II) chloride (80 μM) and methyl viologen dichloride hydrate with concentrations ranging from 0 mM-12 mM were prepared and degassed with water-saturated Ar immediately prior to acquiring their fluorescence spectra. Stern-Volmer plots were prepared by plotting relative fluorescence

intensity against the concentration of methyl viologen quencher; the Stern-Volmer constant was obtained according to:

$$\frac{I^0_f}{I_f} = 1 + k_q \tau_0 \bullet [Q] \qquad [S1]$$

The above-mentioned solutions were converted to Pluronic® F-127 gels for studies of optical self-trapping; absorbance and fluorescence spectra of gels were also obtained. The concentration of methyl viologen in the gel was obtained by using the absorbance spectra. Because gel formation leads to a volume change, the modified concentration of methyl viologen was obtained through the absorbance spectra of the gels.

Regression analysis for Stern-Volmer plots was carried out with StatPlus and was used to confirm that the Stern-Volmer constants obtained from self-trapping and fluorescence were statistically the same.

2.4.2 Intensity-dependence of optical self-trapping

Optical self-trapping with 25% Pluronic® F-127 gels containing 1.3 mM $Ru(bpy)_3Cl_2$ and 0.2 M sodium iodide was studied at intensities ranging from 3.2 W cm^{-2} to 159 W $cm^{-2.}$ Figures 2-5 to 2-9 summarize the temporal evolution of the beam intensity and diameter during self-trapping. Results show that the rate of self-trapping increases with incident intensity. However, at intensities > 159 W cm^{-2}, the Gaussian beam transformed into a single ring (Figure 2-9); greater intensities excite large populations of I_3^- and rapidly generate a flat-top Δn profile (different from the gradient, lens-like profile required for self-trapping) across the beam. Modeling previously showed that this elicits the transformation of a Gaussian beam into a ring-like structure[23]. Upon prolonged

irradiation at intensities > 6 kW cm^{-2}, large NaI_3 crystallites (~100 μm) accumulate and scatter light along the beam path, disrupting the self-trapping process (Figure 2-10). It is possible that a small amount of $Ru(bpy)_2I_2$ can also be generated at these high intensities according to Hoggard and coworkers.[27]

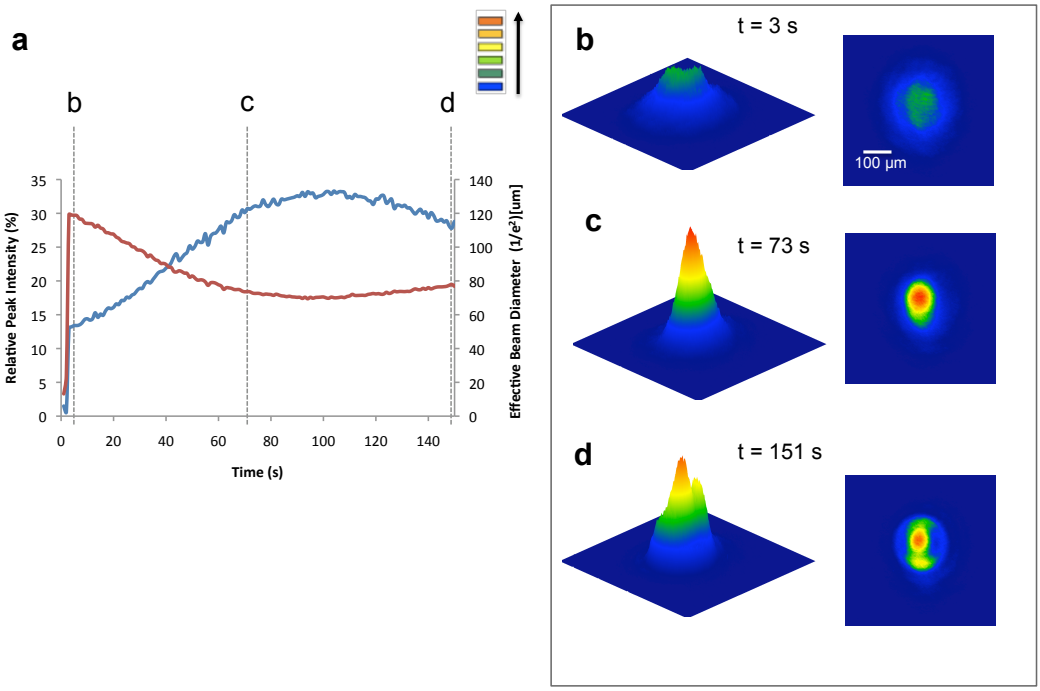

Figure 2-5 Optical self-trapping with Pluronic® F-127 gel containing 1.3 mM $Ru(bpy)_3Cl_2$ and 0.2 M NaI at 3.2 W cm^{-2}. The labeled dotted lines in the (a) graph showing temporal evolution of intensity and beam width correspond to (b-d) spatial intensity profiles of the beam.

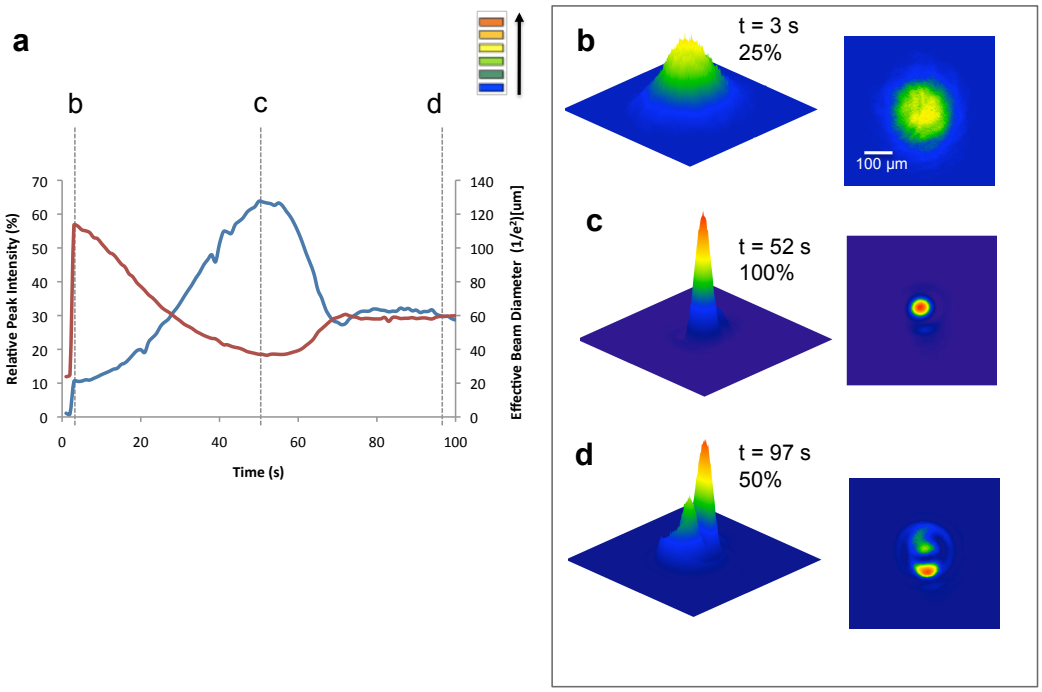

Figure 2-6 Optical self-trapping with Pluronic® F-127 gel containing 1.3 mM $Ru(bpy)_3Cl_2$ and 0.2 M sodium iodide at 8.0 W cm^{-2}. The labeled dotted lines in the (a) graph showing temporal evolution of intensity and beam width correspond to (b-d) spatial intensity profiles of the beam.

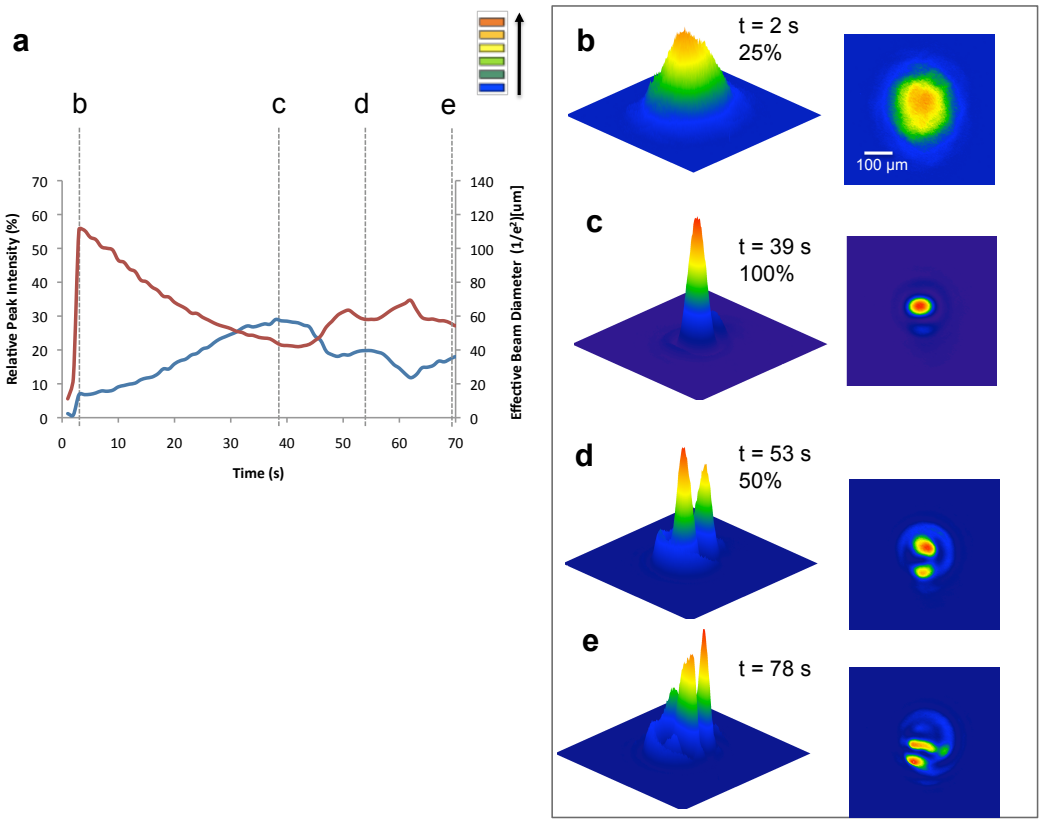

Figure 2-7 Optical self-trapping with Pluronic® F-127 gel containing 1.3 mM $Ru(bpy)_3Cl_2$ and 0.2 M sodium iodide at 16.0 W cm^{-2}. The labeled dotted lines in the (a) graph showing temporal evolution of intensity and beam width correspond to (b-e) spatial intensity profiles of the beam.

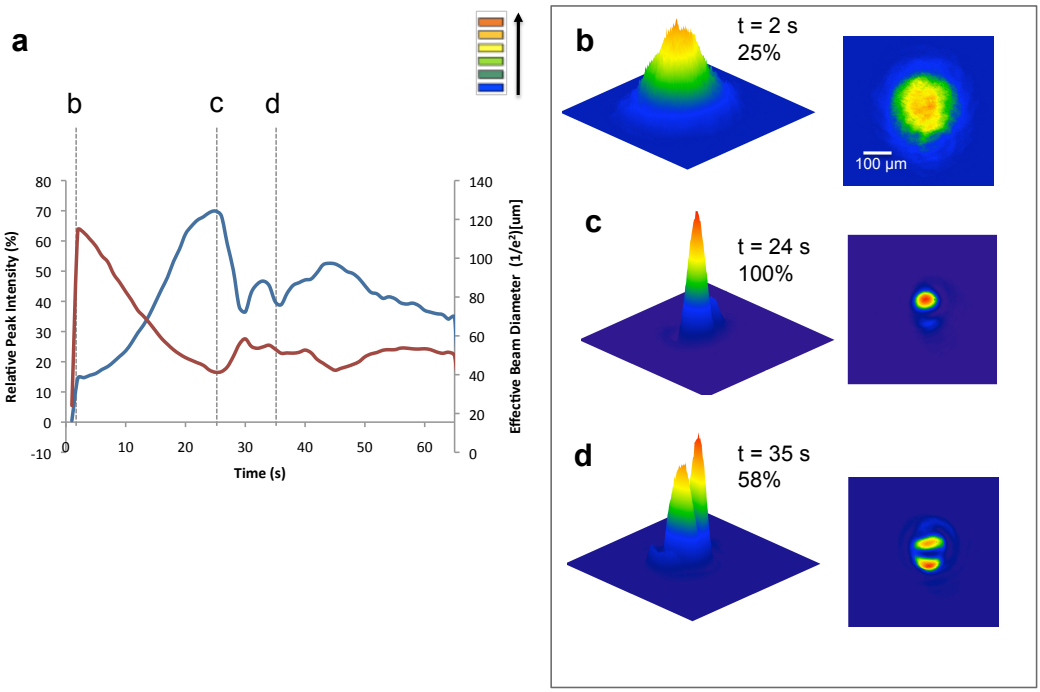

Figure 2-8 Optical self-trapping with Pluronic® F-127 gel containing 1.3 mM $Ru(bpy)_3Cl_2$ and 0.2 M sodium iodide at 32.0 W cm^{-2}. The labeled dotted lines in the (a) graph showing temporal evolution of intensity and beam width correspond to (b-d) spatial intensity profiles of the beam.

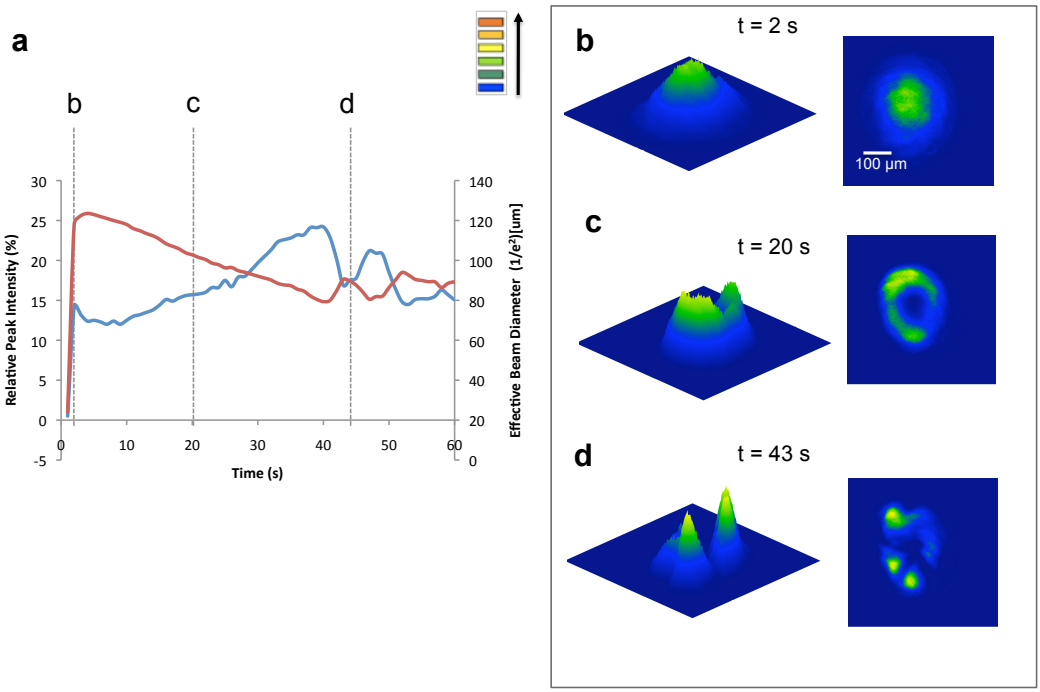

Figure 2-9 Optical self-trapping with Pluronic® F-127 gel containing 1.3 mM $Ru(bpy)_3Cl_2$ and 0.2 M sodium iodide at 159.0 W cm^{-2}. The labeled dotted lines in the (a) graph showing temporal evolution of intensity and beam width correspond to (b-d) spatial intensity profiles of the beam.

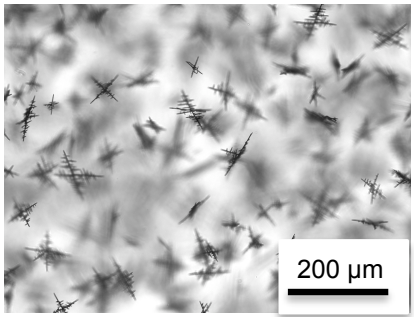

Figure 2-10 Optical micrograph of crystals formed after prolonged laser irradiation.

2.4.3 Optical self-trapping due to a secondary photo-oxidative process

This Section describes the irreversible self-trapping that occurs in hydrogels containing $Ru(bpy)_3Cl_2$ alone in the absence of NaI. The process generates a permanent waveguide and takes over 4000 s to form at 159 W cm^{-2}. The series of experiments described below suggest that Δn in this case originates from crosslinking of the Pluronic® F-127 hydrogel due to photogenerated singlet oxygen. An intensity study revealed that self-trapping is saturable, but no formation of rings occurred, most probably due to the slow evolution time within this system (Figures 2-11 to 2-14).

It was confirmed that Δn in this system did not originate from laser-induced heating and phase transitions in the hydrogel[28,29,30,31]: self-trapping did not occur in hydrogels in the absence of $Ru(bpy)_3^{2+}$ (Figure 2-15) nor was it induced by heat dissipated by non-radiative relaxation of photoexcited chromophores; for example, self-trapping was not observed when $Ru(bpy)_3^{2+}$ was replaced with methyl orange, which has even greater absorbance at 532 nm (Figure 2-16).

We found that the secondary self-trapping rate decreased with increasing concentrations of quencher, methyl viologen (Figures 2-17 to 2-22).[32] Stern-Volmer plots comparing the effect of methyl viologen on secondary self-trapping rate and separately, photoluminescence of $Ru(bpy)_3^{2+}$, yielded statistically equal K_{SV} constants confirming that photoexcited $Ru(bpy)_3^{2+}$ was critical to this secondary process (Figures 2-23 to 2-25). Specifically, singlet oxygen generated by $Ru(bpy)_3^{2+*}$ played a key role[33]; for e.g., there was a significant decrease in self-trapping rate in the presence of scavenger furfuryl alcohol (Figure 2-26).[34] The photodegradation of $Ru(bpy)_3Cl_2$ at long times is also likely due to

singlet oxygen (Figure 2-27). Indeed, hydrogels containing a range of sensitizers capable of producing singlet oxygen including fluorescein, rhodamine b and methyl violet displayed secondary self-trapping, with the greatest rate found with chromophores possessing the largest quantum yields (Figures 2-28 to 2-30).[35,36]

The fluorescence intensity of $Ru(bpy)_3^{2+}$ remained unchanged by the furfuryl alcohol, indicating that the excited complex does not react directly with its gel medium (Figure 2-31). However, the hydrogel is essential as self-trapping was not observed in water or a siloxane matrix containing $Ru(bpy)_3^{2+}$ (Figures 2-32 to 2-33). Pluronic® copolymers can enhance the production of singlet oxygen,[37] which is highly reactive towards olefins, ethers, and other electron-rich groups,[3333,38,39] and can effect crosslinking of collagen gels when illuminated in the presence of a photosensitizer[40] through a complex mechanism involving several radical species including hydroxyl radicals.[41,42]

Based on the above-described observations, we conclude that singlet oxygen generated by photoexcited $Ru(bpy)_3^{2+}$ leads to the irreversible oxidation and subsequent crosslinking of the Pluronic® F-127 hydrogel (Figure 2-34). While matrix densification due to cross-linking was not detected by ^1H NMR or IR spectroscopy, differential scanning calorimetry showed a shift of ~1ºC in the micellization temperature of the laser-irradiated Pluronic® F-127 medium containing $Ru(bpy)_3^{2+}$ (Figure 2-35). Crosslinking in the hydrogel localized to the beam path generates Δn, which underlies secondary self-trapping. In the presence of NaI however, the slow, secondary self-trapping is negligible and self-trapped beams can be quickly and reversibly generated.

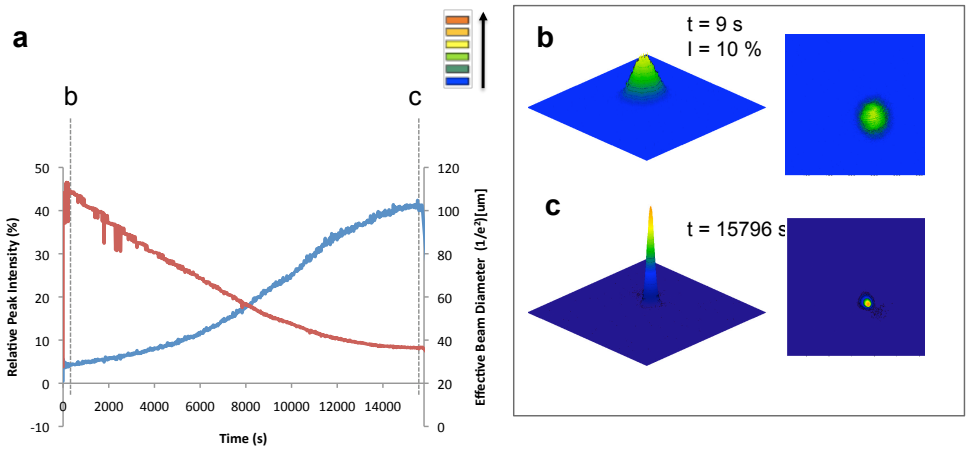

Figure 2-11 Optical self-trapping with Pluronic® F-127 gel containing 12 μM $Ru(bpy)_3Cl_2$ at 6.4 W cm^{-2}. The labeled dotted lines in the (a) graph showing temporal evolution of intensity and beam width correspond to (b-c) spatial intensity profiles of the beam.

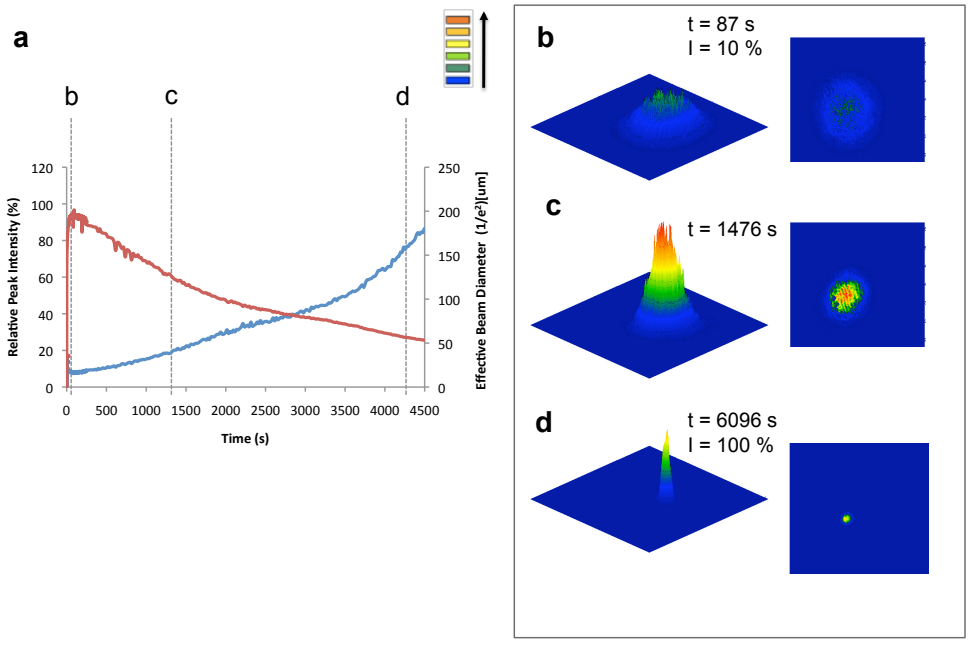

Figure 2-12 Optical self-trapping with Pluronic® F-127 gel containing 12 μM $Ru(bpy)_3Cl_2$ at 32 W cm^{-2}. The labeled dotted lines in the (a) graph showing temporal evolution of intensity and beam width correspond to (b-d) spatial intensity profiles of the beam.

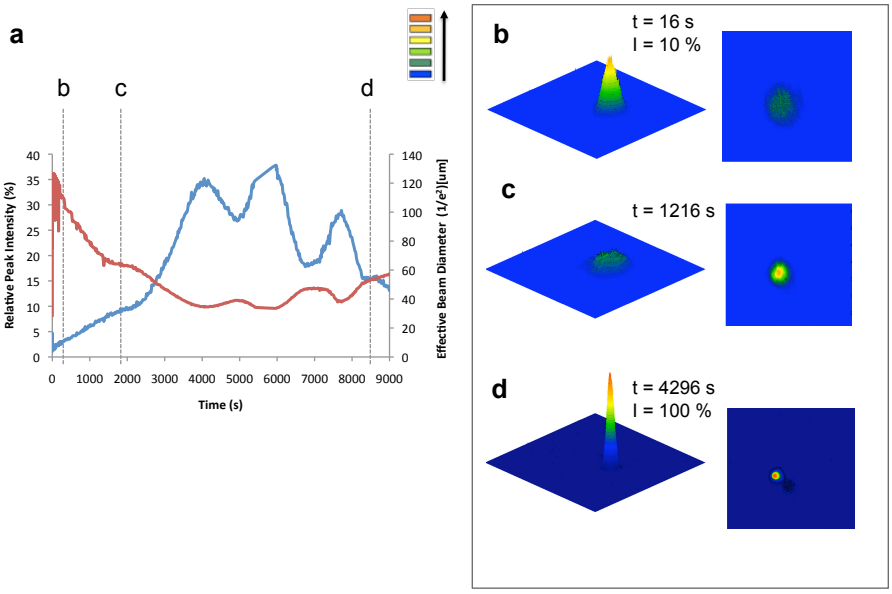

Figure 2-13 Optical self-trapping with Pluronic® F-127 gel containing 12 μM $Ru(bpy)_3Cl_2$ at 64 W cm^{-2}. The labeled dotted lines in the (a) graph showing temporal evolution of intensity and beam width correspond to (b-d) spatial intensity profiles of the beam.

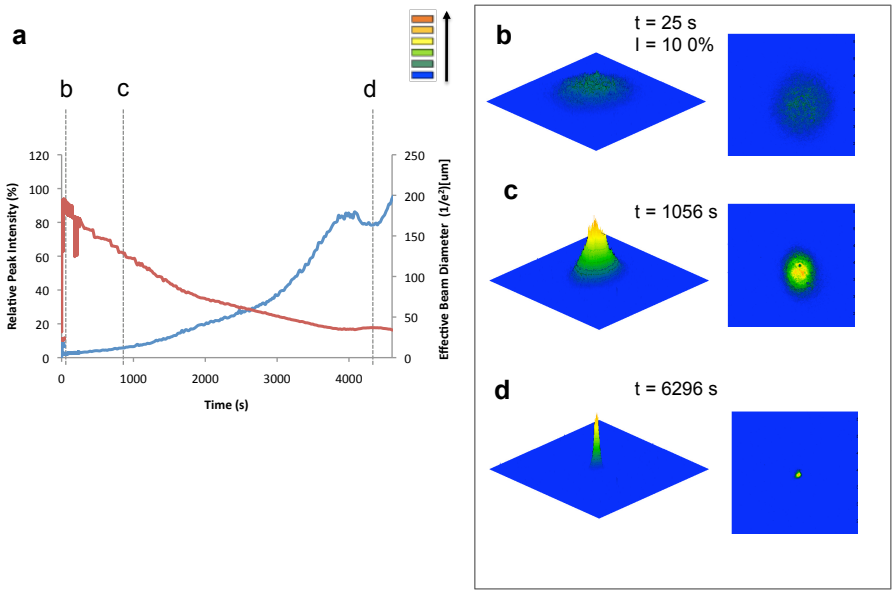

Figure 2-14 Optical self-trapping with Pluronic® F-127 gel containing 12 μM $Ru(bpy)_3Cl_2$ at 159 W cm^{-2}. The labeled dotted lines in the (a) graph showing temporal evolution of intensity and beam width correspond to (b-d) spatial intensity profiles of the beam.

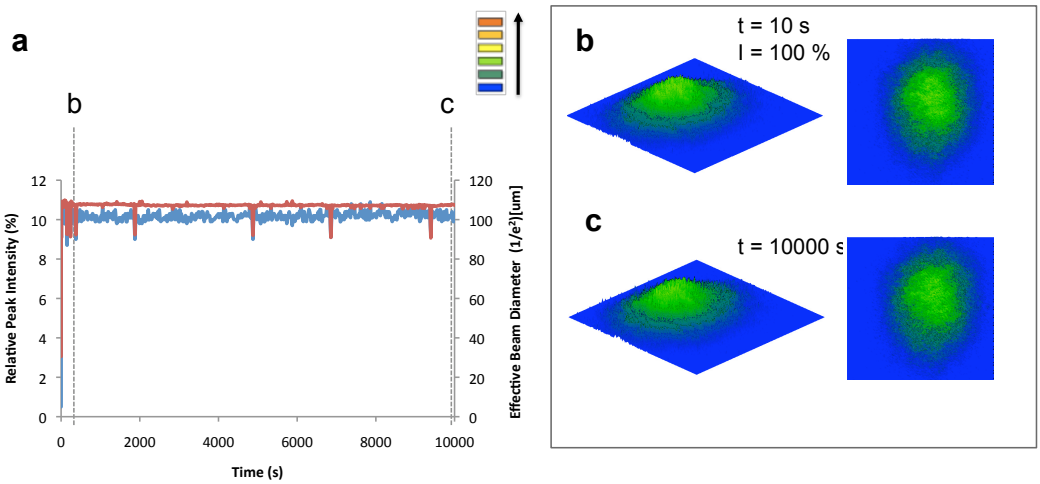

Figure 2-15 Optical self-trapping with Pluronic® F-127 gel at 159 W cm^{-2}. The labeled dotted lines correspond to the included spatial intensity profiles.

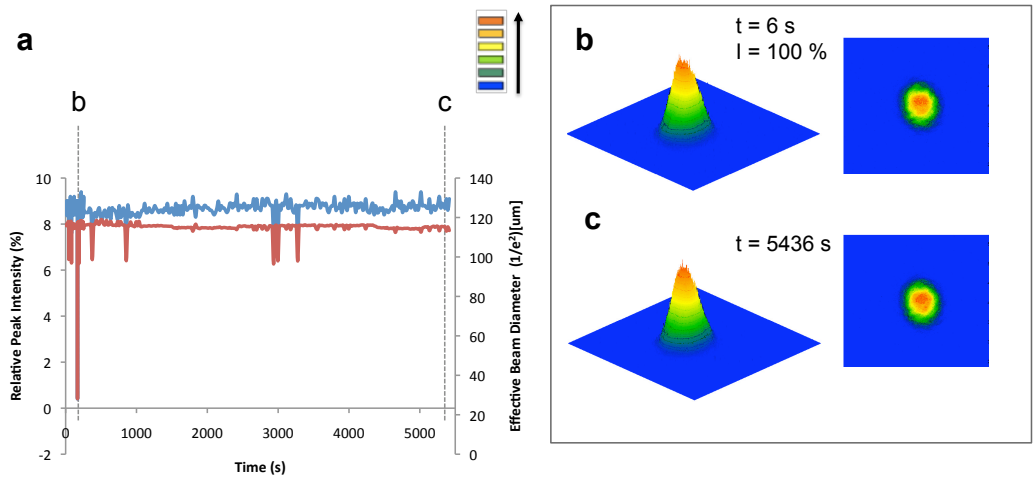

Figure 2-16 Optical self-trapping with Pluronic® F-127 gel containing 100 mM methyl orange at 159 W cm^{-2}. The labeled dotted lines in the (a) graph showing temporal evolution of intensity and beam width correspond to (b-d) spatial intensity profiles of the beam.

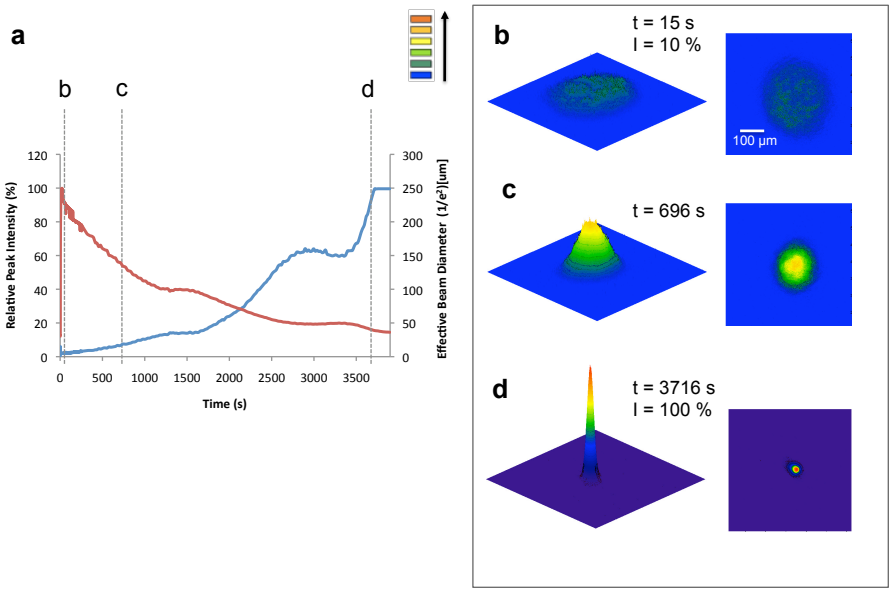

Figure 2-17 Optical self-trapping with Pluronic® F-127 gel containing 80 µM $Ru(bpy)_3Cl_2$ and no methyl viologen at 159 W cm^{-2}. The labeled dotted lines in the (a) graph showing temporal evolution of intensity and beam width correspond to (b-d) spatial intensity profiles of the beam.

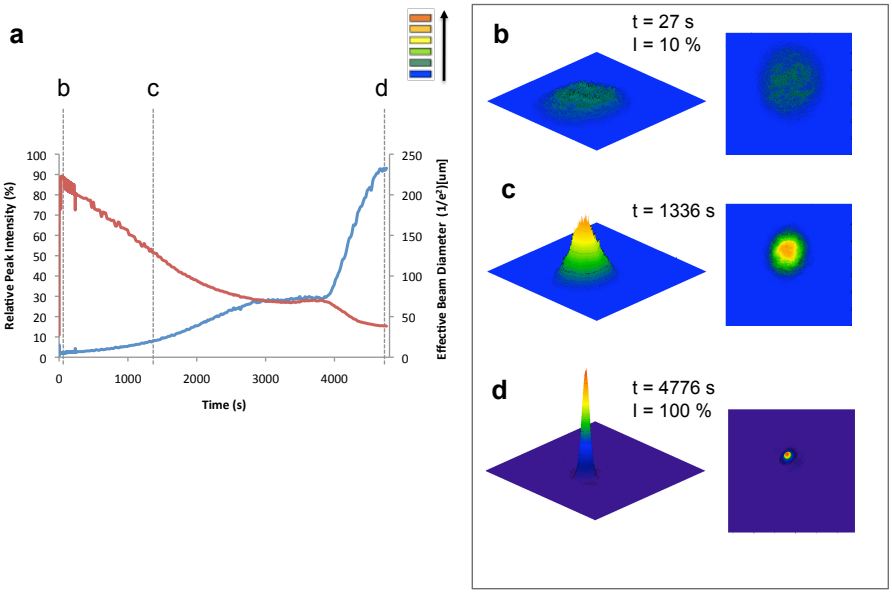

Figure 2-18 Optical self-trapping with Pluronic® F-127 gel containing 80 µM $Ru(bpy)_3Cl_2$ and 6.0 mM methyl viologen at 159 W cm^{-2}. The labeled dotted lines in the (a) graph showing temporal evolution of intensity and beam width correspond to (b-d) spatial intensity profiles of the beam.

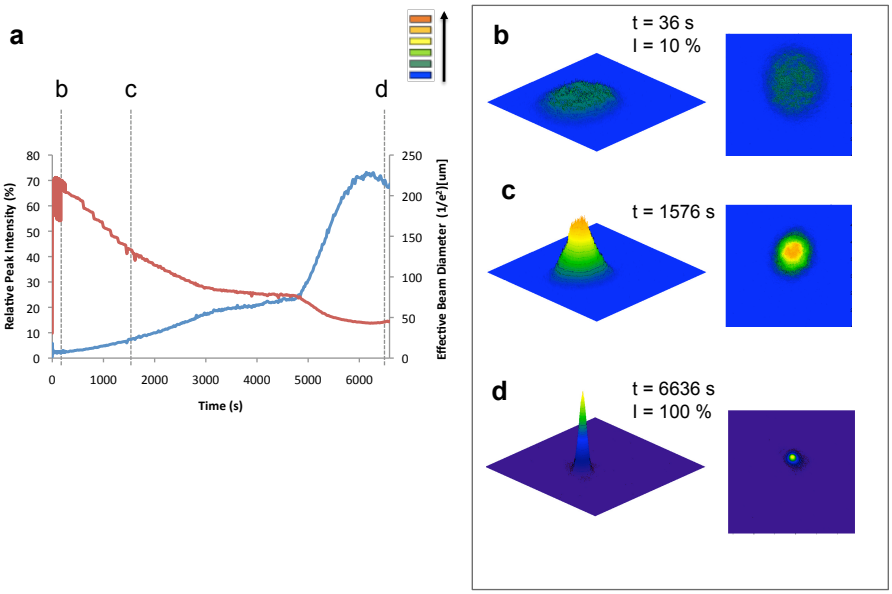

Figure 2-19 Optical self-trapping with Pluronic® F-127 gel containing 80 μM $Ru(bpy)_3Cl_2$ and 11.9 mM methyl viologen at 159 W cm^{-2}. The labeled dotted lines in the (a) graph showing temporal evolution of intensity and beam width correspond to (b-d) spatial intensity profiles of the beam.

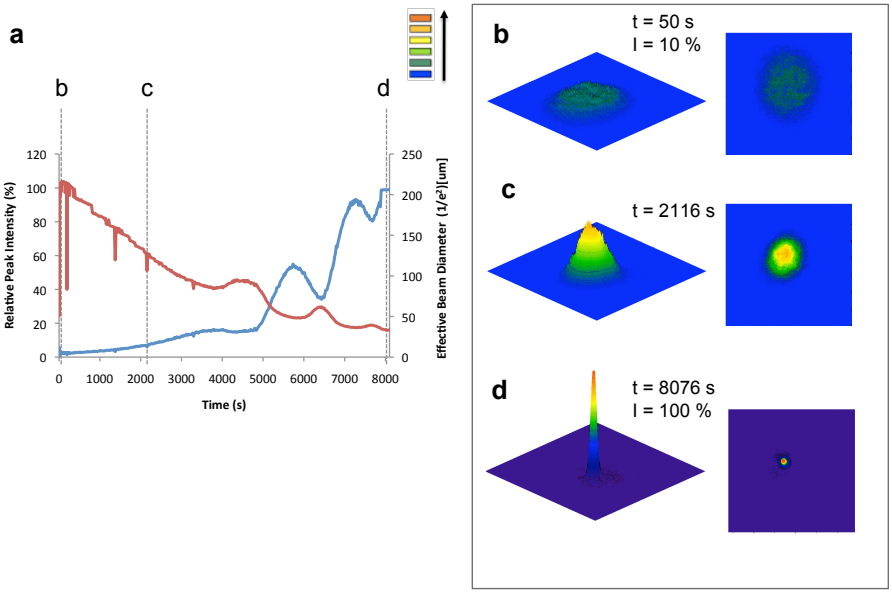

Figure 2-20 Optical self-trapping with Pluronic® F-127 gel containing 80 μM $Ru(bpy)_3Cl_2$ and 14.8 mM methyl viologen at 159 W cm^{-2}. The labeled dotted lines in the (a) graph showing temporal evolution of intensity and beam width correspond to (b-d) spatial intensity profiles of the beam.

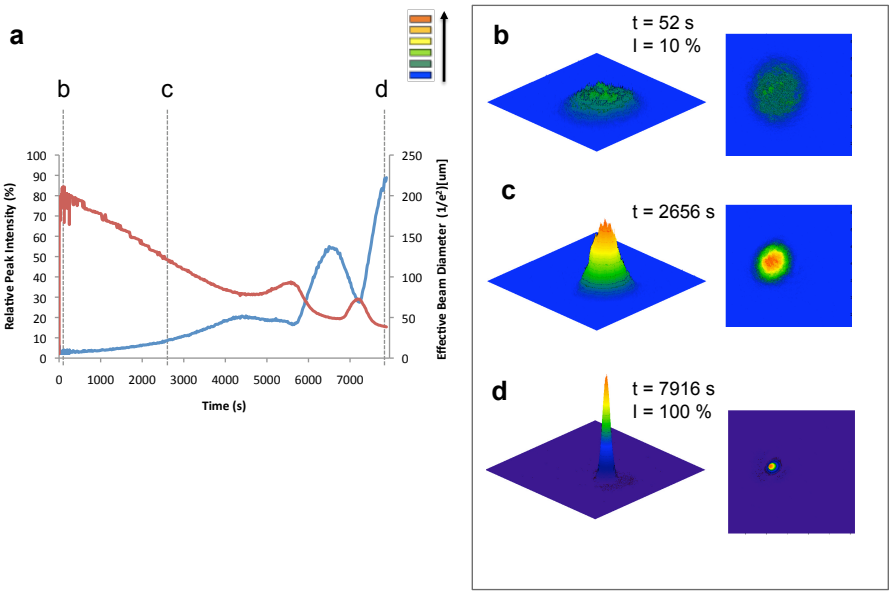

Figure 2-21 Optical self-trapping with Pluronic® F-127 gel containing 80 μM $Ru(bpy)_3Cl_2$ and 22.9 mM methyl viologen at 159 W cm^{-2}. The labeled dotted lines in the (a) graph showing temporal evolution of intensity and beam width correspond to (b-d) spatial intensity profiles of the beam.

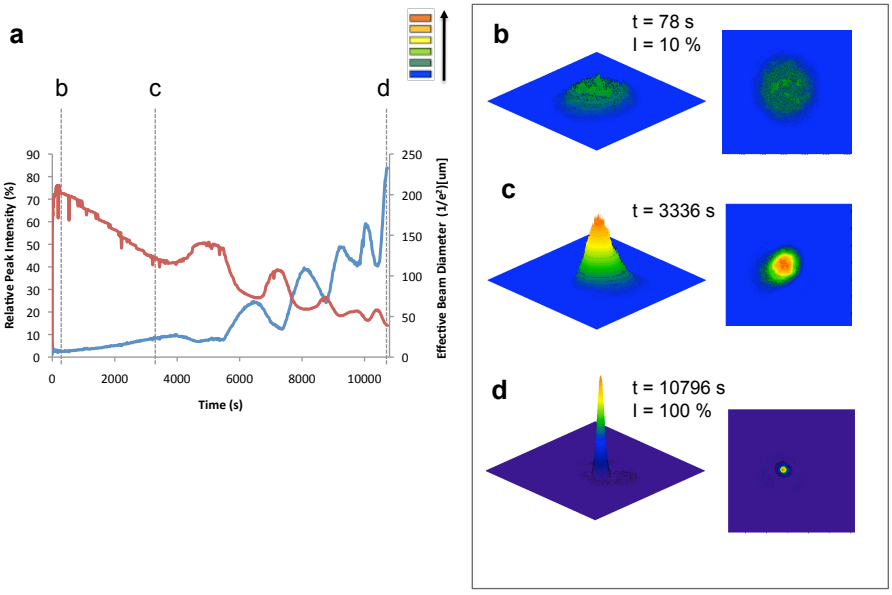

Figure 2-22 Optical self-trapping with Pluronic® F-127 gel containing 80 μM $Ru(bpy)_3Cl_2$ and 35.7 mM methyl viologen at 159 W cm^{-2}. The labeled dotted lines in the (a) graph showing temporal evolution of intensity and beam width correspond to (b-d) spatial intensity profiles of the beam.

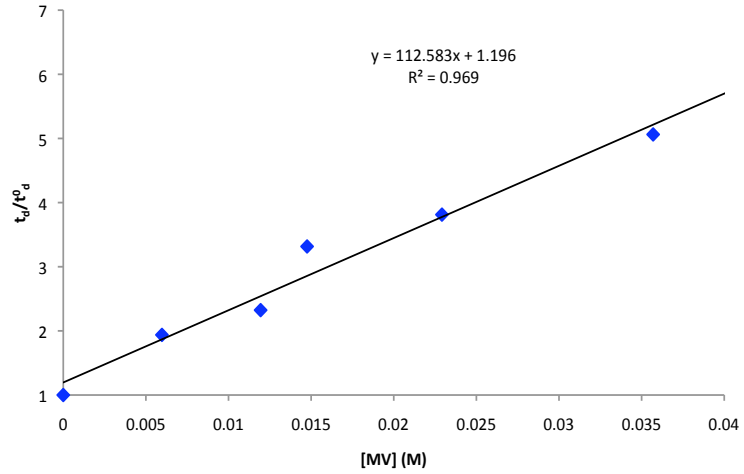

Figure 2-23 Stern-Volmer plot for self-trapping in Pluronic® gels containing tris(bipyridine)ruthenium(II) chloride and methyl viologen dichloride.

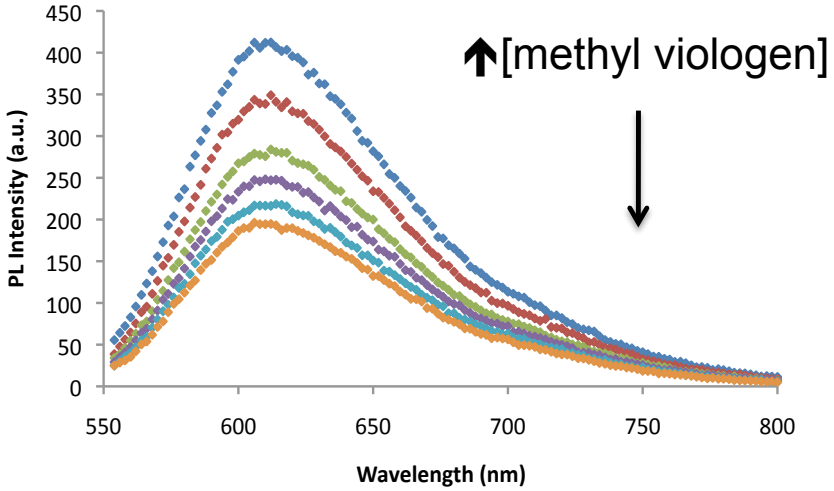

Figure 2-24 Photoluminescence spectra of $Ru(bpy)_3^{2+}$ in Pluronic® gels as the concentration of methyl viologen increases. Increased concentration of quencher results in decreased photoluminescence.

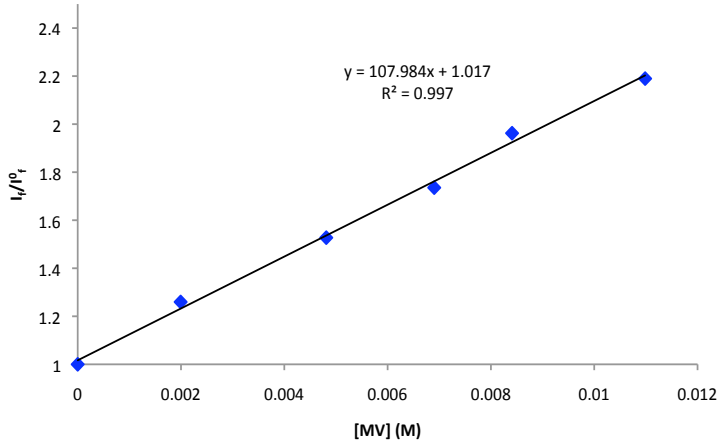

Figure 2-25 Stern Volmer-plot for photoluminescence in Pluronic® gels containing tris(bipyridine)ruthenium(II) chloride (80 μM) and methyl viologen dichloride (0 mM-12 mM).

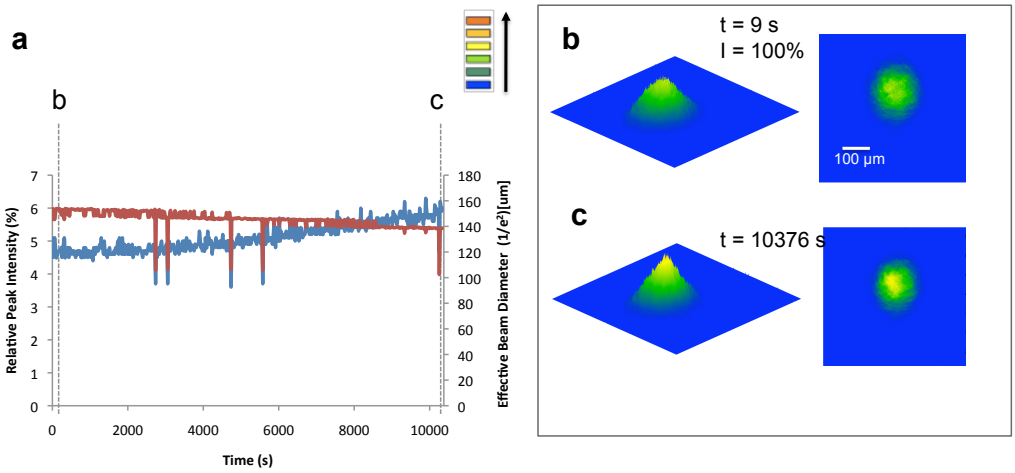

Figure 2-26 Self-trapping in Pluronic® gels containing tris(bipyridine)ruthenium(II) chloride in the presence of furfuryl alcohol. The labeled dotted lines in the graph showing temporal evolution of beam intensity and diameter correspond to (b-c) spatial intensity profiles of the beam.

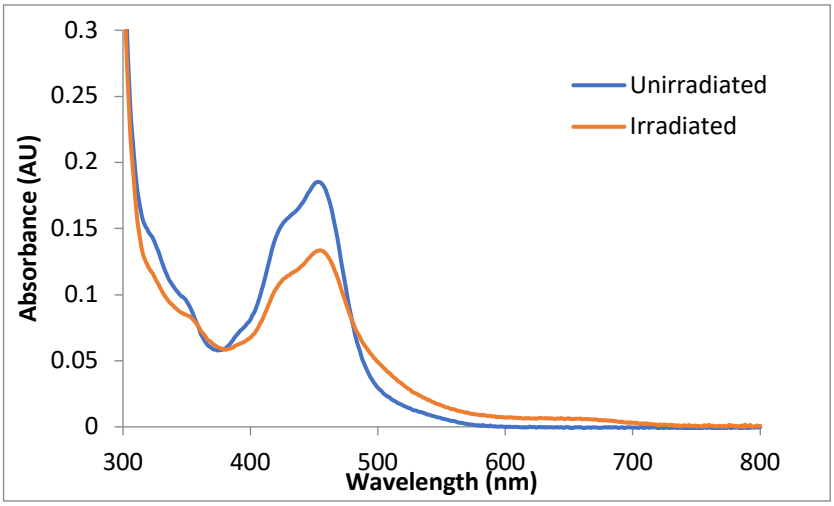

Figure 2-27 UV-visible absorbance spectrum of $Ru(bpy)_3^{2+}$ in 25% Pluronic® F-127 gel before and after extended irradiation at high intensities.

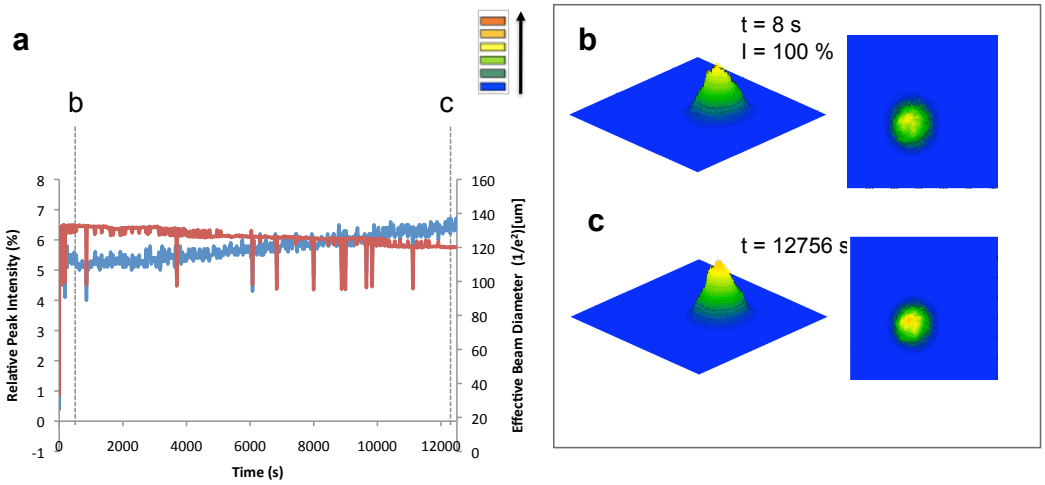

Figure 2-28 Optical self-trapping with Pluronic® F-127 gel containing 5 mM methyl violet at 159 W cm^{-2}. The labeled dotted lines in the graph showing temporal evolution of beam intensity and diameter correspond to (b-c) spatial intensity profiles of the beam.

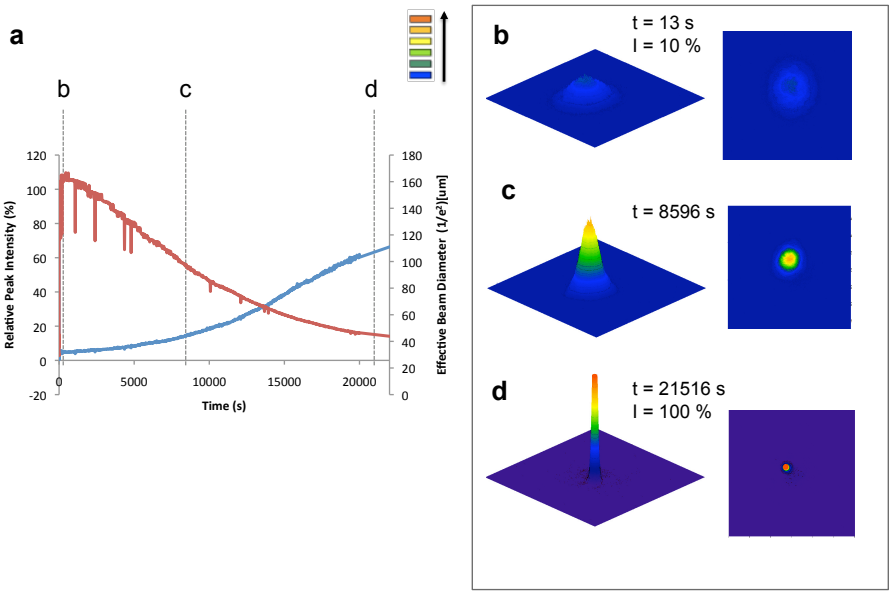

Figure 2-29 Optical self-trapping with Pluronic® F-127 gel containing 400 μM fluorescein at 159 W cm^{-2}. The labeled dotted lines in the graph showing temporal evolution of beam intensity and diameter correspond to (b-d) spatial intensity profiles of the beam.

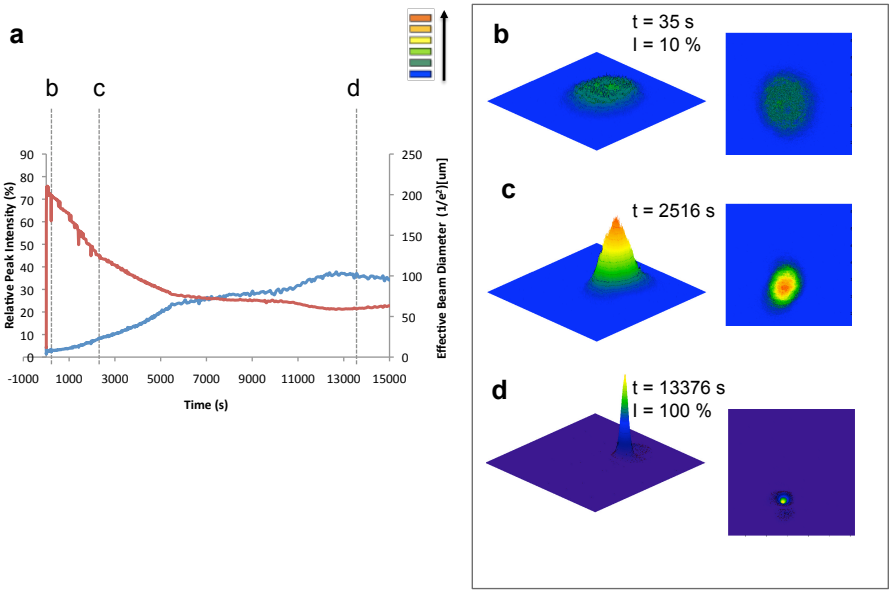

Figure 2-30 Optical self-trapping with Pluronic® F-127 gel containing 400 μM rhodamine B at 159 W cm^{-2}. The labeled dotted lines in the graph showing temporal evolution of beam intensity and diameter correspond to (b-c) spatial intensity profiles of the beam.

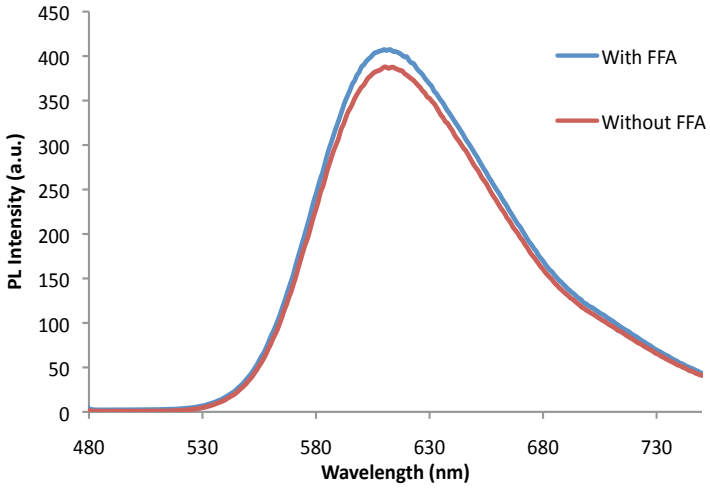

Figure 2-31 UV-visible emission spectrum of $Ru(bpy)_3^{2+}$ in H_2O with and without furfuryl alcohol (FFA).

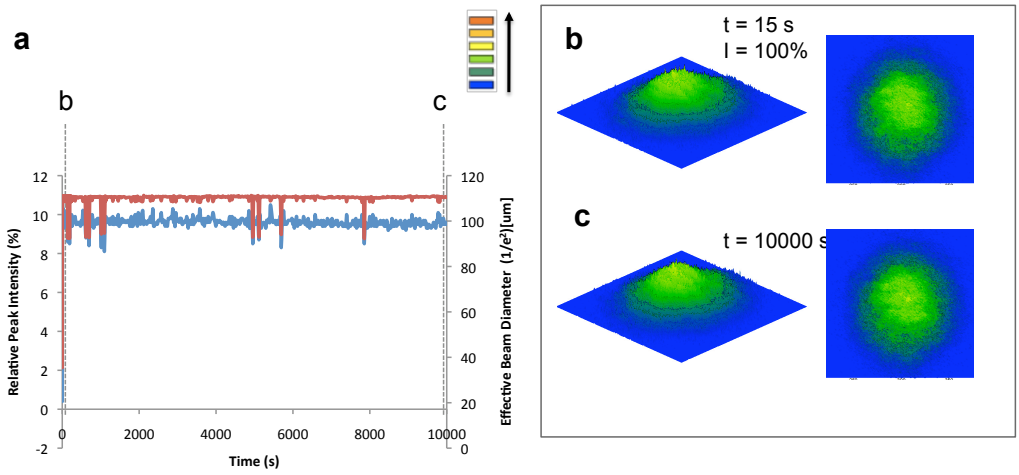

Figure 2-32 Optical self-trapping in an aqueous solution containing 80 μM $Ru(bpy)_3Cl_2$ at 159 W cm^{-2}. The labeled dotted lines in the graph showing temporal evolution of beam intensity and diameter correspond to (b-c) spatial intensity profiles of the beam.

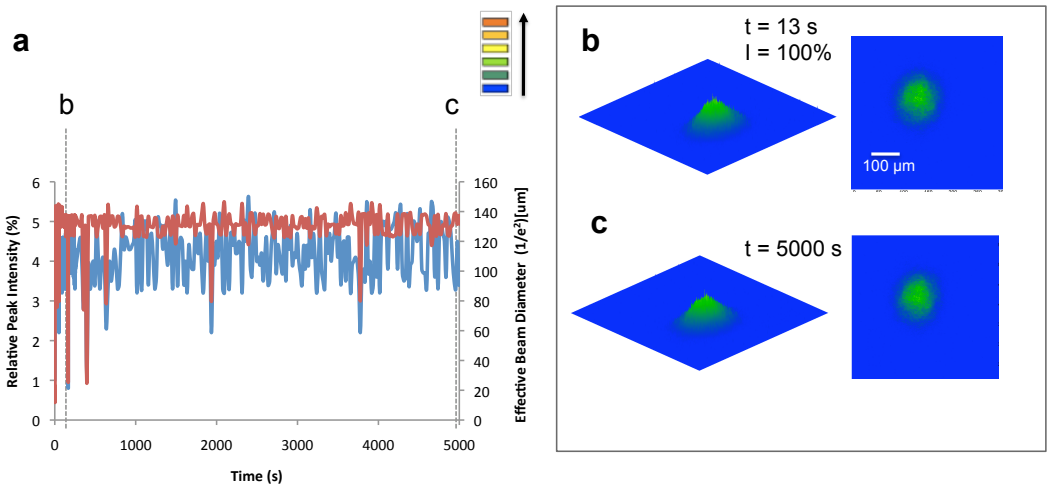

Figure 2-33 Optical self-trapping within a siloxane gel containing 12 µM $Ru(bpy)_3Cl_2$ at 159 W cm^{-2}. The labeled dotted lines correspond to the included spatial intensity profiles. The labeled dotted lines in the graph showing temporal evolution of beam intensity and diameter correspond to (b-c) spatial intensity profiles of the beam.

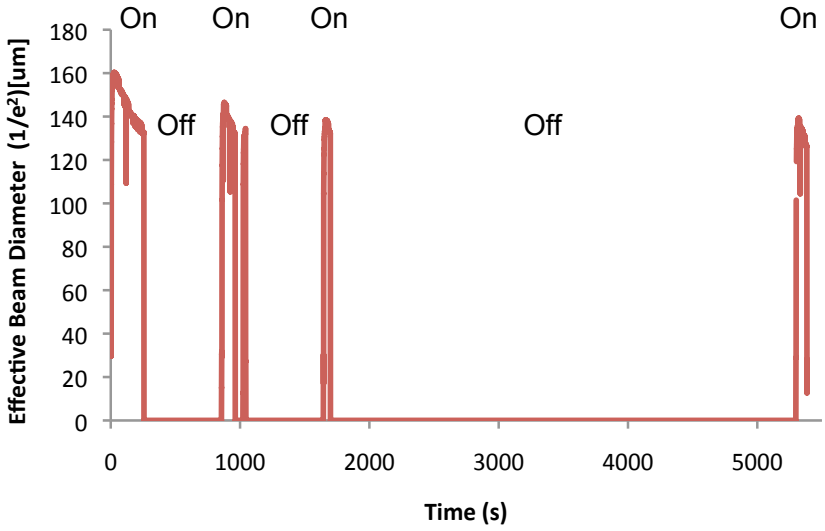

Figure 2-34 Optical self-trapping of a Pluronic® F-127 gel containing $Ru(bpy)_3^{2+}$ at 159 W cm^{-2}; the beam was blocked for extended periods of time in order to determine that the system is irreversible. "On" denotes that the beam is incident on the sample and "Off" denotes that the beam has been blocked to allow the sample to relax. The beam profile does not change even when blocked for over an hour, suggesting an irreversible process has occurred.

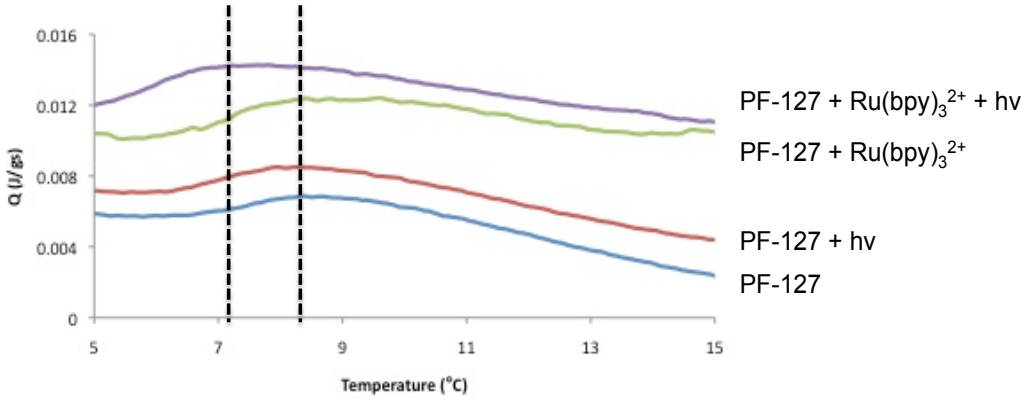

Figure 2-35 DSC traces for Pluronic® F-127 gels with and without $Ru(bpy)_3^{2+}$. Scans were acquired for both samples prior to and after irradiation.

2.4.4 Description of movies

The following movies are available from the original article with:
DOI: 10.1021/acs.jpclett.6b00126

MOVIE_S1: Optical self-trapping due to iodide oxidation

Temporal evolution and dynamics of the spatial intensity profile of laser beam (532 nm, 8 W cm^{-2}) at the exit face of a 25% Pluronic® F-127 gel containing 1.3 mM $Ru(bpy)_3Cl_2$ and 0.2 M sodium iodide.

MOVIE_S2: Optical self-trapping due to oxidation of Pluronic® F-127

Temporal evolution and dynamics of the spatial intensity profile of laser beam (532 nm, 159 W cm^{-2}) at the exit face of a 25% Pluronic® F-127 gel doped with 12 μM $Ru(bpy)_3Cl_2$ compared to a 25% Pluronic® F-127 gel without $Ru(bpy)_3Cl_2$.

2.5 References

(1) Trillo, S.; Torruellas, W. *Spatial Solitons*; Springer: New York, 2001.
(2) Chiao, R. Y.; Garmire, E.; Townes, C. H. Self-Trapping of Optical Beams. *Phys. Rev. Lett.* **1964**, *13*, 479–482.
(3) Snyder, A. W.; Ladouceur, F. Light Guiding Light: Letting Light Be the Master of Its Own Destiny. *Opt. Photonics News* **1999**, *10*, 35.
(4) Peccianti, M.; Brzdkiewicz, K. A.; Assanto, G. Nonlocal Spatial Soliton Interactions in Nematic Liquid Crystals. *Opt. Lett.* **2002**, *27*, 1460–1462.
(5) Crosignani, B.; Di Porto, P.; Degasperis, A.; Segev, M.; Trillo, S. Three-Dimensional Optical Beam Propagation and Solitons in Photorefractive Crystals. *JOSA B* **1997**, *14*, 3078–3090.
(6) Burak, D.; Nasalski, W. Gaussian Beam to Spatial Soliton Formation in Kerr Media. *Appl. Opt.* **1994**, *33*, 6393–6401.
(7) Monro, T. M.; De Sterke, C. M.; Poladian, L. Catching Light in Its Own Trap. *J. Mod. Opt.* **2001**, *48*, 191–238.
(8) Caspar, J. V; Meyer, T. J. Photochemistry of Ru(Bpy)32+. Solvent Effects. **1983**, *3*, 5583–5590.
(9) Campagna, S.; Francesco, P.; Bergamini, G.; Balzani, V.; Inorganica, C.; Analitica, C. Photochemistry and Photophysics of Coordination Compounds : Ruthenium. **2007**, No. June, 117–214.
(10) Yoon, T. P.; Ischay, M. a; Du, J. Visible Light Photocatalysis as a Greener Approach to Photochemical Synthesis. *Nat. Chem.* **2010**, *2*, 527–532.
(11) Marton, A.; Clark, C. C.; Srinivasan, R.; Freundlich, R. E.; Narducci Sarjeant, A. A.; Meyer, G. J. Static and Dynamic Quenching of Ru(II) Polypyridyl Excited States by Iodide. *Inorg. Chem.* **2006**, *45*, 362–369.
(12) Gardner, J. M.; Abrahamsson, M.; Farnum, B. H.; Meyer, G. J. Visible Light Generation of Iodine Atoms and I-I Bonds: Sensitized I - Oxidation and I3- Photodissociation. *J. Am. Chem. Soc.* **2009**, *131*, 16206–16214.
(13) Clark, C. C.; Marton, A.; Srinivasan, R.; Narducci Sarjeant, A. a; Meyer, G. J. Triiodide Quenching of Ruthenium MLCT Excited State in Solution and on TiO2 Surfaces: An Alternate Pathway for Charge Recombination. *Inorg. Chem.* **2006**, *45*, 4728–4734.
(14) Farnum, B. H.; Jou, J. J.; Meyer, G. J. Visible Light Generation of I – I Bonds by Ru-Tris (Diimine) Excited States. **2012**, *2012*.
(15) Boschloo, G.; Hagfeldt, A.; Spectus, C. O. N. Characteristics of the Iodide / Triiodide Redox Mediator in Dye-Sensitized Solar Cells. **2009**, *42*, 1819–1826.
(16) Lynden-Bell, R. M.; Kosloff, R.; Ruhman, S.; Danovich, D.; Vala, J. Does Solvation Cause Symmetry Breaking in the I3− Ion in Aqueous Solution? *J. Chem. Phys.* **1998**, *109*.
(17) Barba, A. A.; D'Amore, M.; Grassi, M.; Chirico, S.; Lamberti, G.; Titomanlio, G. Investigation of Pluronic© F127-Water Solutions Phase Transitions by DSC and Dielectric Spectroscopy. *J. Appl. Polym. Sci.* **2009**, *114*, 688–695.
(18) Landazuri, G.; Fernandez, V. V. A.; Soltero, J. F. A.; Rharbi, Y. Kinetics of the

Sphere-to-Rod like Micelle Transition in a Pluronic Triblock Copolymer. *J. Phys. Chem. B* **2012**, *116*, 11720–11727.
(19) Pina, F.; Hatton, T. A. Photochromic Soft Materials: Flavylium Compounds Incorporated into Pluronic F-127 Hydrogel Matrixes. *Langmuir* **2008**, *24*, 2356–2364.
(20) Su, Y.; Wang, J.; Liu, H. FTIR Spectroscopic Study on Effects of Temperature and Polymer Composition on the Structural Properties of PEO−PPO−PEO Block Copolymer Micelles. *Langmuir* **2002**, *18*, 5370–5374.
(21) Villafranca, A. B.; Saravanamuttu, K. An Experimental Study of the Dynamics and Temporal Evolution of Self-Trapped Laser Beams in a Photopolymerizable Organosiloxane. *J. Phys. Chem. C* **2008**, *112*, 17388–17396.
(22) Monro, T. M.; de Sterke, C. M.; Poladian, L. Analysis of Self-Written Waveguide Experiments. *J. Opt. Soc. Am. B* **1999**, *16*, 1680–1685.
(23) Villafranca, Ana; Saravanamuttu, K. Spontaneous and Sequential Transitions of a Gaussian Beam into Diffraction Rings, Single Ring and Circular Array of Filaments in a Photopolymer. *Opt. Express* **2011**, *19*, 15560–15573.
(24) Pandit, N. K.; Kisaka, J. Loss of Gelation Ability of Pluronic F127 in the Presence of Some Salts. *Int. J. Pharm.* **1996**, *145*, 129–136.
(25) Ruff, I.; Friedrich, V. J.; Csillag, K. Transfer Diffusion. III. Kinetics and Mechanism of the Triiodide-Iodide Exchange Reaction. *J. Phys. Chem.* **1972**, *76*, 162–165.
(26) Papageorgiou, N.; Athanassov, Y.; Armand, M.; Bonho, P.; Pettersson, H.; Azam, A.; Grätzel, M.; others. The Performance and Stability of Ambient Temperature Molten Salts for Solar Cell Applications. *J. Electrochem. Soc.* **1996**, *143*, 3099–3108.
(27) Wallace, W. M.; Hoggard, P. E. A Simple Photochemical Synthesis of Some Bis (Bipyridyl) Ruthenium (II) Complexes. *Inorg. Chem.* **1979**, *18*, 2934–2935.
(28) de Jong, J. J. D.; Hania, P. R.; Pugžlys, A.; Lucas, L. N.; de Loos, M.; Kellogg, R. M.; Feringa, B. L.; Duppen, K.; van Esch, J. H. Light-Driven Dynamic Pattern Formation. *Angew. Chemie Int. Ed.* **2005**, *44*, 2373–2376.
(29) Delaire, J. a; Nakatani, K. Linear and Nonlinear Optical Properties of Photochromic Molecules and Materials. *Chem. Rev.* **2000**, *100*, 1817–1846.
(30) Zhang, B. Z.; Wang, H. C.; She, W. L. Influence of Molecular Reorientation on Photoisomerization Optical Spatial Solitons. *J. Opt. A Pure Appl. Opt.* **2007**, *9*, 395.
(31) Mandal, B. K.; Kumar, J.; Huang, J.-C.; Tripathy, S. Novel Photo-Crosslinked Nonlinear Optical Polymers. *Die Makromol. Chemie, Rapid Commun.* **1991**, *12*, 63–68.
(32) Morton Z. Hoffman, Fabrizio Bolletta, Luca Moggi, and G. L. H. Rate Constants for the Quenching of Excited States of Metal Complexes in Fluid Solution. *J. Phys. Chem. Ref. Data* **1989**, *18*, 219–543.
(33) DeRosa, M. C.; Crutchley, R. J. Photosensitized Singlet Oxygen and Its Applications. *Coord. Chem. Rev.* **2002**, *233–234*, 351–371.
(34) Haag, W. R.; Hoigne´, J.; Gassman, E.; Braun, A. Singlet Oxygen in Surface

Waters — Part I: Furfuryl Alcohol as a Trapping Agent. *Chemosphere*. **1984**, 631–640.
(35) Kubin, R. F.; Fletcher, A. N. Fluorescence Quantum Yields of Some Rhodamine Dyes. *J. Lumin.* **1983**, *27*, 455–462.
(36) Gandin, E.; Lion, Y.; de Vorst, A. Quantum Yield of Singlet Oxygen Production by Xanthene Derivatives. *Photochem. Photobiol.* **1983**, *37*, 271–278.
(37) Park, H.; Na, K. Conjugation of the Photosensitizer Chlorin E6 to Pluronic F127 for Enhanced Cellular Internalization for Photodynamic Therapy. *Biomaterials* **2013**, *34*, 6992–7000.
(38) Choi, M. M. F.; Xiao, D. Single Standard Calibration for an Optical Oxygen Sensor Based on Luminescence Quenching of a Ruthenium Complex. *Anal. Chim. Acta* **2000**, *403*, 57–65.
(39) Sortino, S.; Petralia, S.; Boscà, F.; Miranda, M. A. Irreversible Photo-Oxidation of Propranolol Triggered by Self-Photogenerated Singlet Molecular Oxygen. *Photochem. Photobiol. Sci.* **2002**, *1*, 136–140.
(40) Ibusuki, S.; Halbesma, G. J.; Randolph, M. A.; Redmond, R. W.; Kochevar, I. E.; Gill, T. J. Photochemically Cross-Linked Collagen Gels as Three-Dimensional Scaffolds for Tissue Engineering. *Tissue Eng.* **2007**, *13*, 1995–2001.
(41) Yousif, E.; Haddad, R. Photodegradation and Photostabilization of Polymers, Especially Polystyrene: Review. *Springerplus* **2013**, *2*, 398.
(42) Rabek, J. F. *Photostabilization of Polymers: Priciples and Application*; Springer Science & Business Media, 2012.

3 Opto-chemo-mechanical transduction in photoresponsive gels: switchable self-trapped beams and their remote interactions[‡]

3.1 Abstract

Due to its discrete, linear "on-off" photoresponse, spiropyran isomerization is one of the most extensively employed photoswitching mechanisms in applications ranging from drug delivery and microfluidics to optical data storage and sensing. Here, we show that this photoisomerization process generates unique nonlinear conditions, which elicit a new class of rapidly switchable self-trapped beams that control each other's propagation dynamics both in the short range - where there is significant overlap in the optical fields of the beams - and even in the long range - where such overlap is negligible. Through comprehensive experiments and simulations, we find that these nonlinear processes occur when optical energy is reversibly transduced to mechanical deformation in a spiropyran-functionalized hydrogel: a Gaussian beam self-traps when localized photoisomerization and consequent contraction of the hydrogel generate a transient waveguide, which entraps the optical field and suppresses divergence. The waveguide is erased and reformed within seconds when

[‡] *Submitted*. The authors of the manuscript are Derek R. Morim, Amos Meeks, Ankita Shastri, Andy Tran, Anna V, Shneidman, Fariha Mahmood, Joanna Aizenberg and Kalaichelvi Saravanamuttu. Contribution: DRM, AM and AS contributed equally to this manuscript. DRM, AS, AT, FM, KS designed, carried out and analysed data from experimental studies. AM developed and wrote the numerical model and carried out the simulations as well as experiments supporting parameter choices. DRM, AS, AM, AVS, JA, KS co-wrote the manuscript.

the optical field is sequentially removed and reintroduced; this allows the self-trapped beam to be rapidly and repeatedly switched *on* and *off* at remarkably low powers in the milliwatt regime. This opto-*chemo*-mechanical transduction of energy mediated by the spiropyran-functionalized, 3D crosslinked hydrogel network creates unique conditions for long-range, pairwise communication between multiple self-trapped beams and their mutual tunability over separation distances up to ten times the beam width. The discovery of a material that enables switchable and strongly interacting self-trapped beams holds significant potential in the development of next generation, circuitry-free, reconfigurable photonics systems and logic gates for computing, as well as dynamic light-activatable soft robotics.

3.2 Introduction

Self-trapped light beams and spatial solitons emerge in a rich variety of photoresponsive materials that display intensity-dependent changes in refractive index.[1–4] These nonlinear waves propagate without diverging through self-inscribed waveguides and exhibit intriguingly particle-like interactions such as collisions,[5] fusion and birth,[6] annihilation[7] and spiraling,[8] typically in the short-range (where there is significant overlap in their optical fields) and in rare cases, over long distances (where overlap is negligible and beams are remote).[9,10] Because they travel without changing shape, self-trapped beams hold potential for optical interconnects and fiber optics,[11] applications in image transmission,[12] rerouting light,[13,14] and logic gates for computing.[15] Importantly, they form the basis of the next-generation light-guiding-light approach to optical signal processing, which envisions a circuitry-free, reconfigurable and multi-layered photonics technology powered by the dynamic interactions of self-trapped beams.[13,14] Advances, however, have

been limited by the need for robust photoresponsive materials with switchable—rather than irreversible—changes in refractive index, Δn, which would generate the rapidly reconfigurable self-trapped beams and transient waveguide architectures necessary for repeated dynamic interactions. Extensive studies of self-trapped beams in reversibly responsive media such as photorefractive crystals,[16] liquid crystals,[17] atomic vapour[18] and Kerr media[19] have focused predominantly on steady-state self-trapping conditions due to their generally fast dynamics. Moreover, Δn in these materials can only be generated at large powers (several W) or in the presence of an external electric field.[2,3,6–10] While reversible self-trapping of a single relatively low power beam (25 μW) due to iodide photo-oxidation has been reported in a gel for two cycles spanning hundreds of seconds, the persistence of triiodide within the sample prevented further cycling.[20]

Here we show that reversible opto-*chemo*-mechanical transduction in a spiropyran-functionalized hydrogel elicits rapidly switchable self-trapped laser beams at low powers (μW-mW) and facilitates their dynamic, mutually tuneable pairwise interactions both in the short range and remotely. We demonstrate that self-trapped laser beams form repeatedly within seconds with excellent reproducibility and no evidence of material fatigue over at least 45 fully reversible cycles. Rapidly switchable self-trapping in this material originates from the generation of a transient waveguide appearing due to the reversible laser-initiated isomerization of spiropyran chromophores and concomitant contraction of the host gel in the irradiated region.[21,22] The same mechanism serves as an elegant photoswitch in drug release,[23] data storage,[24,25] sensing,[26] nanofluidics,[27] self-assembly[28] and, when incorporated into polymers,[29] enables tuning of stiffness,[30] surface wettability,[31] and

photonic bandgaps.[32] Isomerization-related swelling in hydrogels[21,32,33] has been used in the design of microfluidics,[34] multi-responsive polymers,[35] and photo-controllable surface topographies[36] and can be achieved with a variety of photoswitches[37,38]. In these wide-ranging applications, photoisomerization is a discrete event with a linear correlation to the photoresponse of the medium. Self-trapping, by contrast, relies on the positive nonlinear feedback between the optical field and nascent refractive index changes in the hydrogel. Our detailed theoretical and experimental results suggest that self-trapping of laser beams in the chromophore-functionalized hydrogel is enabled by the transduction of optical energy to mechanical deformation of the flexible, three-dimensionally (3D) interconnected matrix. Significantly, the deformation is delocalized beyond the incident optical field in the medium, which permits long-range communication between self-trapped beam pairs. These findings address the critical need for rapidly switchable self-trapped beams in soliton-driven photonics such as light-guiding-light computing[24,25] and opens entirely new opportunities in the design of intelligent light-responsive materials such as autonomous light-activatable soft robotics,[39] drug-delivery mechanisms[23] and transient waveguide circuitry.[14]

3.3 Results and discussion

To generate and study the interactions of self-trapped laser beams, we synthesized pH-responsive poly(acrylamide-co-acrylic acid) (p(AAm-*co*-AAc)) hydrogel containing covalently attached dangling spiropyran (SP) moieties (Figure 3-1). Details of the synthesis and gel composition are provided in the Materials and Methods Section and Supplementary 3.7.1.[21,22,40,41] Figure 3-1a is a scheme of the merocyanine to spiropyran isomerization in

the hydrogel and Figure 3-1b is a photograph of samples employed in experiments. When immersed in water, the chromophores exist predominantly in the ring-open merocyanine form due to the presence of vicinal acrylate anions.[40] When this chromophore-modified p(AAm-*co*-AAc) gel is irradiated with visible light, the isomerization of merocyanine to its closed-ring spiropyran[1] form triggers a cascade of events, which culminates in an increase in the refractive index (Δn) of the hydrogel. Specifically, if the merocyanine is protonated then the proton release that accompanies isomerization causes a decrease in the local pH and, in turn, a decrease in the concentration of charged hydrophilic carboxylate moieties that govern swelling in the hydrogel (Figure 3-1a).[22,33] Even without being protonated, however, the spiropyran form is much more hydrophobic than the charged merocyanine form. The result of the change of the hydrophobicity of the polymer backbone is the local expulsion of water and contraction of the hydrogel. Evidence for photoisomerization is shown in Figure 3-1c where the depletion of the absorbance band (λ_{max} = 420 nm), attributed to the π-π^* electronic transition of the protonated merocyanine, is accompanied by growth of an absorbance band in the UV region (λ_{max} = 320 nm), associated with the π-π^* electronic transition of the chromene moiety in the spiropyran isomer.[40] Isomerization is reversible so that in the absence of visible radiation, spiropyran thermally relaxes back to the merocyanine isomer.

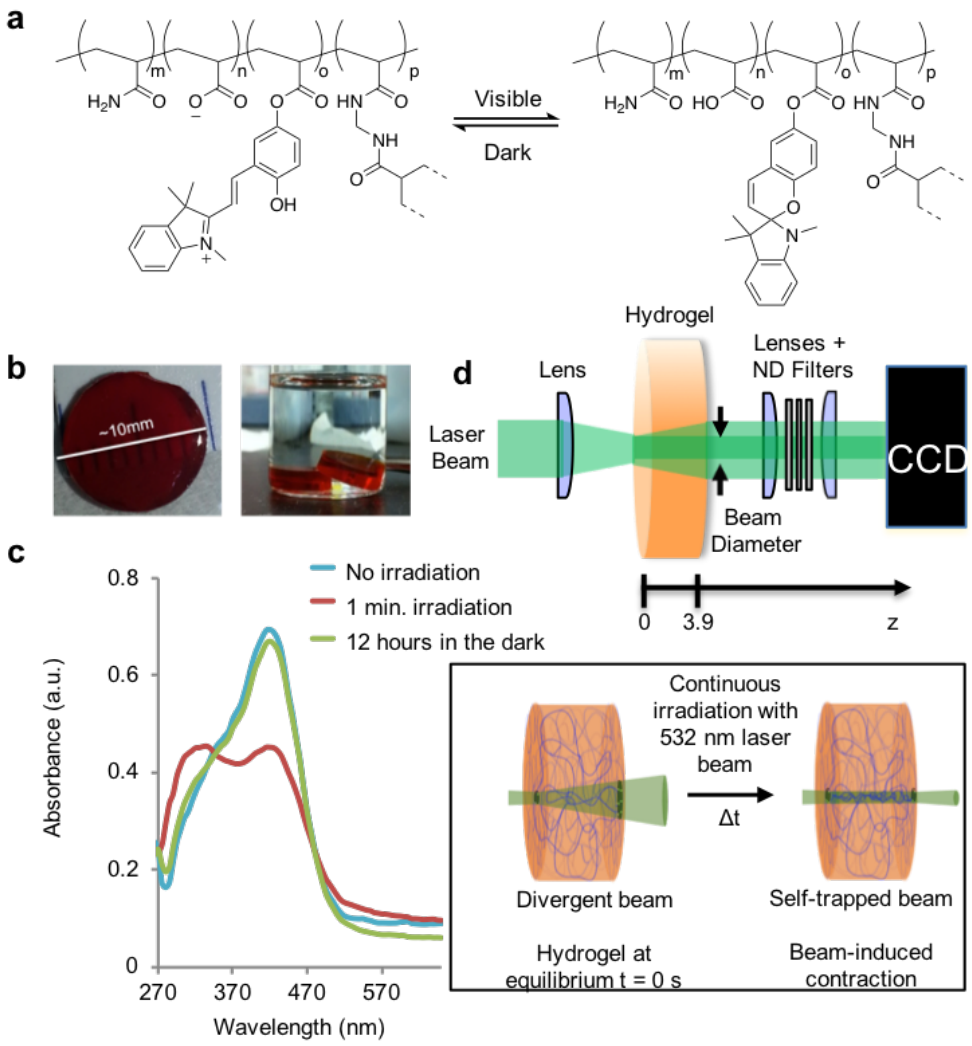

Figure 3-1 Spiropyran-modified hydrogels (a) Photoisomerization scheme of chromophore substituents from the protonated merocyanine (MC, left) to spiropyran (SP, right) forms in the methylenebis(acrylamide) cross-linked p(AAm-*co*-AAc) hydrogel. (b) Photographs of chromophore-containing p(AAm-*co*-AAc) hydrogel monoliths employed in experiments. (c) UV-visible absorbance spectra demonstrating reversible isomerization of MC (absorption λ_{max} = 420 nm) to SP (λ_{max} = 320 nm) in solution. (d) Experimental set-up (top) to probe laser self-trapping due to photo-induced local contraction of the hydrogel, schematically depicted on the bottom (see also MOVIE_S1). A laser beam is focused onto the entrance face of the hydrogel while its exit face is imaged onto a CCD camera.

3.3.1 Self-trapping of visible laser light

We exploit the light-triggered contraction and corresponding increase in refractive index, Δn, of the SP-modified p(AAm-*co*-AAc) hydrogel to elicit rapid, efficient and reversible self-trapping of a visible laser beam. In our experimental design (Figure 3-1d), a continuous wave (c.w.) visible (532 nm) laser beam is focused onto the optically flat entrance face (z = 0 mm) of the hydrogel monolith shown in Figure 3-1b immersed in deionized water within a glass sample holder. In all cases herein, the beam diameter is defined in the conventional way, as the axial distance at which the beam intensity drops to $1/e^2$ of its maximum value, and is set to be 20 μm at z = 0 mm. The spatial intensity profile of the beam at the sample exit face (z = 3.9 mm) is imaged and monitored over time through a pair of plano-convex lenses onto a CCD camera. Under linear conditions, where there are no photo-induced changes along its path (*i.e.*, at low powers or in the absence of isomerizable chromophores), the beam divergence is calculated to be ~130 μm for a propagation distance of 3.9 mm (greatly exceeding the Rayleigh length of 0.6 mm) through the gel.[4] We anticipated that this natural optical divergence would be strongly suppressed when the beam initiates isomerization of protonated merocyanine moieties and in turn, contraction of the pH-responsive hydrogel along its propagation path (Figure 3-1d, right). Because this contracted region contains a greater volume fraction of polymer, its refractive index is greater compared to its immediate surroundings, which now contains an increased proportion of water (refractive indices of the polymer and water are n ~ 1.49 and n ~1.33, respectively[42]). This densified region serves as a cylindrical microscopic waveguide[19,43–46]

– a self-induced optical fibre – that entraps the laser beam as its fundamental optical mode and guides it through the medium without diverging.

Experimental results confirming our hypothesis are shown in Figure 3-2. A visible laser beam, which under linear conditions would broaden and diminish in intensity with distance, self-traps and propagates without diverging through the SP-modified p(AAm-*co*-AAc) hydrogel. We launched a c.w. laser beam (λ = 532 nm; power = 6.0 mW) with a width of 20 μm (corresponding peak intensity = 3.77 kW cm^{-2}) into the hydrogel and monitored its spatial intensity profile at the exit face. Under linear conditions— in the absence of photo-induced changes—the beam diverges along the 3.9 mm pathlength to a width of 120 μm (in agreement with the calculated value of 130 μm; Figure 3-6). The temporal dynamics of the beam as it self-traps in the hydrogel is contained in plots of peak intensity and width and corresponding spatial intensity profiles (Figure 3-2a). The peak intensity refers to the greatest intensity within the camera's linear dynamic range as a % (details are provided in Supplementary 3.7.3.1). Within 50 s, the beam undergoes a ~20-fold increase in peak intensity from approximately 10% to 200% with a concurrent ~3-fold decrease in width from 120 μm to 40 μm (Figure 3-2a). With time, the beam continues to increase in relative intensity to 390% with a corresponding decrease in width to 22 μm, which is comparable to its width of 20 μm at the entrance face. This signifies that the self-trapped beam now propagates from the entrance to the exit face without significant divergence.

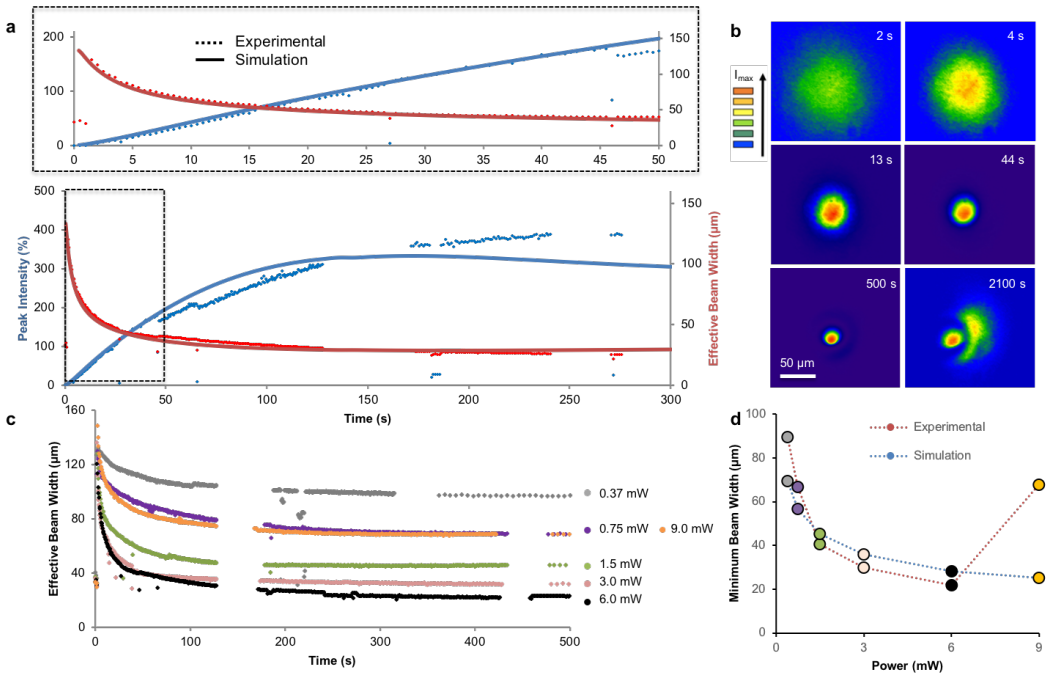

Figure 3-2 Evolution of self-trapping in the spiropyran-modified hydrogel; experiments and simulations (a) Experimentally measured temporal evolution of peak intensity (blue) and effective width (red) of a laser beam (532 nm, 6 mW) acquired at the sample exit face; the beam is turned on at t = 0. Breaks in plots are time lapses between image logs. The experimental plots (dotted lines) are compared to numerical simulations (solid lines); the dashed black box above provides a zoomed-in view from 0 to 50 s. (b) 2-D spatial intensity profiles experimentally acquired at select times. (c) Temporal evolution of beam width during self-trapping experiments at different optical powers. (d) Comparison of calculated and experimental values of minimum self-trapped beam width as a function of beam power.

We find that self-trapping dynamics depends strongly on optical intensity. Temporal plots of beam width (Figure 3-2c) trace self-trapping at powers (intensities) ranging from 0.37 mW (232 W cm^{-2}) to 9.0 mW (5.65 kW cm^{-2}). Detailed plots and beam profiles are provided in Figure 3-7. Self-trapping efficiency defined as the greatest % change in beam width relative to the initial diverged width increases monotonically from roughly 30% to 80% (with a concomitant decrease in minimum beam width from ~110 μm to ~20 μm) when optical power was increased from 0.37 mW to 6 mW. However, the efficiency

decreased to ~54% when the power was increased further to 9 mW. These trends were observed in at least nine repeat experiments at each intensity.

To describe and provide insight into the self-trapping process, we developed a numerical model that couples the photoisomerization of chromophores with localized volume changes in the hydrogel; details are provided in the Methods Section and Supplementary 3.7.3.3. Briefly, the model couples the photo-induced isomerization of spiropyran to the local swelling and contraction of the hydrogel and calculates the resulting impact on light propagation in the medium.[47–49] As the covalently tethered SP moieties cannot diffuse freely, they are transported with their host polymer chains upon swelling and contraction of the hydrogel. The amount of isomerized spiropyran within a given volume – *i.e.*, its concentration – therefore depends on the flux of polymer chains as well as the optical intensity-dependent rate constant associated with merocyanine-to-spiropyran isomerization and the intensity-independent rate of thermal relaxation of spiropyran to merocyanine. The osmotic pressure induced by the isomerization process leads to a local change in the polymer volume fraction. The corresponding changes in refractive index (Δn) and isomerization-dependent light absorption are calculated and employed in the nonlinear paraxial wave equation to determine the intensity distribution of light within the gel. This new distribution of optical intensity is then employed to calculate the isomerization dynamics and associated Δn in the gel. This cycle is repeated iteratively until the desired time is reached.

Consistent with experiments, the model accurately captures the short-term (<500 s) self-focusing dynamics along with the intensity-dependent self-trapping efficiency of a

single laser beam in the hydrogel (see Figure 3-2a and Figure 3-8). As in experiments, the simulated self-trapping efficiency increases monotonically with beam power spanning 0.37 mW to 6.0 mW (Figure 3-2d). This trend originates from the intensity-dependence of the photoisomerization process: at lower intensities, the proportion of protonated merocyanine isomerized to spiropyran does not extend far enough into the hydrogel to create the Δn needed for appreciable self-focusing; as the intensity increases, the concentration of isomerized spiropyran molecules rapidly saturates to a plateau in self-trapping efficiency. At the higher intensities, the spiropyran-rich region surrounding the beam leads to contraction of the hydrogel that is large enough to prevent significant divergence of the beam, enabling a greater proportion of the optical energy to extend further into the gel. This triggers more isomerization and thus additional focusing of the beam in a nonlinear feedback loop. At greater powers and longer times, the material exhibits a decrease in self-trapping efficiency due to the excitation of high order modes[43] as the saturation of isomerization at large intensities forms a flat-top concentration profile that extends beyond the beam width, creating a wider waveguide (Figure 3-9).

3.3.2 Reversibility of self-trapping

Photoisomerization of merocyanine moieties enables the self-trapped beam to be controllably switched on and off >45 times in the same hydrogel. Here, the c.w. visible laser beam self-traps within ~30 s and is then blocked for "dark periods", which were varied from 40 s to 300 s. Temporal plots of relative peak intensity and beam width (Figure 3-3) show that after each dark period, the relaunched beam always diverges to approximately 120 μm – its original diverged form under linear conditions (*vide supra*). This can only

occur if the waveguide previously induced by the self-trapped beam is completely erased and the hydrogel relaxes to its equilibrium state. Accordingly, self-trapping efficiency is consistent between experiments with typical values ranging from 57% to 65% (corresponding to minimum beam widths of 42 µm and 56 µm, respectively).

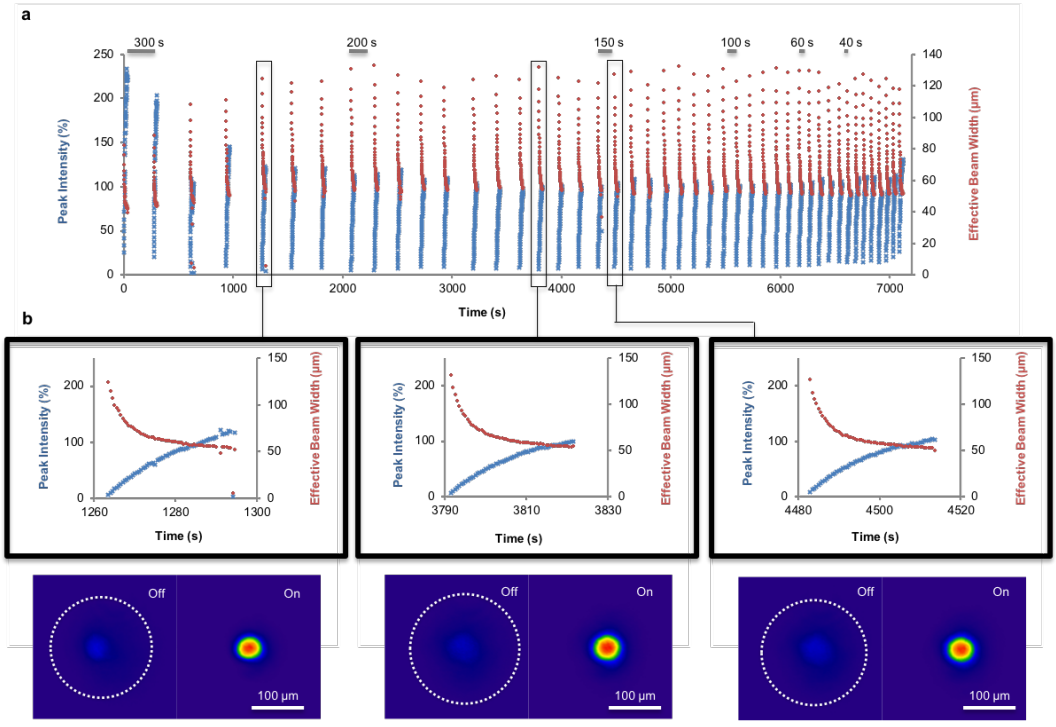

Figure 3-3 Rapidly reversible self-trapping in the spiropyran-modified p(AAm-*co*-AAc), experiments (a) Temporal plots of peak intensity (blue) and effective diameter (red) over 45 cycles of self-trapping of a laser beam. Cycles were separated by dark periods ranging from 300 s to 40 s (indicated above the plots). (b) Scheme and spatial intensity profiles showing the "off" (divergent) and "on" (self-trapped) states of the laser beam over select cycles. White circles trace the diameter ($1/e^2$) of the initially divergent beam in the "off" state.

3.3.3 Mechanism of self-trapping

We elucidated the mechanistic origins of reversible self-trapping in the hydrogel through a carefully designed series of control experiments (Figure 3-4; Figures 3-10 to 3-

12; Supplementary 3.7.3.4) in conjunction with simulations. Experiments involving p(AAm-*co*-AAc) gel without chromophore (Figure 3-4a), a solution of free spiropyran without a gel (Figure 3-4b), p(AAm-*co*-AAc) hydrogel dispersed with untethered spiropyran molecules (Figure 3-4c), and a non-pH responsive poly(hydroxyethyl)methacrylate p(AAm-*co*-HEMA) hydrogel with covalently bound spiropyran (Figure 3-4d) exhibited negligible or significantly suppressed self-focusing compared to the pH-responsive p(AAm-*co*-AAc) incorporating covalently bound spiropyran (Supplementary 3.7.3.4). These studies, further supported by time-dependent UV-Visible Spectroscopy (Figure 3-13a-c; Supplementary 3.7.3.5) and Fluorescence Recovery After Photobleaching (FRAP) measurements (Figure 3-13d-e; Supplementary 3.7.3.6), show that all of the following features are critical in eliciting the nonlinear conditions required for efficient self-trapping: i) the photoisomerization, (ii) presence of a gel network, (iii) chromophore tethering, and (iv) acidic moieties on the polymer backbone, supporting the hypothesis that self-trapping originates from a sequence of events triggered by the photoisomerization of the merocyanine isomer and consequent contraction of the pH-responsive hydrogel.[22,34,40,48] This transduction of optical-to chemical-to mechanical energy is most efficient and reversible when the chromophore units are covalently tethered to the 3D-interconnected hydrogel (Figure 3-2).

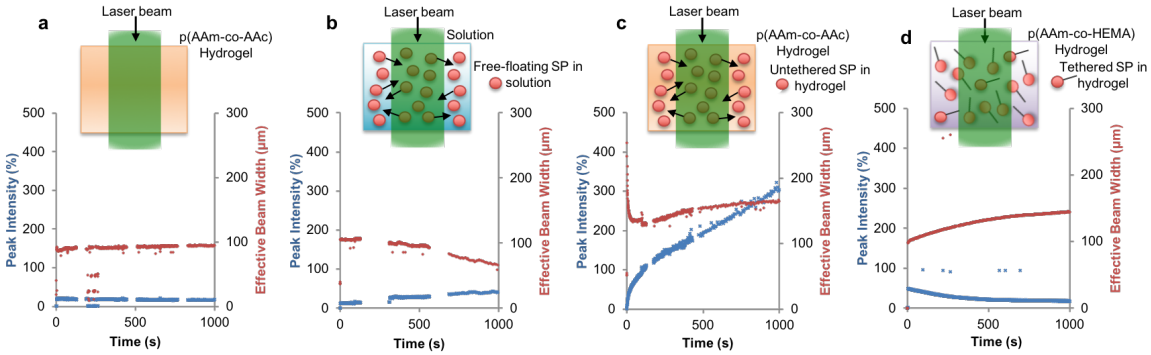

Figure 3-4 Self-trapping in control systems; experimental measurements. Temporal plots of peak intensity (blue) and width (red) of a laser beam acquired at the exit face of (a) an unmodified p(AAm-*co*-AAc) hydrogel, (b) solution of spiropyran in DMSO:water, (c) p(AAm-*co*-AAc) hydrogel dispersed with untethered spiropyran, and (d) spiropyran-modified poly(hydroxyethyl)methacrylate p(AAm-*co*-HEMA) hydrogel. Laser power of 9 mW (5.65 kW cm^{-2}) was employed in (a) and 6 mW (3.77 kW cm^{-2}) in (b) – (d).

3.3.4 Remote interactions of a parallel pair of self-trapped beams

We found that a self-trapped beam could be dynamically and reciprocally controlled by launching a second, parallel-propagating counterpart into the medium. Remarkably, this communication between the self-trapped beam pair occurs remotely—even over separation distances (Δx) that greatly exceed (by at least 10-fold) the widths of either self-trapped beam. This behaviour is significant because the interactions between self-trapped beams typically rely on the overlap of the optical fields and therefore decrease exponentially with Δx. For example, self-trapped beams in a photopolymer did not interact when separated by four times the beam width.[45] Although there are multiple examples of nonlocal photoresponses based on the diffusion of heat, matter, or charge carriers, there are only two previous experimental examples of long-range interactions between self-trapped beams.[9,10] This was achieved in a liquid crystal system where cooperative motion of liquid crystals

extended the index changes outside of the light field,[9] but only under an externally applied electric field. Nonlocal interactions were also achieved in a thermally conductive lead glass where the nonlocal diffusion of heat extended the photoresponse outside of the optical field,[10] but only at optical intensities that were three orders of magnitude greater than those employed in our study.

Interactions between self-trapped beams in our material are facilitated by the reversible photoresponse and mediated through the 3D-interconnected, flexible network of the SP-modified p(AAm-*co*-AAc) hydrogel. The former enables a self-trapped beam to rapidly and reversibly alter its intensity profiles in response to a second beam. The latter enables the two self-trapped beams to communicate even when overlap between their optical fields is negligible. Temporal plots of relative intensity capture the rich internal dynamics of two identical and parallel beams propagating through the SP-modified p(AAm-*co*-AAc) hydrogel; Δx in these experiments ranged from ~25 μm to ~200 μm (limited only by the experimental assembly), which were 1.25 to 10 times larger, respectively, than the input beam diameter of 20 μm (Figure 3-5; Figure 3-14). To enable ease of comparison of the interacting beams, the intensity of each beam in these studies was scaled to its initial intensity and reported as a dimensionless ratio termed relative peak intensity; such plots trace the dynamics of each beam when its counterpart is blocked for some time (Figure 3-5a-b, left). At all values of Δx, the beams self-trapped significantly to widths of ~20 μm individually (Figure 3-2; Figure 3-14) but mutually suppressed self-trapping efficiency when propagating together. This is evident even in the remote interactions at Δx = ~200 μm (Figure 3-5a).

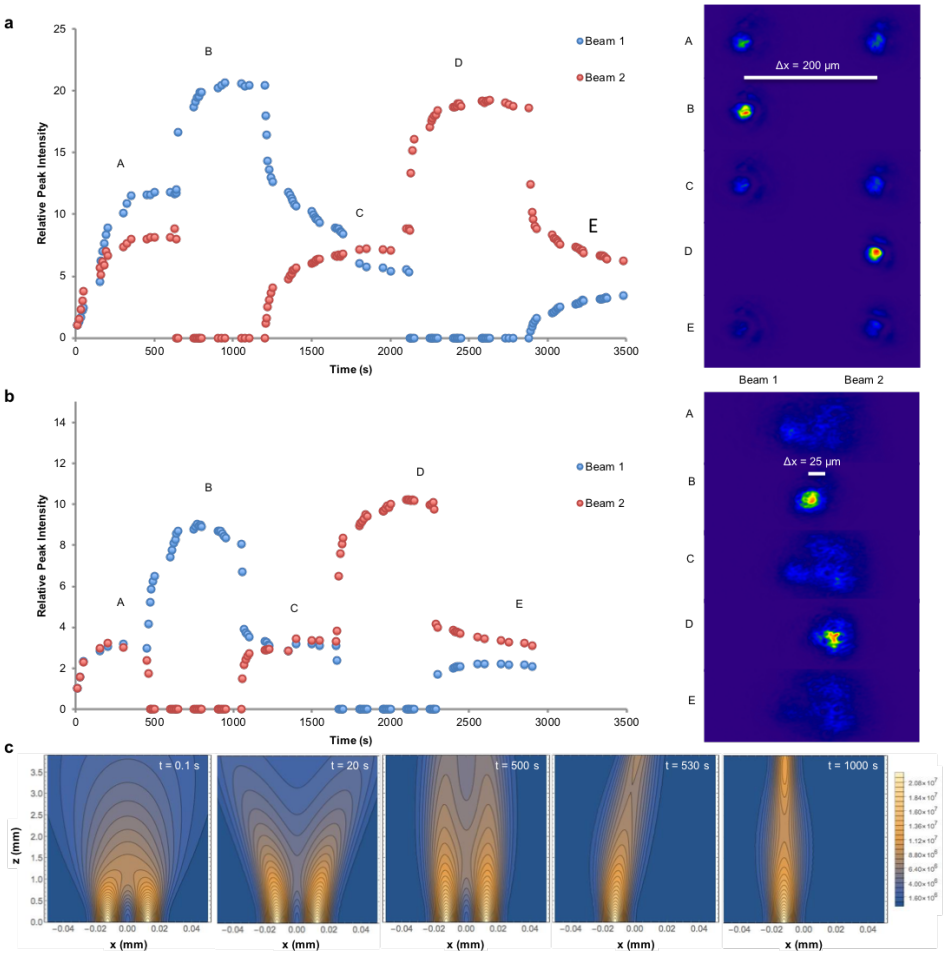

Figure 3-5 Dynamic interactions of two parallel self-trapped beams. (a) Temporal plots of relative peak intensities (left) and corresponding 2-D spatial intensity profiles (right) acquired at select times at the sample exit face for two beams separated by Δx = ~200 µm. When propagating together, beam 1 (blue) and beam 2 (red) self-trapped over 625 s to a relative peak intensity of 12 and 9, respectively (from an initial value of 1), and comparable widths of ~ 40 µm (details in Supplementary 3.7.4.1). When Beam 2 was selectively blocked, Beam 1 rapidly returned to high self-trapping efficiency, increasing in relative intensity to ~20 with a minimum width of ~28 µm over 250 s. When Beam 2 was reintroduced however, Beam 1 diminished in self-trapping efficiency, decreasing in relative peak intensity to 5.3 and broadening again ~40 µm over 800 s. Beam 2 also showed reduced efficiency, attaining a maximum relative peak intensity of only 7 and a width of ~40 µm. The equivalent effect was observed when Beam 1 was blocked in the next cycle of the same experiment. (b) Temporal plots of relative peak intensities and corresponding 2-D spatial intensity profiles for two beams separated by Δx = 25 µm. (c) Simulations snapshots of the interactions of two self-trapped beams with Δx = 25 µm. Color shows the intensity in W m^{-2}. See also Figure 3-15, MOVIE_S2 and MOVIE_S3.

Spatial intensity profiles of the two beams acquired at different times during these cycles highlight the striking differences between single and co-propagating self-trapped beams (Figure 3-5a-b, right). By measuring the self-trapping rates of two beams introduced sequentially into the hydrogel, we further show that there is strong reciprocal correlation between the photo-induced Δn (and therefore, the extent of contraction) between the two remote regions of the hydrogel (Figure 3-14; Supplementary 3.7.4.1).

Initial simulations of the dynamics of two proximal beams (Δx = 25 μm) confirm that all of the experimentally observed behaviours are strongly influenced by photo-induced deformation of the hydrogel network (Figures 3-5c and 3-15, Supplementary MOVIE_S3; Supplementary 3.7.4.2). As the gel contracts along the propagation path of the beam, expelled solvent causes the surrounding matrix to swell. Competition arises when a second self-trapped beam induces contraction in a neighbouring region. Solvent is now expelled by both beams leading to opposing forces of expansion so that at early times (20 *s*), the beams briefly repel each other. Simultaneous self-trapping prevents either beam from eliciting the maximum possible Δn and therefore, neither beam is able to attain its optimum self-trapping efficiency. Simulated beams launched simultaneously attain a minimum width of ~35 μm (Figure 3-15), and when one beam is removed, the other decreases in width to ~20 μm and doubles in relative peak intensity – behaviour consistent with experiments. A full and detailed understanding of how the beams communicate in this material at longer separation distances will be the subject of future work, but regardless of the mechanism, these unique interactions between self-trapped beams in a photoresponsive hydrogel reveal intriguing dynamics for optically modulating beams of light.

3.4 Conclusions

We showed that rapidly switchable and strongly interacting self-trapped beams of visible laser light can be elicited in a soft, processable hydrogel functionalized with a chromophore. Our material system relies on the photoisomerization of spiropyran moieties, which is extensively employed as a binary "on-off" photoswitching mechanism.[40] We showed that the same isomerization process can serve as the conduit that transduces optical energy through reversible chemical transformations into mechanical forces in the gel, which in turn generate unique nonlinear conditions required for self-trapping. More specifically, a visible laser beam self-traps by initiating isomerization of photoacidic merocyanine substituents tethered to a p(AAm-*co*-AAc) hydrogel network. The concomitant protonation of acrylate groups in the vicinity of the isomerized chromophore along with the changing hydrophobicity of the polymer chain results in the local expulsion of water, contraction of the gel and consequent increase in refractive index (Δn). This creates a reciprocal, positive feedback between the optical field and nascent Δn along its propagation path, thus generating a transient waveguide. When the optical field is removed, isomerization is reversed, and the hydrogel relaxes to its original state; in this way, the self-trapped beam is reversibly and reproducibly switched on and off by sequentially removing and reintroducing the Gaussian beam. Intriguingly, interactions between beams extend well beyond the confines of the incident optical field in this material. As a result of this nonlocal response, a pair of parallel-propagating self-trapped beams exhibits strong, mutually responsive interactions in the

short and long range. Our numerical model provides valuable mechanistic insight into these interactions, by coupling photoisomerization to osmotic-pressure-driven contraction of the gel.

In conventional nonlinear materials,[1–4,16–19] self-trapping suffers from one or more of the following disadvantages: (i) the need for large incident beam powers (~W),[19] (ii) presence of an external field,[16,17] (iii) loss of beam interactions at distances beyond the overlap of their electromagnetic fields, [2,13] and (iv) it is slow and irreversible.[11,45] By striking contrast, our materials system demonstrates highly efficient self-trapping (i) at small easily accessible (~mW) beam powers, (ii) under ambient conditions; it is (iii) rapid (~50 s), (iv) fully reversible at relatively fast timescales (~100 s), and shows (v) sustained repeatability over multiple cycles (at least ~50) and (vi) almost instantaneous beam interactions for separation distances up to 10 beam widths. These exceptional properties are enabled by the large Δn created by gel contraction, reversibility of all chemical reactions (*i.e* chromophore isomerization and gel protonation) and 3D interconnectivity of a polymer network. Importantly, our study elucidates an opto-*chemo*-mechanical transduction pathway to elicit nonlinear optical conditions in a photochromic hydrogel. In this way, it lays the foundation for rational design of other classes of photoresponsive hydrogels as rewritable optical media for self-modulating beams. The possibility to reversibly modulate beams of visible light remotely at relatively low powers opens the door to all-optical computing with ambient light,[24,25] autonomous stimuli-responsive soft robotic systems[39] and actuators for a wide range of applications including drug delivery[23] and dynamic optics – devices that modify their optical properties with external stimuli.[40]

3.5 Materials and methods

(Please see Supplementary 3.7.1 for additional experimental details.)

3.5.1 Preparation of hydrogel samples

The polymerizable hydrogel matrix was prepared by dissolving acrylamide:acrylic acid (1:1 wt./wt.) or acrylamide:HEMA (1:1 wt./wt.) in a mixture of DMSO:deionized water (4:1 vol./vol.) before addition of the crosslinker N,N'-methylenebis(acrylamide) at 2 % wt./vol. Acrylated spiropyran (for tethered samples) or hydroxyl-substituted spiropyran (1',3',3'-trimethylspiro[chromene-2,2'-indolin]-6-ol) at 0.25 mol.% of total monomer was then added to the unpolymerized hydrogel matrix followed by ammonium persulfate (2% wt./vol.) and a drop of tetramethylethylenediamine (TEMED) catalyst. The components were mixed and transferred into a circular plastic mold (d = 10 mm, h = 3 to 4 mm thick) sandwiched between two glass slides, protected from exposure to light and cured at ambient temperature for up to three days. Cured hydrogel samples were immersed in HCl (1 mM) for up to four days in order to remove excess, unreacted monomers. For optical experiments, samples were placed in semi-circular, transparent cells (thickness = 4 mm) containing deionized water.

3.5.2 Optical experiments

Self-trapping experiments were carried out on an optical assembly that focused either one or two beams (c.w., 532 nm, d = 20 μm) onto the entrance window of the cell containing the hydrogel sample (Supplementary Figure 3-6c, e. In the case of two parallel and orthogonally polarized beams, the separation distance (Δx) was varied from 20 μm to 200 μm. The spatial intensity profile of the beam(s) at the exit face of the cell was imaged by a

plano-convex lens pair onto a charge-coupled device (CCD) camera, with neutral density filters placed between the plano-convex lenses used for imaging. The resulting images were used to create plots of relative peak intensity and diameter. Images were acquired every second with short time lapses between logs. Due to the dynamic range of the camera, values below 10% peak responsivity were omitted as the calculated beam diameter is affected at low intensities.

3.5.3 Simulations

Supplementary 3.7.3.3 provides details of the model employed for simulations. Briefly, a Gaussian beam is launched into the medium that initially has a uniform refractive index profile. The intensity-dependent rate of photoisomerization leads to corresponding changes in local osmotic pressures, calculated by solving the linearized equations of gel dynamics.[47] Changes in the refractive index (Δn) originating from changes in the volume fraction of polymer chains are then input into the nonlinear Schrödinger equation to simulate the resulting modified distribution of light intensity in the medium. In this way, the rate equations for photoisomerization, osmotic-pressure induced gel deformation and optical intensity are solved iteratively until a steady state is reached. The model was implemented in Mathematica version 11.1.1 and solved numerically using the built in NDSolve differential equation solver. Single beam simulations were carried out by employing cylindrical coordinates while double beam simulations employed a 2D coordinate system.

3.6 Acknowledgements

This work was supported by the US Army Research Office under Award # W911NF-17-1-0351 and by the Natural Sciences and Engineering Research Council, Canadian Foundation for Innovation and McMaster University. A.M. was supported by the Department of Defense (DoD) through the National Defense Science & Engineering Graduate Fellowship (NDSEG) Program. We acknowledge the participation of Dr. Liqun Qiu in preliminary experiments. We are grateful to Prof. Anna Balazs and Dr. Victor Yashin for their advice and help in developing the model of self-focusing. We thank Dr. Ian B. Burgess for the suggestion of attempting optical self-trapping in photochromic hydrogels.

3.7 Supplementary information

3.7.1 Preparation and characterization of spiropyran-modified hydrogels

3.7.1.1 Materials

Acrylamide, acrylic acid, N,N'-methylenebis(acrylamide), tetramethylethylenediamine (TEMED), dimethyl sulfoxide (DMSO), triethylamine (TEA), tetrahydrofuran (THF), acryloyl chloride, trifluoroacetic acid (TFA), acetonitrile, ethyl acetate, sodium bicarbonate, (hydroxyethyl)methacrylate (HEMA), and hydrochloric acid were all purchased from Sigma-Aldrich. 1',3',3'-trimethyl-6-hydroxyspiro(2*H*-1-benzopyran,2-2'-indoline) (Acros Organics), and OmniPur® ammonium persulfate (APS, EMD Millipore) were used without further purification.

Buffered solutions of different pH were prepared by mixing monosodium phosphate, monohydrate and disodium phosphate heptahydrate in 100 mL of deionized water at 50 mM concentration to generate the desired pH. The pH of the resulting buffers was measured by a Thermo Scientific Orion 3 STAR pH meter.

3.7.1.2 Preparation of SP gels and controls for optical self-trapping

3.7.1.2.1 Synthesis of spiropyran acrylate monomer (1',3',3'-trimethylspiro[chromene-2,2'-indolin]-6-yl acrylate)

Spiropyran acrylate monomer (1',3',3'-trimethylspiro[chromene-2,2'-indolin]-6-yl acrylate) was synthesized based on a procedure described previously.[50] Briefly, 1',3',3'-trimethyl-6-hydroxyspiro(2*H*-1-benzopyran,2-2'-indoline) was treated with acryloyl chloride and triethylamine in THF at 0°C and reacted for 15 h at 25°C. The product was washed in ethyl acetate with saturated aqueous sodium bicarbonate solution and brine. After evaporation of solvent, the crude product was dissolved in DMSO at 1-5 mg/mL and purified by HPLC-P (Agilent 1200 Preparative High-Performance Liquid Chromatography) with a C18 column at a rate of 20 mL/min Elution solvent consisted of a mixture ranging from 5-95% v/v acetonitrile in deionized water, with 0.1% trifluoroacetic acid (TFA). The purified product was characterized by LC-MS (Agilent 1290/6140 Ultra High-Performance Liquid Chromatography/Mass Spectrometer containing a Quadrupole MSD system, electrospray ionization) $[M + H^+] = 348.2$ m/z. The solvent was evaporated to yield the red-colored product (yield ~65%).

3.7.1.2.2 Synthesis of hydrogels

1:1 w/w acrylamide:acrylic acid or 1:1 w/w acrylamide:HEMA were dissolved in 4:1 v/v DMSO:deioinized water. To this solution, 2% w/v N,N'-methylenebis(acrylamide) was added as crosslinker. Acrylated spiropyran (for tethered samples) or unacrylated spiropyran, 1',3',3'-trimethylspiro[chromene-2,2'-indolin]-6-ol (for untethered samples) at 0.25 mol% of total monomer was dissolved in the pre-polymer solution. Before curing, 2% w/v APS was added to the solution. Upon addition of TEMED catalyst, the hydrogel pre-polymer solution was dispensed into a circular plastic mold (3 mm thick and 10 mm in diameter) sandwiched between two glass slides and left to cure in the dark at ambient temperature for at least 2-3 days. Cured hydrogel samples were then immersed in 1 mM HCl (aq) water bath for 3-4 days to remove excess, unreacted monomers (Figure 3-6a). Finally, the hydrogel was transferred to a half-ring cell containing deionized water for optical measurements. Samples containing (hydroxyethyl)methacrylate (HEMA) were prepared by substituting acrylic acid for HEMA. Control hydrogels were prepared by not including the chromophores into the hydrogel.

3.7.1.2.3 Preparation of solution containing free-flowing spiropyran

Hydroxyl spiropyran [1',3',3'-trimethylspiro[chromene-2,2'-indolin]-6-ol] (4.0 mg) was dissolved in DI water (971 μL) and DMSO (498 μL). The solution, which consists primarily of the MCH^+ form of the chromophores, was filtered by an Acrodisk syringe filter (Pall Corp., Michigan) and stored in the dark under ambient conditions prior to its use in optical experiments.

3.7.2 Characterization methods of spiropyran-modified hydrogel samples

3.7.2.1 Photoactuation of spiropyran-modified and unmodified hydrogel

Hydrogels were prepared in a manner similar to that described above, but as films sandwiched between two glass slides glued together without a spacer. The resulting cured thin film hydrogel was washed in 1 mM HCl (aq.) solution and cut into smaller pieces to observe within the field of view of the optical microscope. Hydrogel samples were immersed in DI water for photoactuation measurements and imaged under a Leica DMRX optical microscope with a 5X objective. The entire hydrogel sample was irradiated with green light from a halogen light source passed through a filter cube (N2.1 BP 515-560 nm) for a period of 6 min and imaged at 2 min intervals. The power of the light source was measured with X-cite® power meter at 538 nm to be 0.2 mW and focused onto a region of interest (ROI) on the hydrogel sample with a radius of around ~2 mm. Visible light-induced shrinkage in the hydrogel is sufficiently large to be observed macroscopically. Transmission optical micrographs showed that a hydrogel thin film shrank by up to ~3% in area when completely irradiated with low power green light (~$\Delta\lambda$ = 515nm - 560 nm, 0.2 mW) for six minutes (Figure 3-6b, top). In a control experiment, an undoped but otherwise identical p(AAm-*co*-AAc) hydrogel remained unchanged when irradiated under the same conditions (Figure 3-6b, bottom).

3.7.2.2 Swelling ratio measurements

Pre-polymer solutions were prepared in the same way as described above and deposited in an Eppendorf® cap (~10 mm diameter and ~0.5-1 mm thick) and cured at ambient temperature for 1-2 days in the dark. Cured hydrogels were washed in 0.1 mM

HCl (aq) water bath to wash away unreacted monomers. Washed hydrogels were then immersed in each of the 50 mM phosphate-buffered solutions of different pH. After equilibration in the pH buffer, the swollen mass of each hydrogel was measured after removing excess water with filter paper. The hydrogels were then allowed to dry in air over several days and their dried weight recorded. The swelling ratio for each pH buffered solution was calculated as SR = (mass swollen – mass dry)/mass dry.

3.7.2.3 UV-Visible spectroscopy kinetics

Absorbance spectra were acquired by a Cary 50 spectrophotometer (Agilent Technologies). The absorbance spectra were recorded over time under continuous irradiation in order to monitor the isomerization kinetics between merocyanine and spiropyran within different 1 mm samples. The intensity of the incident incandescent light (5 mW, Cole-Parmer horizontal fiber optic illuminator 09790-series) was the same for each sample in order to make comparisons. The relaxation of spiropyran to merocyanine was also monitored by recording the spectra in the absence of light after irradiation. Data was fit to (eq 3.1) according to Tork, et al.[51]

$$-\ln\left[\frac{[A(t)-A_e]}{[A(0)-A_e]}\right] = kt\ , \tag{3.1}$$

where $A(t)$ represents the absorbance at time t and $A(0)$ represents the absorbance at time zero. A_e is the absorbance measured at the photostationary state, and k is the photoreaction rate constant.

3.7.2.4 Confocal microscopy: fluorescence recovery after photobleaching (FRAP)

Samples were prepared in a manner similar to those for self-trapping experiments with a sample height of 1 mm achieved by sandwiching the pre-polymer solution between two glass slides with a 1 mm plastic spacer. The upright Zeiss LSM 710 Confocal microscope was used to conduct FRAP measurements in which imaging was done at 100-210 μW at 514 nm and bleaching was done at 5.7 mW at 514 nm on a 40 μm diameter ROI, with a 10X water immersion objective. Fluorescence emission was collected from 525-599 nm (where fluorescence signal was strongest). Resulting fluorescence recovery curves were normalized to correct for acquisition bleaching effects and by taking pre-bleach fluorescence intensity as 1 and bleach intensity as 0.[49] Igor Pro was used to fit single- and bi-exponential curves of the resulting normalized FRAP data.

3.7.3 Self-trapping of single beams

3.7.3.1 Optical assembly for self-trapping experiments

The optical assembly for single beam self-trapping experiments is shown in Figure 3-6c. A continuous wave diode-pumped solid-state laser (Verdi V5 Coherent, Inc., California) was used as the excitation source. The source produced a beam (λ = 532 nm) with a diameter of 2.25 mm at a power of 100 mW. The beam was passed through a $\lambda/2$ waveplate (W) and a polarizing beam splitter cube (C). It was then passed through an absorption filter (F) and was guided by a mirror (M) onto a focusing lens (L1, f = 75.6 cm). This produced a beam focused to a diameter of ~20 μm onto the entrance face of a hydrogel sample within the sample cell (S). The profile of the beam at the exit face of the

sample was imaged by a pair of planoconvex lenses (L2, f = 100 mm; L3, f = 300 mm) onto a charge-coupled device (CCD) camera (736 (H) x 484 (V) pixels, 4.8 μm (H) x 5.58 μm (V) pixel size; LaserCam IIID 1⁄4", Coherent Inc., CA, USA). The software associated with this camera was BeamView Analyzer, which calculated the beam diameter ($1/e^2$) and peak intensity. The peak intensity is a linear scale that is dependent on the intensity range of the camera; the value corresponds to the maximum intensity present for any pixel on the CCD camera and is represented as a percentage. To avoid oversaturation of the camera, a series of absorption filters (F) on three separate rotatable wheels (VARM, Coherent Inc. California) was placed between L2 and L3; the peak intensity was corrected each time these filters were changed. The imaging components were mounted onto carriers that could be moved along the path of beam propagation (z-axis). In all self- trapping experiments, the beam diameter was measured at the exit face of the sample.

A hydrogel or solution containing free-flowing spiropyran was placed in the sample holder. DI water was added to the sample cell holder in the case of a hydrogel sample. Hydrogel thickness was measured using an electronic caliper (The L.S. Starrett Co., Massachusetts). Samples were typically 3.63 – 3.93 mm thick and the imaging components were adjusted to view the beam at the exit face. The output power of the source was tuned by adjusting the λ/2 waveplate and measured by a power meter (Coherent Inc., CA, USA) (Figure 3-6c). For experiments in which the reversibility of self-trapping was measured, each self-trapping trial was performed at the same position on a spiropyran-modified or untethered spiropyran hydrogel sample. The sample was

irradiated for approximately 30 s. Laser irradiation was then temporarily removed by blocking the source between the mirror and L1 (Figure 3-6c). A period of time in the dark, ranging from 40 s to 300 s, was given before restoring laser irradiation by unblocking the source. This irradiation and relaxation processes were repeated until the desired number of experiments was completed (>40). The magnification was accounted for when preparing plots of spatial intensity profiles using SigmaPlot™ graphing software. The beam divergence was examined within a control hydrogel without chromophores (Figure 3-6d) in order to determine the beam profile under linear conditions.

Double beam self-trapping experiments were carried out on an optical assembly similar to the single beam setup, but with the introduction of a second beam parallel to the first beam (Figure 3-6e). The output beam was passed through a λ/2 waveplate and split into two beams using a polarizing beam splitter cube. The λ/2 waveplate orientation was adjusted to change the ratio of intensities between the two beams. The beams were directed by mirrors and a second polarizing beam splitter cube, through a set of filters and a planoconvex lens [focal length = 75.6 mm], which focused the beams to a diameter of 20 μm onto the entrance face of the sample in the sample cell. The separation distance between the focused beams could be adjusted using the dials on the beam splitter cube adjustable mounts. The result was two orthogonally polarized beams of light separated by 25 to 200 μm at the entrance of the sample.

The spatial intensity profile of the beam at the exit face of the sample was imaged by a pair of planoconvex lenses (f. l. = 75.6 mm and f. l. = 250.0 mm) onto a CCD camera

[2040 horizontal × 1532 vertical pixels; pixel size = 3.20 μm x 3.20 μm; WinCamD XHR, DataRay Inc., California, USA]. Combinations of neutral density filters mounted on three separate rotatable wheels (VARM, Coherent, Inc.) were placed between imaging lenses to prevent saturation of the CCD camera. All imaging optical components could be translated along the z direction with a resolution of 0.25 mm. Images were collected every second for 50 s logs. The camera used Data Ray software (Version 7.1H25Bk), which calculates beam diameter ($1/e^2$) and peak intensity, generates two-dimensional (2D) and three-dimensional (3D) intensity profiles, and corrects for image magnification by the lenses. The effective beam diameter corresponds to the circular area of all pixels with relative intensity > 13.5% ($1/e^2$) of the maximum (peak) intensity. The relative peak intensity was scaled with respect to the initial intensity for two-beam experiments as cross-sectional intensity distributions had to be used due to the overlap of the beams. This value is a ratio that is linear with respect to the intensity. Plots of spatial intensity profiles of the beam were generated with SigmaPlot™ software.

3.7.3.2 Dependence of optical self-trapping on incident light power

Optical self-trapping within spiropyran-modified hydrogels was studied at incident light powers ranging from 0.37 mW to 9 mW. Figure 3-7 summarizes the temporal evolution of the beam intensity and diameter during self-trapping. Results show that the rate of self-trapping increases with incident intensities and plateaus at 6 mW (Figure 3-2). At higher intensities, a flat-top Δn profile is generated, allowing for the formation of rings.[52] This occurs because the system is saturable and intensities above the saturation

limit cause the beam to generate a different Δn profile compared to the lens-like profile required for self-trapping. Generating this type of profile affects the manner in which the polymer contracts and ultimately affects the profile of light that is observed leaving the sample. At lower intensities, the degree of change to the beam diameter is less than at 6 mW since not enough light is incident on the sample to isomerize sufficient merocyanine to spiropyran to trigger the polymer to contract and generate a fully self-trapped beam.

For all powers, at very long times (> 500 s), the emergence of intensity features around the fundamental mode lead to an effective decrease in relative peak intensity. This redistribution of intensity originates from high order modes, which are excited as the flat-top profile of saturated spiropyran creates a refractive index distribution of a cylindrical waveguide that is significantly wider than the radius of the beam.[52]

3.7.3.3 Model of self-trapping in SP-functionalized p(AAm-co-AAc) hydrogels

The numerical model couples the photochemical isomerization of spiropyran to the local swelling and contraction of the hydrogel, from which a change in the index of refraction is calculated and used in the nonlinear paraxial wave equation to calculate the intensity distribution of light within the gel.[4] The new intensity distribution of light is then used to calculate the isomerization dynamics of the gel, and the cycle is repeated. Detailed descriptions of each process are provided below.

3.7.3.3.1 Spiropyran photochemical isomerization

The spiropyran moiety undergoes a photochemical isomerization from the ring-open merocyanine (MC) form to the ring-closed spiropyran (SP) form.[5] From the SP form it thermally isomerizes back to the MC form. Since the spiropyran molecules are covalently bonded to the polymer backbone they do not undergo diffusion, but they are transported along with the polymer chains. These three factors (MC->SP, SP->MC, and polymer transport) give the following differential equation for the change of the spiropyran isomerization:

$$\frac{\partial c}{\partial t} = -\nabla \cdot \left(c\mathbf{J}_{\psi} \right) + k_1 I(1 + \psi - c) - k_0 c \,, \tag{3.2}$$

where J_{ψ} is the polymer flux, defined as:

$$\mathbf{J}_{\psi} = -\Lambda(\phi_{eq})[(\lambda + 2\mu)\nabla\psi - \chi_{sp} C_0 \phi_{eq} \nabla c] \,; \tag{3.3}$$

c and ψ are the percentage of MC isomerization to SP and the relative variation of gel volume fraction, respectively, defined as:

$$c = \frac{C}{C_0} \tag{3.4}$$

$$\psi = \frac{\phi - \phi_{eq}}{\phi_{eq}} \tag{3.5}$$

and $\Lambda(\phi_{eq})$ is the kinetic coefficient:

$$\Lambda(\phi_{eq}) = \frac{1 - \phi_{eq}}{\zeta(\phi_{eq})} \,, \tag{3.6}$$

where $\zeta(\phi_{eq})$ is the coefficient of friction between the water and polymer, C is the concentration of SP, C_0 the total equilibrium concentration of MC molecules, ϕ is the volume fraction of polymer in the gel, ϕ_{eq} is the equilibrium volume fraction of polymer,

λ and μ are Lamé's first and second parameters (related to the elastic and shear moduli, respectively), χ_{sp} is the fitting parameter coupling the spiropyran isomerization to the gel deformation, I is the light intensity, k_1 is the ring-closing rate constant, and k_0 is the thermal ring-opening rate constant. No-flux boundary conditions were used.

3.7.3.3.2 Gel dynamics

Our model of gel dynamics follows the model previously laid out by Yashin and Balazs,[47] and Kuksenok and Balazs.[53] The spiropyran isomerization reaction is coupled to the gel deformation through an induced osmotic pressure characterized by the parameter χ_{sp}, which we leave as a fitting parameter in the model. This results in the following equation governing the gel dynamics:

$$\frac{\partial \psi}{\partial t} = -\nabla \cdot \mathbf{J}_{\psi} = -\nabla \cdot \Lambda(\phi_{eq})[(\lambda + 2\mu)\nabla^2\psi - \chi_{sp}C_0\phi_{eq}\nabla^2 c] \,. \qquad (3.7)$$

This equation shows that there is a competition between the first term on the right-hand side of (eq 3.7), in which the elastic properties of the gel diffusively spread out higher concentrations of polymer, and the second term, in which the isomerization of spiropyran leads to the local concentration of polymer. The time scale of this competition is set by the kinetic coefficient $\Lambda(\phi_{eq})$. Fixed boundary conditions were used for the gel.

3.7.3.3.3 Light propagation

The propagation of light through the gel is modeled by the nonlinear paraxial wave equation:

$$\frac{\partial A}{\partial z} = \frac{1}{2ik}\,\nabla_T^2 A - ik\frac{\Delta n}{n_0}A - \alpha A, \tag{3.8}$$

where A is the complex field amplitude, z is the direction of propagation, k is the wavenumber ($k = 2\pi/\text{wavelength}$), α is the isomerization-dependent absorption coefficient of the spiropyran-doped gel, defined as:

$$\alpha = \alpha_0 + (\alpha_1 - \alpha_0)c \tag{3.9}$$

n_0 is the unperturbed refractive index of the gel, and the change in the index of refraction Δn is defined as:

$$\Delta n = (n_p - n_s)\phi_{eq}\psi \ , \tag{3.10}$$

where n_p and n_s are the refractive indices of the polymer and solvent, respectively. The transverse Laplacian ∇_T^2 is defined as:

$$\nabla_T^2 = \frac{\partial^2}{\partial x^2} + \frac{\partial^2}{\partial y^2} \ . \tag{3.11}$$

For boundary conditions, A was set to zero at infinity in the x and y directions, and $A = I_0 e^{\frac{-2(x^2+y^2)}{w_0^2}}$ at $z = 0$, where I_0 is the initial peak intensity of the beam and w_0 is the waist radius of the Gaussian beam focused onto the entrance face of the gel.

3.7.3.3.4 Parameter values

All parameter values utilized in the model can be located in Table 3-1. λ and μ were estimated based on the measured modulus of elasticity of the spiropyran-doped poly(AAm-*co*-AA) gels and the poisson ratio of similar PAAm gels.[54] The coefficient of friction was estimated by measuring the poroelastic diffusivity using the method by Hu et. al.[54] χ_{sp} was a fit parameter, as mentioned above. C_0 and ϕ_{eq} are known from the fabrication of the gels, while k, I_0, and w_0 are prescribed by the optical setup of the experiments.

k_1 was estimated by matching the initial rate of self-focusing. k_0 was estimated based on the observation from the cycling tests shown in Figure 3-3 that full relaxation of the gel does not occur for dark periods of 60 s or less. Assuming that the SP->MC isomerization limits the relaxation time gives an isomerization timescale of approximately 1/60 s ≈ 0.015 s^{-1}.

n_p was taken to be an average of the index of refraction of poly(acrylic acid) (1.53) and poly(acrylamide) (1.45) and n_s is the index of refraction of water (1.33).[9] α_0 was estimated based on measuring the relative initial maximum beam intensity after passing through the sample compared to passing through the sample holder filled with water only. α_1 was chosen to match the rate and extent of self-focusing to the experiments.

3.7.3.3.5 Single beam results

This model was used to simulate the self-focusing process at a variety of intensities matching experimental intensities. Model results are in good agreement with experiments both in the dynamics of self-focusing and the minimum degree of focusing reached as a function of intensity, as seen in Figure 3-2 and Figure 3-8. Discrepancies arise primarily due to the use of a single set of parameters for simulations, while experiments were done with different samples at different times leading to some variation in actual gel properties for different experiments. At long times (>500 s), higher order modes arise as the waveguide grows to be larger than the beam width, which is captured in the model for some choice of parameters but not others. The discrepancy may be explained either by a mismatch between the exact experimental conditions and those utilized in simulation, as well as by the ellipticity of the experimental beam. Indeed, at higher beam powers, the ellipticity of the beam may lead to the formation of two focused points of lower intensity rather than a single focused point of higher intensity and lower width surrounded by a ring, as is observed in the perfectly cylindrical simulations.

3.7.3.4 Examination of relevant parameters that support efficient self-trapping of light and the proposed mechanism

To verify the mechanism of self-trapping, optical experiments were performed on a series of control samples in order to ensure that the contraction of the polymer was responsible for the refractive index change that elicits self-trapping. Furthermore, experiments were done to determine the effects of pH and monomer chemistry on the

ability of the system to self-trap light by substituting (hydroxyethyl)methacrylate for acrylic acid in the hydrogel. The kinetics of spiropyran isomerization in different hydrogels was further studied to relate the observed dynamics to self-trapping behaviors observed in experiments. This was done by using absorbance spectroscopy and fluorescence recovery after photobleaching (FRAP).

3.7.3.4.1 Effect of spiropyran tethering and hydrogel matrix on self-trapping

To show that photoisomerization is the critical first step in a sequence of events that generates Δn, we launched the laser beam into a p(AAm-*co*-AAc) hydrogel without spiropyran substituents (z = 3.2 mm). The beam diverged to a width of ~95 μm and did not display significant changes in width or intensity over 1000 s (Figure 3-4a), confirming that spiropyran is necessary for self-trapping. We then found that the hydrogel matrix plays an equally important part in self-trapping by running an experiment in a solution of free-floating spiropyran molecules in a DMSO/water mixture. We kept the chromophore concentration in solution the same as it had been in the SP-modified p(AAm-*co*-AAc) hydrogel (Figure 3-4b). The control sample exhibited only very weak self-trapping over a significantly longer time-scale; the beam decreased in width to ~70 μm over 1000 s compared to a decrease of width to ~44 μm in just 30 s in the spiropyran-modified p(AAm-*co*-AAc) hydrogel (Figure 3-2).

Further experiments showed that self-trapping is most efficient when spiropyran moieties are covalently tethered to the hydrogel matrix. Although the beam did self-trap in a p(AAm-*co*-AAc) hydrogel dispersed with untethered spiropyran molecules (Figure 3-

4c, Figure 3-10a), the efficiency of self-trapping was just above 10%, much smaller than the ~80% self-trapping efficiency of SP-modified p(AAm-*co*-AAc) hydrogel (Figure 3-2).

3.7.3.4.2 Effect of solution pH on self-trapping

Changes in pH affects the amount of available merocyanine initially present that can be converted to spiropyran and elicit refractive index changes within the sample (Figure 3-10b). It also changes the degree with which the hydrogel samples swell, as acrylic acid-containing polymers are pH-responsive. At higher pH, the hydrogels swell due to the deprotonation of carboxylic acid moieties within the hydrogel (Figure 3-10b). In order for self-trapping to occur effectively, deionized water must be employed. In pH 4.8 buffer, the self-trapping efficiency decreased over time as the sample swelled over the course of three days (Figure 3-11a). Higher pH values decrease the self-trapping efficiency even more significantly, preventing the beam from narrowing and increasing the beam diameter as time progresses (Figure 3-11b).

3.7.3.4.3 Effect of monomer chemistry and pH-response of hydrogel on self-trapping

Self-trapping did not occur when the acidic pH-sensitive acrylate substituents of p(AAm-*co*-AAc) were replaced by non-pH responsive moieties in the SP-modified p(AAm-*co*-HEMA) gel (Figure 3-4d; Figure 3-12). The former exhibits significant pH-dependent volume changes: when immersed in phosphate buffer solutions, its swelling

ratio increased by ten-fold from 1.6 to 16.6 as the pH was increased from 3.2 to 7.4 (Figures 3-10 to 3-11). By contrast, neither the chromophore-modified p(AAm-*co*-HEMA) nor the undoped p(AAm-*co*-HEMA) undergoes pH-induced volume changes (Figure 3-12).

Moreover, the protonated ring-open merocyanine form is predominant in p(AAm-*co*-HEMA) when immersed in water (Figure 3-12b), illustrating that photoisomerization of merocyanine to spiropyran is still occurring within the SP-functionalized p(AAm-*co*-HEMA) gels. Light propagation experiments showed that the optical beam was defocused over time instead of being guided, likely due to a decrease in refractive index. This change in behavior must be due to the replacement of acrylic acid monomers with HEMA, which changes both the responsiveness of the gel to the release of protons as well as the distribution of spiropyran molecules between their different isomers.

3.7.3.5 UV-Visible spectroscopy kinetics

We carried out time-dependent UV-Visible spectroscopy to ensure that this difference in behaviour originates from the pH-responsiveness—rather than differences in photoisomerization kinetics—of the two materials (Figure 3-13a-c). SP-modified hydrogel samples were irradiated continuously with white light (5 mW) and their absorbance measured over time. As expected, continuous visible light irradiation resulted in a decrease in the absorbance band of merocyanine (420 nm). Indeed, photoisomerization rates were comparable: 0.05 ± 0.01 s^{-1} and 0.02 ± 0.01 s^{-1} for p(AAm-*co*-HEMA) and p(AAm-*co*-AAc), respectively (Table 3-2). Corresponding rates for thermal relaxation of spiropyran to protonated merocyanine were also comparable at

$0.0020 \pm 0.0005\ s^{-1}$ and $0.0010 \pm 0.0004\ s^{-1}$, respectively (Table 3-2). Despite the comparable rates of photoisomerization in both materials, no self-trapping occurred in the p(AAm-*co*-HEMA) system (Figure 3-4d, Figure 3-12); in fact, the beam propagating through this gel increased in width with a concomitant decrease in relative peak intensity and became more diffuse over time.

These results suggest that the photostationary state was reached faster in the p(AAm-*co*-HEMA) hydrogel based on the rate constants obtained (Table 3-2). The percentage of conversion of merocyanine to spiropyran upon visible light irradiation is comparable in both hydrogels. However, self-trapping is only observed in the p(AAm-*co*-AAc) hydrogel, indicating that the acrylic acid and its pH-induced contraction of the hydrogel is necessary for the observed self-trapping behaviour.

The forward isomerization rates for the conversion of merocyanine to spiropyran are intensity dependent, and therefore these rates cannot be directly applied to our 3.9 mm samples that are used for self-trapping. The comparison does allow us to identify that although both samples undergo a merocyanine to spiropyran isomerization under light irradiation with rates on the same order of magnitude, only hydrogel samples containing acrylic acid generate self-trapped beams.

3.7.3.6 Fluorescence recovery after photobleaching (FRAP)

We employed Fluorescence Recovery After Photobleaching (FRAP) to further probe differences in the mobility of chromophores that were either tethered or simply dispersed in the p(AAm-*co*-AAc) hydrogel and to understand the impact of this parameter on self-

trapping dynamics. In FRAP experiments, an excitation laser beam (488 nm) of a confocal microscope activates isomerization in a specific area of the sample. The recovery of fluorescence (as protonated merocyanine is replenished) in this bleached region is imaged over time and fit to an exponential curve with time constant τ ($y = y_o + A\exp(-\tau \cdot t)$). The fluorescence recovery curves were also fit to bi-exponential curves ($y = y_o + A_1\exp(-\tau_1 \cdot t) + A_2\exp(-\tau_2 \cdot t)$), in order to extract two different time constants that would describe the two processes of isomerization and diffusion (Table 3-3).

This study relied on the fluorescence of the ring-open form merocyanine, which allowed the hydrogels to fluoresce in the visible region. In contrast, control p(AAm-*co*-AAc) hydrogels that contained no spiropyran showed no fluorescent signal. Laser light at 488 nm from the confocal microscope was briefly irradiated onto a small area of the hydrogel sample (region of interest (ROI) indicated by the 40 μm circle in Figure 3-13d,e), bleaching merocyanine fluorescence in that area. After the light was turned off, recovery of the fluorescence by isomerization and diffusion of the surrounding untethered spiropyran molecules into the area was measured over time to generate a fluorescence recovery curve. When light at 405 nm was irradiated on an area of the hydrogel containing spiropyran, the fluorescence instead increased (Figure 3-13d,e), signifying the isomerization from the ring-closed form of spiropyran to the fluorescent ring-open form at shorter wavelengths.

The fluorescence recovery of spiropyran in prepolymer solution was compared to that of untethered spiropyran dispersed in the p(AAm-*co*-AAc) hydrogel and spiropyran tethered to the p(AAm-*co*-AAc) hydrogel (Figure 3-13d,e). It is evident that the fastest

recovery occurs for spiropyran in solution (green curve), while that of spiropyran untethered in the hydrogel (blue curve) is faster than that of spiropyran tethered to the hydrogel (red curve). Since there is little, if any, diffusive component in the hydrogel to which spiropyran is tethered, the fluorescence recovery observed relies on the thermal relaxation of spiropyran back to the ring-open form, after irradiation with intense visible light isomerized most of the ring-open form to the closed-ring form. This suggests that there are two processes occurring in the fluorescence recovery: 1) diffusion of spiropyran into the bleached area, and 2) thermal isomerization of spiropyran back to the ring-open form. We expect spiropyran tethered to the hydrogel to be comprised mainly of the second process while the untethered systems would contain both processes.

The τ value determined for samples where spiropyran was tethered to the hydrogel, ~0.01 s^{-1}, was found to be comparable to the τ_1 values obtained for the more diffusive systems when they were fit with a double exponential (Table 3-3). This value likely represents the isomerization kinetics of spiropyran back to the ring-open form in each of the systems after the intense visible light is turned off. The τ_2 value of the double exponential fit represents the diffusivity of spiropyran in the system. τ_2 for untethered spiropyran in solution and in the hydrogel are both ~0.1 s^{-1}. The immobile fraction of spiropyran in the hydrogel that contains some molecules that are fully bleached is represented by the grey line in Figure 3-13e. Interaction of the spiropyran with the hydrogel network leads to immobile fractions, influencing its measured recovery, whereas in solution there is more fluidity of all components and thus more recovery. For spiropyran tethered to the hydrogel in which most of the spiropyran is immobilized by

covalent attachment, full photobleaching of some of the spiropyran molecules by the intense irradiation of light could similarly account for less fluorescent recovery over a longer time (plateaus at lower fluorescence).

FRAP studies revealed that τ in the case of untethered chromophores was reduced by at least 35% to 0.030 ± 0.004 s^{-1} relative to the solution-only system (0.046 ± 0.003 s^{-1}). Importantly, self-trapping is most efficient in the spiropyran-modified p(AAm-*co*-AAc) hydrogel, where covalently tethered chromophores possess the least mobility as indicated by a $\tau = 0.012 \pm 0.006$ s^{-1}. The differences in spiropyran mobility between each of the systems help to explain the self-trapping efficiencies observed; the presence of immobile spiropyran within a hydrogel matrix leads to sharper refractive index gradients and an increase in self-trapping efficiency over those in solution.

These results highlight the collaborative roles of the tethered spiropyran moieties and the p(AAm-*co*-AAc) matrix in eliciting the nonlinear conditions required for self-trapping. They show that local pH-induced contraction of the gel triggered by photoisomerization generates the Δn necessary for self-trapping. The efficiency and rate of self-trapping is optimal when chromophores are covalently tethered to the matrix and thus have limited mobility. Equally important, self-trapping is absent in the pH-independent spiropyran-modified poly(AAm-*co*-HEMA) material. This confirms that neither laser-induced local heating of the hydrogel nor changes in its optical density due to chromophore depletion generate the nonlinear conditions required for self-trapping.

3.7.4 Interactions of two self-trapped beams

3.7.4.1 Self-trapping inhibition in double beam experiments

The introduction of a second beam in the chromophore-modified p(AAm-*co*-AAc) hydrogel results in the decrease of the self-trapping efficiency of the first self-trapped beam. The two beams reach an equilibrium condition that is dependent on the intensity of each beam. (Figure 3-14).

As one of the beams is blocked, the beam that remains is then able to change its refractive index sufficiently in order to generate a more fully self-trapped beam, and this process occurs regardless of the distance between the beams (Figures 3-14). We fit the temporal intensity plots of Beams 1 and 2 (Figure 3-5) to the phenomenological equation

$$I = I_0 + Ae^{R_0 t}, \tag{3.12}$$

where I represents intensity in arbitrary units and t, time in seconds (Figures 3-14), R_o corresponds to the initial rate of change in intensity, and A is a proportionality constant. We then compared R_o values of both beams after the initially blocked Beam 2 was reintroduced into the medium. R_o values associated with the consequent decrease in intensity of Beam 1 and concomitant increase in intensity of Beam 2 as it began to self-trap were –0.034 s^{-1} and +0.023 s^{-1}, respectively. R_o values measured after first blocking and then reintroducing Beam 1 were +0.021 s^{-1} and –0.028 s^{-1}, respectively. These results show that the rate of self-trapping of a newly introduced beam is commensurate with the decrease in self-trapping of an already formed self-trapped beam in the hydrogel. In other words, there is strong reciprocal correlation between the change in refractive index (and extent of contraction) between the two regions of the hydrogel. Similar effects are

observed even when the two beams possess different initial intensities although the absolute changes in intensity are smaller (Figure 3-14).

3.7.4.2 Double beam simulations

Initial 2D simulations of two co-propagating beams were carried out for separations of 25, 50, 100, and 200 μm. The choice to use a 2D coordinate system was made to reduce computation time in initial simulations, but also has a significant effect on simulation results. Specifically, it corresponds to an infinite focused line of optical intensity rather than cylindrical beams. This leads to decreased loss of optical intensity as light propagates through the gel, changing the dynamics of self-focusing. In this work we used unrealistic parameter values for double beam simulations in order to show that qualitative dynamics are well captured for small separation distances by the relevant physics, while a precise match between double beam simulations and experiments is left for future work. The parameters that differed between single and double beam simulations were $\chi_{sp} = 4.4 \times 10^5$ Pa M^{-1}, $k_1 = 6 \times 10^{-6}$ m^2 W^{-1} s^{-1}, $k_0 = 10$ s^{-1}, $\alpha_0 = \alpha_1 = 90$ m^{-1}, and $I_0 = 3.8 \times 10^7$ W m^{-2}. While significant inhibition between the beams was observed with these parameters for a separation of 25 μm, inhibition was not observed for a much larger separation of 200 μm, contrary to the experimental evidence.

The qualitative dynamics of the two beams with a separation of 25 μm match the observed experimental dynamics. When two beams propagate in parallel, they mutually inhibit self-focusing, but when one beam is turned off, the remaining beam focuses to ~20 μm (Figure 3-15a). The model also reveals the internal dynamics of the beams (Supplementary MOVIE S3), which is inaccessible experimentally. Beams are seen to

initially repel and bend away from each other. Then, when one beam is blocked, the remaining beam bends towards the blocked beam's prior position before eventually straightening. A comparison of the exit face intensity distribution for the experiments and models suggests that these dynamics are qualitatively representative of the experimental system (Figure 3-15b).

This mechanism does not, however, explain the interactions of self-trapped beams separated by ten times the beam width as it cannot account for the almost instantaneous response of one beam to the introduction or blocking of the other over long distances. Indeed, as the poro-elastic diffusivity describing the swelling mechanism is on the order of $D \sim 10^{-11}$ m^2 s^{-1} (Table 3-1), and the relevant length scale (beam separation) is on the order of 100 μm, gel deformation-related effects are expected to occur on the order of 1,000 s given the solvent-expulsion swelling mechanism described above; this is orders of magnitude slower than the observed interaction timescale. Thus, we anticipate an alternative mechanism to dominate at large beam separations within this material. Heat-induced swelling of the gel upon light absorption may lead to long-range inhibition of self-trapped beams.[40] We have observed experimentally that the p(AAm-*co*-AAc) gels swell as temperature is increased, which we confirm with simulations has an inhibitory effect on self-focusing. Thermal defocusing has been observed in other systems as refractive index tends to decrease with heat.[55] In addition, heat is transported very quickly relative to poroelastic effects, as the thermal diffusivity in water is on the order of 10^{-7} m^2 s^{-1},[56] leading to an interaction timescale on the order of 0.1 s for a separation of 200 μm. Proton diffusion can occur on a timescale of 1-10 s given the distances between the

beams and may also contribute to these interactions. Further studies are ongoing to investigate these interactions under further conditions.

3.7.5 Description of movies

MOVIE_S1

Schematic representation of reversible optical self-trapping of a single Gaussian beam within a SP-functionalized hydrogel at 6 mW.

MOVIE_S2

Schematic representation of optical self-trapping within SP-functionalized hydrogels with two remote beams; each beam is switched on and off to control the interaction.

MOVIE_S3

Simulation results for two beams with a separation distance of 25 μm.

3.7.6 Supplementary figures

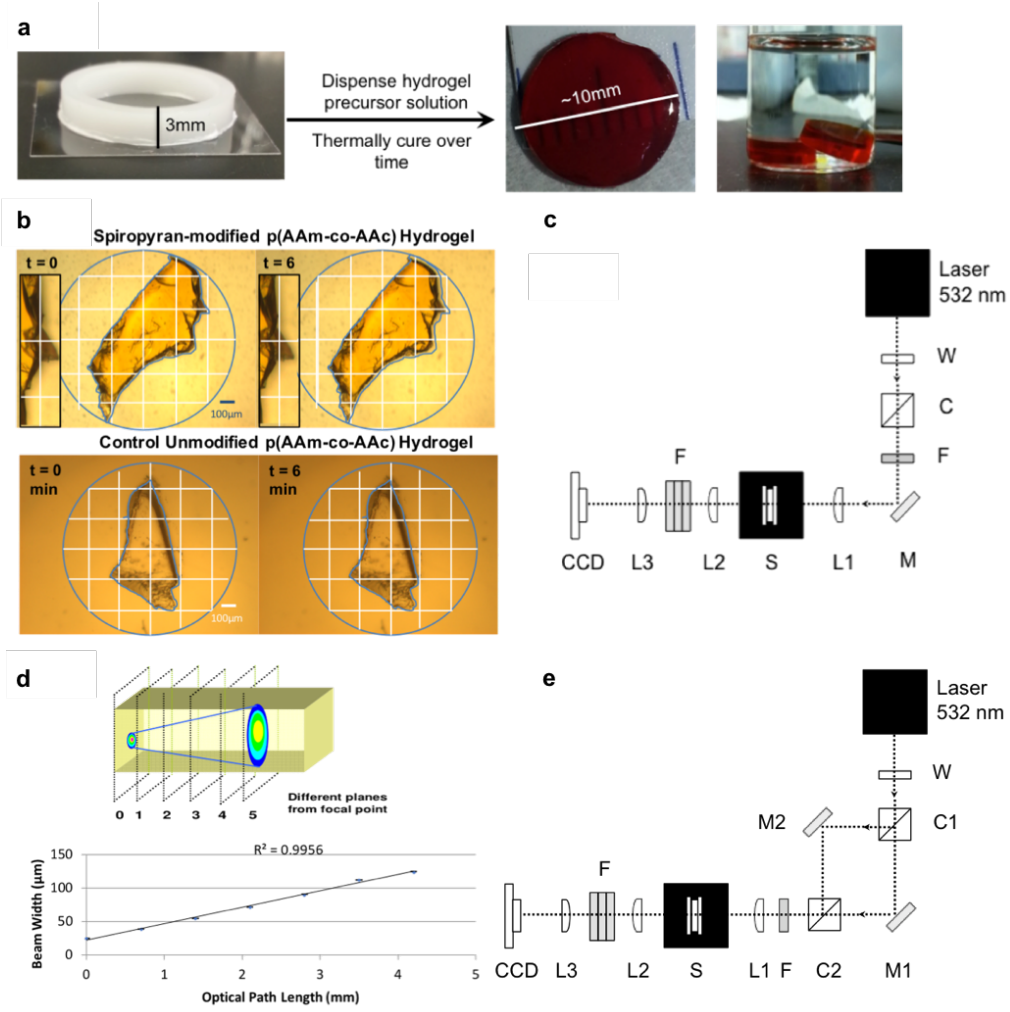

Figure 3-6 (a) SP-modified hydrogel sample preparation (b) Optical micrographs showing (top) shrinkage/contraction of spiropyran-modified p(AAm-*co*-Aac) after 6 min of visible light irradiation of the entire hydrogel and (bottom) corresponding control study with unmodified p(Aam-*co*-Aac). The blue line indicates the original boundaries of the gel prior to irradiation. (c) Optical assembly for single-beam self-trapping experiments featuring the sample (S), a λ/2 wave plate (W), polarizing beam splitter cube (C), absorption filters (F), mirror (M), planoconvex lenses (L1-L3) and a CCD camera. (d) Control study of beam divergence in an unmodified control sample and resulting experimental plot with fitted linear trendline. € Optical assembly for self-trapping in two beam experiments with additional mirror (M2) and polarizing beamsplitter cube (C2) (L1 = L2 = plano-convex lenses with f.p. 75.6 mm; L3 = plano-convex lens with f.p. of 250 mm).

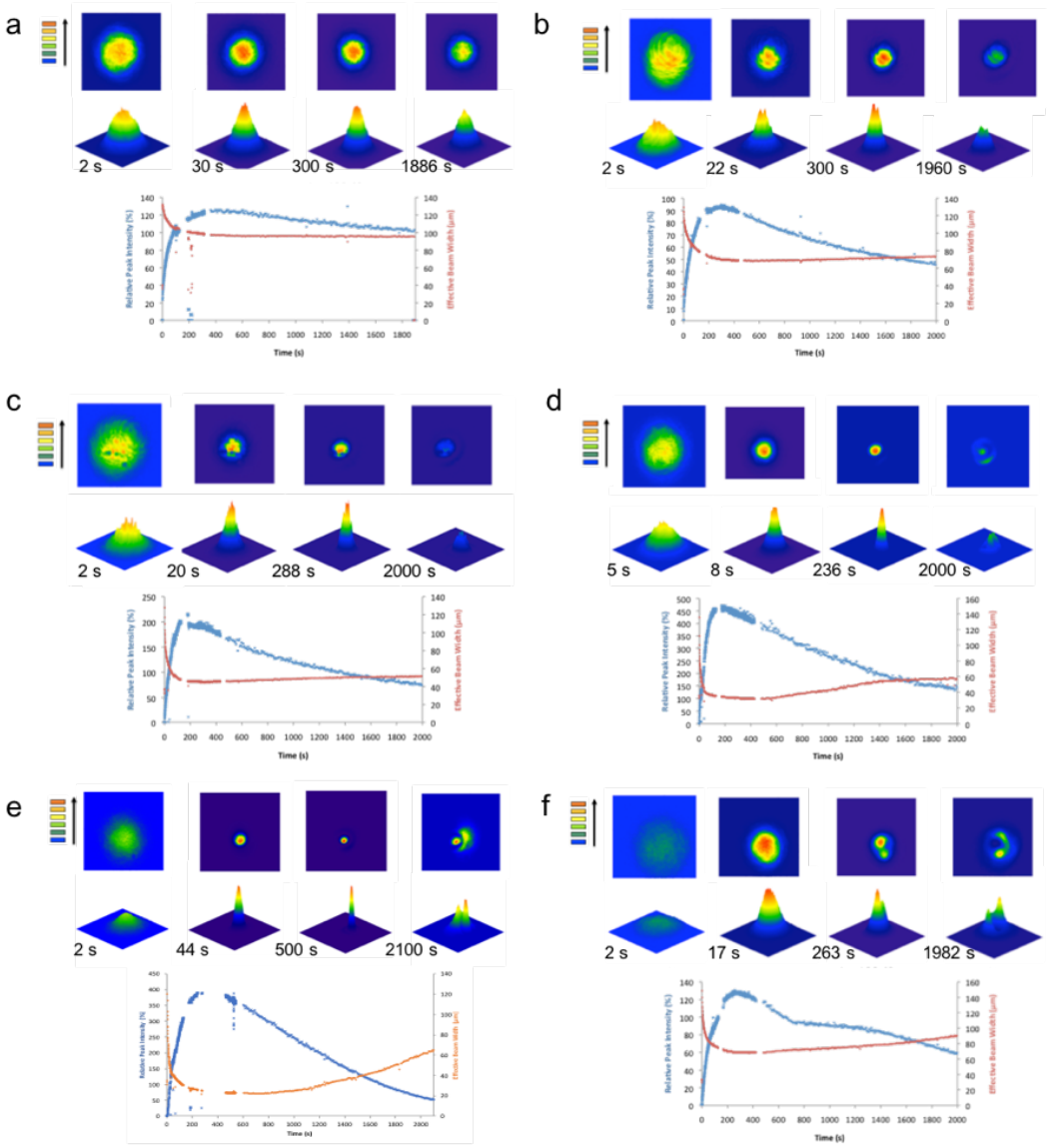

Figure 3-7 Spatial intensity profiles for the self-trapping of light in spiropyran-modified p(AAm-*co*-AAc) and the corresponding relative peak intensity (blue) and effective beam diameter (red) as a function of time. Incident beam power is (a) 0.37 mW, (b) 0.75 mW, (c) 1.5 mW, (d) 3 mW, (e) 6 mW and (f) 9 mW. Intensity scale of spatial intensity profiles changed at different times to improve visualization.

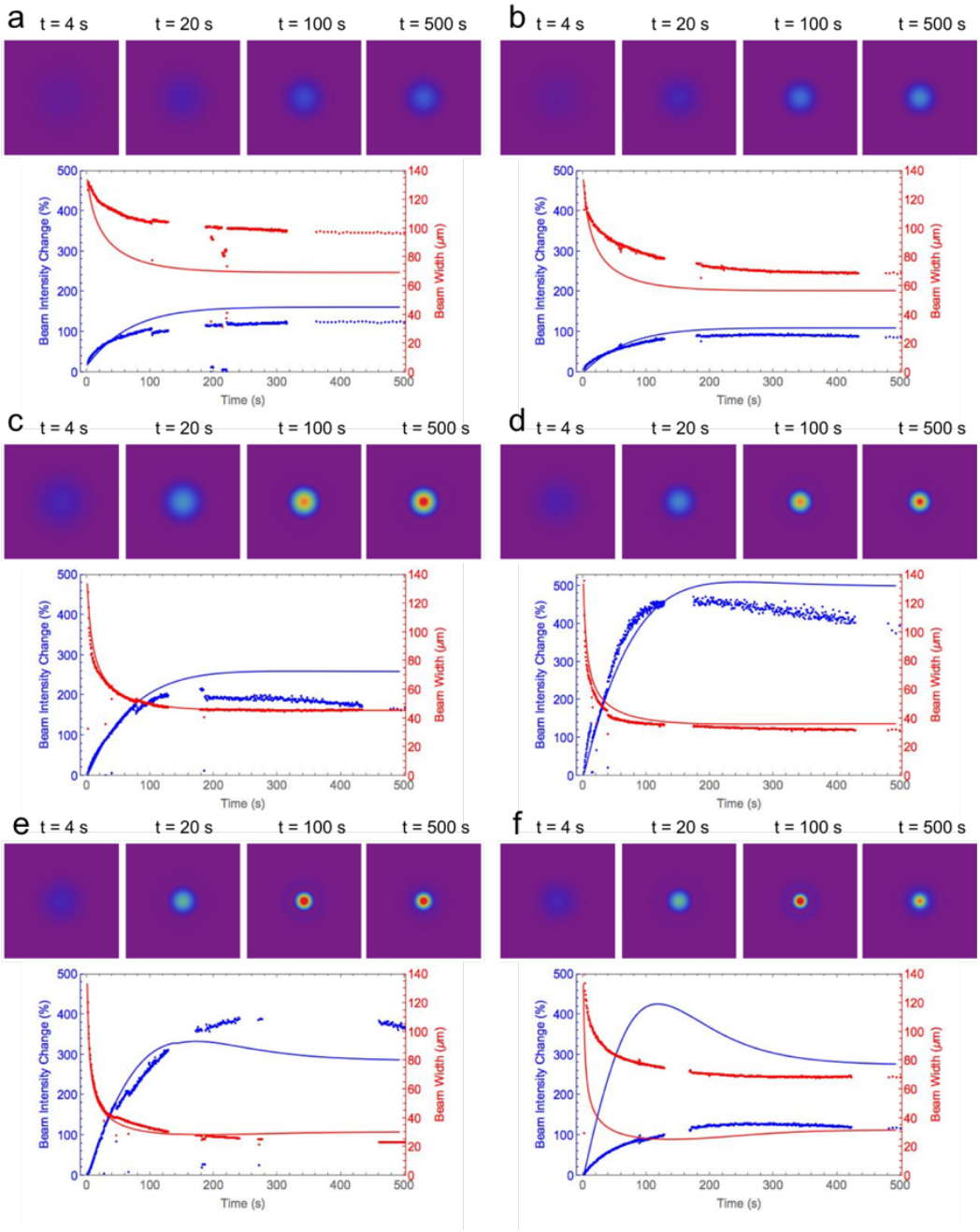

Figure 3-8 Simulated spatial intensity profiles for the self-trapping of light in spiropyran-modified p(AAm-*co*-AAc) and the corresponding peak intensity (blue, solid line is simulated) and beam diameter (red, solid line is simulated) as a function of time. Incident beam power is (a) 0.37 mW, (b) 0.75 mW, (c) 1.5 mW, (d) 3 mW, (e) 6 mW, and (f) 9 mW.

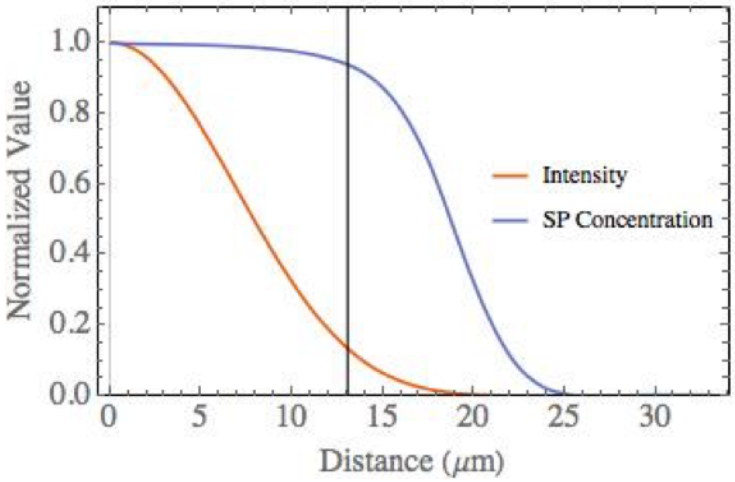

Figure 3-9 Spiropyran concentration and intensity profile within the SP-modified p(AAm-*co*-AAc) at 500 s looking at z = 0.5 mm for a 6 mW simulation. The black vertical line indicates the beam radius.

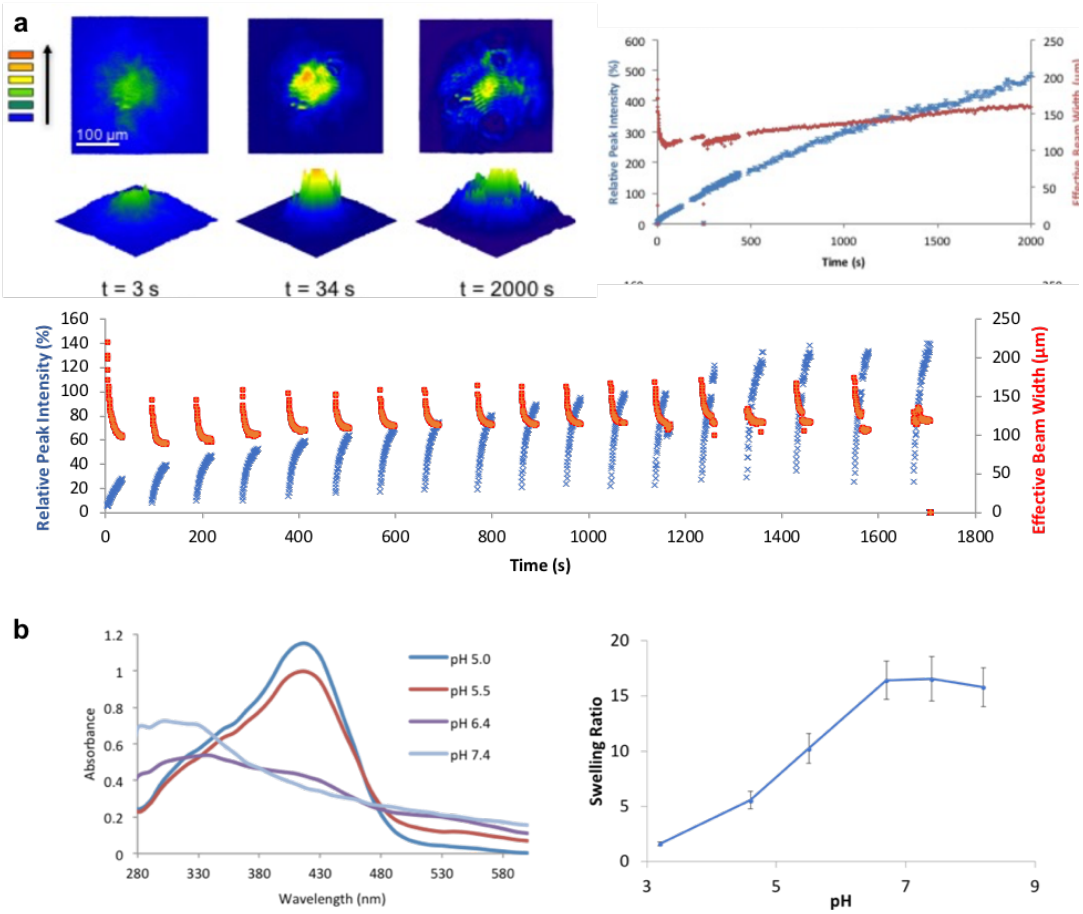

Figure 3-10 (a) Spatial intensity profiles for the self-trapping of light in a p(AAm-*co*-AAc) hydrogel containing spiropyran that is not attached covalently. Beam power is 6 mW. Left: Intensities scaled for better beam visualization. Right: Corresponding relative peak intensity (blue) and effective beam diameter (red) as a function of time. Bottom: Relative peak intensity (blue) and effective beam diameter (red) as a function of time showing the reduced reversibility and repeatability of self-trapping in a p(AAm-*co*-AAc) hydrogel containing untethered spiropyran units. (b) Absorbance spectra of spiropyran acrylate in solutions buffered at varied pH (left) and swelling ratio of spiropyran-modified p(AAm-*co*-AAc) hydrogels immersed in solutions buffered at varied pH (right). Error bar represents standard deviation, n = 5.

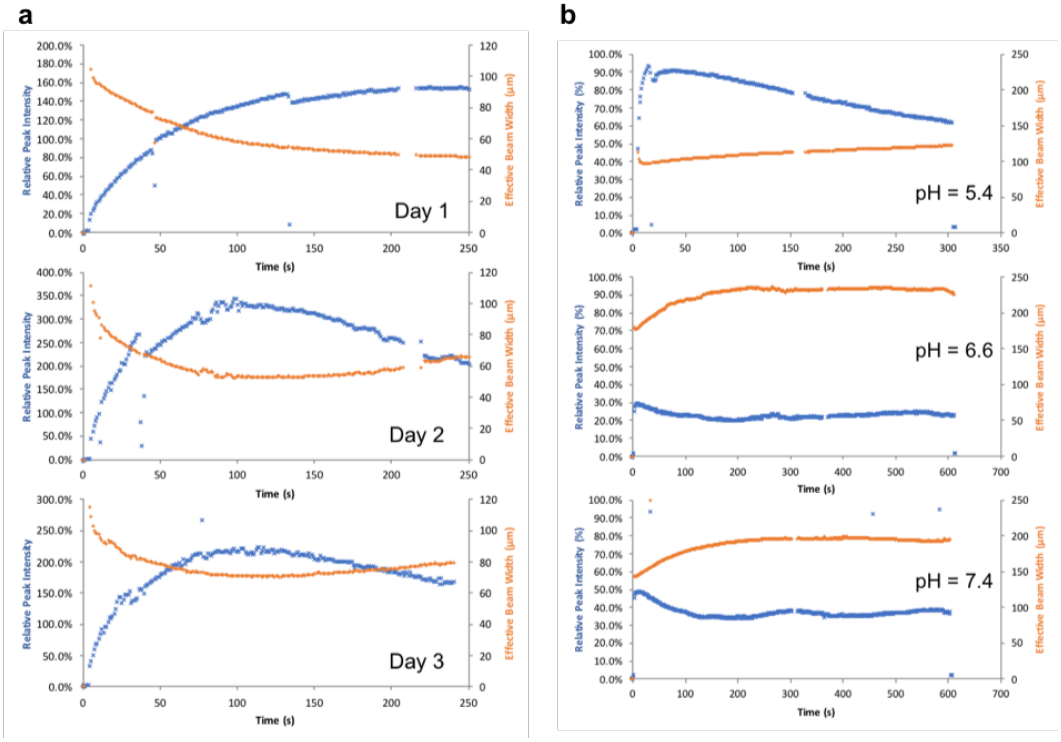

Figure 3-11 Self-trapping of light in spiropyran-modified p(AAm-*co*-AAc) hydrogel. (a) swollen in solution of pH 4.8 on different days. (b) immersed in solutions of different acidity. Relative peak intensity (blue) and effective beam diameter (red) as a function of time are shown, for which the incident beam power is 6 mW.

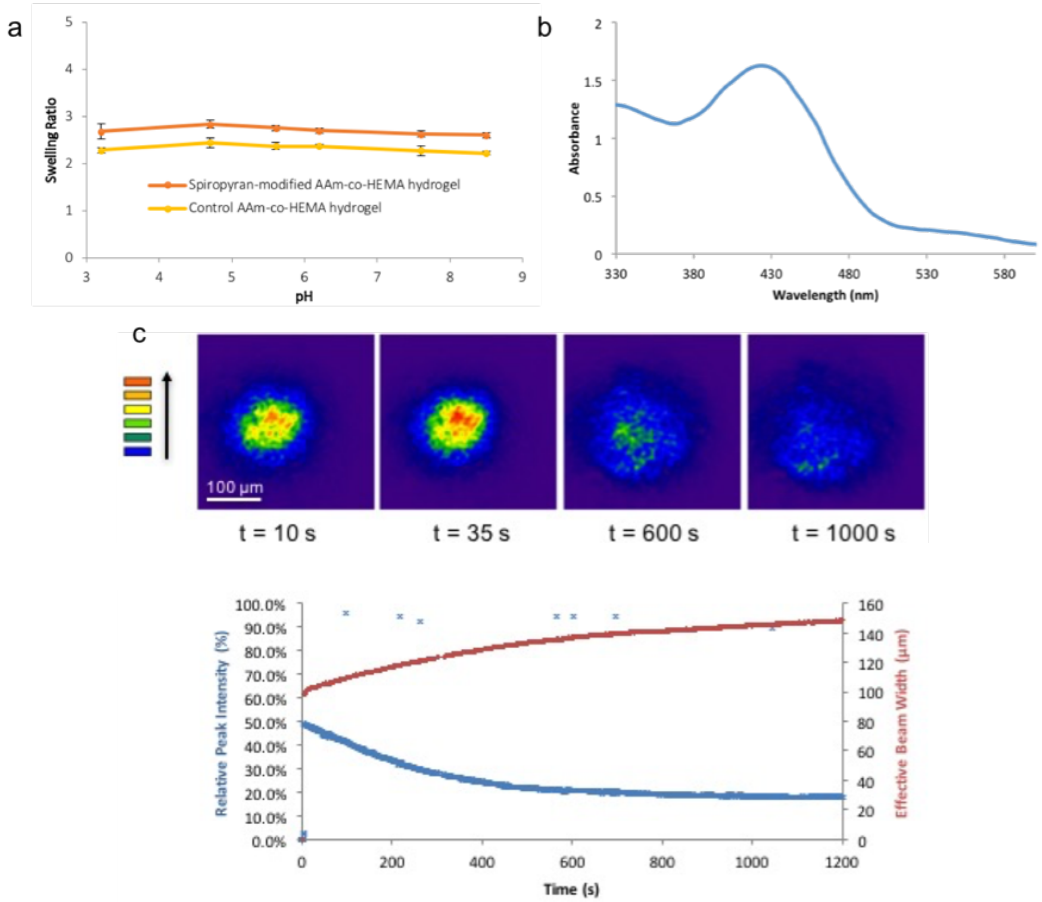

Figure 3-12 Investigations of a spiropyran-modified p(AAm-*co*-HEMA) hydrogel to confirm the importance of the AAc groups in the self-focusing mechanism. (a) Swelling ratio of spiropyran-modified p(AAm-*co*-HEMA) hydrogel immersed in solutions buffered at different pH. There is no significant volume change over the pH range tested. Error bar represents standard deviation, n = 6. (b) Absorbance spectrum of spiropyran-modified p(AAm-*co*-HEMA) hydrogel in water. Absorbance peak at λ_{max} = 420 nm corresponds to a π-π* transition of the protonated ring-open form, merocyanine. (c) Spatial intensity profiles for the self-trapping of light in non-pH-responsive SP-modified p(AAm-*co*-HEMA) hydrogel (intensities scaled for better visualization) and the corresponding relative peak intensity (blue) and effective beam diameter (red) as a function of time for which the incident beam power is 6 mW.

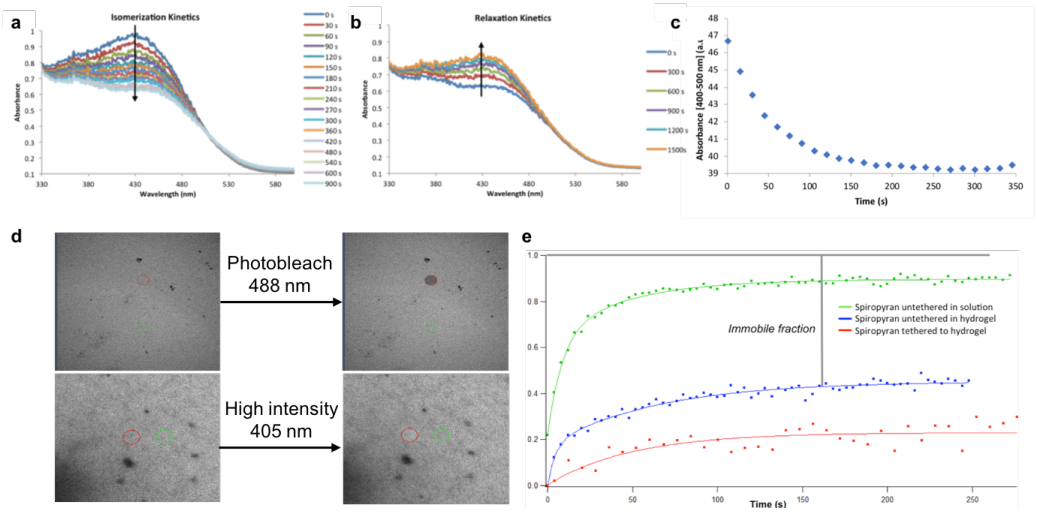

Figure 3-13 Change in absorbance spectra of a piece of spiropyran-modified p(AAm-*co*-AAc) hydrogel upon (a) irradiation with 5 mW of white light and (b) relaxation process in the dark. (c) Changes in integrated absorbance from 400 to 500 nm over time of a spiropyran-modified p(AAm-*co*-HEMA) hydrogel upon irradiation with 5 mW of white light. (d) Fluorescence recovery after photobleaching studies; confocal photobleaching images show the effect on the fluorescence of p(AAm-*co*-AAc) hydrogel containing spiropyran when the area within the red circle (40 µm diameter) is irradiated with 488 nm or 405 nm light. (e) Representative normalized fluorescence recovery curves after photobleaching of different systems containing spiropyran.

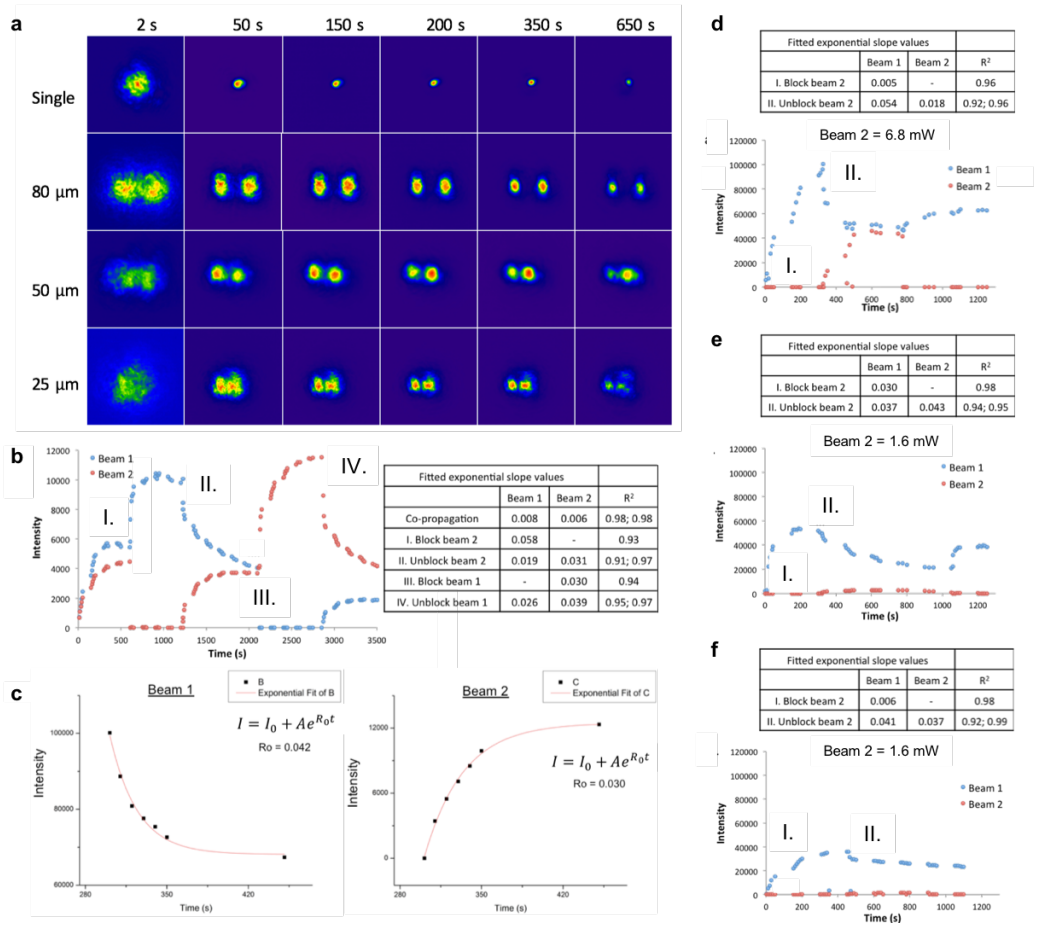

Figure 3-14 (a) Spatial 2D intensity profiles at the exit face of spiropyran-modified p(AAm-*co*-AAc) at various times illustrating the effect of beam separation on two-beam interactions in the spiropyran-modified hydrogel. (b)-(f) Plots and tables detailing the changes to the intensity of two co-propagating beams (Δx = 200 µm) when a beam is blocked and unblocked as denoted by the labels in Roman numerals (I-IV). (c) Example of exponential fit using ORIGIN software for beam blocking experiments using $I = I_o + Aexp(R_o t)$. Exponentially fitted values represent the rate at which self-trapping occurs for each beam in the initial 150-200 s. (b)-(f) Beam 1 = 6.7 mW. (b),(d) Beam 2 = 6.8 mW (e),(f) Beam 2 = 1.6 mW.

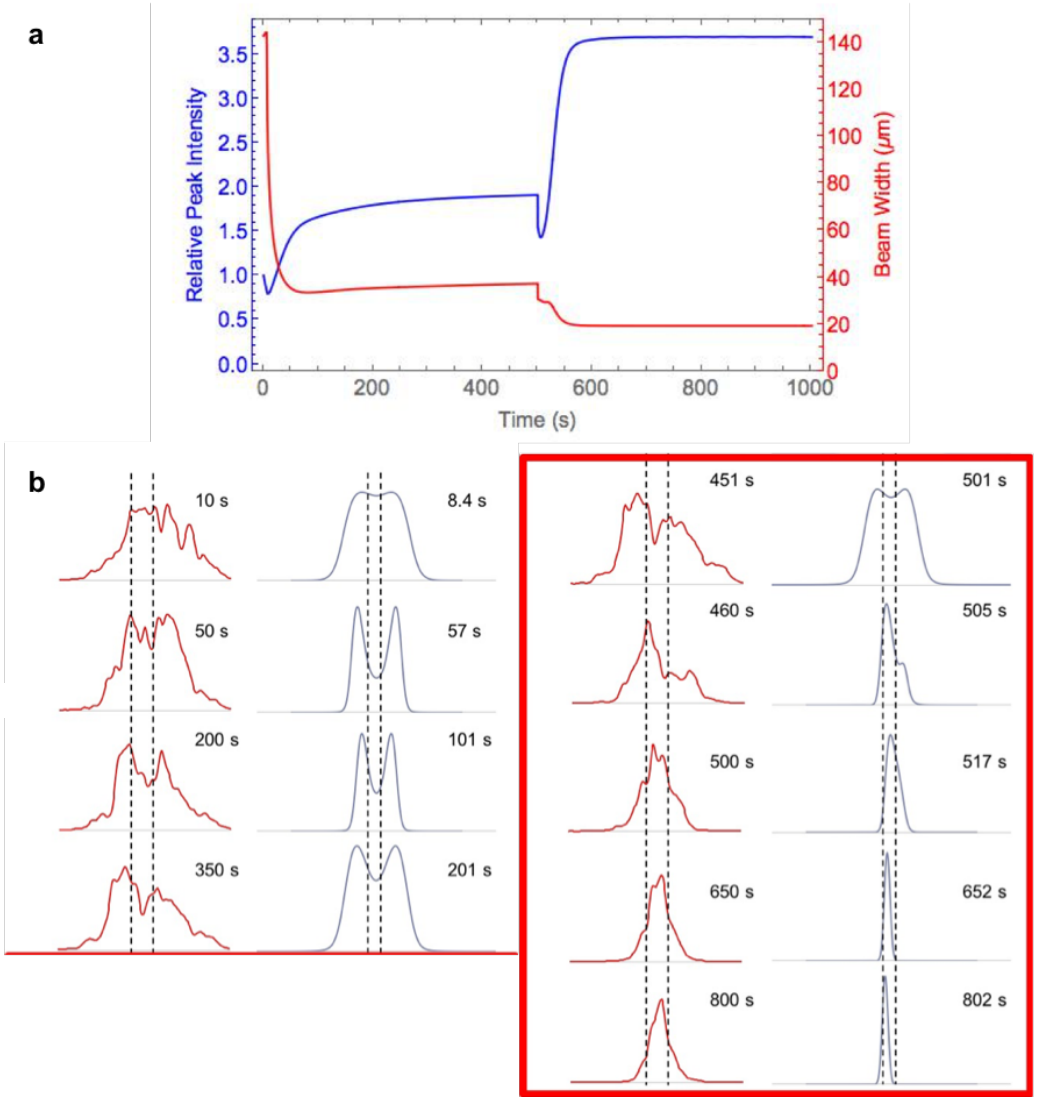

Figure 3-15 (a) Simulated relative peak intensities and corresponding beam widths for two co-propagating 6.7 mW beams with a separation of 25 **μ**m. The second beam is turned off at 500 s, resulting in full self-focusing of the remaining beam. (b) Comparison between transverse intensity cross-sections on the outlet face of the gel in experiment (left columns) and simulation (right columns). The red box denotes when the beam on the right side (Beam 2) is blocked. Beams are observed in both cases to initially focus and repel each other, and when one beam is blocked the remaining beam bends towards the blocked beam's position.

3.7.7 Supplementary tables

Table 3-1 Parameter values used for the model.

Parameter	Value Used	Units
ϕ_{eq}	0.4	-
$\zeta(\phi_{eq})$	1×10^{15}	Pa s m^{-2}
C_0	1.14×10^{-3}	M
λ	58	kPa
μ	3.4	kPa
χ_{sp}	8.8×10^{5}	Pa M^{-1}
k_1	1.53×10^{-7}	m^2 W^{-1} s^{-1}
k_0	0.015	s^{-1}
k	1.2×10^{7}	m^{-1}
α_0	1200	m^{-1}
α_1	800	m^{-1}
n_p	1.49	-
n_s	1.33	-
I_0	0.24×10^{7} to 5.7×10^{7}	W m^{-2}
w_0	1×10^{-5}	m

Table 3-2 Photoreaction rate constants for isomerization of merocyanine to spiropyran using a 5 mW white light source and relaxation rate constants for conversion of spiropyran to merocyanine in the dark.

	Photoreaction Rate Constant (k) [s^{-1}]	Relaxation Rate Constant (k) [s^{-1}]
Spiropyran tethered to p(AAm-*co*-AAc) hydrogel	0.02± 0.01	0.0010 ± 0.0004
Spiropyran tethered to p(AAm-*co*-HEMA) hydrogel	0.05 ± 0.01	0.0020 ± 0.0005

Table 3-3 Table of average time constants of fluorescent recovery from single and bi-exponential fits of the fluorescence recovery curves of each of the systems. Error represents standard deviation, n = 3-6.

	Single-exp. fit	Double-exp. fit	
	Average τ (s^{-1})	Average τ_1 (s^{-1})	Average τ_2 (s^{-1})
Spiropyran in AAm-AAc pre-polymer solution	0.046 ± 0.003	0.014 ± 0.002	0.076 ± 0.005
Spiropyran untethered in p(AAm-*co*-AAc) hydrogel	0.030 ± 0.004	0.011 ± 0.008	0.099 ± 0.042
Spiropyran tethered to p(AAm-*co*-AAc) hydrogel	0.012 ± 0.006		

3.8 References

(1) Biria, S.; Morim, D. R.; An Tsao, F.; Saravanamuttu, K.; Hosein, I. D. Coupling Nonlinear Optical Waves to Photoreactive and Phase-Separating Soft Matter: Current Status and Perspectives. *Chaos An Interdiscip. J. Nonlinear Sci.* **2017**, *27*, 104611.

(2) Stegeman, G. I. Optical Spatial Solitons and Their Interactions: Universality and Diversity. *Science* **1999**, *286*, 1518–1523.

(3) Chiao, R. Y.; Garmire, E.; Townes, C. H. Self-Trapping of Optical Beams. *Phys. Rev. Lett.* **1964**, *13*, 479–482.

(4) Trillo, S.; Torruellas, W. *Spatial Solitons*; Springer: New York, 2001.

(5) Snyder, a W.; Sheppard, a P. Collisions, Steering, and Guidance with Spatial Solitons. *Opt. Lett.* **1993**, *18*, 482–484.

(6) Królikowski, W.; Holmstrom, S. a. Fusion and Birth of Spatial Solitons upon Collision. *Opt. Lett.* **1997**, *22*, 369–371.

(7) Królikowski, W.; Luther-Davies, B.; Denz, C.; Tschudi, T. Annihilation of Photorefractive Solitons. *Opt. Lett.* **1998**, *23*, 97–99.

(8) Buryak, A. V.; Kivshar, Y. S.; Shih, M.-F. S. M.-F.; Segev, M. Induced Coherence and Stable Soliton Spiraling. *Tech. Dig. Summ. Pap. Present. Quantum Electron. Laser Sci. Conf.* **1999**.

(9) Peccianti, M.; Brzdkiewicz, K. A.; Assanto, G. Nonlocal Spatial Soliton Interactions in Nematic Liquid Crystals. *Opt. Lett.* **2002**, *27*, 1460–1462.

(10) Rotschild, C.; Alfassi, B.; Cohen, O.; Segev, M. Long-Range Interactions between Optical Solitons. *Nature Physics*. 2006, pp 769–774.

(11) Jradi, S.; Soppera, O.; Lougnot, D. J. Fabrication of Polymer Waveguides between Two Optical Fibers Using Spatially Controlled Light-Induced Polymerization. *Appl. Opt.* **2008**, *47*, 3987–3993.

(12) Yang, J.; Zhang, P.; Yoshihara, M.; Hu, Y.; Chen, Z. Image Transmission Using Stable Solitons of Arbitrary Shapes in Photonic Lattices. *Opt. Lett.* **2011**, *36*, 772–774.

(13) Kivshar, Y. Spatial Solitons: Bending Light at Will. *Nature Physics*. 2006, pp 729–730.

(14) Snyder, A. W.; Ladouceur, F. Light Guiding Light: Letting Light Be the Master of Its Own Destiny. *Opt. Photonics News* **1999**, *10*, 35.

(15) Peccianti, M.; Conti, C.; Assanto, G.; De Luca, A.; Umeton, C. All-Optical Switching and Logic Gating with Spatial Solitons in Liquid Crystals. *Appl. Phys. Lett.* **2002**, *81*, 3335–3337.

(16) Shih, M.; Garrett, M. H.; Salamo, G.; Valley, G. C.; Leach, P.; Segev, M. Two-Dimensional Steady-State Photorefractive Screening Solitons. *Opt. Lett.* **1996**, *21*, 324–326.

(17) Conti, C.; Peccianti, M.; Assanto, G. Observation of Optical Spatial Solitons in a Highly Nonlocal Medium. *Phys. Rev. Lett.* **2004**, *92*, 113902–1.

(18) Bjorkholm, J. E.; Ashkin, A. A. CW Self-Focusing and Self-Trapping of Light in Sodium Vapor. *Phys. Rev. Lett.* **1974**, *32*, 129.

(19) Ashkin, A.; Dziedzic, J. M.; Smith, P. W. Continuous-Wave Self-Focusing and Self-Trapping of Light in Artificial Kerr Media. *Opt. Lett.* **1982**, *7*, 276–278.
(20) Morim, D. R.; Vargas-Baca, I.; Saravanamuttu, K. Reversibly Trapping Visible Laser Light through the Catalytic Photo-Oxidation of I-by Ru (Bpy) 32+. *J. Phys. Chem. Lett.* **2016**.
(21) Sumaru, K.; Takagi, T.; Sugiura, S.; Kanamori, T. Spiropyran-Functionalized Hydrogels. In *Soft Actuators*; Springer, 2014; pp 219–229.
(22) Zió\lkowski, B.; Florea, L.; Theobald, J.; Benito-Lopez, F.; Diamond, D. Self-Protonating Spiropyran-Co-NIPAM-Co-Acrylic Acid Hydrogel Photoactuators. *Soft Matter* **2013**, *9*, 8754–8760.
(23) Tong, R.; Hemmati, H. D.; Langer, R.; Kohane, D. S. Photoswitchable Nanoparticles for Triggered Tissue Penetration and Drug Delivery. *J. Am. Chem. Soc.* **2012**, *134*, 8848–8855.
(24) Hudson, A. D.; Ponte, M. R.; Mahmood, F.; Pena Ventura, T.; Saravanamuttu, K. A Soft Photopolymer Cuboid That Computes with Binary Strings of White Light. *Nat. Commun.* **2019**, *10*, 2310.
(25) Andréasson, J.; Pischel, U.; Straight, S. D.; Moore, T. A.; Moore, A. L.; Gust, D. All-Photonic Multifunctional Molecular Logic Device. *J. Am. Chem. Soc.* **2011**, *133*, 11641–11648.
(26) Ren, J.; Tian, H. Thermally Stable Merocyanine Form of Photochromic Spiropyran with Aluminum Ion as a Reversible Photo-Driven Sensor in Aqueous Solution. *Sensors* . 2007.
(27) Zhang, M.; Hou, X.; Wang, J.; Tian, Y.; Fan, X.; Zhai, J.; Jiang, L. Light and PH Cooperative Nanofluidic Diode Using a Spiropyran-Functionalized Single Nanochannel. *Adv. Mater.* **2012**, *24*, 2424–2428.
(28) Maity, C.; Hendriksen, W. E.; van Esch, J. H.; Eelkema, R. Spatial Structuring of a Supramolecular Hydrogel by Using a Visible-Light Triggered Catalyst. *Angew. Chemie Int. Ed.* **2015**, *54*, 998–1001.
(29) Florea, L.; Diamond, D.; Benito-Lopez, F. Photo-Responsive Polymeric Structures Based on Spiropyran. *Macromol. Mater. Eng.* **2012**, *297*, 1148–1159.
(30) Samoylova, E.; Ceseracciu, L.; Allione, M.; Diaspro, A.; Barone, A. C.; Athanassiou, A. Photoinduced Variable Stiffness of Spiropyran-Based Composites. *Appl. Phys. Lett.* **2011**, *99*, 201905.
(31) Wang, J.; Han, Y. Tunable Multiresponsive Methacrylic Acid Based Inverse Opal Hydrogels Prepared by Controlling the Synthesis Conditions. *Langmuir* **2009**, *25*, 1855–1864.
(32) Kamenjicki Maurer, M.; Lednev, I. K.; Asher, S. A. Photoswitchable Spirobenzopyran-Based Photochemically Controlled Photonic Crystals. *Adv. Funct. Mater.* **2005**, *15*, 1401–1406.
(33) Zió\lkowski, B.; Florea, L.; Theobald, J.; Benito-Lopez, F.; Diamond, D. Porous Self-Protonating Spiropyran-Based NIPAAm Gels with Improved Reswelling Kinetics. *J. Mater. Sci.* **2016**, *51*, 1392–1399.
(34) Sugiura, S.; Sumaru, K.; Ohi, K.; Hiroki, K.; Takagi, T.; Kanamori, T. Photoresponsive Polymer Gel Microvalves Controlled by Local Light Irradiation.

Sensors Actuators A Phys. **2007**, *140*, 176–184.
(35) Kulawardana, E. U.; Kuruwita-Mudiyanselage, T.; Neckers, D. C. Dual Responsive Poly (N-Isopropylacrylamide) Hydrogels Having Spironaphthoxazines as Pendant Groups. *J. Polym. Sci. Part A Polym. Chem.* **2009**, *47*, 3318–3325.
(36) Stumpel, J. E.; Zió\lkowski, B.; Florea, L.; Diamond, D.; Broer, D. J.; Schenning, A. P. H. J. Photoswitchable Ratchet Surface Topographies Based on Self-Protonating Spiropyran--NIPAAM Hydrogels. *ACS Appl. Mater. Interfaces* **2014**, *6*, 7268–7274.
(37) Su, X.; Aprahamian, I. Hydrazone-Based Switches, Metallo-Assemblies and Sensors. *Chem. Soc. Rev.* **2014**, *43*, 1963–1981.
(38) Russew, M.-M.; Hecht, S. Photoswitches: From Molecules to Materials. *Adv. Mater.* **2010**, *22*, 3348–3360.
(39) Hines, L.; Petersen, K.; Lum, G. Z.; Sitti, M. Soft Actuators for Small-Scale Robotics. *Adv. Mater.* **2017**, *29*, 1603483.
(40) Klajn, R. Spiropyran-Based Dynamic Materials. *Chem. Soc. Rev.* **2014**, *43*, 148–184.
(41) Breslin, V. M.; Barbour, N. A.; Dang, D.-K.; Lopez, S. A.; Garcia-Garibay, M. A. Nanosecond Laser Flash Photolysis of a 6-Nitroindolinospiropyran in Solution and in Nanocrystalline Suspension under Single Excitation Conditions. *Photochem. Photobiol. Sci.* **2018**, *17*, 741–749.
(42) Chemical Retrieval on the Web (CROW). (polymerdatabase.com)
(43) Villafranca, A. B.; Saravanamuttu, K. An Experimental Study of the Dynamics and Temporal Evolution of Self-Trapped Laser Beams in a Photopolymerizable Organosiloxane. *J. Phys. Chem. C* **2008**, *112*, 17388–17396.
(44) Shoji, S.; Kawata, S.; Sukhorukov, A. A.; Kivshar, Y. S. Self-Written Waveguides in Photopolymerizable Resins. *Opt. Lett.* **2002**, *27*, 185–187.
(45) Malallah, R.; Li, H.; Muniraj, I.; Cassidy, D.; Al-Attar, N.; Healy, J. J.; Sheridan, J. T. Controlling the Trajectories of Self-Written Waveguides in Photopolymer. *J. Opt. Soc. Am. B* **2018**, *35*, 2046–2056.
(46) Kivshar, Y. S.; Agrawal, G. P. *Optical Solitons*; Academic Press, 2003.
(47) Yashin, V. V; Balazs, A. C. Theoretical and Computational Modeling of Self-Oscillating Polymer Gels. *J. Chem. Phys.* **2007**, *126*, 124707.
(48) Satoh, T.; Sumaru, K.; Takagi, T.; Kanamori, T. Fast-Reversible Light-Driven Hydrogels Consisting of Spirobenzopyran-Functionalized Poly (N-Isopropylacrylamide). *Soft Matter* **2011**, *7*, 8030–8034.
(49) Hammarson, M.; Nilsson, J. R.; Li, S.; Beke-Somfai, T.; Andréasson, J. Characterization of the Thermal and Photoinduced Reactions of Photochromic Spiropyrans in Aqueous Solution. *J. Phys. Chem. B* **2013**, *117*, 13561–13571.
(50) Sugiura, S.; Szilágyi, A.; Sumaru, K.; Hattori, K.; Takagi, T.; Filipcsei, G.; Zrínyi, M.; Kanamori, T. On-Demand Microfluidic Control by Micropatterned Light Irradiation of a Photoresponsive Hydrogel Sheet. *Lab Chip* **2009**, *9*, 196–198.
(51) Tork, a; Boudreault, F.; Roberge, M.; Ritcey, a M.; Lessard, R. a; Galstian, T. V. Photochromic Behavior of Spiropyran in Polymer Matrices. *Appl. Opt.* **2001**, *40*, 1180–1186.

(52) Villafranca, Ana; Saravanamuttu, K. Spontaneous and Sequential Transitions of a Gaussian Beam into Diffraction Rings, Single Ring and Circular Array of Filaments in a Photopolymer. *Opt. Express* **2011**, *19*, 15560–15573.
(53) Kuksenok, O.; Balazs, A. C. Modeling the Photoinduced Reconfiguration and Directed Motion of Polymer Gels. *Adv. Funct. Mater.* **2013**, *23*, 4601–4610.
(54) Hu, Y.; Zhao, X.; Vlassak, J. J.; Suo, Z. Using Indentation to Characterize the Poroelasticity of Gels. *Appl. Phys. Lett.* **2010**, *96*, 121904.
(55) Tolstik, E.; Kashin, O.; Matusevich, V.; Kowarschik, R. Broadening of the Light Self-Trapping Due to Thermal Defocusing in PQ-PMMA Polymeric Layers. *Opt. Express* **2011**, *19*, 2739–2747.
(56) Touloukian, Y. S.; Liley, P. E.; Saxena, S. C. *Thermophysical Properties of Matter. The TPRC Data Series.*; New York, 1970.

4 Interactions between collinear photochemically-formed self-trapped beams[§]

4.1 Abstract

Self-trapped beams suppress diffraction and maintain their shape as they propagate through light-induced changes in refractive index and can be generated in materials based on a photochemical response. The interactions between self-trapped beams within these materials rely on the spatial distribution of light and chemical species. We demonstrate that the interaction between two self-trapped beams of light is dependent on the spatial proximity of the beams relative to one another, the rate of the light-induced chemical changes in refractive index and the locality of the index change. These processes were investigated in two distinct types of optochemical systems relying on a photopolymerization and a photo-oxidation reaction. In one, polymerization of monomer units with a suitable photoinitiator results in permanently inscribed light-guiding structures – self-written waveguides that are embedded in the resin. The interaction between two self-trapped beams results in merging only when the beams are close; the output of light intensity revealed the swapping of beam positions within the self-inscribed waveguide due to the lens-like eyes that form in high intensity regions. These

[§]*In preparation*. The authors of the manuscript are Derek R. Morim, Ankita Shastri, Joanna Aizenberg, Ignacio Vargas-Baca and Kalaichelvi Saravanamuttu. Contribution: DRM, AS, KS designed, carried out and analysed data from experimental studies. DRM, IVB wrote the numerical model and carried out the simulations. DRM, JA, IVB, KS co-wrote the manuscript.

observations were supplemented with simulations that describe the behaviour of these high-index regions. In the second system, photo-oxidation of iodide to triiodide using a tris(bipyridine)ruthenium(II) catalyst within a Pluronic® F-127 gel creates a waveguide that dissipates over time due to equilibrium and diffusion processes. Nonlocal diffusion of triiodide from the photo-oxidation resulted in the nonlocal attraction of the beams over long periods of time. These studies demonstrate that self-trapping in optochemical systems is reliant on the mechanism and the associated rates of these processes dictate the behaviour of two beams interacting within.

4.2 Introduction

Spatial solitons and self-trapped beams are self-reinforcing waves capable of traveling long distances without divergence or significant changes to their intensity profiles.[1,2] Self-trapped beams form through the process of self-trapping when light both causes and responds to photo-induced refractive index changes and can be found in materials such as photorefractive crystals[3], Kerr media[4], atomic vapours[5] , liquid crystals[6–9] and photopolymers[10–13]. Optochemical systems such as photopolymers are able to change their refractive index (Δn) through photochemical reactions, eliciting non-instantaneous spatially varying and cumulative refractive index patterns that are dependent on the underlying chemistry within the system. Self-trapped beams can become permanently embedded waveguides within the material (i.e. photopolymers) or they may form and disappear once the optical field is removed (i.e. Kerr media). Photopolymers have been used to create individual self-written waveguides,[14–17] optical

interconnects[18,19] and microstructured lattices[20] and have been applied to holography,[17,21] computing,[22] photolithography,[23] and 3D printing.[24]

Self-trapped beams are able to interact with one another as a consequence of their ability to change the index within the materials they are travelling through. Two beams with partial overlap of their optical fields will induce changes that influence the other based on their self-induced gradients in refractive index, allowing them to guide or affect neighbouring beams.[25–27] The concept of interacting self-trapped beams in nonlinear materials would potentially allow for advanced signal processing by controlling the input and observing the output from the interaction. For example, soliton collisions have been used to develop logic operations governed by the change in beam position upon interaction with a second beam.[28] Behaviours ranging from soliton bending, fusion[29] and repulsion, to birth and annihilation[30] and even spiraling beams[27,31] have been studied. These responses tend to be localized to the incident optical field, such as those observed in Kerr media.[9] Nonlocal media, however, exhibit changes in refractive index that extend beyond the optical field. Rotschild et al. reported a lead glass which comprises a highly nonlocal nonlinear medium in which nonlinear interactions are propagated by thermal diffusion.[6] Liquid crystals also possess nonlocal responses mediated by dipole interactions between adjacent molecules – a light-induced reorientation of the liquid crystals results in twisting of neighbouring liquid crystals.[9] A reversible, photoresponsive spiropyran-functionalized hydrogel was recently shown to self-trap visible light through the contraction of the hydrogel matrix (Chapter 3). Within this system, two beams are able to influence each other remotely based on the contraction of the interconnected

network. Soliton interactions can also depend on distance between beams,[13] relative phase of beams,[32] intensity,[9] beam angles,[31] and medium response.[6,9] Intensity-dependent nonlinear systems tend to interact strongest when the diffracting optical profiles initially overlap.[33]

By monitoring changes to the optical profile over time, we investigated the dynamics of two interacting self-trapped beams in two different optochemical systems with different degrees of reversibility and locality: a photopolymerization and a photo-oxidation. The photopolymer system is comprised of Irgacure® 784 photoinitiator and 3-methacryloxypropyltrimethoxysilane (MAPTMS)[10] and the photo-oxidative system employs a tris(bipyridine)ruthenium(II) photocatalyst to oxidize iodide within a Pluronic® F-127 matrix (Chapter 2). The concept of interactions between self-trapped beams may present a method of all-optical logic operations between beams by exploiting the dynamic chemistries and index changes between beams.[22,26]

4.3 Results and discussion

4.3.1 Interactions between self-trapped beams in photopolymers: Experimental and theoretical

The following describes the interaction between two collinear, orthogonally-polarized laser beams of equal intensity and how the systematic alteration of the beam separation distances affects their behaviour within these non-instantaneous soft-matter systems. In the organosiloxane photopolymer, the light-induced polymerization causes an increase in density and associated increase in refractive index, which leads to self-

trapping of the laser beam and formation of a permanent waveguide[10]. Prior to optical self-trapping, this system is partially polymerized to make a viscous gel; otherwise, the rapid diffusion of monomers prevents the self-trapping process from occurring at nW powers (Supplementary 3.6.1). By altering the prepolymerization time, we can control the amount of remaining monomer available for the inscription process and thereby change the initial rate of polymerization during self-trapping. Less polymerized samples have been shown to exhibit a faster response time due to the availability of more monomer for polymerization.

A typical self-trapping experiment is conducted by focusing a 532 nm laser beam onto the entrance face of a sample containing photopolymer (Figure 4-1A, Supplementary 3.6.2). Light exiting the sample is imaged over time using a CCD camera to obtain spatiotemporal intensity plots of the beams. A single initially diffracted, 8 mW cm^{-2} Gaussian beam transformed into a self-trapped beam with an approximate width of 20 μm ($1/e^2$) at z = 6 mm within 50 s (Figure 4-1B). This process was confirmed to occur for each individual beam in the prepolymerized (8 min) sol. The titanocene photoinitiator initiates polymerization along its propagation path and the subsequent reactions give rise to spatial changes in the refractive index profile of the medium. The photochemical changes lead to a decrease in the beam diameter from ~120 μm to 20 μm – a 5-fold decrease in diameter.

In order to examine their interactions, two parallel beams were launched concurrently into the medium and continuously monitored at z = 6 mm. With a centre-to-centre separation of Δx = 50 μm (2.50x beam width), each beam self-trapped independently to

form two separate self-trapped beams (Figure 4-1C). The intensity of each beam at the beginning of this process is initially greatest near the entrance of the sample which consequently results in poor optical overlap between these beams (< 1%) throughout the self-trapping process. The correspondingly small refractive index changes between the beams allows for each self-written waveguide to develop separately.

As the beams are moved closer to one another (Δx = 25 μm; 1.25x beam width) such that greater partial optical overlap exists, the subsequent changes that occur are consistent with the beams interacting (Figure 4-1D). The initially diffracted beams decrease in size as the photoreaction progresses. The beams also appear to merge into a single waveguide, with the spatial position of the beams moving to the centre, followed by the reformation of each beam. The change from two individual beams to a single beam and back again occurs multiple times. The oscillation of the spatial position of each beam suggests that light from each beam is being guided by its co-propagating partner. These fluctuations in light intensity contribute to the overall refractive index changes that occur, but they do not indicate the refractive index pattern that has been inscribed in the medium.

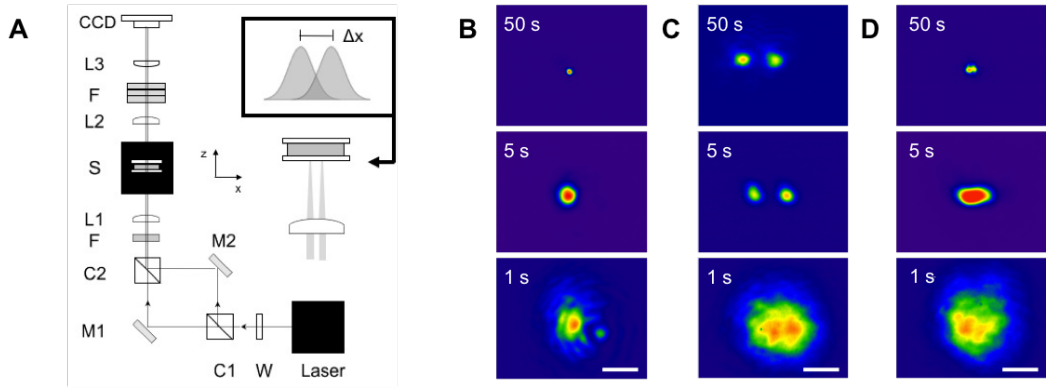

Figure 4-1 (A) (left) Optical assembly for self-trapping with (right) a zoomed-in view of the sample (CCD = charge coupled device camera; L1 = L2 = plano-convex lens with f.p. of 75.6 mm; L3 = plano-convex lens with f.p. of 250 mm; S = sample; F = filters; C1 = C2 = polarizing beamsplitter cube; M1 = M2 = mirror; W = λ/2 waveplate [10] and Δx represents the separation between the beams. (B-D) Spatial intensity profile of images collected at the exit face (z = 6 mm) of the sample during self-trapping experiments of (B) a single beam and two beams separated by Δx = (C) 50 μm and (D) 25 μm at select points in time within MAPTMS photopolymer. Scale bar = 50 μm.

In order to determine the corresponding refractive index profile for the given spatiotemporal intensity profiles, optical micrographs were obtained. The acquisition of optical micrographs required the use of a 5 mm glass cuvette and a change in the orientation of the beams from horizontal to vertical. The resultant trends in behavior of the beams was consistent with the results obtained from the horizontally positioned beams. Micrographs of the single beam and the beams separated by Δx = 50 μm (2.50x beam width) were shown to form separate channels that propagate independently (Figure 4-2A, B), matching the images of the spatial intensity profile (Figure 4-1B, C).

Micrographs of the organosiloxane with beams separated by Δx = 25 μm (1.25x beam width) illustrate that the beams merge into a single waveguide around z = 1.9 mm in samples prepolymerized for 10 min. Although there were fluctuations to the spatial intensity profile at the exit face throughout the self-trapping experiment, the

corresponding index profile show that the two beams have combined to form a single beam. The same procedure was carried out with two other samples: an organosiloxane-epoxy composite prepolymerized for 4 min, and MAPTMS that was prepolymerized for 12 min (Figure 4-7). The rate of oscillation in light intensity was slower for these two systems and resulted in the beams merging further along z (at 3.3 mm and 3.8 mm) (Figure 4-7). This behaviour suggests that slower polymerization kinetics results in different interaction behaviour, delaying the merging of the beams within the sample.

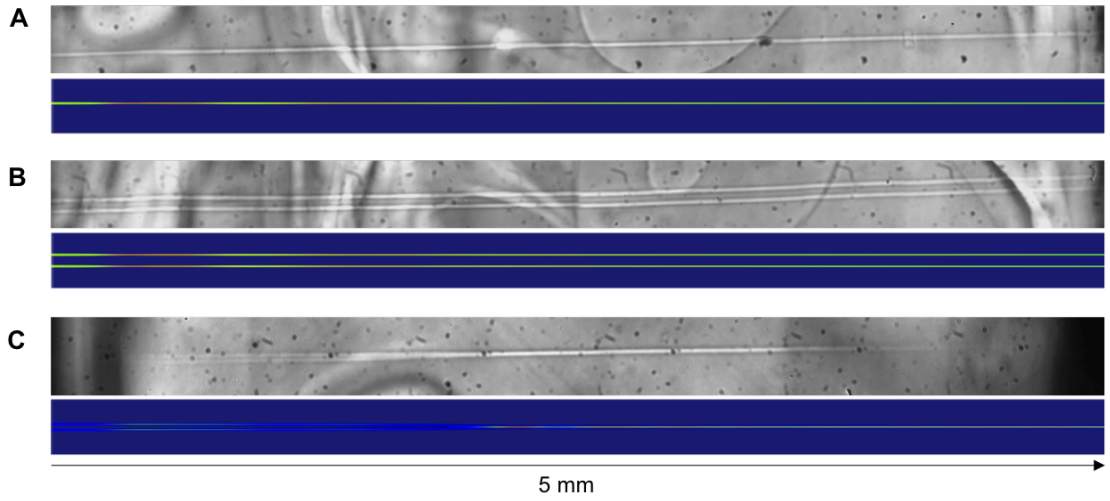

Figure 4-2 Optical micrographs (top) and simulated refractive index profiles (bottom) of (A) a single beam and two beams separated by (B) Δx = 50 μm (2.50x beam width) and (C) Δx = 25 μm (1.25x beam width). Samples were prepolymerized for 10 min at 1.5 mW. Simulations utilized an exposure time of 125 s and an A-parameter of $1x10^{-6}$ cm^2 mW^{-1} s^{-1}; path length of z = 5 mm; I = 8 mW cm^{-2}.

This observation is consistent with the rapid rates in Kerr media which often result in merging very early on – the near-instantaneous response causes each beam to interact strongly throughout propagation.[27] Within liquid crystals, intensity-dependent interactions have illustrated that higher intensities often result in the interaction occurring earlier along the propagation direction.[7,9] Larger or more rapid refractive index changes appear

to cause the merging and interaction of two self-trapped beams to be stronger. The intensity-dependence of this interaction was not studied in detail within our organosiloxane as higher intensities can result in effects such as self-phase modulation and the formation of higher order modes, rings and filaments.[34–36]

Simulations were carried out using a model that solves for the optical profile using (eq 4.1) and uses the spatial intensity profile obtained ($(x,z) = |E(x,z)|^2$) to be related to an updated refractive index (eq 4.2):

$$ik_0 n_0 \frac{\partial \varepsilon}{\partial z} + \frac{1}{2}\nabla_t^2 \varepsilon + k_0^2 n_0 \Delta n \varepsilon + \frac{i}{2} k_0 n_0 \alpha \varepsilon = 0 \quad (4.1)$$

where the electric field amplitude (E) can be described in terms of the free-space wavenumber of the optical field (k_0), the attenuation coefficient of the medium (α), and nonlinear refractive index changes inherent in the material's response to light (Δn)[37–39] and:

$$\frac{\partial \Delta n(\mathrm{x,z,t})}{\partial t} = A\, I(x,z,t)^p \left(1 - \frac{\Delta n(x,z,t)}{\Delta n_s}\right) \quad (4.2)$$

where a material-dependent A-parameter is related to the initial rate of increase. As the refractive index changes, Δn, approaches the saturable index change, Δn_s, the development in index over time approaches zero. These changes are also linear with respect to the intensity ($I(x,z,t)$) provided that the photoexcitation is a one-photon process ($p = 1$).[11,14,40–43] Full details into these simulations can be found in Supplementary 4.6.4. The behaviour of the distance-dependent interactions shows qualitative agreement with an A-parameter of 1 x 10^{-6} cm^2/mWs, with only the $\Delta x = 25$ μm beams merging into a single waveguide.

To better understand the temporal development of two beams with $\Delta x = 25$ µm (1.25x beam width), individual beam blocking experiments were performed during the development of each self-trapped beam. Each beam was rapidly blocked throughout the experiment in an 8 min (Figure 4-3; Supplementary 4.6.5) prepolymerized sample of MAPTMS. Throughout the development of these self-written waveguides separated by $\Delta x = 25$ µm, one of the beams was blocked in order to observe the spatial position of the complementary beam. The close proximity of the beams often makes it difficult to identify an individual beam in the CCD images without blocking. Blocking of beams in an organosiloxane with a path length of 6 mm revealed that the two beams swap positions twice during the self-trapping process within the first 50 s (Figure 4-3).

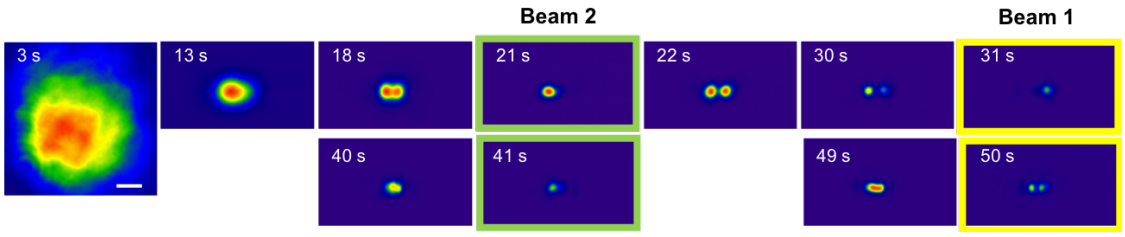

Figure 4-3 2D spatial intensity profiles collected at the exit face of the sample during self-trapping experiments ($I = 8$ mW cm^{-2}) of two beams separated by $\Delta x = 25$ µm at select points in time within MAPTMS photopolymer prepolymerized for 8 min with one beam blocked rapidly throughout (green box = beam 1 blocked; yellow box = beam 2 blocked). Scale bar = 25 µm.

Beam 2 (green, originally on the right) at 21 s is positioned on the left relative to the opposite beam. At 31 s, Beam 1 (yellow, originally on the left) is found on the right. At 41 s, Beam 2 is still positioned on the left and at 50 s, the intensity of the first beam appears to be coupled into both beams. The same switching behaviour occurs in a sample that was prepolymerized for 5 min, albeit at a faster rate and resulted in 3 swapping

events (Figure 4-8; Supplementary 4.6.5). This behaviour demonstrates the additive effect of overlapping intensity on interactions between beams that are in close proximity to one another.

Simulations were carried out to better understand this phenomenon and suggest that regions of higher refractive index along the propagation path – often referred to as eyes – form and act as lenses that influence the two beams after they have merged (Figure 4-4A).[14] Within the intensity simulations (Figure 4-4B), the primary eye is observed at iteration 17 s with a secondary eye observed at 33 s. These eyes act as lenses that cause the beams to swap positions. Simulations of individual beams launched into index profiles written by two beams illustrates that the position of each beam changes position at the exit face of the sample as time progresses (Figure 4-4C, D).

The formation of eyes occurs in materials that possess cumulative refractive index changes such as photopolymers and photosensitive glasses.[14,44–47] The point of maximum intensity generates a primary eye – often a precursor to waveguide formation – and moves further along z as time progresses.[44,47] For individual beams, this maximum occurs near the entrance of the sample, but the maximum for two beams with $\Delta x = 25$ μm (1.25x beam width) occurs in the region of overlap between the beams (Figure 4-4E). Primary eye formation is followed by the formation of secondary eyes from other high intensity regions along the waveguide. The spacing between eyes in one-photon systems tends to be nearly equal based on past studies carried out with single beams.[44,46,47]

The refractive index increases that occur during eye formation creates a gradient-index lens on the input beam.[44] As time progresses, the refractive index continues to

increase, and the associated focal length of that lens decreases. This results in the secondary maximum shifting towards the entrance face along z. This was observed in simulations with the 1st 2° eye shifting significantly to the left as time progresses (Figure 4-4E). The formation of these eyes explains the swapping behaviour of the beam positions as self-trapping occurs. Each eye acts as a lens and inverts the position of the beams in the merged waveguide; similar to a Fourier Transform that inverts the image.[14] As new eyes form along the growing waveguide, the two beams switch positions again, which is also evident in the 5 min prepolymerized sample (Supplementary 4.6.5).

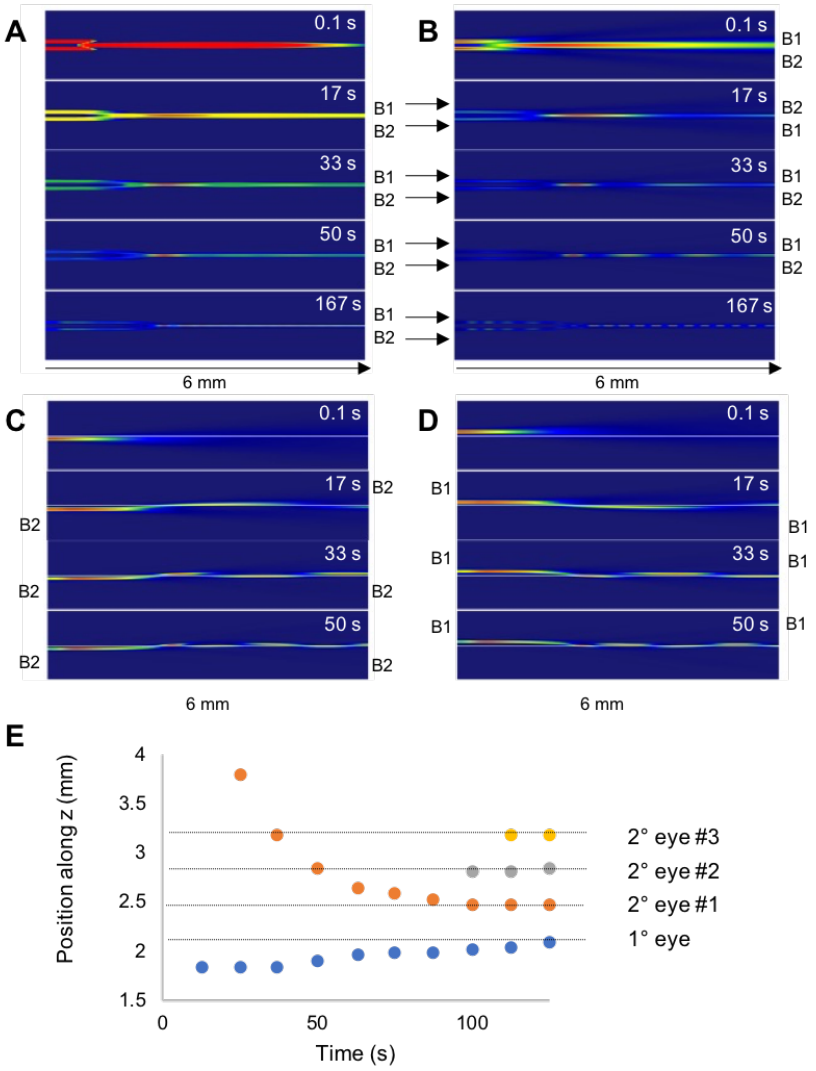

Figure 4-4 (A) Refractive index profiles for two interacting beams separated by 25 µm using A = 1 x 10^{-6} cm^2 mW^{-1} s^{-1} at 8 mW cm^{-2} input intensity , and the corresponding intensity profiles launched into those refractive index patterns: (B) both beams , (C) beam 2 and (D) beam 1. Dotted line in C and D indicates the centre point between the beams. Each eye that forms throughout the self-trapping process acts like a lens capable of swapping the positions of the beams. (E) Plot tracking the positions of eye formation during the self-trapping process. Dotted lined indicates final position of eyes at 125 s.

From simulations, we have observed that larger A-parameters result in beams merging earlier along z (Figure 4-7). By adjusting the rate of polymerization, we can tailor the interaction of the beams separated by 25 µm. An A-parameter of 8 x

10^{-7} cm^2/mWs, for example, demonstrates that a slower rate of index change given the same exposure time, results in a refractive index profile where the beams merge further along z (Supplementary 4.6.5).

4.3.2 Interactions between self-trapped beams in Pluronic® F-127 with $Ru(bpy)_3^{2+}$ and NaI: Experimental

Pluronic® F-127 containing $Ru(bpy)_3^{2+}$ and sodium iodide constitutes a photochemical system that results in a refractive index change that dissipates over time. A self-trapped beam within this material erases in 2000 s after 200 s of light exposure at 25 μW (Chapter 2). $Ru(bpy)_3^{2+}$ becomes excited to a reactive triplet state by the irradiation of visible light; this excited species reacts with iodide and ultimately leads to the generation of triiodide due to a photo-oxidation reaction.[48, 49] The Pluronic® F-127 hydrogel decreases diffusion of the chemical species within, localizing the initial index changes and allowing self-trapping to occur.

Irradiation with a focused laser beam of 20 μm results in self-focusing and formation of a self-trapped beam in less than 1 min at 8 W cm^{-2} (Figure 4-5A; Chapter 2). Two self-trapped beams travelling within this system initially interact in a local fashion; interactions are not observed within the first 50 s with Δx = 80 μm (4.00x beam width) and 50 μm (2.50x beam width) (Figure 4-5B,C). Although two beams separated by Δx = 50 μm do no interact over short time scales, they do move closer to one another over thousands of seconds. The iodide-triiodide equilibrium leads to diffusion due to a Grotthuss-like exchange mechanism that occurs over a longer time scale relative to

triiodide formation.[50] The diffusion of triiodide creates a nonlocal refractive index gradient that becomes apparent when the beams are separated by $\Delta x = 50$ μm (2.50x beam width). The spatial positions of the beams shift towards one another and illustrate a nonlocal attraction between the beams. There exists a larger concentration of triiodide between the beams relative to the periphery of the beams, as both beams produce triiodide that can diffuse into the region between the beams. The gradient in refractive index results in the nonlocal attraction and is highly reminiscent of other nonlocal systems (liquid crystals and the photothermal glass).[6,9]

At $\Delta x = 25$ μm (1.25x beam width), the beams swap positions once within the first minute due to primary eye formation (Figure 4-5D). The beams remain in the same relative position throughout the remainder of the experiment, and eventually move further apart from one another at the exit face. Diffusion within this system only permits the cumulative buildup of the primary eye, with secondary eye formation being slow relative to diffusion. This permits a single inversion to occur and explains why the beams swap positions only once, unlike in the photopolymer MAPTMS where the cumulative formation of eyes along the merged waveguide results in multiple swapping events due to multiple eyes.

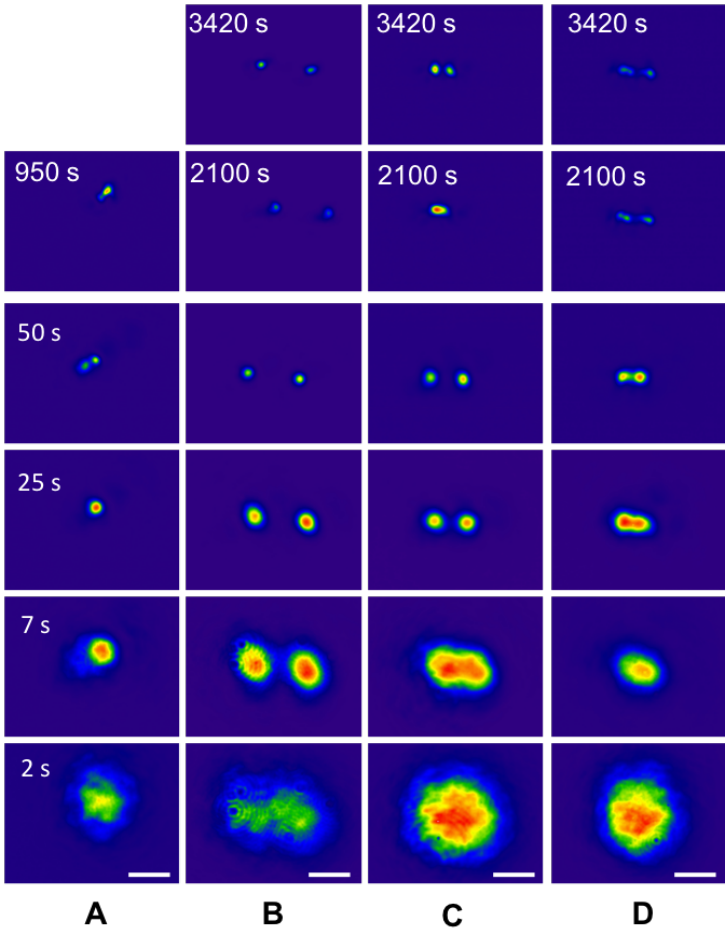

Figure 4-5 Spatial intensity profile of images collected at the exit face of the sample during self-trapping experiments of (A) a single beam and two beams separated by Δx = (B) 80 µm, (C) 50 µm and (D) 25 µm at select points in time within the doped Pluronic® F-127 gel. Scale bar = 50 µm.

The diffusive nature of this system underlies its nonlocal refractive index change and is responsible for the nonlocal attraction of the beams that we observe. We are unable to confirm the refractive index profile within these samples because the resulting structures do not provide enough index contrast for microscopy and dissipate over time, so the spatiotemporal profiles from the CCD camera were used. The chemical kinetics of this system were approximated based on the times taken to reach a stable self-trapped beam without accounting for diffusion (Supplementary 4.6.5). Chemical systems with

more rapid diffusion coefficients may provide an interesting platform for studying nonlocal interactions further.

4.4 Conclusions

Time-dependent interactions between two self-trapped beams in two separate photoresponsive systems have been studied. The type of interaction is dependent on the underlying reactions and their kinetics. Two orthogonally polarized self-trapped beams in close proximity ($\Delta x = 25$ μm; 1.25x beam width) merge into a single waveguide and high-index eyes along the waveguide swap the positions of the beams. Due to its diffusive nature, only a single eye forms within doped Pluronic® F-127 gels.

As the beams are moved apart ($\Delta x = 50$ μm; 2.50x beam width), there is less overlapping intensity between the initially diffractive beams, resulting in beams that do not interact within the first 50 s. The Grotthuss mechanism within the Pluronic® F-127 gels allows the beams to interact over long timescales due to an increased nonlocal response. Enhancing the nonlocal response with a more diffusive system may enable interactions between beams separated by greater distances.

Simulations exhibit qualitative agreement with the experimental results in the photopolymer system and also reveal that the lens-like eyes that develop along the growing waveguide are responsible for the inversion of the beam positions along z throughout the self-trapping process. The separation-dependent interactions were shown to depend on the kinetics of the system, and the corresponding A-parameters simulated were related to the chemical kinetics.

Materials that change in response to an input can produce a particular output based on a mathematical operation. For example, metastructures have been designed to solve equations;[51] broad beams in photopolymers have been observed to transfer information between beams based on the ordering of the output beam filaments;[22] changes to beam position have been observed based on interacting beams in photorefractive crystals.[52] The all-optical manipulation of light in photoresponsive media may be realized by increasing the complexity (e.g. Gaussian, Bessel, Laguerre-Gauss beams) and number of input beams, and using new materials with different, perhaps even spatially varying or anisotropic, responses. Visualization of the output and determining its relationship to the optical inputs would provide a means of transforming light with light.

4.5 Acknowledgements

Financial support was provided by the Natural Sciences and Engineering Research Council of Canada, the Canada Foundation for Innovation, and the Ontario Innovation Trust.

4.6 Supplementary information

4.6.1 Preparation of samples

4.6.1.1 Materials

3-Methacryloxypropyltrimethoxysilane (MAPTMS), 0.1 N hydrochloric acid, 2,4-Epoxycyclohexylmethyl 3,4-epoxycyclohexanecarboxylate, Poly(tetrahydrofuran), Camphorquinone, Pluronic® F-127 polymer, and sodium iodide were purchased from Millipore Sigma. Irgacure® 784 (Bis(η5-cyclopentadien-1-yl)-bis(2,6-difluoro-3-(1H-

pyrrol-1-yl)-phenyl) titanium(IV) (max = 393 nm, 460 nm) obtained from Ciba Specialty Chemicals Inc. Tris(bipyridine)ruthenium(II) chloride hexahydrate was obtained from Strem Chemicals Inc. (4-octyloxyphenyl) phenyliodonium hexafluoroantimonate (OPPI) purchased from Hampford Research Inc. Epoxypropoxypropyl terminated polydimethylsiloxane was purchased from Gelest.

4.6.1.2 Preparation of 3-Methacryloxypropyltrimethoxysilane (MAPTMS) photopolymer

The photopolymerizable organosiloxane photopolymer was prepared through acid-catalyzed hydrolysis and condensation of 3-methacryloxypropyltrimethoxysilane. 0.3 g (1.5×10^{-5} mol) of 0.05 N hydrochloric acid (diluted from a standardized 0.1 N HCl aqueous solution) was added to 4.9 g (0.020 mol) of MAPTMS. Magnetic stirring transformed the phase-separated mixture into a homogeneous, transparent, colourless fluid. The sol was sensitized to visible light by adding 0.027 g of Irgacure® 784 (bis(η5-cyclopentadien-1-yl)-bis(2,6-difluoro-3-(1H-pyrrol-1-yl)-phenyl) titanium(IV), a free-radical photoinitiator. The sol was shielded from ambient light by aluminum foil and stirred continuously for a minimum of 16 h. As the hydrolysis and polycondensation reaction occurs, the refractive index gradually increases. In order to maintain consistency, samples were used between 5-7 days after initial preparation. For self-trapping experiments, 1.0 mL of photosensitized sol was injected through a small opening into a cylindrical cell (z = 6 mm) with flat and transparent windows. The cell consisted of microscope coverslips (25 x 25 mm) glued onto both sides of a 6 mm Delrin® ring with an external diameter of 16 mm. The organosiloxane sol was then uniformly irradiated in a

fabricated irradiation chamber with an aluminum foil interior to evenly distribute the light onto the sample. White light from a quartz-tungsten-halogen lamp (3 mW, Cole-Parmer 09790-series) was directed into the chamber for 8 min, causing partial polymerization of methacrylate groups, and converting the liquid into a gel. Micrographs were obtained in z = 5 mm glass cuvettes; irradiation conditions were adjusted such that 0.3 mL was irradiated for 10 min at 1.5 mW, taking care to ensure no microstructures formed within the sample through modulation instability.[53]

4.6.1.3 Preparation of organosilane:epoxy hybrid (MAPOXY)

2.5 g Epoxycyclohexylmethyl 3,4-epoxycyclohexanecarboxylate, 1.3 g epoxypropoxypropyl terminated polydimethylsiloxane, 1 g poly(tetrahydrofuran), 100 mg camphorquinone, and 100 mg (4-octyloxyphenyl) phenyliodonium hexafluoroantimonate (OPPI) were stirred together for 12 days while shielded by aluminum foil. This epoxy mixture was combined with 6-day-old MAPTMS in a ratio of 3:7 (i.e. 3 parts epoxy: 7 parts organosiloxane). This hybrid mixture was stirred for 1 hour before use. This hybrid photopolymer was formulated in order to increase the viscosity of the medium and decrease the prepolymerization time. Prepolymerization of 0.3 mL MAPOXY in a 5 mm (z dimension) glass cuvette was performed by irradiating at 1.5 mW for 4 min.

4.6.1.4 Preparation of doped Pluronic® F-127 hydrogels

A solution of 1.3 mM $Ru(bpy)_3Cl_2$ and 0.2 M NaI was prepared using deionized water (Milli-Q®, 18.2 MΩcm). 1.0 g of Pluronic® F-127 was added to 3 mL of this solution. This mixture of Pluronic® F-127 polymer was cooled below its lower critical solution temperature (LCST) using an ice bath and mixed with a glass rod to solubilize the polymer. The sample was

then injected into the opening of a 6 mm ring cell while cold. Equilibration to room temperature resulted in the formation of a gel due to the dehydration of the PPO segments of the triblock copolymer.

4.6.2 Experimental setup for self-trapping

Self-trapping experiments were carried out on an optical assembly adapted from previous studies (Figure 4-1).[10] The excitation source was the TEM_{00} mode (Gaussian beam, $M^2 < 1.1$) of c.w. visible ($\lambda = 532$ nm) light emitted by a diode-pumped solid-state laser (Verdi V2, Coherent, Inc., California, USA). The output beam, which had a diameter 2.25 mm and power of 500 mW, was passed through a $\lambda/2$ waveplate and split into two beams of equal intensity using a polarizing beam splitter cube. The beams were directed by mirrors and a second beam splitter cube, through a set of filters and through a planoconvex lens (focal length = 75.6 mm), which focused the beams to a diameter of 20 μm onto the entrance window of the sample cell. The separation distance (Δx) and angles between the focused beams were adjusted with the beam splitter mounts. The setup produced two orthogonally polarized beams of light that are parallel to one another and coplanar in y.

The spatial intensity profile of the beam at the exit face of the cell was imaged by a pair of planoconvex lenses (f. l. = 75.6 mm and f. l. = 250.0 mm) onto a charge-coupled device (CCD) camera (2040 horizontal × 1532 vertical pixels; pixel size = 3.20 μm x 3.20 μm; WinCamD XHR, DataRay Inc., California, USA). Combinations of neutral density filters (F) mounted on three separate rotatable wheels (VARM, Coherent, Inc.) were

placed between imaging lenses to prevent saturation of the CCD camera. All imaging optical components could be translated along the z direction with a resolution of 0.25 mm. Images were collected every second. The camera used Data Ray software (Version 7.1H25Bk), which calculates beam diameter ($1/e^2$) and relative peak intensity, generates two-dimensional (2D) and three-dimensional (3D) intensity profiles and corrects for image magnification by the lenses (×3.3). The effective beam diameter corresponds to the circular area of all pixels with relative intensity > 13.5% ($1/e^2$) of the maximum (peak) intensity. The relative peak intensity is the ratio between the greatest intensity on one or more pixels in an image and the saturation intensity of the camera. Plots of spatial intensity profiles of the beam were generated with Python v2.7 (modules: os, scipy, numpy, matplotlib).

4.6.3 Material characterization

4.6.3.1 Optical microscopy

Samples that were prepared in 5 mm glass cuvettes were imaged with an optical microscope (Olympus BX51) under transmission mode to visualize the waveguide structures obtained from the self-trapping process (MAPOXY, 4 min, 1.5 mW; MAPTMS, 10 min and 12 min, 1.5 mW).

4.6.3.2 Shore hardness

Shore hardness measurements were performed on photopolymerized, cylindrical MAPTMS samples (thickness: 6 mm; diameter; 15 mm) with prepolymerization times of

5, 8, 12, and 30 min at 3 mW. A Shore OO durometer was used to take multiple measurements to compare the hardness of samples polymerized for different times.

4.6.3.3 Refractive index measurements

The refractive index of the MAPTMS sol prior to prepolymerization was measured using a refractometer (ABBE-3L^{TM}, Fisher). A precise value of the prepolymerized refractive index was difficult to obtain as a gel, therefore the literature values for MAPTMS films of $n_0 = 1.460$ and $\Delta n = 0.006$ were used for simulations.[54]

4.6.3.4 UV-Visible spectroscopy

The UV-Visible spectrum was acquired for MAPTMS samples on a Cary50 Spectrophotometer (Agilent Technologies) in 1 cm path length cuvettes. Kinetic studies were performed by monitoring the changes in absorbance over time for an irradiated sample.

4.6.4 Simulations

The description of light in space can be obtained from solving the paraxial wave equation that assumes small changes along z (eq 4.1), where the electric field amplitude (E) can be described in terms of the free-space wavenumber of the optical field (k_0), the attenuation coefficient of the medium (α), and nonlinear refractive index changes inherent in the material's response to light (Δn).[37–39]

$$ik_0 n_0 \frac{\partial \varepsilon}{\partial z} + \frac{1}{2}\nabla_t^2 \varepsilon + k_0^2 n_0 \Delta n \varepsilon + \frac{i}{2} k_0 n_0 \alpha \varepsilon = 0 \qquad (4.1)$$

The transverse profile of light ($\nabla_{\perp}^{2} = \partial^2/\partial x^2 + \partial^2/\partial y^2$) changes with the changes in photo-induced refractive index – self-focusing of the beam occurs as the refractive index increases. The beam propagation method (BPM) is a technique often implemented for modelling fiber optic photonic devices and uses the slowly varying envelope approximation. These simulations were carried out by combining simulations of the spatial intensity profile (eq 4.1) using BeamProp™ software (RSoft™) with a model used for saturable systems (eq. 4.2).

$$\frac{\partial \Delta \mathrm{n(x,y,z,t)}}{\partial t} = AI(x,y,z,t)^{p}\left(1 - \frac{\Delta n(x,y,z,t)}{\Delta n_s}\right) \tag{4.2}$$

The initial refractive index (n_0) is set as homogeneous and the attenuation of the medium (α) determined using UV-visible spectroscopy. Simulations were carried out with the phenomenological model employing a material-dependent A-parameter and later related to the chemical kinetics of each system (Supplementary 4.6.5 and 4.6.6).[11,14,40–42] As the refractive index Δn approaches the saturable index, Δn_s, the changes in index over time approaches zero. These changes are also linear with respect to the intensity ($I(x,z,y,t)$) provided that the photoexcitation is a one-photon process ($p = 1$).[11,14,40–43]

The program BeamProp™ was used to solve for the electric field amplitude, E, given a particular refractive index, $n(x,z)$. The problem is formulated using a scalar field (i.e. omitting polarization effects) and incorporating paraxiality (i.e. propagation angles restricted). The geometry of the problem is dependent on the refractive index distribution, $n(x,z)$, and the input Gaussian wave field, which is submitted into the simulation. There

are advantages and disadvantages associated with the assumptions implemented in BeamProp™ software. The assumption of the slowly varying field allows for coarser numerical simulations, allowing for higher efficiency. This assumption can be made due to the noninstantaneous nature of the medium (i.e. the response rate << rate phase variation). The above simplification also converts a second order boundary problem to a first order initial value problem, the efficiency of which is dictated by the number of longitudinal grid points (Nz). The Crank-Nicolson method is a finite difference method that is used by the software to solve the wave equation along the propagation directions (z) in a stepwise fashion. This improves the accuracy of the simulation at points far from the beam input along z.[55–57]

The following simulations investigate two orthogonally polarized beams. The resultant electric field amplitude obtained from (eq 4.1) can be converted to an intensity distribution via: $I(x,z) = |E(x,z)|^2$. This intensity distribution can be related to a new refractive index profile according to a phenomenological model (eq 4.2) which employs a parameter (A) that is dependent on a material's properties. This parameter is dependent on the kinetics of the various processes that results in a changing refractive index (i.e. rate constants associated with photoinitiation, propagation, and termination). The refractive index change is a saturable process and approaches a maximum index change, Δn_s, which accounts for the depletion of reactive monomers and the formation of a permanent structure. The new refractive index obtained from this equation can be updated and reintroduced into eq 4.1. This process was done iteratively and also allowed for snapshots

of the intensity and index distributions in the material at several exposure times. The associated parameters for the simulations are included in Table 4-1.

Table 4-1 Parameter values used for simulations

Parameter	Value Used
λ	532 nm
I	8 mW cm^{-2}
w_0	20 μm
Nx	2000
Nz	60
n_0	1.46
Δn_s	0.006
dt	0.125 s
A-parameters	1x 10^{-6} cm^2 mW^{-1} s^{-1} 8 x 10^{-7} cm^2 mW^{-1} s^{-1}

Simulations were carried out on a single beam and two beams separated by $\Delta x = 25$ μm (1.25x beam width) and $\Delta x = 50$ μm (2.50x beam width). For Figure 4-4 C,D, the refractive index profiles from select time points from a two-beam self-trapping simulation were used to launch a single beam into the structure. This virtual beam blocking experiment was done to confirm the swapping of the beam positions at the exit face of the sample ($\Delta x = 25$ μm) as the eyes form.

4.6.5 Influence of chemical kinetics on self-trapping behaviour: Photopolymerization

Simulations of an individual beam launched into a medium with a refractive index of 1.460, a maximum refractive index of 1.466, an intensity of 8 mW cm^{-2}, and an A-parameter of 1 x 10^{-6} cm^2 mW^{-1} s^{-1} were carried out. The corresponding refractive index and intensity plots at select points in time illustrate the behaviour of the beam as self-trapping occurs (Figure 4-6 A,B). The same conditions were used to simulate two beams separated by 50 µm (2.50x beam width) (Figure 4-6 C,D)

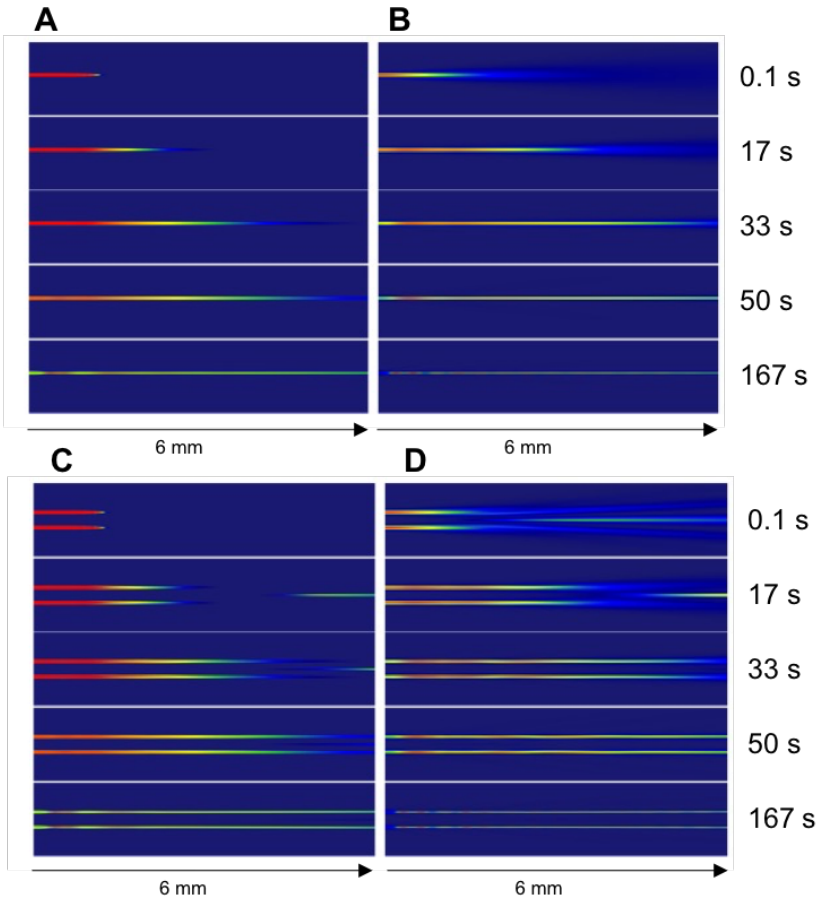

Figure 4-6 Simulated profiles of (A) refractive index and (B) intensity of a single 20 µm beam with an A-parameter of 1 x 10^{-6} cm^2 mW^{-1} s^{-1} and (C, D) the corresponding profiles of 2 beams separated by 50 µm (2.50x beam width).

Simulations of two beams separated by 25 μm with A-parameters of 1×10^{-6} cm^2 mW^{-1} s^{-1} and 8×10^{-7} cm^2 mW^{-1} s^{-1} irradiated for 125 s revealed that the point of merging between the beams can vary depending on the kinetics. Slower kinetics resulted in the beams merging further along z. Optical micrographs within a hybrid photopolymer (MAPOXY) and in MAPTMS with less available monomer (12 min prepolymerization) resulted in micrographs where the merging of the beams occurred further along z in the slower sample containing less monomer.

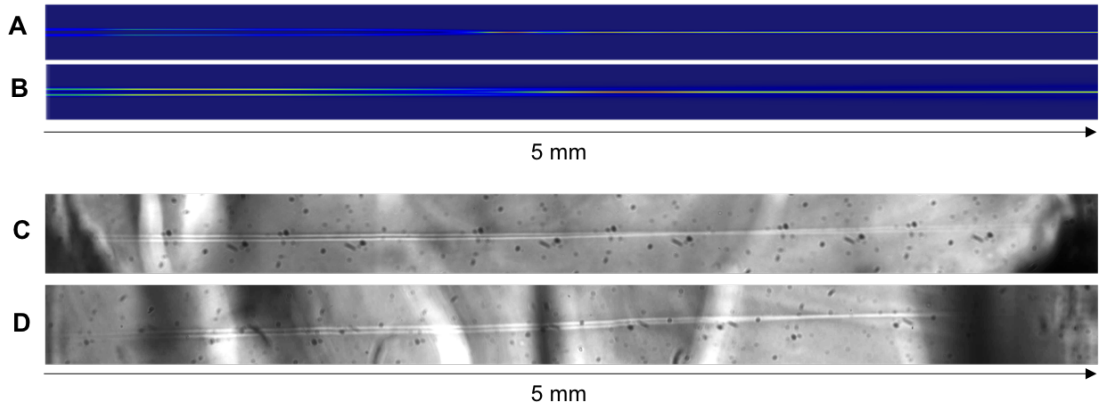

Figure 4-7 Simulated refractive index profiles of 25 μm separated beams with A-parameters of (A) 1×10^{-6} cm^2 mW^{-1} s^{-1} and (B) 8×10^{-7} cm^2 mW^{-1} s^{-1} exposed for 125 s. Optical micrographs illustrating the refractive index profiles of (C) MAPOXY prepolymerized for 4 min and (D) MAPTMS prepolymerized for 12 min. Structures in (C) and (D) were both formed from 125 s of irradiation at 8 mW cm^{-2}.

The swapping of beam positions in two separate MAPTMS samples ($\Delta x = 25$ μm) revealed that faster swapping occurs in samples with more available monomer (prepolymerization time = 5 min) due to the faster merging of the beams and subsequent formation of eyes within the shared waveguide (Figure 4-8).

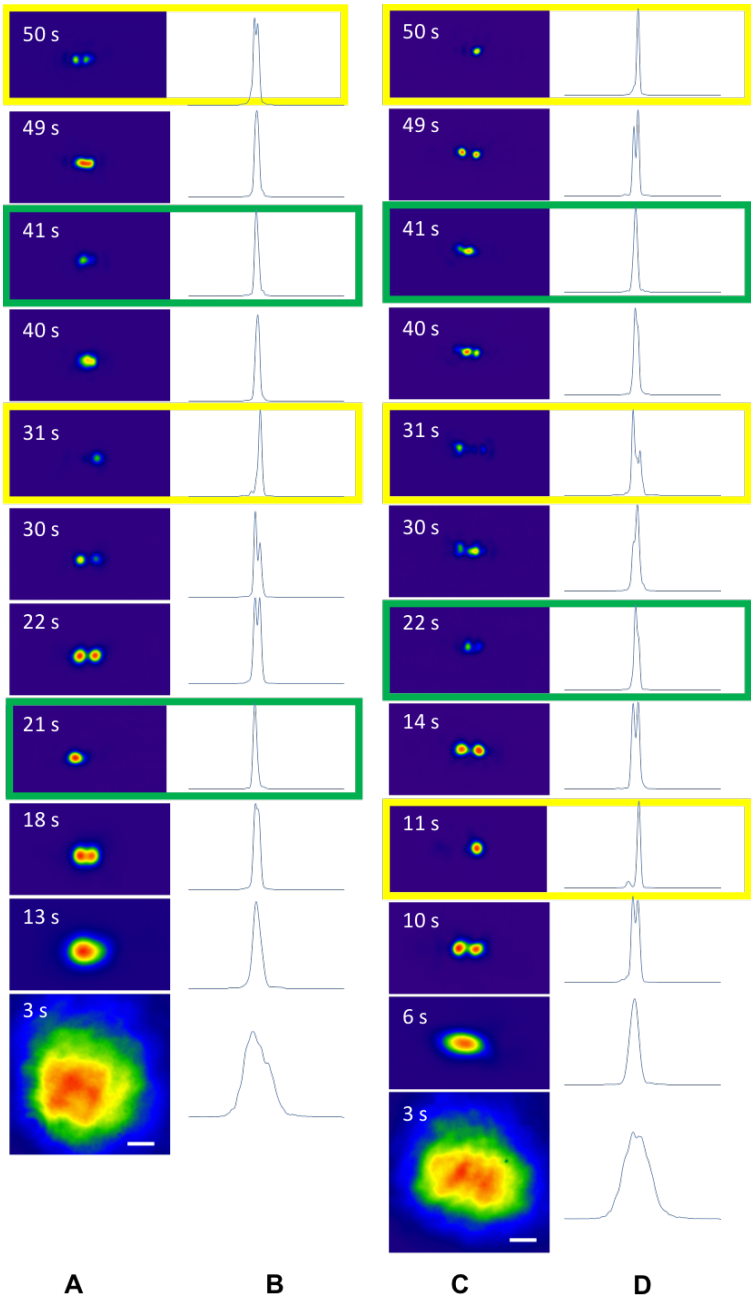

Figure 4-8 2D (A, C) XY spatial intensity profiles and corresponding intensity plots along X through the centroid (B and D) collected at the exit face of the sample during self-trapping experiments (I = 8 mW cm^{-2}) of two beams separated by Δx = 25 μm at select points in time within MAPTMS photopolymer prepolymerized for (A, B) 8 minutes and (C, D) 5 min with one beam blocked rapidly throughout (green box = beam 1 blocked; blue box = beam 2 blocked). Scale bar = 25 μm.

Shore Hardness for gels irradiated for times of 5, 8, 12, and 30 min at 3 mW were acquired and resulted in Shore OO values of 73, 78, 88, and 71, respectively. At 5 and 8 min, the resulting gels still have large amounts of monomer available for polymerization. At 12 min, there is less available monomer, resulting in significantly slower changes to the beam profile during self-trapping experiments. At 30 min, the Shore Hardness had decreased significantly, owing to the increasingly brittle nature of the sample from excessive crosslinking. Samples were not irradiated to the point of saturation for this reason.

Refractive index measurements of the hydrolyzed organosiloxane gave a value of 1.4265 for 6-day old sample, and continued to increase daily, likely due to partial escape of methanol from the vial over time and formation of larger molecular weight oligomers from crosslinking (Figure 4-9). These studied were performed to determine an ideal time to leave samples which allowed consistency.

The refractive index of this system has been previously reported at 1.46 with a change to 1.466 after photopolymerization of a film.[14] These values were used for simulations since we were unable to obtain the refractive index of prepolymerized samples. The absorbance of the sample prior to self-trapping is 0.36 at 532 nm for a 6 mm sample based on UV-Vis spectroscopy.

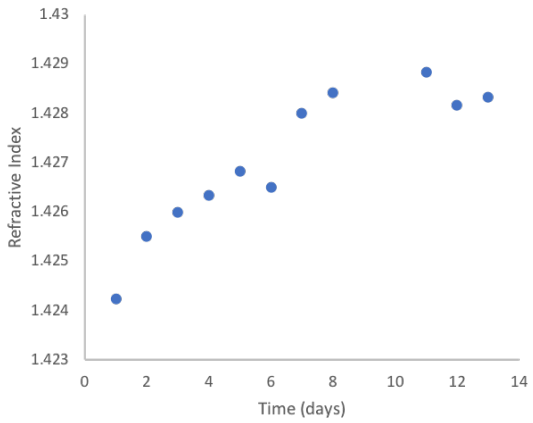

Figure 4-9 The refractive index of MAPTMS taken on an Abbe refractometer at sodium D-line over time during hydrolysis without prepolymerization.

By monitoring the UV-visible absorbance spectrum of a sample of MAPTMS irradiated at 20 mW (λ = 532 nm) for 45 s, a quantum yield of 0.52 (Figure 4-11A) was obtained for Irgacure® 784 within this photopolymer environment according to eq 4.6.

$$\frac{\partial[PI]}{\partial t} = -\phi|E|^2[1 - \exp(-\varepsilon l[PI])] \tag{4.6}$$

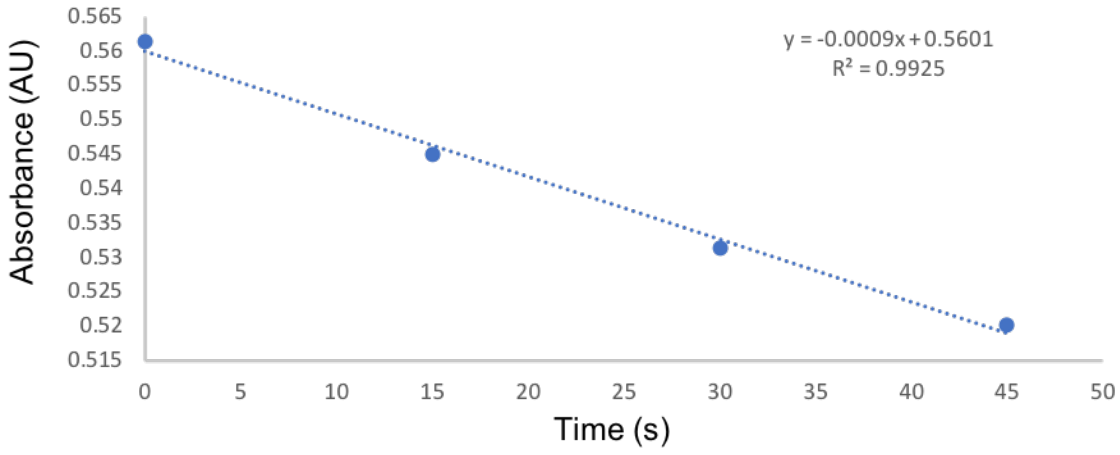

Figure 4-10 Absorbance of Irgacure® 784 in MAPTMS after irradiation at 20 mW (λ = 532 nm).

As photopolymerization occurs, monomer is depleted, and the rate of polymerization can be described by the depletion of monomer (eq 4.7) based on steady state kinetics.

$$\frac{\partial[M]}{\partial t} = \frac{k_p}{k_t^{0.5}}[M]\phi|E|^2[1 - \exp(-\varepsilon l[PI])]^{0.5} \quad (4.7)$$

Based on the above expression, the depletion of monomer is highly dependent on the propagation (k_p) and termination rate constants (k_t). The saturation in refractive index for a system with an A-parameter of 1 x 10^{-6} cm^2 mW^{-1} s^{-1} occurs at ~ 2000 s; the corresponding ratio of $k_p/k_t^{0.5}$ required to saturate the index is ca. 10 (Figure 4-11). These rates are difficult to confirm due to increased scattering and decreased solubility that occurs when these samples are polymerized for extended periods of time, preventing the acquisition of rate constants using infrared spectroscopy. Even with a different initial monomer concentration, the time at which all the monomer has been consumed remains the same (based on k_p and k_t). Although the time to reach saturation is the same, larger monomer depletion would be expected to create a larger overall change in refractive index and would be represented by a larger A-parameter in simulations (Δn_s).

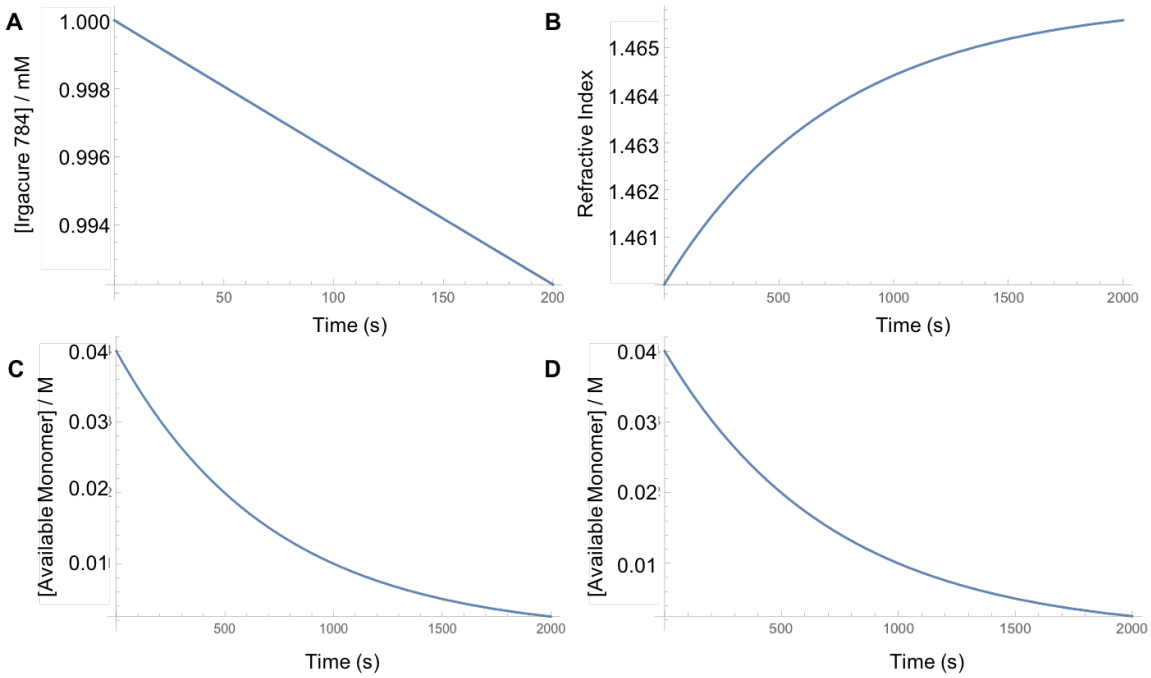

Figure 4-11 (A) Simulated plot of Irgacure® 784 concentration at 8 mW cm^{-2}. (B) The simulated refractive index of a constant 8 mW cm^{-2} region with an A-parameter of 1 x 10^{-6} cm^2 mW^{-1} s^{-1}. (C, D) The simulated concentration of monomer over time with k_p=1 x 10^4 M^{-1} s^{-1}, k_t = 1 x 10^6 M^{-1} s^{-1} and the quantum yield of 0.52 at 8 mW cm^{-2}. The time taken to reach saturation is the same, regardless of the amount of initial available monomer, but the total amount of monomer converted and therefore the refractive index rate/A-parameter changes.

The kinetics were expressed without consideration of oxygen, which has been documented to cause a delay in the polymerization.[12,23,58–61] A second model exists that considers this delay, and implements a critical exposure value, but both models have been shown to portray the same behaviour in materials that exhibit permanent changes in refractive index. [11,12,14,23,40–42,60] Our simulations still show excellent qualitative agreement between our experimental results and illustrate the importance of the rates on the interaction behaviour.

4.6.6 Influence of chemical kinetics on self-trapping behaviour: Photo-oxidation

The kinetics of the photo-oxidation of iodide to triiodide are more difficult to investigate due to the small index contrast and nonlocal nature of the response, both of which preclude observations of the index profile with microscopy. The rate of the photoreaction is dependent on the formation of the excited state, $Ru(bpy)_3^{2+*}$, and therefore depends on the number of photons absorbed ($A = \varepsilon l[Ru(bpy)_3^{2+}]$), the incident intensity ($I = |E|^2$) and the quantum yield for the photo-oxidation of iodide to generate an iodide radical (ϕ_{PO}). The rate of formation for triiodide can therefore be described by (4.8) based on pseudo-first order kinetics due to the large concentration of iodide relative to $Ru(bpy)_3^{2+}$.

$$\frac{\partial[I_3^-]}{\partial t} \propto \phi_{PO}|E|^2[1 - \exp(-\varepsilon l[Ru(bpy)_3{}^{2+}])] \tag{4.8}$$

The initial rate of triiodide formation was determined using UV-Visible spectroscopy for a diluted sample of $Ru(bpy)_3^{2+}$ (0.05 mM) in water with sodium iodide (0.2 M). A plot of the change in triiodide concentration (ε = 23,200 M^{-1} cm^{-1} at 360 nm) against irradiation time (532 nm, 260 mW) resulted in a linear correlation with little consumption of $Ru(bpy)_3^{2+}$ or iodide. This resulted in a ϕ_{PO} value of ca. 0.03 for the photo-oxidation reaction in water under these dilute conditions – a value comparable to luminescence quantum yields in water.[62–64]

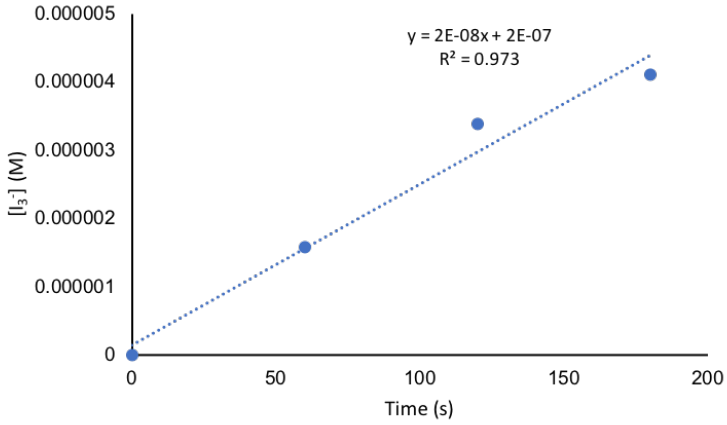

Figure 4-12 Pseudo-first order kinetics of triiodide formation with irradiation at 260 mW (532 nm) based on UV-Vis spectroscopy and ε = 23,200 M^{-1} cm^{-1} at 360 nm for triiodide.

Assuming that the system is initially local and the rates of the reactions that generate triiodide are larger than recombination or diffusion, this system saturates around 200 s at 8 W cm^{-2} (Chapter 2). Given the larger intensities required to observe self-trapping in this system, the A-parameter of this system would be expected to be on the order of 10^{-8}-10^{-11} cm^2 mW^{-1} s^{-1} if we assume a refractive index change on the order of 10^{-3} to 10^{-4} at saturation. In the absence of recombination, the reaction requires two photons to create a single molecule of triiodide, and given the concentrations within this system, the depletion of $Ru(bpy)_3^{2+}$ is the limiting reagent that determines the point of saturation. The net equation without considering recombination and the other elementary reactions can be described by (4.9).

$$2Ru(bpy)_3^{2+} + 3I^- + 2h\nu \rightarrow Ru(bpy)_3^{+} + I_3^- \quad (4.9)$$

Over long periods of time, the equilibrium reaction (4.10) and diffusion processes allow the chemical species to move throughout the sample, resulting in the dissipation of the index profile. Nonlocal diffusion processes are much slower than the photoreaction within

the first 50 s which explains why the beams separated at $\Delta x = 50$ μm only interact over long periods of time.

$$I^- + I_2 \rightleftharpoons I_3^- \tag{4.10}$$

Future work will involve modelling this system and other diffusive systems to investigate nonlocal beam interactions further.

4.7 References

(1) Biria, S.; Morim, D. R.; An Tsao, F.; Saravanamuttu, K.; Hosein, I. D. Coupling Nonlinear Optical Waves to Photoreactive and Phase-Separating Soft Matter: Current Status and Perspectives. *Chaos* **2017**, *27*, 104611.

(2) Trillo, S.; Torruellas, W. *Spatial Solitons*; Springer: New York, 2001.

(3) Crosignani, B.; Di Porto, P.; Degasperis, A.; Segev, M.; Trillo, S. Three-Dimensional Optical Beam Propagation and Solitons in Photorefractive Crystals. *JOSA B* **1997**, *14*, 3078–3090.

(4) Burak, D.; Nasalski, W. Gaussian Beam to Spatial Soliton Formation in Kerr Media. *Appl. Opt.* **1994**, *33*, 6393–6401.

(5) Bjorkholm, J. E.; Ashkin, A. A. CW Self-Focusing and Self-Trapping of Light in Sodium Vapor. *Phys. Rev. Lett.* **1974**, *32*, 129.

(6) Rotschild, C.; Alfassi, B.; Cohen, O.; Segev, M. Long-Range Interactions between Optical Solitons. *Nat. Phys.* **2006**, *2*, 769–774.

(7) Izdebskaya, Y.; Shvedov, V.; Desyatnikov, A.; Krolikowski, W.; Assanto, G.; Kivshar, Y. Incoherent Interaction of Nematicons in Bias-Free Liquid-Crystal Cells. *J. Eur. Opt. Soc.* **2010**, *5*.

(8) Karpierz, M. A.; Assanto, G. Light Self-Trapping in Nematic Liquid Crystals. In *Localized States in Physics: Solitons and Patterns*; Springer, 2011; pp 3–16.

(9) Peccianti, M.; Brzdkiewicz, K. A.; Assanto, G. Nonlocal Spatial Soliton Interactions in Nematic Liquid Crystals. *Opt. Lett.* **2002**, *27*, 1460–1462.

(10) Villafranca, A. B.; Saravanamuttu, K. An Experimental Study of the Dynamics and Temporal Evolution of Self-Trapped Laser Beams in a Photopolymerizable Organosiloxane. *J. Phys. Chem. C* **2008**, *112*, 17388–17396.

(11) Malallah, R.; Li, H.; Muniraj, I.; Cassidy, D.; Al-Attar, N.; Healy, J. J.; Sheridan, J. T. Controlling the Trajectories of Self-Written Waveguides in Photopolymer. *J. Opt. Soc. Am. B* **2018**, *35*, 2046–2056.

(12) Kewitsch, a S.; Yariv, a. Self-Focusing and Self-Trapping of Optical Beams upon Photopolymerization. *Opt. Lett.* **1996**, *21*, 24–26.

(13) Kasala, K.; Saravanamuttu, K. An Experimental Study of the Interactions of Self-

Trapped White Light Beams in a Photopolymer. *Appl. Phys. Lett.* **2008**, *93*, 051111.
(14) Malallah, R.; Cassidy, D.; Muniraj, I.; Ryle, J. P.; Healy, J. J.; Sheridan, J. T. Self-Written Waveguides in Photopolymer. *Appl. Opt.* **2018**, *57*, E80–E88.
(15) Shoji, S.; Kawata, S.; Sukhorukov, A. A.; Kivshar, Y. S. Self-Written Waveguides in Photopolymerizable Resins. *Opt. Lett.* **2002**, *27*, 185–187.
(16) Jisha, C. P.; Kishore, V. C.; John, B. M.; Kuriakose, V. C.; Porsezian, K.; Kartha, C. S. Self-Written Waveguide in Methylene Blue Sensitized Poly(Vinyl Alcohol)/Acrylamide Photopolymer Material. *Appl. Opt.* **2008**, *47*, 6502–6507.
(17) Malallah, R.; Li, H.; Kelly, P. D.; Healy, J. J.; Sheridan, T. J. A Review of Hologram Storage and Self-Written Waveguides Formation in Photopolymer Media. *Polymers*. 2017, p 337.
(18) Kagami, T. M. and T. Y. and M. Improvement in Positioning Accuracy of Light-Induced Self-Written Polymeric Optical Waveguide Using an "Optical Solder" Effect. *Jpn. J. Appl. Phys.* **2006**, *45*, L1033.
(19) Jradi, S.; Soppera, O.; Lougnot, D. J. Fabrication of Polymer Waveguides between Two Optical Fibers Using Spatially Controlled Light-Induced Polymerization. *Appl. Opt.* **2008**, *47*, 3987–3993.
(20) Hosein, I. D.; Lin, H.; Ponte, M. R.; Basker, D. K.; Brook, M. A.; Saravanamuttu, K. Waveguide Encoded Lattices (WELs): Slim Polymer Films with Panoramic Fields of View (FOV) and Multiple Imaging Functionality. *Adv. Funct. Mater.* 1702242–n/a.
(21) Li, H.; Qi, Y.; Guo, C.; Malallah, R.; Sheridan, J. T. Holographic Characterization of Diffraction Grating Modulation in Photopolymers. *Appl. Opt.* **2018**, *57*, E107–E117.
(22) Hudson, A. D.; Ponte, M. R.; Mahmood, F.; Pena Ventura, T.; Saravanamuttu, K. A Soft Photopolymer Cuboid That Computes with Binary Strings of White Light. *Nat. Commun.* **2019**, *10*, 2310.
(23) Kewitsch, A. S.; Yariv, A. Nonlinear Optical Properties of Photoresists for Projection Lithography. *Appl. Phys. Lett.* **1996**, *68*, 455–457.
(24) Basker, D. K.; Cortes, O. A. H.; Brook, M. A.; Saravanamuttu, K. 3D Nonlinear Inscription of Complex Microcomponents (3D NSCRIPT): Printing Functional Dielectric and Metallodielectric Polymer Structures with Nonlinear Waves of Blue LED Light. *Adv. Mater. Technol.* **2017**, *2*, 1600236–n/a.
(25) Monro, T. M.; De Sterke, C. M.; Poladian, L. Catching Light in Its Own Trap. *J. Mod. Opt.* **2001**, *48*, 191–238.
(26) Snyder, A. W.; Ladouceur, F. Light Guiding Light: Letting Light Be the Master of Its Own Destiny. *Opt. Photonics News* **1999**, *10*, 35.
(27) Stegeman, G. I. Optical Spatial Solitons and Their Interactions: Universality and Diversity. *Science* **1999**, *286*, 1518–1523.
(28) Shi, T.-T.; Chi, S. Nonlinear Photonic Switching by Using the Spatial Soliton Collision. *Opt. Lett.* **1990**, *15*, 1123–1125.
(29) Królikowski, W.; Holmstrom, S. a. Fusion and Birth of Spatial Solitons upon Collision. *Opt. Lett.* **1997**, *22*, 369–371.

(30) Królikowski, W.; Luther-Davies, B.; Denz, C.; Tschudi, T. Annihilation of Photorefractive Solitons. *Opt. Lett.* **1998**, *23*, 97–99.
(31) Buryak, A. V.; Kivshar, Y. S.; Shih, M.-F. S. M.-F.; Segev, M. Induced Coherence and Stable Soliton Spiraling. *Tech. Dig. Summ. Pap. Present. Quantum Electron. Laser Sci. Conf.* **1999**.
(32) Ku, T.-S. Sen; Shih, M.-F. F.; Sukhorukov, A. A.; Kivshar, Y. S. Coherence Controlled Soliton Interactions. *Phys. Rev. Lett.* **2005**, *94*, 063904.
(33) Stegeman, G. I.; Segev, M. Optical Spatial Solitons and Their Interactions: Universality and Diversity. *Science* **1999**, *286*, 1518–1523.
(34) Villafranca, A. B.; Saravanamuttu, K. Diversity and Slow Dynamics of Diffraction Rings: A Comprehensive Study of Spatial Self-Phase Modulation in a Photopolymer. *J. Opt. Soc. Am. B* **2012**, *29*, 2357.
(35) Villafranca, A. B.; Saravanamuttu, K. Diffraction Rings Due to Spatial Self-Phase Modulation in a Photopolymerizable Medium. *J. Opt. A Pure Appl. Opt.* **2009**, *11*, 125202.
(36) Villafranca, Ana; Saravanamuttu, K. Spontaneous and Sequential Transitions of a Gaussian Beam into Diffraction Rings, Single Ring and Circular Array of Filaments in a Photopolymer. *Opt. Express* **2011**, *19*, 15560–15573.
(37) Feit, M. D.; Fleck, J. A. Light Propagation in Graded-Index Optical Fibers. *Appl. Opt.* **1978**, *17*, 3990–3998.
(38) Yevick, D. A Guide to Electric Field Propagation Techniques for Guided-Wave Optics. *Opt. Quantum Electron.* **1994**, *26*, S185–S197.
(39) Scarmozzino, R.; Gopinath, A.; Pregla, R.; Helfert, S. Numerical Techniques for Modeling Guided-Wave Photonic Devices. *IEEE J. Sel. Top. Quantum Electron.* **2000**, *6*, 150–162.
(40) Shoji, S.; Kawata, S. Optically-Induced Growth of Fiber Patterns into a Photopolymerizable Resin. *Appl. Phys. Lett.* **1999**, *75*, 737–739.
(41) Monro, T. M.; de Sterke, C. M.; Poladian, L. Analysis of Self-Written Waveguide Experiments. *J. Opt. Soc. Am. B* **1999**, *16*, 1680–1685.
(42) Ben Belgacem, M.; Kamoun, S.; Gargouri, M.; Honorat Dorkenoo, K. D.; Barsella, A.; Mager, L. Light Induced Self-Written Waveguides Interactions in Photopolymer Media. *Opt. Express* **2015**, *23*, 20841–20848.
(43) Li, H.; Qi, Y.; Ryle, J. P.; Sheridan, J. T. Self-Written Waveguides in a Dry Acrylamide/Polyvinyl Alcohol Photopolymer Material. *Appl. Opt.* **2014**, *53*, 8086–8094.
(44) Monro, T. M.; Poladian, L. Analysis of Self-Written Waveguides in Photopolymers and Photosensitive Materials. **2006**, *57*, 1104–1113.
(45) Meneghini, C.; Villeneuve, A. As2S3 Photosensitivity by Two-Photon Absorption: Holographic Gratings and Self-Written Channel Waveguides. *J. Opt. Soc. Am. B* **1998**, *15*, 2946–2950.
(46) Monro, T. M.; Sterke, C. M. De; Poladian, L. Investigation of Waveguide Growth in Photosensitive Germanosilicate Glass. **2006**, *13*, 2824–2832.
(47) Monro, T. M.; Moss, D.; Bazylenko, M.; Martijn de Sterke, C.; Poladian, L. Observation of Self-Trapping of Light in a Self-Written Channel in a

Photosensitive Glass. *Phys. Rev. Lett.* **1998**, *80*, 4072–4075.
(48) Gardner, J. M.; Abrahamsson, M.; Farnum, B. H.; Meyer, G. J. Visible Light Generation of Iodine Atoms and I-I Bonds: Sensitized I - Oxidation and I3- Photodissociation. *J. Am. Chem. Soc.* **2009**, *131*, 16206–16214.
(49) Farnum, B. H.; Jou, J. J.; Meyer, G. J. Visible Light Generation of I – I Bonds by Ru-Tris (Diimine) Excited States. **2012**, *2012*.
(50) Ruff, I.; Friedrich, V. J.; Csillag, K. Transfer Diffusion. III. Kinetics and Mechanism of the Triiodide-Iodide Exchange Reaction. *J. Phys. Chem.* **1972**, *76*, 162–165.
(51) Mohammadi Estakhri, N.; Edwards, B.; Engheta, N. Inverse-Designed Metastructures That Solve Equations. *Science* **2019**, *363*, 1333 LP-1338.
(52) Andrade-Lucio, J. A.; Alvarado-Méndez, B.; Rojas-Laguna, R.; Ibarra-Manzano, O. G.; Torres-Cisneros, M.; Jaime-Rivas, R.; Kuzin, E. A. Optical Switching by Coherent Collision of Spatial Solitons. *Electronics Letters*. 2000, p 1403.
(53) Burgess, I. B.; Shimmell, W. E.; Saravanamuttu, K. Spontaneous Pattern Formation Due to Modulation Instability of Incoherent White Light in a Photopolymerizable Medium. *J. Am. Chem. Soc.* **2007**, *129*, 4738–4746.
(54) Saravanamuttu, K.; Du, X. M.; Najafi, S. I.; Andrews, M. P. Photoinduced Structural Relaxation and Densification in Sol-Gel Derived Nanocomposite. *Can. J. Chem.* **1998**, *76*, 1717–1729.
(55) Chung, Y.; Dagli, N. An Assessment of Finite Difference Beam Propagation Method. *IEEE J. Quantum Electron.* **1990**, *26*, 1335–1339.
(56) Scarmozzino, R.; Osgood, R. M. Comparison of Finite-Difference and Fourier-Transform Solutions of the Parabolic Wave Equation with Emphasis on Integrated-Optics Applications. *J. Opt. Soc. Am. A* **1991**, *8*, 724–731.
(57) Yevick, D.; Hermansson, B. Efficient Beam Propagation Techniques. *IEEE J. Quantum Electron.* **1990**, *26*, 109–112.
(58) Chen, F. H.; Pathreeker, S.; Biria, S.; Hosein, I. D. Synthesis of Micropillar Arrays via Photopolymerization: An in Situ Study of Light-Induced Formation, Growth Kinetics, and the Influence of Oxygen Inhibition. *Macromolecules* **2017**, *50*, 5767–5778.
(59) O'Brien, A. K.; Bowman, C. N. Modeling the Effect of Oxygen on Photopolymerization Kinetics. *Macromol. Theory Simulations* **2006**, *15*, 176–182.
(60) Bhole, K.; Gandhi, P.; Kundu, T. On the Evolution of Cured Voxel in Bulk Photopolymerization upon Focused Gaussian Laser Exposure. *J. Appl. Phys.* **2014**, *116*, 43105.
(61) Dendukuri, D.; Panda, P.; Haghgooie, R.; Kim, J. M.; Hatton, T. A.; Doyle, P. S. Modeling of Oxygen-Inhibited Free Radical Photopolymerization in a PDMS Microfluidic Device. *Macromol.* **2008**, *41*, 8547–8556.
(62) Alnaed, M. K.; Endicott, J. F. Chemical Scavenging Yields for Short-Lived Products from the Visible Light Photoionization of the Tris(Bipyridine)Ruthenium(II) Triplet Metal-to-Ligand Charge-Transfer Excited State. *J. Phys. Chem. A* **2018**, *122*, 9251–9266.
(63) Troian-Gautier, L.; Turlington, M. D.; Wehlin, S. A. M.; Maurer, A. B.; Brady, M.

D.; Swords, W. B.; Meyer, G. J. Halide Photoredox Chemistry. *Chem. Rev.* **2019**, *119*, 4628–4683.

(64) Caspar, J. V.; Meyer, T. J. Photochemistry of Tris(2,2'-Bipyridine)Ruthenium(2+) Ion ($Ru(bpy)_3^{2+}$). Solvent Effects. *J. Am. Chem. Soc.* **1983**, *105*, 5583–5590.

5 3D spiraling self-trapped light beams in photochemical systems[**]

5.1 Abstract

We report that a pair of visible laser beams self-trap and spiral about each other as they propagate through soft, polymer gels undergoing two different types of photochemical reactions. When launched into gels that undergo photopolymerization of methacrylate substituents and separately, photo-oxidation of iodide anion, two non-coplanar (skewed) Gaussian beams collide and then spiral about each other as they advance through the evolving medium. In the absence of chemical reactions, the linearly polarized beams – which possess no angular velocity - broaden naturally and propagate along their original, straight-pathed trajectories. By contrast, refractive index gradients generated by the photochemical reaction both elicit self-trapping and introduce an attractive interaction between the self-trapped beams. These self-trapped beams spiral when their mutual attraction perfectly counterbalances their original tendency to diverge away from each other. Remarkably, these findings show that the photochemically-mediated interactions of incident optical fields within the gel-medium impart curvature and angular velocity to the self-trapped beams. The ability to precisely control the

[**]*Submitted*. The authors of the manuscript are Derek R. Morim, Damian Bevern, Ignacio Vargas-Baca and Kalaichelvi Saravanamuttu. Contribution: DRM and DB performed experimental work. DRM, IVB, KS conceived experiments, analyzed data and wrote the manuscript.

interactions and trajectories is critical for next-generation light-guiding-light photonics, soliton-based computing and photolithography of 3-D structures.

5.2 Introduction

Self-trapped beams are spatially localized, nonlinear optical waves, which induce refractive index changes (Δn) along their paths and in this way, counter their natural tendency to broaden.[1,2] Described by the nonlinear Schrödinger equation, self-trapped beams are fundamentally similar to - and serve as experimentally accessible models of – diverse nonlinear waveforms ranging from Bose Einstein condensates to rogue ocean waves. They characteristically exhibit particle-like interactions[3,4] such as attraction and repulsion,[5,6] fusion[7] and annihilation.[8] The most intriguing but least studied of these is their pairwise spiraling,[3,9,10] which is elicited only under exquisitely controlled experimental conditions.[11-13] It is moreover important to note that this differs fundamentally from the behavior of vortices, which inherently possess orbital angular momentum, and can induce spiral relief structures in photoresponsive films.[14] By strong contrast and reminiscent of planetary motion,[15] the spiraling self-trapped beams raise fundamental questions about angular momentum conservation in the system, the centripetal and centrifugal forces underlying their circular motion and the relative phase, coherence and energy exchange between these nonlinear waves.[11]

Spiraling self-trapped beams have until now been observed exclusively in photophysical systems, namely photorefractive crystals,[11] liquid crystals[13] and

photothermal glasses[12] – and only under steady state conditions. Our experiments demonstrate that this extraordinary behavior of self-trapped beams can be elicited through fundamental photochemical mechanisms such as free-radical polymerization[16] and photo-oxidation of iodide anion.[17] The relatively slow (*ms* to minutes) kinetics of chemical reactions allows us to trace the evolution of the self-trapped beam pair and gain direct insight into the dynamics that govern spiraling.

5.3 Experimental observation of spiraling self-trapped beams

We launched a pair of continuous wave (c.w.), visible (λ = 532 nm) laser beams (A and B) onto the entrance face (z = 0.0 mm) of a transparent cell containing photopolymerizable methacrylate-derivatized siloxane gel[15] (Section 5.6.1). Beams A and B are mutually orthogonally polarized but otherwise identical with widths ($1/e^2$) and powers of 20 μm and 30 nW, respectively. The beams are non-coplanar, each slightly inclined from the z axis, and converge to their closest separation distance (Δs_{min}) before veering away from each other (Figure 5-1, Figure 5-7). To study their interactions, we tuned the angular separation (θ) – skewness - of beams A and B from 0.23º to 0.86º while keeping Δs_{min} constant at ~20 μm (Section 5.8.3). We monitored the temporal evolution of the beam-pair at the exit face (z = 6.0 mm) with a charge-coupled device (CCD) camera.

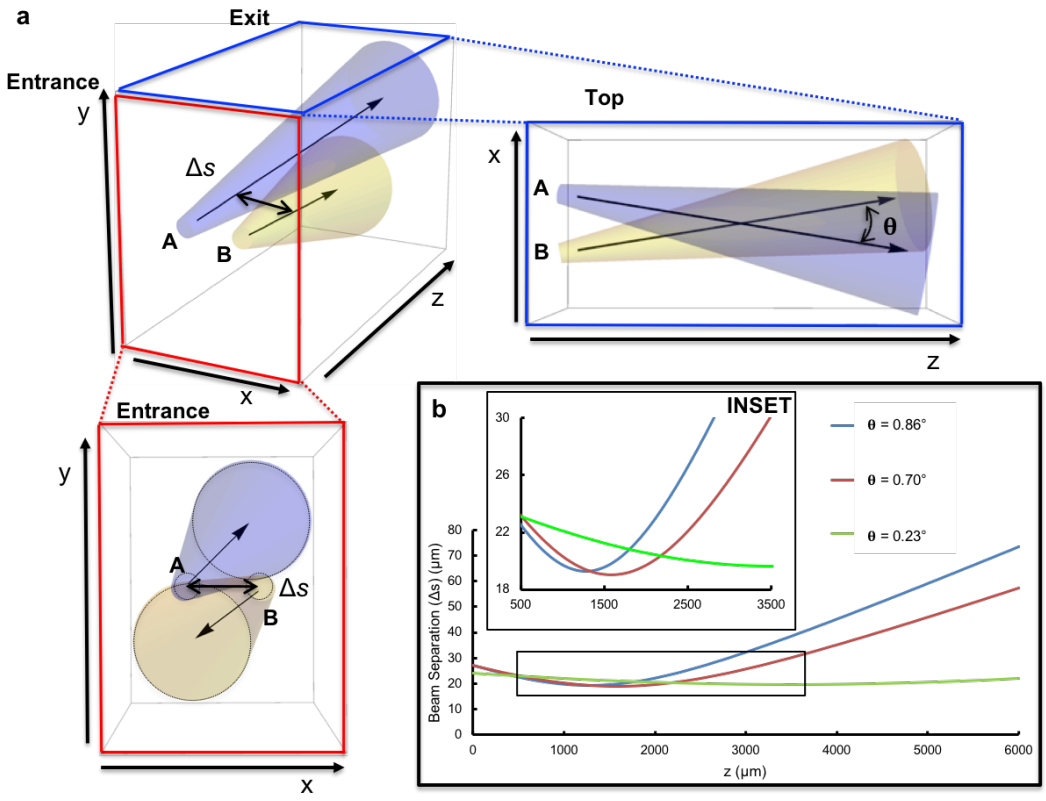

Figure 5-1 Experimental configuration: (a) beams A (blue) and B (yellow) with angular separation θ are launched into a cuvette containing photopolymerizable sol. Black arrows represent the beam propagation axes while cones depict their broadening under linear conditions. (b) Plots of their centre-to-centre separation (Δs) versus z show that beams reach $\Delta s_{min} \sim 20$ μ**m** (INSET); their skewness (extent to which they diverge from Δs_{min}) depends on θ.

Beams A and B self-trap and spiral about each other as they propagate through the gel, initiating free-radical polymerization of methacrylate moieties and corresponding Δn[15] along z (Figure 5-2a). Intensity profiles at $z = 6.0$ mm show that the beams self-trap and simultaneously rotate about their mid-point (Figure 5-2b-d). Because they are not coplanar, this mutual rotation indicates that the self-trapped beams must spiral or orbit about each other along z.

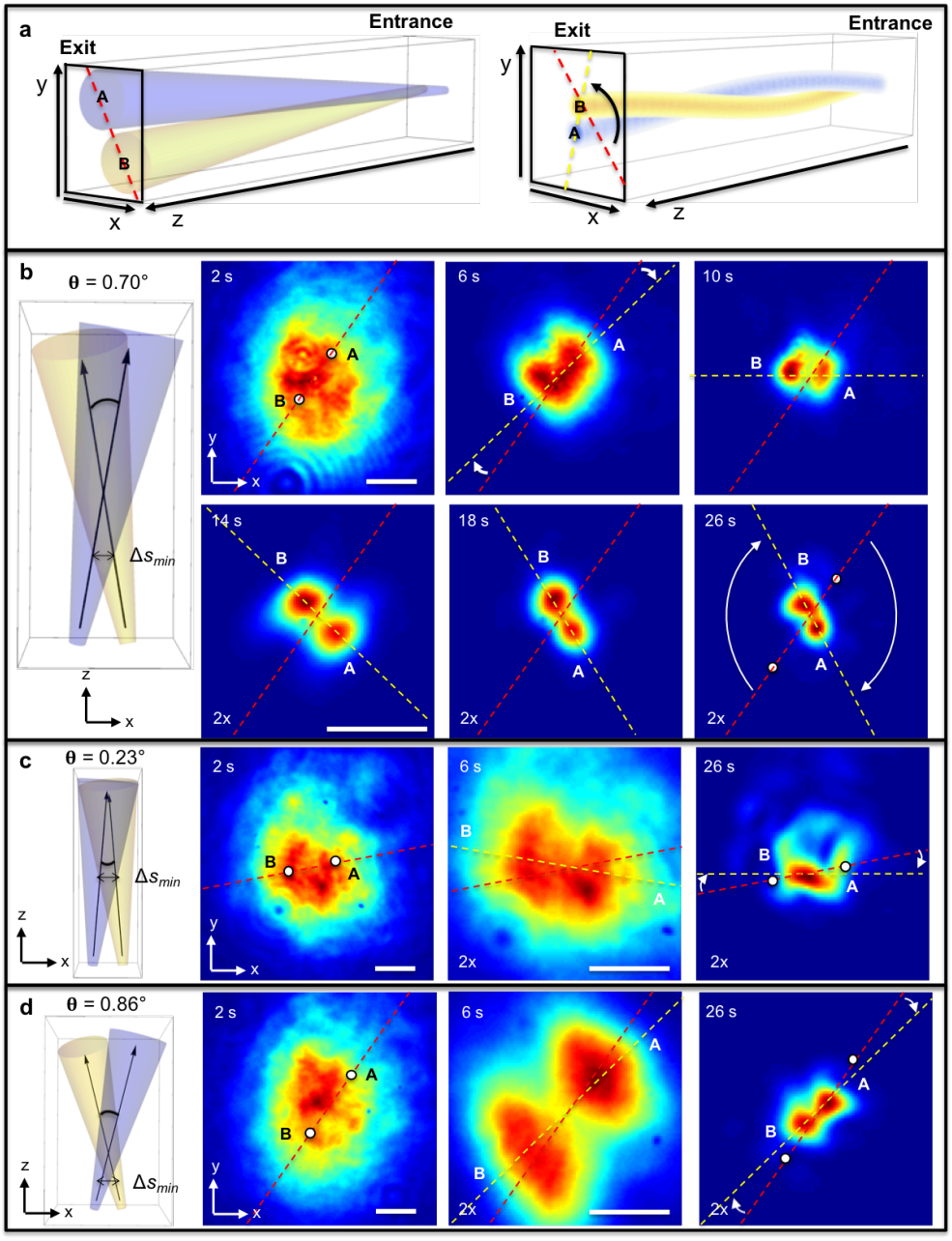

Figure 5-2 (a) Schemes of linear propagation (left) and polymerization-induced self-trapping and spiraling (right) of beams A (blue) and B (yellow). Experimental evolution of intensity profiles acquired at z = 6.0 mm at θ = (b) 0.70°, (c) 0.23° and (d) 0.86°. In (b-d), white dots at t = 2 s and 26 s, represent beam-centres under linear conditions. Red and white dotted lines respectively show the initial and current orientation of beams. The scheme (left) depicts the beams' trajectories under linear conditions. Scale bar = 25 μm. For clarity, some images are 2x magnified. (See also Figure 5-8).

The extent of spiraling maximizes at θ = 0.70° (Figure 5-2b): here, at early times (t = 2 s) the gel behaves as a linear (non-photoresponsive) medium and the beams each broaden due to natural diffraction from 20 μm to 130 μm as they travel from z = 0.0 mm to z = 6.0 mm. Broadening renders the beams indistinguishable at z = 6.0 mm but their centres (denoted as white points) confirm that they follow their original skewed trajectories and do not interact. However, within seconds (t = 6 s) of photopolymerization, the beams exhibit striking changes in intensity distribution and relative orientation: they each undergo a > three-fold decrease in width to ~ 40 μm and simultaneously rotate about their midpoint by ~11° (yellow line) relative to their original positions (red line). Over the next 20 s, the beams each narrow to ~21 μm and rotate by ~117°; this corresponds to a twist angle of ~242° from the entrance (z = 0.0 mm) to the exit (z = 6.0 mm) face of the gel.

5.4 Mechanism of self-trapping and spiraling

Self-trapping and spiraling arise from spatially non-uniform photopolymerization reactions, which in turn induce temporally and spatially anisotropic Δn in the gel according to:[i, ii]

$$\frac{\partial \Delta n(x,y,z,t)}{\partial t} = AI(x,y,z,t)\left(1 - \frac{\Delta n(x,y,z,t)}{\Delta n_s}\right) \tag{5.1}$$

where I = incident optical intensity, A = material-dependent parameter and Δn_s = maximum Δn at saturation. Because it is intensity dependent, Δn mirrors the

Gaussian profile of each beam – maximizing at and then decaying radially from the most intense, axial region. The resulting Δn gradient – a lens - at $z = 0.0$ mm focuses each beam and counters its natural divergence. A symbiotic, nonlinear interaction ensues in which the beams become entrapped and continue to initiate polymerization within two strongly localized reaction fronts.[15] These fronts are in fact cylindrical waveguides, which guide each beam as the fundamental mode ($m = 0$), enabling them to propagate as self-trapped beams (Figure 5-2b-d). Self-trapping is possible only because Δn saturates when accessible methacrylate units in the gel are depleted. A non-saturating Δn by contrast would cause continuous self-focusing of the beam and ultimately, damage the medium due to a catastrophic increase in intensity.

The self-trapped beams collide at $\Delta s_{min} = \sim 20$ μm - where there is maximum overlap of their tightly confined optical fields (Figure 5-1b). Because beams A and B are mutually orthogonally polarized, their overlapping fields do not interfere but superpose instead to increase the overall intensity - and thereby Δn - in the region between them. Through a nonlinear, positive feedback mechanism, intensity from both self-trapped beams now spontaneously tunnels into this interstitial region increasing Δn even further and serving effectively as a mutually attractive force. At $\Delta s_{min} = \sim 20$ μm, this attraction between the self-trapped beams is sufficiently strong to elicit an out-of-plane collision, which significantly disrupts and imparts curvature to their initially straight-pathed trajectories.

The self-trapped beams, which individually would possess only linear velocity, acquire curved trajectories and angular velocity upon collision.[11] This is because their

propensity to continue along their paths skewed away from each other is now countered by mutual attraction, which maximizes at Δs_{min}. Upon collision, the self-trapped beams, which can be considered equivalent because they are both single-moded and possess the same intensity, are akin to a two-body system. The dynamic competition between their opposing tendencies - reminiscent of centripetal and centrifugal forces – triggers spiraling. The greatest extent of spiraling occurs at $\theta = 0.70°$ during the time t = 2 s to 26 s when the attraction between the self-trapped beams exactly counterbalances their tendency to follow their original, skewed paths (Figure 5-2b). Under these conditions, the self-trapped beams possessed a maximum calculated angular velocity of ~ 0.24 $rads^{-1}$.

To further confirm the above-proposed mechanism, we show that the self-trapped beams can either be made to fuse or follow their original trajectories by varying the balance between their attraction and skewness: when $\theta < 0.70°$, the attractive force remains the same and the self-trapped beams collide at Δs_{min} ~20 μm but diverge away from each other to a smaller extent (Figure 5-1b). As a result, at $\theta = 0.56°$, the attractive force is strong enough to diminish spiraling by ~25 % to ~88° (compared to ~117° when $\theta = 0.70°$) (Figure 5-8). At $\theta = 0.23°$, the attractive force dominates so that after rotating by ~21°, the self-trapped beams fuse (Figure 5-2c). Conversely, the tendency of the self-trapped beams to diverge from each other dominates at $\theta > 0.70°$; this also suppresses orbiting so that at $\theta = 0.86°$, the beams rotate by only ~10° (Figure 2d). When $\theta = 0.96°$, the attractive force is insufficient to elicit interactions between the self-trapped beams, which follow their original trajectories (Figure 5-8).

Because they are orthogonally polarized, we could monitor beams A and B individually during spiraling by inserting the appropriate crossed polarizer in the imaging optics. Figure 5-3 selectively traces the evolution of each beam at $z = 6.0$ mm during two separate but identical experiments at $\theta = 0.74°$. When superposed, the orthogonally polarized image-sets provide direct insight into the mechanism underlying spiraling: at t = 2 s, there is significant overlap of the beams but once photopolymerization is initiated, their intensity rapidly segregates into two tightly-focused lobes corresponding to the self-trapped beams. Significantly, these lobes are interconnected by a clearly delineated, narrow region containing intensity from both beams – this is the attractive interaction, which draws intensity from both self-trapped beams into the high-Δn, interstitial region between them (*vide supra*). This intensity overlap remains strongly localized during rotation of the self-trapped beam-pair over ~110°. This is because their attraction exactly counterbalances their tendency to follow skewed trajectories and is not strong enough to facilitate intensity-exchange or fusion. Indeed, spiraling ceases when this interstitial region disappears at t = 26 s and intensity from self-trapped beam B pervades A. Here, the attractive force dominates, suppressing spiraling, facilitating intensity-exchange and ultimately, fusion of the self-trapped beams at t > 30 s.

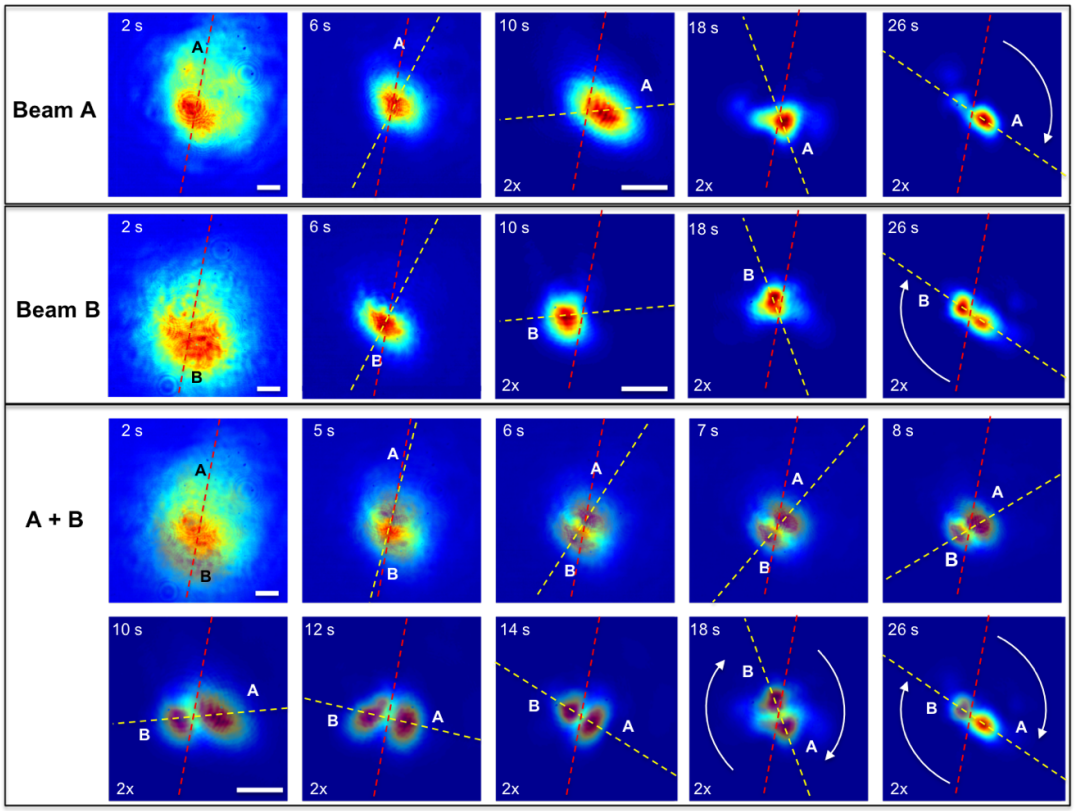

Figure 5-3 Polarized spatial intensity profiles of Beams A and B (top two rows) acquired in two separate, identical experiments at θ = 0.74° were overlaid (bottom row) to selectively reveal intensity distribution of each beam during self-trapping and spiraling. Scale bar = 25 μm.

5.5 3D spiraling trajectory

We reconstructed the 3-D spiraling trajectories of the self-trapped beams by measuring their maximum rotation at increasing propagation distances (Figure 5-3a-c). Figure 5-3c captures their curved trajectories, which become strikingly pronounced at z = 2.0 mm, their point of collision (Δs_{min}), which disrupts their original paths and triggers spiraling. For these experiments, we employed a different photochemical system: Pluronic® F-127 gels doped with $Ru(bpy)_3^{2+}$ and NaI. We previously demonstrated that Δn due to photo-oxidation of I^- in this system elicits self-trapping of 532 nm light

(Chapter 2).[16] In our current experiment, we first confirmed that Beams A and B self-trap and exhibit spiraling. We then exploited the processability of these gels to prepare monolithic samples with three different pathlengths, 2.0 mm, 4.0 mm and 6.0 mm (identical samples with different pathlengths are challenging to generate with organosiloxane gels, which must undergo a pre-polymerization step that can introduce variations in samples of different dimensions.) Figure 5-4 collates results of experiments carried out at $\theta = 0.78°$ in each Pluronic® F-127 sample; in all cases, $\Delta s_{min} = 20$ μm. At t = 0 s (under linear conditions), the beams each broaden with pathlength from 20 μm to ~ 43 μm, ~87 μm and ~130 μm at 2.0 mm, 4.0 mm and 6.0 mm, respectively. Accordingly, self-trapping is rapider at shorter distances: at 15 s, the beams narrow in width to ~27 μm at 2.0 mm, to ~51 μm at 4.0 mm and ~70 μm at 6.0 mm. The self-trapped beams rotate to a maximum of 62° (t = 15 s) at 2.0 mm, 104° (t = 30 s) at 4.0 mm and 169° (t = 45 s) at 6.0 mm. All rotations were measured with respect to the expected beam positions at that pathlength. The 3-D reconstruction of their trajectories through the gel is based on their final positions (at t = 45 s) at each pathlength.

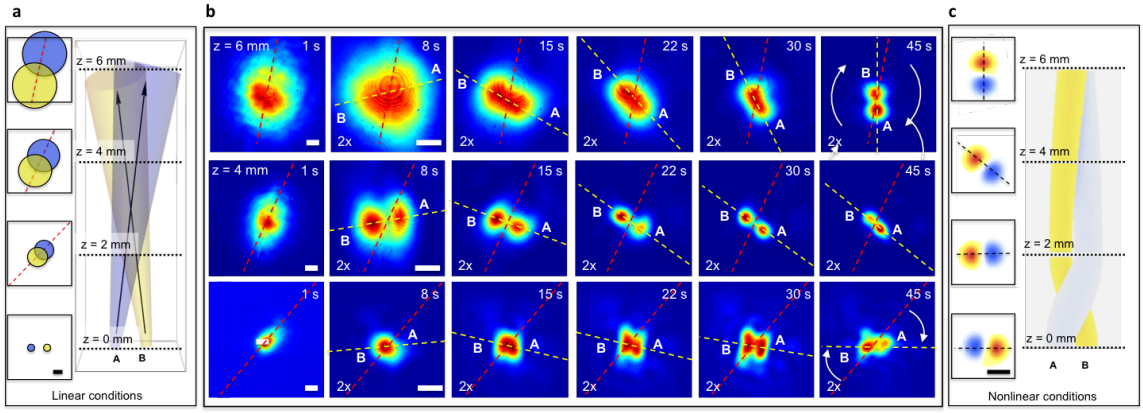

Figure 5-4 (a) Scheme of Beams A and B propagating through the photo-oxidation system (Pluronic® F-127 gels doped with $Ru(bpy)_3^{2+}$ and NaI) at $\theta = 0.78°$; longitudinal and select cross-sectional profiles are provided, (b) their rotation due to photooxidation at $z = 6.0$ mm (top), 4.0 mm (middle) and 2.0 mm (bottom) and (c) corresponding 3-D reconstruction of their spiraling trajectories with select transverse profiles. Scale bar = 25 μm.

5.6 Conclusions

These investigations showed that a skewed pair of laser beams self-trap and spiral as they propagate through two different, nascent photochemical systems. The nonlinear evolution of Δn originating from photopolymerization and separately, photo-oxidation engenders an attractive interaction between the beams and imparts angular velocity during spiraling. In the absence of the photochemical reaction, the beams do not self-trap but instead, broaden as they follow their straight-pathed trajectories. It is important to note that the incident optical fields in our system do not themselves possess angular momentum. Instead, the linearly polarized, self-trapped beams spiral only because of their reciprocal interactions with the photochemically responsive medium. To ensure reproducibility of these delicate experiments, we repeated each set of experiments

at least thrice. Our findings highlight the richly unique opportunities provided by photochemical systems to host and study in real time the dynamics of nonlinear light waves, which in turn is critical in the development of light-guiding-light photonics,[20] photolithography of complex 3-D structures and soliton-based computing.[21]

5.7 Acknowledgements

We thank Prof. R. Nejat for valuable discussions. We gratefully acknowledge funding from the Natural Sciences and Engineering Research Council of Canada, Canadian Foundation for Innovation and McMaster University.

5.8 Supplementary information

5.8.1 Preparation of photoresponsive gels

5.8.1.1 Materials

3-(Trimethoxysilyl) propyl methacrylate (MAPTMS), 0.1 N hydrochloric acid, Pluronic® F-127 polymer, and sodium iodide were purchased from Millipore Sigma. (Bis(η5-cyclopentadien-1-yl)-bis(2,6-difluoro-3-(1H-pyrrol-1-yl)-phenyl) titanium(IV) was obtained from Ciba Specialty Chemicals Inc., Canada. Tris(bipyridine)ruthenium(II) chloride hexahydrate was obtained from Strem Chemicals Inc.

5.8.1.2 Photopolymerizable gel

Adapted from our previous work[16], this photopolymer was prepared by combining 1.1 g (5.5×10^{-5} mol.) of 0.05 N hydrochloric acid (diluted from a standardized 0.1 N HCl aqueous solution) and 17.6 g (0.0708 mol) of 3-methacryloxypropyltrimethoxysilane. Approximately 5 minutes of stirring creates a homogeneous mixture, to which 0.05 wt. %

of (bis(η5-cyclopentadien-1-yl)-bis(2,6-difluoro-3-(1H-pyrrol-1-yl)-phenyl) titanium(IV) was added. The sample was shielded from ambient light with aluminum foil and stirred continuously for 6 days. 1.0 ml of photosensitized sol was injected through a small opening into a 6 mm-long cylindrical cell with flat and transparent windows. This organosiloxane sol was then uniformly irradiated in a homemade irradiation chamber with a reflective, aluminum foil interior to uniformly distribute the light onto the sample. White light from a quartz- tungsten-halogen lamp (3 mW) was directed into the chamber for 8 minutes (Cole-Parmer 09790-series, IL, USA), partially polymerizing the liquid into the gel that was employed for optical experiments.

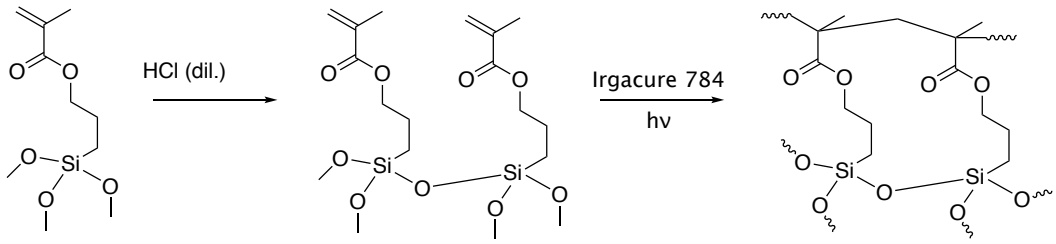

Figure 5-5 Preparation of 3-methacryloxypropyltrimethoxysilane (MAPTMS) photopolymer and subsequent photopolymerization.

5.8.1.3 Photo-oxidation system

Adapted from our previous work[17], a solution of $Ru(bpy)_3Cl_2$ (1.3 mM) and NaI (0.2 M) was prepared with deionized H_2O (Milli-Q®, 18.2 MΩcm). 3 mL of this solution was added 1.0 g of Pluronic® F-127 and cooled below its lower critical solution temperature (LCST) using an ice bath and mixed with a glass rod until homogeneous. The sample was then injected into the opening of a 6 mm ring cell while cold and left at room temperature (shielded with aluminium foil) until a gel formed.

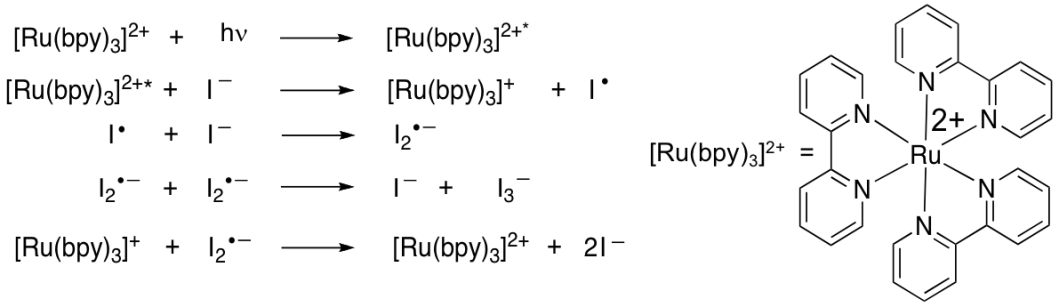

Figure 5-6 Photochemical conversion of iodide to triiodide occurs through multiple radical processes.

5.8.2 Optical assembly

Optical experiments were carried on an assembly adapted from our previous studies (Figure 5-7).[13] The excitation source was the TEM_{00} mode (Gaussian beam, M2 < 1.1) of c,w. visible (532 nm) light emitted by a diode-pumped solid-state laser (Verdi V2, Coherent, Inc., California, USA). The output beam was passed through a λ/2 waveplate and split into two beams by a polarizing beam splitter cube, creating two orthogonally polarized beams. The λ/2 waveplate orientation was adjusted to ensure that the intensity of each beam was equal. The beams were directed by mirrors and a second beam splitter cube, through a set of filters and a planoconvex lens [focal length = 75.6 mm], which focused each of the beams to a diameter of 20 μm onto the entrance window of the sample cell. The separation distance (Δs) and separation angle (θ) of the beams was tuned by varying the orientation of the beam splitter cube.

The spatial intensity profile of the beams at the exit face of the cell was imaged by a pair of planoconvex lenses (f. l. = 75.6 mm and f. l. = 250.0 mm) onto a charge-coupled device (CCD) camera [2040 horizontal × 1532 vertical pixels; pixel size = 3.20 μm x 3.20 μm; WinCamD XHR, DataRay Inc., California, USA]. Neutral density filters (F) (VARM, Coherent, Inc.) were used to prevent saturation of the CCD camera. All components are translatable along the *z*

direction of the optical rail with a resolution of 0.25 mm. Images were collected every second for 50 second data logs on DataRay software (Version 7.1H25Bk), which calculates beam diameter ($1/e^2$) and relative peak intensity. Corrections for image magnification by the lenses (×3.3) and filters were applied to the images and normalized for better visualization of the beam (the diffracted beam is less intense than the self-trapped beam). The effective beam diameter corresponds to the circular area of all pixels with relative intensity > 13.5% ($1/e^2$) of the maximum (peak) intensity.

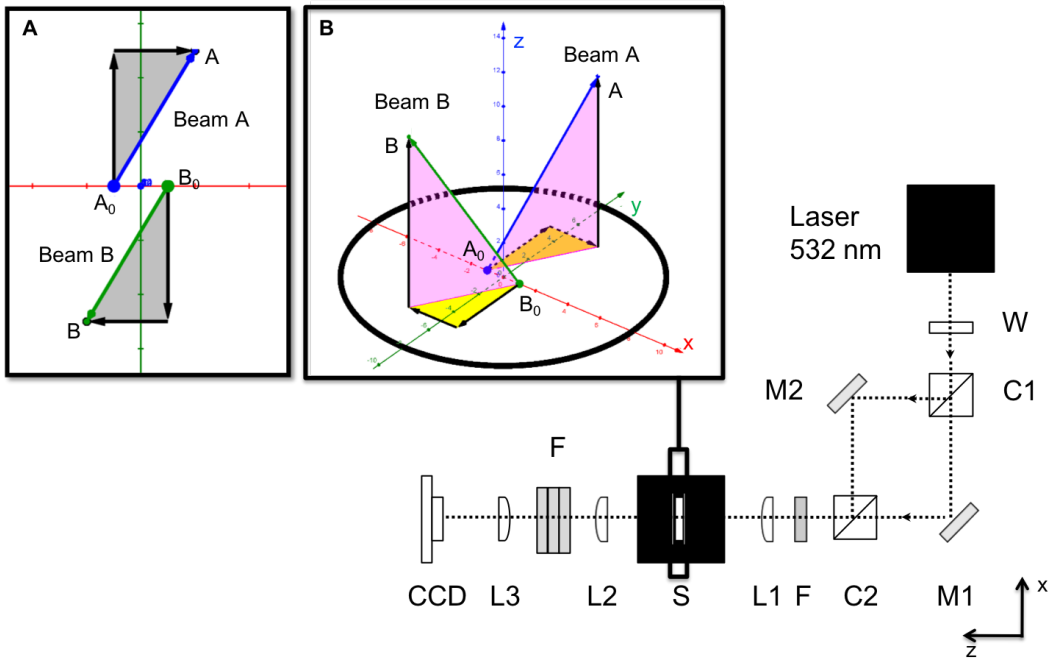

Figure 5-7 Optical assembly employed to launch two skewed laser beams into photoresponsive gels. W = λ/2 waveplate; C1,C2 = polarizing beamsplitter cubes; L1, L2, L3 = planoconvex lenses; F = filters, S = sample, and CCD = charge coupled device camera for imaging the optical profile of the output of the sample. (A) The beam vectors in the *xy*-plane. (B) The beam vectors in 3D representing the trajectory of the beams under linear conditions.

5.8.3 Calculations of beam trajectories

The trajectories on the beams were determined from the positions of their centres at the entrance: $\mathrm{p}_0 = (x_0, y_0, z_0)$, and exit: $\mathrm{p}_f = (x_f, y_f, z_f)$ faces of the sample under linear conditions. From those values, the beam propagation vectors were obtained:

$$\vec{v} = (x_f - x_0, y_f - y_0, z_f - z_f) \tag{5.2}$$

The separation distance between the beams $\vec{a}$ and $\vec{b}$ at the input of the sample (Δs) can be determined by:

$$\Delta s = x_{a0} - x_{b0} \tag{5.3}$$

and

$$\Delta s = \sqrt{(x_{a0} - x_{b0})^2 + (y_{a0} - y_{b0})^2} \tag{5.4}$$

in case of any small deviation in the *y* position of the beams. The angular separation between the beams, θ, was determined through:

$$\vec{a} \cdot \vec{b} = \overrightarrow{\|a\|}\,\overrightarrow{\|b\|} \cos\theta \tag{5.5}$$

where the magnitude of the vectors is determined according to:

$$\overrightarrow{\|v\|} = \sqrt{(x_0 - x_f)^2 + (y_0 - y_f)^2 + (z_0 - z_f)^2} \tag{5.6}$$

Finally, the minimum separation of the beams in space (Δs_{min}) can be determined by finding a vector perpendicular to both beams such that:

$$\vec{a} \cdot \vec{c} = 0 = \vec{b} \cdot \vec{c}. \tag{5.7}$$

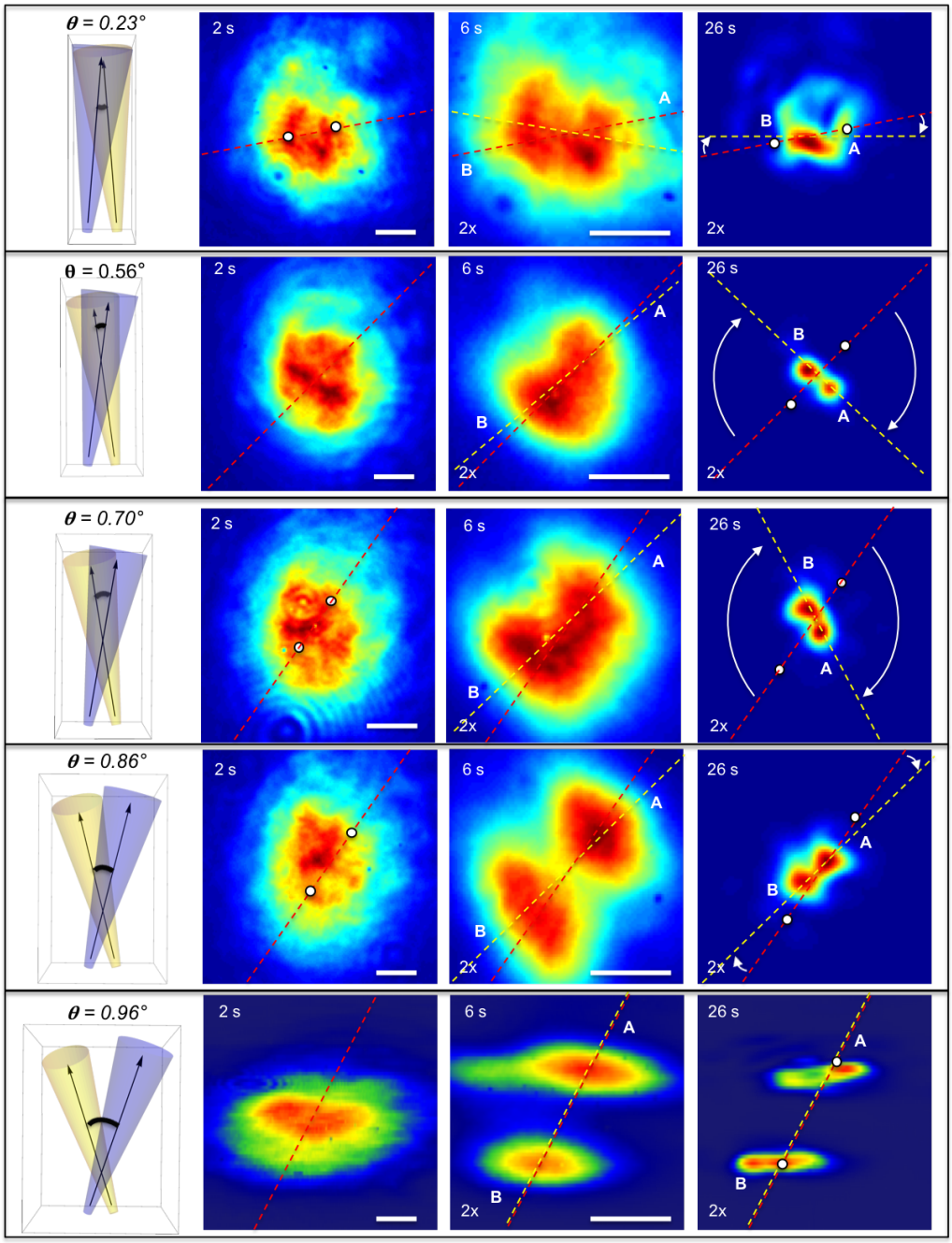

Figure 5-8 A scheme on the left (not to scale) illustrates the differences between the launch conditions of 5 experiments with Δs = 20 μm and different angles. The spatial intensity profiles of light leaving the sample (z = 6 mm) is shown over time. A red line is placed through the centre of each beam under linear conditions at the exit face and the yellow line is placed through the centre of each beam under nonlinear conditions; as the photopolymerization proceeds in MAPTMS. Scale bar = 25 μm.

5.9 References

(1) Trillo, S.; Torruellas, W. *Spatial Solitons*; Springer: New York, 2001.

(2) Biria, S.; Morim, D. R.; An Tsao, F.; Saravanamuttu, K.; Hosein, I. D. Coupling Nonlinear Optical Waves to Photoreactive and Phase-Separating Soft Matter: Current Status and Perspectives. *Chaos An Interdiscip. J. Nonlinear Sci.* **2017**, *27* (10), 104611.

(3) Stegeman, G. I. Optical Spatial Solitons and Their Interactions: Universality and Diversity. *Science* **1999**, *286*, 1518–1523.

(4) Snyder, A. W.; Sheppard, A. P. Collisions, Steering, and Guidance with Spatial Solitons. *Opt. Lett.* **1993**, *18*, 482–484.

(5) Królikowski, W.; Denz, C.; Stepken, A.; Saffman, M.; Luther-Davies, B. Interaction of Spatial Photorefractive Solitons. *J. Opt. B Quantum Semiclassical Opt.* **1998**, *10*, 823–837.

(6) Ku, T.-S.; Shih, M.-F.; Sukhorukov, A.; Kivshar, Y. Coherence Controlled Soliton Interactions. *Phys. Rev. Lett.* **2005**, *94*, 063904.

(7) Królikowski, W.; Holmstrom, S. a. Fusion and Birth of Spatial Solitons upon Collision. *Opt. Lett.* **1997**, *22*, 369–371.

(8) Królikowski, W.; Luther-Davies, B.; Denz, C.; Tschudi, T. Annihilation of Photorefractive Solitons. *Opt. Lett.* **1998**, *23*, 97–99.

(9) Poladian, L.; Snyder, A. W.; Mitchell, D. J. Spiralling Spatial Solitons. *Opt. Commun.* **1991**, *85* (1), 59–62.

(10) Buryak, A. V.; Kivshar, Y. S.; Shih, M.-F. S. M.-F.; Segev, M. Induced Coherence and Stable Soliton Spiraling. *Tech. Dig. Summ. Pap. Present. Quantum Electron. Laser Sci. Conf.* **1999**.

(11) Shih, M.; Segev, M.; Salamo, G. Three-Dimensional Spiraling of Interacting Spatial Solitons. *Phys. Rev. Lett.* **1997**, *78*, 2551–2554.

(12) Rotschild, C.; Alfassi, B.; Cohen, O.; Segev, M. Long-Range Interactions between Optical Solitons. *Nat. Phys.* **2006**, *2*, 769–774.

(13) Fratalocchi, A.; Peccianti, M.; Conti, C.; Assanto∗, G. Spiraling and Cyclic Dynamics of Nematicons. *Mol. Cryst. Liq. Cryst.* **2004**, *421* (1), 197–207.

(14) Ambrosio A.; Marrucci L.; Borbone F.; Roviello A.; Maddalena P. Light-induced spiral mass transport in azo-polymer films under vortex-beam illumination. *Nat Commun.* **2012**; *3,* 989.

(15) Schjødt-Eriksen, J.; Schmidt, M. R.; Juul Rasmussen, J.; Christiansen, P. L.; Gaididei, Y. B.; Bergé, L. Two-Beam Interaction in Saturable Media. *Physics Letters A*. **1998**, *246*, 423–428.

(16) Villafranca, A. B.; Saravanamuttu, K. An Experimental Study of the Dynamics and

Temporal Evolution of Self-Trapped Laser Beams in a Photopolymerizable Organosiloxane. *J. Phys. Chem. C* **2008**, *112* (44), 17388–17396.

(17) Morim, D. R.; Vargas-Baca, I.; Saravanamuttu, K. Reversibly Trapping Visible Laser Light through the Catalytic Photo-Oxidation of I^- by $Ru(bpy)_3^{2+}$. *J. Phys. Chem. Lett.* **2016**, *7*, 1585-1589.

(18) Malallah, R.; Li, H.; Muniraj, I.; Cassidy, D.; Al-Attar, N.; Healy, J. J.; Sheridan, J. T. Controlling the Trajectories of Self-Written Waveguides in Photopolymer. *J. Opt. Soc. Am. B* **2018**, *35* (8), 2046–2056.

(19) Monro, T. M.; de Sterke, C. M.; Poladian, L. Analysis of Self-Written Waveguide Experiments. *J. Opt. Soc. Am. B* **1999**, *16* (10), 1680–1685.

(20) Snyder, A. W.; Ladouceur, F. Light Guiding Light: Letting Light Be the Master of its Own Destiny. *Opt. Photonics News* **1999**, *10*, 35.

(21) Hudson, A. D.; Ponte. M. R.; Mahmood, F.; Pena Ventura, T.; Saravanamuttu. K. A soft photopolymer cuboid that computes with binary strings of white light. *Nat. Commun.*, **2019**, *10*, 2310.

6 Prismatic 3D printing: Seamless elements from nonlinear waves[††]

6.1 Abstract

Prismatic 3D printing is an atypical method for 3D printing seamless micro- and macroscopic structures by employing nonlinear waves from light emitting diodes (LEDs). This technique takes advantage of optical self-trapping that occurs in the presence of photo-induced refractive index changes; these changes arise from the free-radical photopolymerization of acrylate monomers and is elicited by the incident light pattern to inscribe permanent structures into a photopolymer resin. This technique differs from traditional layer-by-layer 3D printing approaches in that each launched optical pattern creates a prismatic element in a single step. A set of rules was created to establish the structures that can be realized and how a mesh can be decomposed into printable prismatic elements. The resultant prisms can be combined into a complete object by fusing the prisms together, as a form a post-processing or as part of the printing process. This technique was also extended to overlapping prismatic elements, illustrating our ability to minimize the number of printable elements and increase printing speeds to faster than 100x the speed of conventional stereolithographic printers. Improved mechanical properties and increased speeds are accompanied by a decrease in resolution

[††] *In preparation.* OAHC and DRM contributed equally to this manuscript. OAH, DRM, DC, EAMH, RA performed experimental work. DRM was responsible for the decomposition of objects into prisms. DRM, KS, IVB, and OAH wrote and edited the manuscript.

compared to stereolithographic printers, but the formation of multi-element components offers a means of imparting different functionality to each element.

6.2 Introduction

3D printing has been harnessed for the fabrication of a variety of objects for applications ranging from biomedical materials to smart robotics — these processes convert digital designs into a physical form.[1–4] A large assortment of printing techniques have emerged over the years including inkjet printing,[5] fused deposition modeling,[6] selective laser sintering,[7] and stereolithography.[8] Many of these technologies are based on the sequential printing of layers of patterned material and boast faster production times[9] and lower production costs[10] than traditional manufacturing approaches. For example, stereolithographic 3D printers write a 2D pattern into a thin layer of photopolymer attached to a stage. The stage is then translated to expose another layer of resin to a new pattern of light, and the process repeated until the object is fabricated.

3D printing techniques that rely on the layer-by-layer assembly of polymer objects can sometimes have long printing times and can impart mechanical weakness along the planes of the printed layers.[11] To circumvent these limitations of printing with layers, continuous printing methods have been introduced which mitigate these weaknesses while obtaining reasonable resolutions. Continuous liquid interface production (CLIP) is a technique that is analogous to stereolithographic printing but uses a resin bath containing an oxygen-permeable window that inhibits photopolymerization; this creates a dead zone that allows the object to be translated more rapidly within the resin.[12] This

process is significantly faster (500 mm/hour) than conventional stereolithography (few mm/hour) as the layers are formed continuously and create more seamless objects. Computed axial lithography (CAL) also overcomes the need for layered printing by calculating the necessary optical profiles required to obtain a 3D object.[13,14] Spadaccini et al. have illustrated the ability to print an object by generating a hologram with 3 orthogonal beams launched into a static resin.[13] This technique has also been extended to using multiple 2D exposures from a DLP projector launched into a resin on a rotating stage.[14] The optical patterns launched into the resin are changed based on tomographic reconstruction at different angles, creating objects within seconds. We have previously introduced another method of fabricating seamless objects — 3D NSCRIPT — a method that exploits nonlinear waves from LEDs and the cationic photopolymerization of epoxides to create 3D objects from 2D amplitude masks.[15] Light employed in traditional stereolithographic techniques broadens due to the natural diffraction of an optical beam as it propagates. The divergence of an optical beam will blur the projected image as it travels in space, minimizing the depth at which a pattern will retain its resolution. 3D NSCRIPT controls the divergence of light as it traverses the resin by taking advantage of the photo-induced changes in refractive index that occur due to photopolymerization, thus allowing an image to retain its shape as it travels. Some additional 3D printing techniques that help to control where polymerization occurs include the use of photochromic molecules to control absorbance[16] and photoinhibitors to hinder polymerization.[17]

Prismatic 3D printing builds on the concepts introduced by 3D NSCRIPT and the ability to suppress diffraction across the sample to fabricate prisms — polyhedra with two

parallel faces. These parallel faces comprise the bases of the prisms, and the shape of both bases is determined by the optical pattern launched into a photopolymerizable resin. We illustrate the buildup of increasingly complex objects composed of prismatic elements using a simpler apparatus and a faster curing photoresin based on the free-radical photopolymerization of acrylate-based monomers. The intensity-dependence of this process is highlighted, illustrating the ability to create tapered and broadened structures, as well as the prismatic elements that maintain their shape as they propagate. A systematic approach is described that breaks down 3D objects into printable volumetric prismatic elements — these elements are permitted to intersect allowing for further buildup of objects from nonlinear waves.

The formation of structures with nonlinear waves relies on the light-induced positive changes in refractive index (Δn) that arise from photopolymerization to counteract the natural divergence of the beam in the medium.[18,19] This process can be described by (eq 6.1) where the electric field amplitude (ε) can be described in terms of the free-space wavenumber of the optical field (k_0), the attenuation coefficient of the medium (α), and the diffraction of the beam described by the transverse Laplacian (∇_t^2).

$$ik_0 n_0 \frac{\partial \varepsilon}{\partial z} + \frac{1}{2}\nabla_t^2 \varepsilon + k_0^2 n_0 \Delta n \varepsilon + \frac{i}{2} k_0 n_0 \alpha \varepsilon = 0 \qquad (6.1)$$

As the refractive index increases, the beam will self-focus and narrow, until diffraction is suppressed, and a self-trapped beam is formed.

6.3 Results and discussion

6.3.1 Prismatic printing process and calibration

Figure 6-1 illustrates the optical apparatus utilized for prismatic 3D printing and a simple case of a circular or near-Gaussian beam introduced into a medium. The process begins by launching a blue beam (λ = 460 nm) through an amplitude mask with a specific pattern onto the entrance face of the cell that contains an acrylate photoresin and a visible light photoinitiator (Figure 6-1a). The majority of the objects presented herein were fabricated in multiple steps, using up to 3 amplitude masks placed on the sides of the resin cell. Once the light pattern imposed to the LED beam creates the desired part of the object by propagating through the sample, the beam is blocked, and the resin bath rotated to launch the beam through another amplitude mask to create a different prismatic element. This process is repeated until the full object is complete. Prismatic elements were also fabricated separately and glued together into final objects in certain instances where the prisms did not overlap.

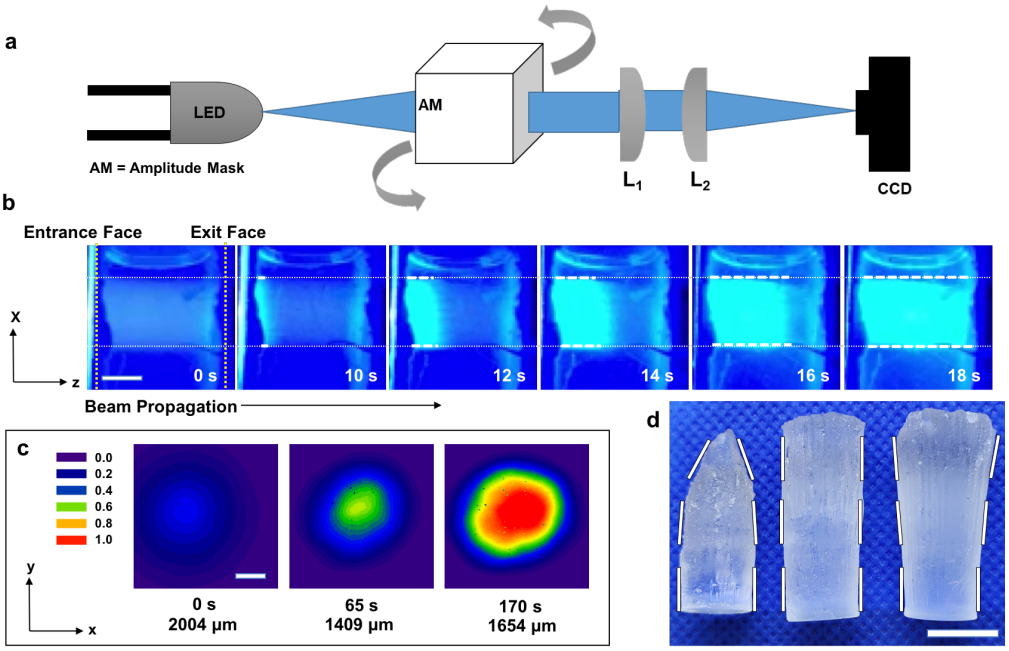

Figure 6-1 (a) Scheme of the optical assembly employed consisting of a blue LED (λ = 460 nm) and up to 3 amplitude masks (AM) placed at the transparent walls of the rotatable resin sample cell. Imaging of the optical profile at the exit face of the resin bath during the formation of cylinders was achieved with a planoconvex lens pair (L1, f.l = 250 mm and L2, f.l. = 250 mm) and a CCD camera. (b) Side-view images of the growing cylinder with input width = 5 mm, length = 11 mm, intensity = 1.1 mW mm^{-2} and scale bar = 2 cm. The sample cell consisted of a cut syringe with glass cover slips glued to each end. (c) Time evolution of the spatial intensity profile at the exit plane of the sample with a growing cylinder with input width = 2 mm, length = 11 mm and scale bar = 1 cm. (d) Final printed polymer cylinders with input width = 10 mm, length = 27 mm and obtained with an LED beam at incident intensities from left to right of 0.47 mW mm^{-2}, 1.1 mW mm^{-2} and 1.9 mW mm^{-2}. Scale bar = 1 cm.

Figure 6-1b illustrates a side-view image of the self-trapping process within the photoresin as a 5 mm circular input beam propagates through the 11 mm sample. After a delay time of ~ 10 s from inhibition due to the presence of oxygen, the propagating polymerization front can be seen travelling at a linear velocity of ~1.3 mm/s, which translates to printing speeds of over 1000 mm/h; speeds faster than traditional SLA methods. Figure 6-1c depicts the spatial intensity profile at the exit face of an 11 mm

sample with a 2 mm input width. As photopolymerization occurs and the corresponding positive changes in refractive index causes the self-trapping of light, the intensity of the light at the exit plane as visualized by the camera increases by 4.4-fold during the course of the experiment. This increase occurs more rapidly in the centre of the beam, giving the impression of a decrease in beam size, but the intensity and beam size subsequently increase until the cylinder is formed.

In order to identify an appropriate operational intensity, we performed several experiments where we fabricated cylinders at different intensities (Figure 6-1d). A 10 mm input beam with an intensity of 0.47 mW mm^{-2} launched into a 27 mm long sample resulted in a tapered structure, with a decreasing cross-section as it propagates along z. This behaviour is attributed to the polymerization occurring predominantly in the centre as the outer regions of the beam are not intense enough to overcome inhibition due to oxygen. In contrast, higher intensities of 1.9 mW mm^{-2} produce a large concentration of initial radicals in regions of the diffracted profile which can initiate polymerization in those regions before self-trapping has time to occur. This resulted in a structure that gets larger as the light propagates. It is only at the intermediate intensity of 1.1 mW mm^{-2} that the propagation of the 2D circular beam results in the inscription of a cylinder. The aforementioned calibration must be carried out for all photopolymer systems due to their varying kinetics.

6.3.2 Decomposition of objects into prismatic elements

The systematic deconstruction of complex objects into prismatic elements requires that an object, O, can be decomposed into prisms, P_n, such that the union of all prismatic elements results in the formation of the object (eq 6.2).

$$O = P_1 \cup P_2 \cup \ldots P_n \tag{6.2}$$

This approach begins by taking a 3D mesh — a file comprised of the vertices, edges and faces that define a 3D object — and sequentially performing operations until prismatic elements are formed. Due to the nature of the printing process, it is necessary that each element takes the shape of a prism (e.g. rectangular prisms, triangular prisms, cylinders, trapezoidal prisms, etc.) and prohibits some geometric features based on 2 basic rules:

Rule 1: If two triangular faces share an edge, the mesh is not printable.

Rule 2: Two non-rectangular/non-trapezoidal faces cannot share an edge.

These rules prevent the prismatic printing of spheres, cones and pyramids, for example, and is a limitation to this printing method. The decomposition of objects can be achieved using computational algorithms that are iteratively applied to 3D meshes. Convex decomposition, for example, is employed to partition a surface into convex clusters.[20–22] Line drawings have been decomposed into separate objects by identifying hidden lines and concealed internal faces that can be used to partition an object into simpler geometric entities.[20] The above methods inspired the breakdown of our objects into prismatic elements using the following steps (Figure 6-2):

Step 1: Edges between attached coplanar faces are removed. This step is taken to ensure that an object is broken down into the fewest number of possible fragments to reduce the number of printing steps.

Step 2: Internal faces are identified based on the work by Liu et al.[20] These internal faces are comprised of visible edges and vertices, and do not intersect with any other edges within the object. Partitioning along these internal faces creates 2 fragments, each possessing a copy of the internal face and its associated vertices and edges.

Step 3: The geometric requirement for printable prisms is the presence of rectangular or trapezoidal faces adjacent to each base. There can therefore be no two adjacent faces that are not rectangular or trapezoidal. If two such faces share an edge, then one must modify the object by creating new edges until this is no longer true. The new edge should be drawn on the face comprised of more edges and it should be drawn either parallel or orthogonal to the shared edge; this process reduces the final number of components by breaking down the more complex polygon.

Step 4: If at any point during the decomposition there exist two adjacent triangles that share an edge, the object is not printable via prismatic 3D printing and the mesh must be modified, and then returning to step 1.

Step 5: If the reduced elements contain no two adjacent non-rectangular/non-trapezoidal faces, then that prismatic element can be printed via this printing method. Elsewise, repeat steps 2, 3 and 4 until this becomes true.

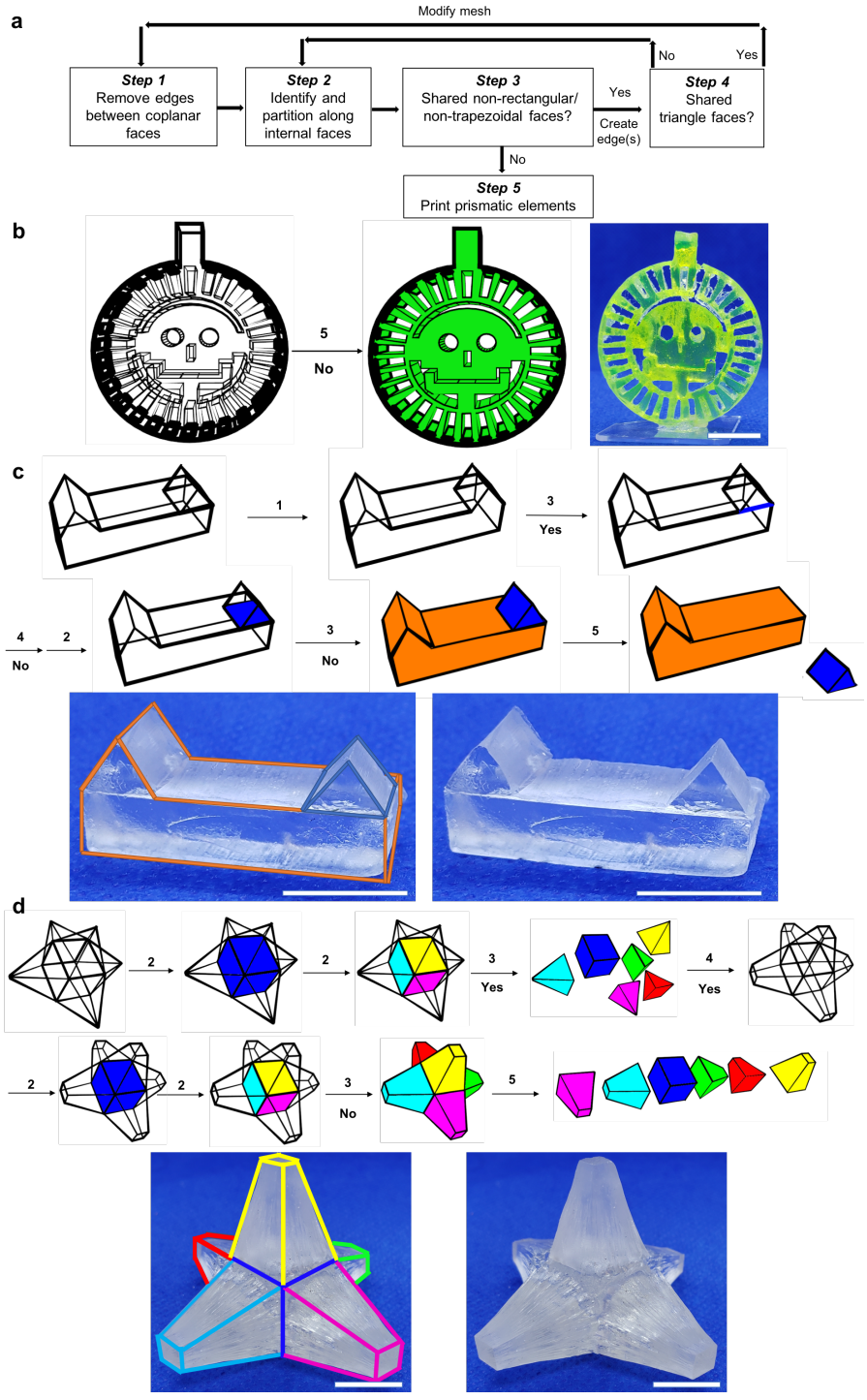

Figure 6-2 (A) Flowchart depicting the decomposition steps that were carried out to convert mesh files into printable prismatic elements and the decomposition of 3 objects (B-D). Scale bar = 1 cm. The printed elements were glued together in (C) and (D).

Figure 6-2 shows a flow chart that includes the necessary steps for the decomposition of objects into prismatic elements. The decomposition of each object is depicted for 3 separate objects alongside the final printed structures, with each prismatic element possessing a different colour. The simplest decomposition occurs when the object is already a prism, such is the case for the disk of death (Figure 6-2b). There exist no edges between coplanar faces (*Step 1*), no internal faces (*Step 2*) and no adjacent non-rectangular/non-trapezoidal faces (*Step 3*). The only two faces with more than 4 edges are the bases of the prism. This object is identified as a printable prismatic element (*Step 5*) and was printed in < 30 s. A coumarin dye was introduced into the photopolymer resin to provide colour to the object.

Figure 6-2c depicts the decomposition of a house with two inequivalent slanted rooftops. Although two triangular prisms and a rectangular prism are clearly visible, the printing of this house would require 3 steps. The removal of edges shared between the coplanar triangular and rectangular faces (*Step 1*) reduces the overall number of printing steps. No internal faces are present (*Step 2*) but there exist two 6-sided faces that share an edge (*Step 3*), so an additional edge was drawn parallel to the shared edge. With no shared triangular faces (*Step 4*), we proceed to identify an internal face that can be partitioned (*Step 2*). The resulting elements have no adjacent non-rectangular/non-trapezoidal faces (*Step 3*) and can therefore be printed. (*Step 5*). The printed elements were printed in a total of ~55 s.

The next example (Figure 6-2d) illustrates what occurs when the algorithm encounters a non-printable element. There are no shared edges between coplanar faces (*Step 1*) and

one internal face (*Step 2*) in the object, resulting in two triangular pyramids after the partitioning. Rectangular pyramids violate *Rule 1* since they possess two shared triangular faces (S*tep 4*). The only way to mitigate this issue is to convert the rectangular pyramids into trapezoidal prisms and repeating *Steps 1-5*. The resulting trapezoidal prisms were fabricated using high intensities, capturing and inscribing the diffracted profile (Figure 6-1d). Printing of 5 trapezoidal prisms and one rectangular prism was completed in a total of ~160 s.

Increasingly complex objects can also be fabricated. Figure 6-3 illustrates the decomposition of a hockey player into 3 prismatic elements. With no shared coplanar edges (*Step 1*), two internal faces (*Step 2*) and no shared non-rectangular/non-trapezoidal faces (*Step 3*), the object is quickly decomposed into the three pieces which are printed within 100 s (*Step 5*).

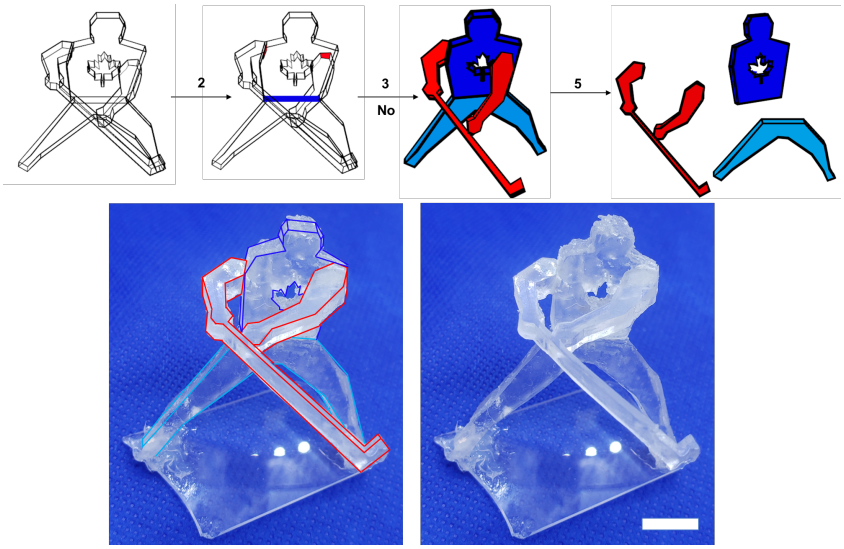

Figure 6-3 Decomposition steps that were carried out to convert a hockey player mesh into printable prismatic elements and the resulting printed object.

This ability to fabricate multiple prismatic elements using nonlinear waves was extended to print other objects found in the Supplementary 6.6.2 alongside their decomposition into prismatic elements.

6.3.3 Printing of intersecting prismatic elements

The union of prismatic elements according to (eq 6.2) remains true in instances when the prismatic elements intersect. The following section highlights our ability to decompose these intersecting prisms, by combining multiple decomposition pathways. Figure 6-4 depicts the decomposition of a runner using the previously described steps.

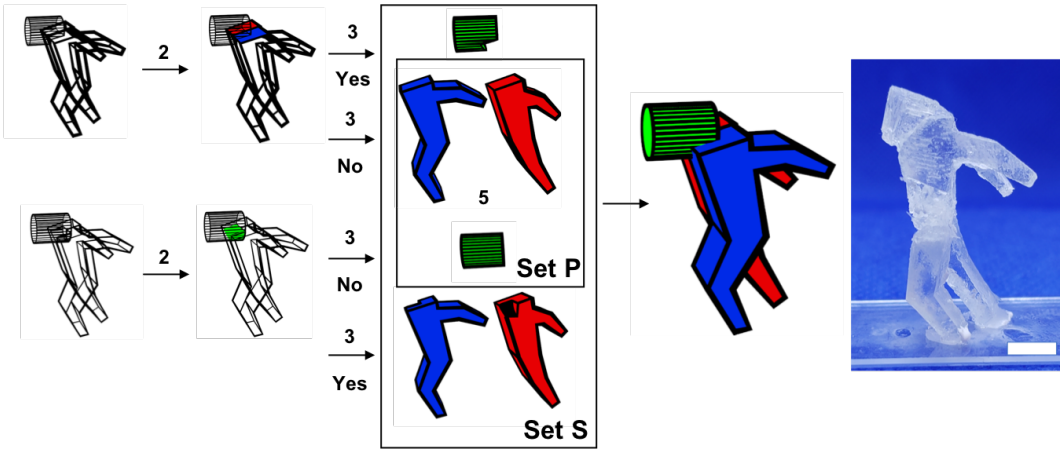

Figure 6-4 Decomposition of a runner using two degenerate methods and the fabrication of a runner. Scale bar = 1 cm.

The runner possesses no shared edges between coplanar faces (*Step 1*) but does possess several internal faces (*Step 2*) based on the mesh of the object. Depending on which partition the algorithm carries out first, one obtains either two prismatic body pieces and one unprintable non-prismatic head OR one prismatic head and two unprintable non-prismatic body pieces. Both routes on their own are unable to create the necessary elements

to build the object, but a subset of prismatic elements (P) within that superset (S) exist (eq 6.3) such that those prisms can combine to create an object according to (eq 6.2).

$$P \subseteq S \tag{6.3}$$

This runner is printed using 3 amplitude masks and the sequential rotation of the sample. The LED beam was first launched through a circular mask to create the head. This was followed by a 90-degree rotation and use of one body mask to create half of the body by stopping the polymerization once the propagating wavefront reached halfway. Finally, the resin bath was rotated 180^{o} and the beam was launched through a second body mask until the second half of the runner's body fused with the other half (Figure 5). The total printing time of the runner was ~43 s, and the process was extended to fabricate 2 additional runners (Supplementary 6.6.2, Figures 6-12 and 6-13). To reaffirm that these intersecting prismatic elements can be created, we printed a lattice of intersecting rods (Figure 6-14) using 3 masks that each contain 9 square apertures. A lattice of 27 intersecting rods was fabricated. The union of prismatic elements to create objects suggests that we can also build up objects from a set of known prisms by creating meshes that comprise of unified prisms.

6.3.4 Speed and resolution

In order to compare the quality and speed of our technique with traditional stereolithography, we printed a runner using an SLA printer with the same photoresin (Figure 6-5). Our technique was significantly faster with a printing time of 161 s compared to 9960 s with the SLA printer. The minimum feature size in the XY direction that can be

printed via prismatic printing is on the order of 500 µm while those obtained with a Form 2 SLA printer are on the order of 100 µm.

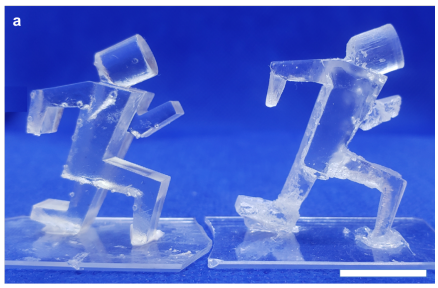

Figure 6-5 Images depicting a runner printed using SLA and prismatic printing. Scale bar = 1 cm.

A summary of the meshes, fragmented models from the manual decomposition and the final printed structures are displayed in Figure 6-6.

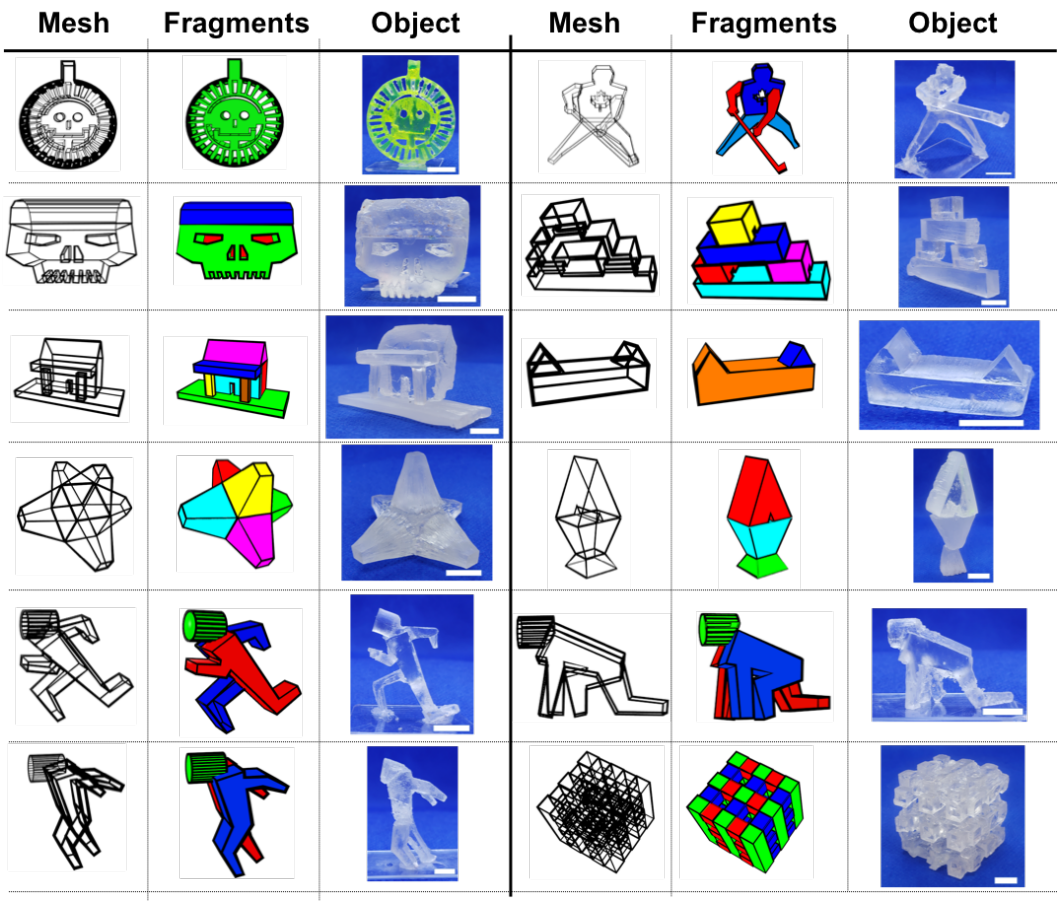

Figure 6-6 Illustration of fragmented model from various meshes and the resulting printed objects.

6.4 Conclusions and outlook

The prismatic printing of three-dimensional objects using nonlinear waves offers a facile and rapid, room temperature method of printing objects that are comprised of multiple prisms using LED sources. The decomposition of these objects into prisms has been determined using an algorithm that reduces the object into smaller elements. The reverse process of building objects starting from prismatic elements can be done by unifying multiple prisms to build an initial mesh. As proof of concept, we showed that self-trapped beams sequentially launched through 3 amplitude masks and 3 directions can

inscribe prismatic elements in situ to make objects including a series of runners, a lattice, and a skull. The higher refractive index of these written structures relative to their surroundings may offer these materials light-guiding properties, allowing us to print different waveguide architectures. Prismatic printing of functional materials that respond to other stimuli and combination of these prismatic elements may enable the formation of more complex, smart polymers for various applications.

6.5 Methods

6.5.1 Materials

Abecryl® 8210, Genomer* 1122TF and Sartomer SR 494 were donated from Allnex, Rahn USA Corp. and Arkema Inc, respectively. Photoinitiators Irgacure® 189 and Irgacure® 819 were obtained from Ciba Specialty Chemicals. Coumarin 6 was obtained from Sigma-Aldrich.

6.5.2 Preparation of photopolymer

The resin used was a modified version of Autodesk Standard clear prototyping Resin (PR48). It was obtained by mixing Abecryl® 8210 (39.1%), Sartomer SR 494 (39.1 %), Genomer* 1122TF (19.6%), Irgacure® 819 (0.2%) and Irgacure® 184 (2.0%). The mixture was stirred for 48 h before using it. For the disk of the death, Coumarin 6 was added to the resin prior to stirring for 48 h.

6.5.3 Optical apparatus and imaging

A blue LED (λ_{max} = 460 nm, Kerber Applied Research Inc.) was used as the main light source. Tapered objects were fabricated at 2.33 mW mm^{-2} with a separate mounted LED (λ_{max} = 470 nm, Thorlabs). The dimensions of each cell varied depending on the target size

for each object. Amplitude masks with the desired pattern to be imposed on the beam were placed at the entrance face of the sample cell. Vinyl amplitude masks were printed using a Graphtec Craft ROBO vinyl cutter. A plano-convex lens pair (L1, f.l = 250 mm and L2, f.l. = 250 mm) and a CCD camera (WinCamD XHR, DataRay Inc.) were used for monitoring the spatial intensity profile at the exit face when printing cylindrical rods during calibration. A Samsung Galaxy S6 phone camera was used for side imaging of the propagating structures.

6.5.4 Post-processing of structures

Large elements were sanded due to excess side polymerization during the photoreaction. Prismatic elements printed separately were glued together using small amounts of photoresin and subsequently irradiating with the LED.

6.5.5 Decomposition of mesh

Mesh files were created in Blender (v.2.79) and manually modified using the decomposition steps (*vide supra*) (prismatic elements coloured differently once decomposed).

6.5.6 SLA Printing

SLA printing of the runner was carried out using a Form 2 printer from Formlabs.

6.6 Supplementary information

6.6.1 Calibration of intensity during printing of cylinders

Cylindrical rods were printed as a means of calibration (Table S1) and yielded optimal printing conditions at 1.1 mW mm^{-2}. At distances larger than 5 cm, there is

greater difficulty in maintaining the beam diameter as the beam propagates, limiting our technique to printing smaller objects.

Table 6-1 Diameter at the entrance and exit face of cylinders fabricated with a beam 10 mm wide at 0.47, 1.1 and 1.9 mW mm^{-2} (3 replicates).

Intensity (mW mm^{-2})	10 mm Pathlength		27 mm Pathlength	
	Diameter at Entrance (mm)	Diameter at Exit (mm)	Diameter at Entrance (mm)	Diameter at Exit (mm)
0.47	9.4 ± 0.2	5.0 ± 2.0	9.5 ± 0.1	8.5 ± 0.5
1.1	9.9 ± 0.1	10.4 ± 0.5	9.9 ± 0.1	10.6 ± 0.3
1.9	10.0 ± 0.1	10.9 ± 0.2	10.1 ± 0.3	13.2 ± 0.1

6.6.2 Prismatic printing of separate elements

The following section describes the printing of multiple prismatic elements and then separately combining those elements into a single object. The same manual decomposition steps are applied to break down an object into the corresponding prismatic elements in Figures S1 and S2.

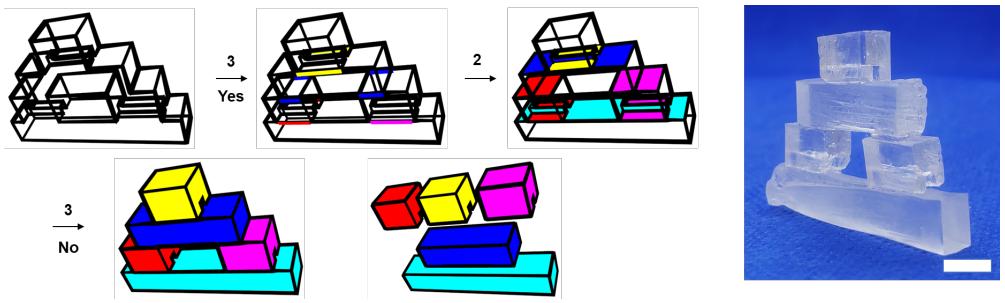

Figure 6-7 Decomposition steps that were carried out to convert a mesh into printable prismatic elements and the resulting printed object. Scale bar = 1 cm.

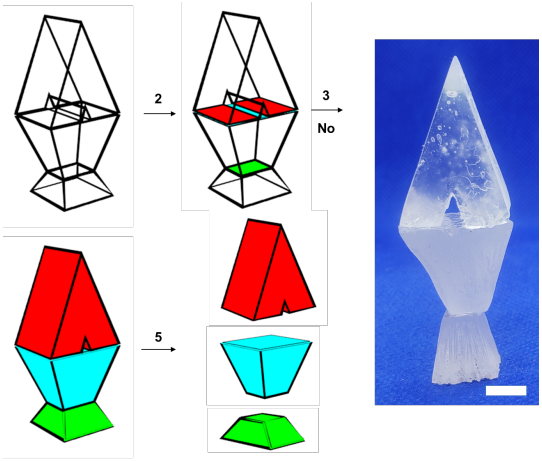

Figure 6-8 Decomposition steps that were carried out to convert a mesh into printable prismatic elements and the resulting printed object. Scale bar = 1 cm.

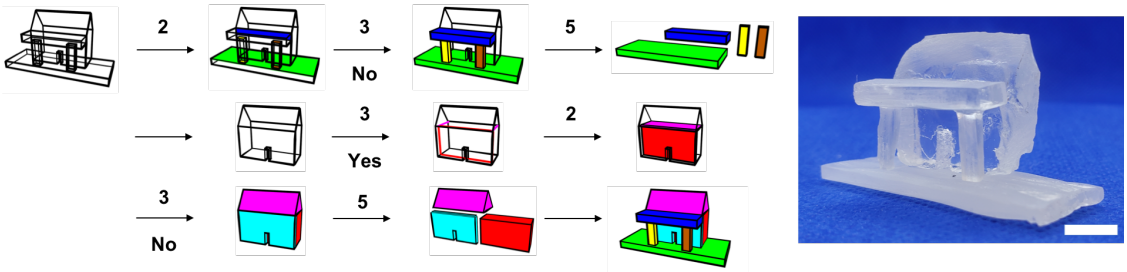

Figure 6-9 Decomposition steps that were carried out to convert a house mesh into printable prismatic elements and the resulting printed object. Scale bar = 1 cm.

6.6.3 Printing objects in situ

Unlike the previous examples that looked at printing individual elements and gluing them together, we are also able to create multiple elements by rotating the stage of the sample. By creating multi-element complex objects with amplitude masks (Figure 6-10) placed at the glass walls of the resin cell, we are able to fuse together elements rather than using adhesive to combine the pieces post-printing. Figures 6-11 to 6-14 illustrate the manual decomposition of objects printed in situ, with Figures 6-12 to 6-14 containing

multiple intersecting prismatic elements which necessitated the use of our decomposition method.

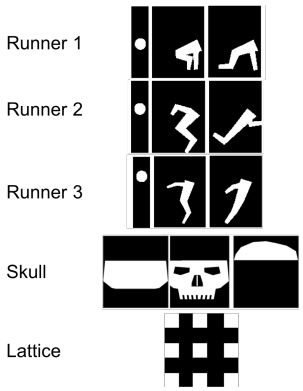

Figure 6-10 Amplitude masks used to print objects in situ.

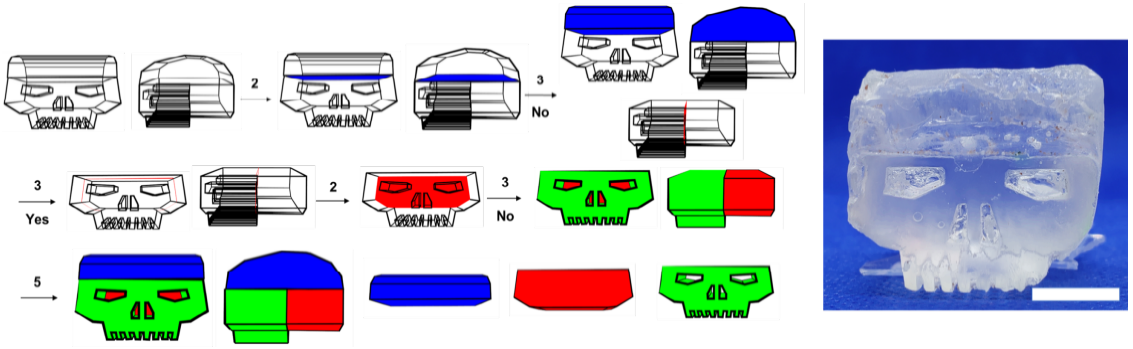

Figure 6-11 Decomposition steps that were carried out to convert a skull mesh into printable prismatic elements and the resulting printed object. Scale bar = 1 cm.

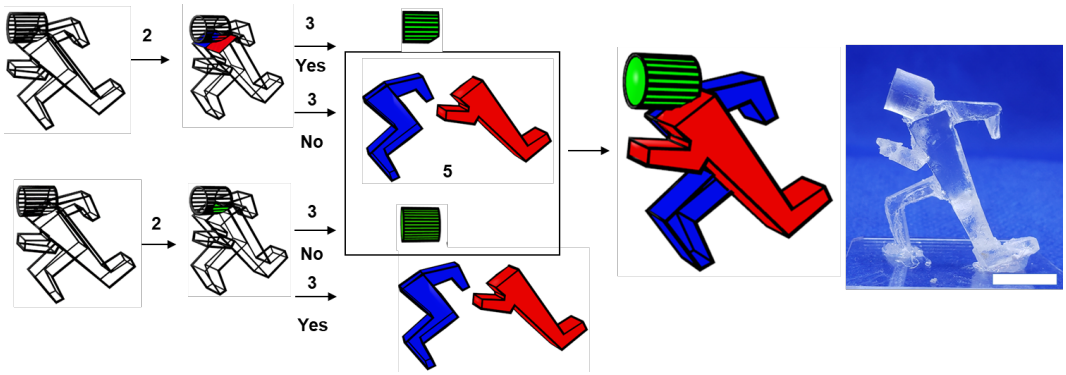

Figure 6-12 Decomposition of a sprinting runner using two methods and the fabrication of the runner. Scale bar = 1 cm.

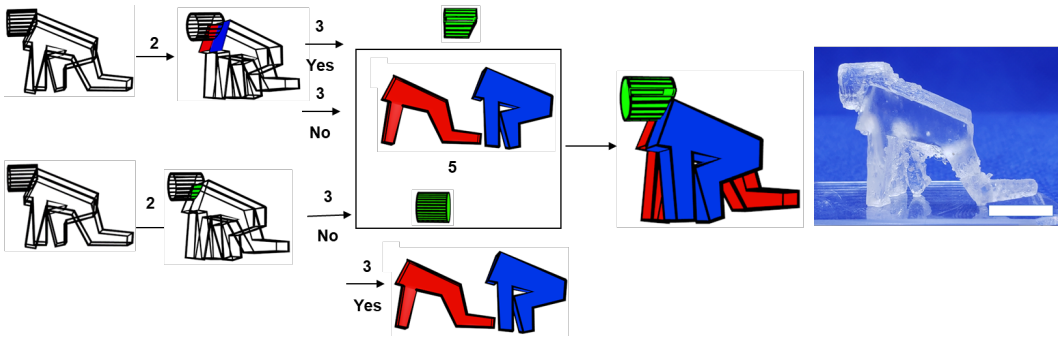

Figure 6-13 Decomposition of a starting runner using two methods and the fabrication of the runner. Scale bar = 1 cm.

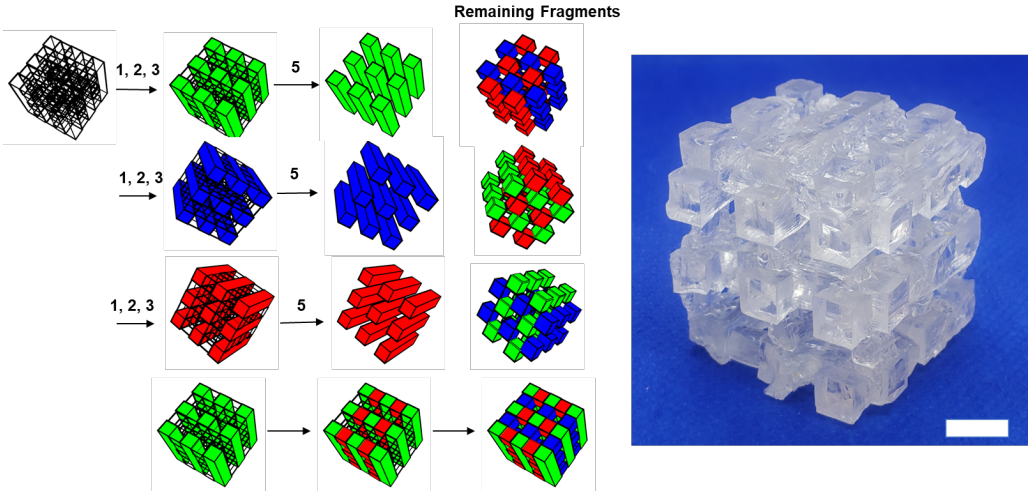

Figure 6-14 Decomposition of a lattice using 3 methods and the fabrication of the lattice in 3 steps with overlapping elements. Scale bar = 1 cm.

6.7 Acknowledgements

We thank Ciba Specialty Chemicals, Allnex, Rahn USA Corp. and Arkema Inc for the generous donation of photoinitiator and resin components. We thank the Moran-Mirabel group for access to the vinyl cutter and The Forge at McMaster Innovation Park for use of the SLA printer. OAHC and DRM acknowledge financial support from the National Council of Science and Technology of Mexico and the Natural Sciences and Engineering Research Council, respectively. Finally, we acknowledge funding from the

Natural Sciences and Engineering Research Council and Canadian Foundation for Innovation.

6.8 References

(1) Stevens, A. G.; Oliver, C. R.; Kirchmeyer, M.; Wu, J.; Chin, L.; Hart, A. J.; Polsen, E. S.; Archer, C.; Boyle, C.; Garber, J. Conformal Robotic Stereolithography. *3D Print. Addit. Manuf.* **2016**, *3* (4), 226–235.

(2) Vithani, K.; Boyd, B. J.; Goyanes, A.; Basit, A. W.; Gaisford, S.; Jannin, V.; Basit, A. W.; Gaisford, S.; Boyd, B. J. An Overview of 3D Printing Technologies for Soft Materials and Potential Opportunities for Lipid-Based Drug Delivery Systems. *Pharm. Res.* **2018**, *36* (1), 4.

(3) Liska, R.; Schuster, M.; Inführ, R.; Turecek, C.; Fritscher, C.; Seidl, B.; Schmidt, V.; Kuna, L.; Haase, A.; Varga, F.; Lichtenegger, H.; Stampfl, J. Photopolymers for Rapid Prototyping. *J. Coatings Technol. Res.* **2007**, *4* (4), 505–510.

(4) Melchels, F. P. W.; Feijen, J.; Grijpma, D. W. A Review on Stereolithography and Its Applications in Biomedical Engineering. *Biomaterials* **2010**, *31* (24), 6121–6130.

(5) de Gans, B.-J.; Duineveld, P. C.; Schubert, U. S. Inkjet Printing of Polymers: State of the Art and Future Developments. *Adv. Mater.* **2004**, *16* (3), 203–213.

(6) Hutmacher, D. W.; Schantz, T.; Zein, I.; Ng, K. W.; Teoh, S. H.; Tan, K. C. Mechanical Properties and Cell Cultural Response of Polycaprolactone Scaffolds Designed and Fabricated via Fused Deposition Modeling. *J. Biomed. Mater. Res.* **2001**, *55* (2), 203–216.

(7) Williams, J. M.; Adewunmi, A.; Schek, R. M.; Flanagan, C. L.; Krebsbach, P. H.; Feinberg, S. E.; Hollister, S. J.; Das, S. Bone Tissue Engineering Using Polycaprolactone Scaffolds Fabricated via Selective Laser Sintering. *Biomaterials* **2005**, *26* (23), 4817–4827.

(8) Choong, Y. Y. C.; Maleksaeedi, S.; Eng, H.; Wei, J.; Su, P.-C. 4D Printing of High Performance Shape Memory Polymer Using Stereolithography. *Mater. Des.* **2017**, *126*, 219–225.

(9) Esmaeilian, B.; Behdad, S.; Wang, B. The Evolution and Future of Manufacturing: A Review. *J. Manuf. Syst.* **2016**, *39*, 79–100.

(10) Thomas, D. Costs, Benefits, and Adoption of Additive Manufacturing: A Supply Chain Perspective. *Int. J. Adv. Manuf. Technol.* **2016**, *85* (5–8), 1857–1876.

(11) Dizon, J. R. C.; Espera, A. H.; Chen, Q.; Advincula, R. C. Mechanical Characterization of 3D-Printed Polymers. *Addit. Manuf.* **2018**, *20*, 44–67.

(12) Tumbleston, J. R.; Shirvanyants, D.; Ermoshkin, N.; Janusziewicz, R.; Johnson, A. R.; Kelly, D.; Chen, K.; Pinschmidt, R.; Rolland, J. P.; Ermoshkin, A.; Samulski, E. T.; DeSimone, J. M. Continuous Liquid Interface Production of 3D Objects. *Science* **2015**, *347* (6228), 1349 LP-1352.

(13) Shusteff, M.; Browar, A. E. M.; Kelly, B. E.; Henriksson, J.; Weisgraber, T. H.;

Panas, R. M.; Fang, N. X.; Spadaccini, C. M. One-Step Volumetric Additive Manufacturing of Complex Polymer Structures. *Sci. Adv.* **2017**, *3* (12), eaao5496.
(14) Kelly, B. E.; Bhattacharya, I.; Heidari, H.; Shusteff, M.; Spadaccini, C. M.; Taylor, H. K. Volumetric Additive Manufacturing via Tomographic Reconstruction. *Science* **2019**, *363* (6431), 1075 LP-1079.
(15) Basker, D. K.; Cortes, O. A. H.; Brook, M. A.; Saravanamuttu, K. 3D Nonlinear Inscription of Complex Microcomponents (3D NSCRIPT): Printing Functional Dielectric and Metallodielectric Polymer Structures with Nonlinear Waves of Blue LED Light. *Adv. Mater. Technol.* **2017**, *2* (5), 1600236–n/a.
(16) Dolinski, N. D.; Page, Z. A.; Callaway, E. B.; Eisenreich, F.; Garcia, R. V; Chavez, R.; Bothman, D. P.; Hecht, S.; Zok, F. W.; Hawker, C. J. Solution Mask Liquid Lithography (SMaLL) for One-Step, Multimaterial 3D Printing. *Adv. Mater. (Weinheim, Ger.* **2018**, *30* (31), n/a.
(17) de Beer, M. P.; van der Laan, H. L.; Cole, M. A.; Whelan, R. J.; Burns, M. A.; Scott, T. F. Rapid, Continuous Additive Manufacturing by Volumetric Polymerization Inhibition Patterning. *Sci. Adv.* **2019**, *5* (1), eaau8723.
(18) Biria, S.; Morim, D. R.; An Tsao, F.; Saravanamuttu, K.; Hosein, I. D. Coupling Nonlinear Optical Waves to Photoreactive and Phase-Separating Soft Matter: Current Status and Perspectives. *Chaos An Interdiscip. J. Nonlinear Sci.* **2017**, *27* (10), 104611.
(19) Trillo, S.; Torruellas, W. *Spatial Solitons*; Springer: New York, 2001.
(20) Liu, J.; Chen, Y.; Tang, X. Decomposition of Complex Line Drawings with Hidden Lines for 3D Planar-Faced Manifold Object Reconstruction. *IEEE Trans. Pattern Anal. Mach. Intell.* **2011**, *33* (1), 3–15.
(21) Liu, J.; Cao, L.; Li, Z.; Tang, X. Plane-Based Optimization for 3D Object Reconstruction from Single Line Drawings. *IEEE Trans. Pattern Anal. Mach. Intell.* **2008**, *30* (2), 315–327.
(22) Changqing, Z.; Shifeng, C.; Hongbo, F.; Jianzhuang, L. Progressive 3D Reconstruction of Planar-Faced Manifold Objects with DRF-Based Line Drawing Decomposition. *IEEE Trans. Vis. Comput. Graph.* **2015**, *21* (2), 252–263.

7 Conclusions and future work

Light and nonlinear materials cooperatively interact in unique ways, allowing us to manipulate light using methods not possible with linear media. By photochemically changing the refractive index of a material, we can create self-trapped beams that are capable of interacting with one another. By changing the divergence of light and spatially changing the refractive index, we can create new 3D structures for various applications or we can harness light and soliton interactions to transfer information between beams. Depending on the reversibility of the photochemistry and the kinetics within the materials, we can investigate these effects in a wide range of materials and expand on the growing knowledge of their interactions for applications in new photonics technologies.

7.1 Self-trapping due to the photocatalytic oxidation of iodide

Initial studies looked at harnessing the catalytic photo-oxidation of iodide to triiodide using $Ru(bpy)_3^{2+}$ within a polymer to generate a refractive index change [Chapter 2]. Self-trapping originates from the reaction and the corresponding Δn along the beam propagation path. In the absence of light, these self-induced waveguides gradually dissipate and allow for the self-trapping process to be carried out once again. This material demonstrated that photochemically generated self-trapped beams can be created in any material capable of changing the Δn and that their reversible formation is possible. Through several control experiments, we confirmed the necessity of the excited state $Ru(bpy)_3^{2+*}$, demonstrated the ability to slow down self-trapping by adding a quencher through Stern-Volmer analysis and even identified the secondary process of oxidative

polymer cross-linking that can occur in the absence of iodide. We also illustrated the intensity-dependence of this nonlinear process.

7.2 Reversible self-trapping and nonlocal interactions in spiropyran-functionalized hydrogels

We demonstrated that reversible, switchable self-trapped beams can be elicited in hydrogels containing covalently-linked spiropyran chromophores that isomerize upon exposure to visible light [Chapter 3]. The "on-off" switching mechanism converts the optical energy from the light field to a physical transformation, that manifests as a photo-induced contraction and produces the change in Δn necessary for self-trapping to occur. Through several control experiments, the necessity of the photoacidic merocyanine substituents covalently attached to the hydrogel and the pH-responsive acrylic acid substituents were determined. The ability to reversibly create self-trapped beams was illustrated and the intensity-dependence of self-trapping was shown. A model that combines the light propagation, photoisomerization and swelling kinetics of the polymer was created and correlated well with experimental observations for single beam self-trapping. The unexpected nonlocal interaction between two self-trapped beams occurred even at 200 μm (10x beam width), allowing for modulation of optical beams that shared no optical overlap. This behaviour resulted from the mechanical forces in the gel that allowed for the beams to communicate with one another throughout the hydrogel, reversibly decreasing the self-trapping efficiency of neighbouring beams and returning to their original self-trapped state when propagating alone.

7.3 Collinear interactions between self-trapped beams in polymers

Studies of collinear interactions between self-trapped beams were carried out in two separate polymer systems as a result of photopolymerization and photo-oxidative reactions, respectively [Chapter 4]. The interactions of self-trapped beams were confirmed to be dependent on their initial separation distances and required initial optical overlap in order for the beams to interact within the first minute of their formation. The interactions in both systems were attractive in nature but the subsequent changes to the beams were both different due to their respective chemical kinetics. The attraction between two self-trapped beams ($1/e^2 = 20$ μm) separated by 25 μm (1.25x beam width) in the photopolymer system resulted in the merging of the beams and formation of a single waveguide. By monitoring the output of the evolving optical profile, we observed the swapping of the positions of each beam over time, a phenomenon that was determined to be due to the formation of high refractive index regions along the propagation path that act as lenses- eyes. While these eyes were previously documented, their effect on two interacting beams and the swapping behaviour were not. These studies were supplemented with beam blocking studies and simulations, to confirm the behaviour. The A-parameter from the simulations was large compared to many of the other polymer systems used for self-trapping studies, and the chemical kinetics and rate constants were also related to the A-parameter that was utilized, illustrating the ability to use the model for any saturable system provided diffusion rates are small. The attractive interaction between self-trapped beams in the photo-oxidative system did not result in multiple lens-like eyes along the propagation path, due to the diffusion that can occur over time. Only a

single lens-like inversion occurs from the primary eye, resulting in the output beams having switched positions when separated by 25 μm. The nonlocal attraction between the beams is observed over long periods of time at 50 μm (2.5x beam width) separation, reinforcing the diffusive nature of the nonlocality within this system.

7.4 Out-of-plane interactions between self-trapped beams that rotate

We demonstrated that the interactions of two out-of-plane beams in the two previous systems can lead to orbiting of the output beams [Chapter 5]. The initial local response from Chapter 4 was extended by studying collisions between two angled beams that contain some partial overlap between the beams. It was determined that the beams required a large enough angle so that they do not merge early on, but not so large that the beams propagate past one another without interacting. By analyzing each beam separately throughout the interaction, we were able to visualize the shared lobe of intensity that has been attributed to be responsible for the spiraling interaction in other materials capable of hosting spatial solitons. The eventual merging of the beams appears to occur based on the optical micrographs, preventing any further spiraling from occurring and is also evident by the decrease in angular velocity throughout the experiment. The behaviour in the photooxidative system showed spiraling under similar conditions, and examination of this process in different sized samples allowed us to gain a sense of the trajectories of the beams during the process. The route to strengthen interactions between self-trapped beams may involve slowing down these reactions to provide them with more time to interact.

7.5 3D printing of objects using nonlinear waves through decomposition to prismatic elements

Building on the previous studies of using nonlinear waves to fabricate 3D structures, we took advantage of self-trapping within photopolymers to create objects from multiple prismatic elements [Chapter 6]. Rather than using conventional layer-by-layer methods that take small repeating units to fabricate 3D objects over the course of hours, we launched 2D optical profiles onto the face of a photopolymerizable resin to create larger three-dimensional prismatic units within the resin, that can be combined to create objects. A set of rules was constructed in order to decompose a 3D object of interest into prismatic elements and allowed us to print the object using multiple exposures from different masks at different angles. Printing speed and mechanical strength were improved compared to objects printed with an SLA printer, but at the expense of resolution. While this method does have some limitations, the ease of printing multi-component objects by using different resins for different components may offer a simple method of imparting different functionalities to different prismatic elements.

7.6 General conclusions

This thesis provides several advancements to the field of nonlinear optics in polymers with different photoresponses. The first two contributions describe new photoresponsive systems that are capable of hosting self-trapped beams. Communication between spatial solitons in the literature allowed us to intuit that self-trapped beams in these materials should also be able to interact, unlike in traditional linear media. This initiated the comparison between the interactions of these spatially self-trapped in these materials and

their comparison to their behaviour in photopolymers. We demonstrated that systems that change photochemically are able to show many similarities to other spatial solitons in other nonlinear media and can be used to manipulate the growing self-induced waveguides. The universality of spatial solitons to many different photoresponses illustrates our ability to harness these nonlinear waves in photochemical systems to manipulate light for patterning and all-optical communication between beams of light. The reversible spiropyran-functionalized gel offers a new way of interacting beams of light through the opto-*chemo*-mechanical interaction that occurs between the beams, decreasing self-trapping of neighbouring beams. Our ability to utilize nonlinear waves in photopolymers to 3D print functional architectures composed of prismatic elements demonstrates one such application of optical self-trapping to create objects with enhanced mechanical properties and with very rapid printing speeds.

7.7 Future work and outlook

Future work into nonlinear photochemical waves can involve interactions of different geometries, investigations into different self-action effects, fabrication of new materials with improved photoresponses and the 3D printing of functional materials with applications in optics, photonics, robotics and smart materials.

7.7.1 Further investigations into beam interactions and computing

7.7.1.1 Orthogonal interactions

Our ability to manipulate self-trapped beams by harnessing their interactions can be extended to different geometries. Orthogonal collisions are not often studied because orthogonal beams would not be expected to transfer momentum if they are travelling 90 degrees to one other. When multiple optical filaments from MI are formed from two orthogonal beams in a free-flowing photopolymer, these filaments align and migrate to maximize intersections.[1] This suggests that the index gradients from orthogonal beams can influence one another. Individual orthogonal beams with partial intersection near the primary eye may provide the gradients necessary to observe these types of interactions in photochemical systems.

7.7.1.2 Reversible computing

Nonlocal and reversible interactions, such as those observed within the spiropyran-functionalized hydrogel, may make it possible to harness a nonlinear response for computing-type operations using light.[2] For example, binary computing has been demonstrated in photopolymers capable of modulation instability, with different ordering of filaments representing a binary string.[1] The position of self-trapped beams has been deliberately altered using a collision with a second beam, and related to an operation.[3,4] Future work would involve creating increasingly complex computing systems with materials patterned with different responses.[5,6] Spiropyran-functionalized hydrogels (contraction and nonlocal deformation), lead glass (nonlocal heat transfer), and liquid crystals (nonlocal reorientation) are some possibilities of reversible material types that

can be patterned into connected channels and other geometries. By varying the input of the beams, different outputs would be obtained based on the interactions and computational operations that occur within the material.

7.7.2 Further investigation into self-action effects within new photoresponsive materials

7.7.2.1 Modulation instability

Self-action effects in photopolymers are intensity-dependent and demonstrate the formation of rings, rings of filaments and arrays of filaments through modulation instability.[7] These types of phenomena can occur in other photochemical systems, including Pluronic® F-127 gels that host the photo-oxidation of iodide to triiodide (Chapter 2). Filaments formed within this system change position over time due to diffusion processes within the gel. Modulation instability in a photochemically reversible system would be interesting to observe and would allow for the simultaneous formation of arrays of self-trapped filaments. Attempts to observe modulation instability in the spiropyran-functionalized hydrogels showed no filament formation, likely due to the nonlocal response that decreases the self-trapping efficiency upon introduction of a second beam. It may be possible to observe modulation instability in a similar material that severs the nonlocal response by creating a supramolecular gel out of polymer particles that contract with visible light.

7.7.2.2 Self-defocusing

Another type of nonlinearity that would be interesting to investigate further is the negative photoresponse which can be elicited by depolymerizing a polymer with light (e.g. positive photoresists, self-immolative polymers).[8,9] Preliminary simulations (same

approach as Chapter 4; negative A-parameter) illustrate that a decrease in refractive index leads to self-defocusing behaviour (Figure 7-1).

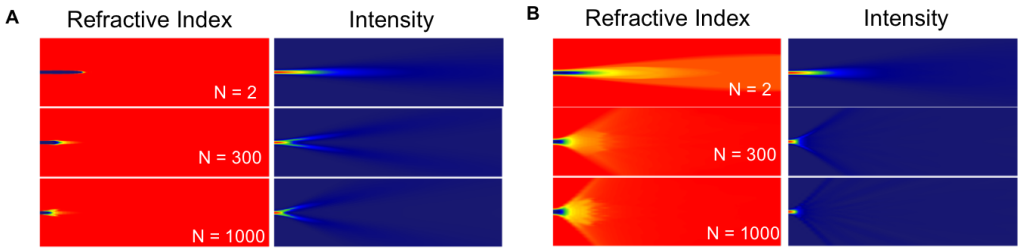

Figure 7-1 Simulations illustrating changes to the index profile and intensity profile as photo-induced refractive index decreases occur, resulting in self-defocusing using the phenomenological model implemented in Chapter 4 with A-parameters of -0.00001 and -0.000001.

Preliminary work resulted in a self-defocusing effect in a Pluronic® F-127 gel with a photoacid system, comprised of $Ru(bpy)_3^{2+}$ and [4-(Octyloxy)phenyl]phenyliodonium hexafluorophosphate (Figure 7-2). Upon irradiation with visible light, the hydrogen bonds are disrupted, and the refractive index decreases as the polymer chains begin to interact more with the surrounding water. The beam changes between a larger, defocused state and a smaller, focused state. Future work would involve applying self-defocusing to create new structures by combining positive and negative nonlinearities into the same material and controlling their rates.

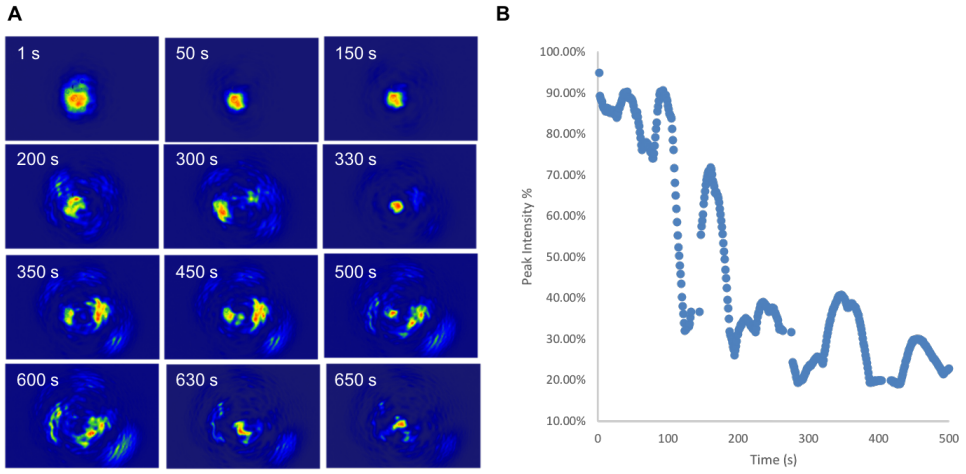

Figure 7-2 (A) Spatial intensity profiles in a 6 mm sample containing Pluronic® F-127, $Ru(bpy)_3^{2+}$ and [4-(Octyloxy)phenyl]phenyliodonium hexafluorophosphate with P = 25 µW. (B) Plot illustrating changes to the maximum relative intensity over time as self-defocusing causes oscillations between a defocused beam or ring and single filaments.

7.7.2.3 Photothermal response

Photothermal responses in lead glass[10] and thermotropic liquid crystals[11,12] tend to be nonlocal in nature, due to thermal diffusion. The diffusion of heat may allow for communication between beams separated by large distances, even when separated by other thermally conductive media.[10] Preliminary attempts to create a new material with a photothermal response resulted in self-defocusing. Thermoresponsive poly(N-isopropylacrylamide) polymer chains undergo a reversible phase transition above the LCST, dispelling water from the irradiated region. This contraction resulted in defocusing of light due to scattering and phase separation within the gel (Figure 7-3). Future work into photothermal responses should focus on materials with larger thermal conductivities such as lead glass, due to the inherent nonlocality of thermal responses.

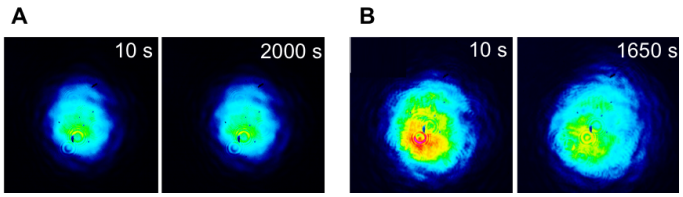

Figure 7-3 Spatial intensity profile of the output plane of a 6 mm hydrogel sample containing thermoresponsive N-isopropylacrylamide. Methyl orange was used as an absorbing dye to nonradiatively release heat. Irradiation at 7 mW caused no noticeable changes (A) but irradiation at 43 mW resulted in self-defocusing, likely due to scattering above the LCST.

7.7.3 Electroactive polymers and materials responsive to other stimuli

The ability to 3D-print prismatic elements to create different objects can be extended to create stimuli-responsive materials and smart robotics technologies. Research into printing electroactive ionic polymers that can be controlled with external electric fields is ongoing. We have demonstrated the ability to print prismatic elements that guide light and bend in the presence of an electric field (Figure 7-4) based on diffusion and swelling processes.[13,14] Simulations of the light distribution in curved passive waveguides at different angles (BeamProp®) shows the types of expected behaviours arising from bending waveguides (Figure 7-5). We have also demonstrated the ability to inscribe arrays of waveguides into these polymers using masks (Figure 7-4), creating an electroactive waveguide array.

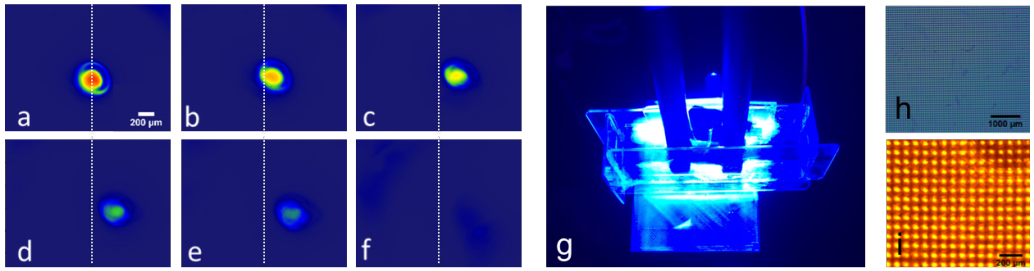

Figure 7-4 CCD images of light guided by an electroactive waveguide printed via prismatic 3D printing using a hydrogel containing acrylic acid to imbue electroactive response (a) prior to electric field and after (b) 30 s, (c) 90 s, (d) 120 s, (e) 150 s, and (f) 180 s. (g) Image of the electroactive waveguide in between two electrodes. (h) CCD image of the self-trapped filaments that have formed. (i) Optical micrograph of the waveguide array (z = 3 mm) formed using electroactive monomers and inscribed using a blue LED and a mask with 80 µm periodicity. Images obtained with Natalie Blanchard and Oscar Alejandro Herrera Cortes.

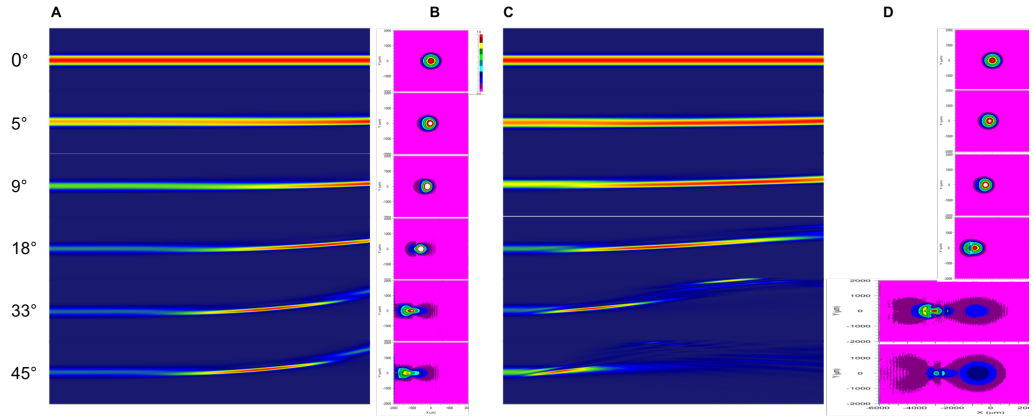

Figure 7-5 Simulations of 0-degree light entering passive waveguides that are curved at an angle (A) or that are slabs at an angle; Δn = 0.4 and z = 6 mm.

Further research is required to improve the response to the electric field. Prismatic printing may also be applied to create other light-guiding materials such as dynamic lenses and couplers. Future work would also involve imparting additional responses to different stimuli to create materials that work cooperatively and behave intelligently.[15]

7.8 References

(1) Hudson, A. D.; Ponte, M. R.; Mahmood, F.; Pena Ventura, T.; Saravanamuttu, K. A Soft Photopolymer Cuboid That Computes with Binary Strings of White Light. *Nat. Commun.* **2019**, *10*, 2310.

(2) Snyder, A. W.; Ladouceur, F. Light Guiding Light: Letting Light Be the Master of Its Own Destiny. *Opt. Photonics News* **1999**, *10*, 35.

(3) Andrade-Lucio, J. A.; Alvarado-Mendez, B.; Rojas-Laguna, R.; Ibarra-Manzano, O. G.; Torres-Cisneros, M.; Jaime-Rivas, R.; Kuzin, E. A. Optical Switching by Coherent Collision of Spatial Solitons. *Electron. Lett.* **2000**, *36*, 1403–1405.

(4) Shi, T.-T.; Chi, S. Nonlinear Photonic Switching by Using the Spatial Soliton Collision. *Opt. Lett.* **1990**, *15*, 1123–1125.

(5) Schneider, G.; Wrede, P. Artificial Neural Networks for Computer-Based Molecular Design. *Prog. Biophys. Mol. Biol.* **1998**, *70*, 175–222.

(6) Schmidhuber, J. Deep Learning in Neural Networks: An Overview. *Neural Networks* **2015**, *61*, 85–117.

(7) Biria, S.; Morim, D. R.; An Tsao, F.; Saravanamuttu, K.; Hosein, I. D. Coupling Nonlinear Optical Waves to Photoreactive and Phase-Separating Soft Matter: Current Status and Perspectives. *Chaos* **2017**, *27*, 104611.

(8) MacDonald, S. A.; Willson, C. G.; Frechet, J. M. J. Chemical Amplification in High-Resolution Imaging Systems. *Acc. Chem. Res.* **1994**, *27*, 151–158.

(9) Sagi, A.; Weinstain, R.; Karton, N.; Shabat, D. Self-Immolative Polymers. *J. Am. Chem. Soc.* **2008**, *130*, 5434–5435.

(10) Rotschild, C.; Alfassi, B.; Cohen, O.; Segev, M. Long-Range Interactions between Optical Solitons. *Nature Physics*. 2006, pp 769–774.

(11) Derrien, F.; Henninot, J. F.; Warenghem, M.; Abbate, G. A Thermal (2D+1) Spatial Optical Soliton in a Dye Doped Liquid Crystal. *J. Opt. A Pure Appl. Opt.* **2000**, *2*, 332–337.

(12) Sasaki, T.; Miura, K.; Ono, H.; Hanaizumi, O. Optically Controlled Light Propagation in Dye-Doped Nematic Liquid Crystals with Homogeneous Alignment. *Key Eng. Mater.* **2012**, *497*, 142–146.

(13) Li, Y.; Sun, Y.; Xiao, Y.; Gao, G.; Liu, S.; Zhang, J.; Fu, J. Electric Field Actuation of Tough Electroactive Hydrogels Cross-Linked by Functional Triblock Copolymer Micelles. *ACS Appl. Mater. Interfaces* **2016**, *8*, 26326–26331.

(14) Han, D.; Farino, C.; Yang, C.; Scott, T.; Browe, D.; Choi, W.; Freeman, J. W.; Lee, H. Soft Robotic Manipulation and Locomotion with a 3D Printed Electroactive Hydrogel. *ACS Appl. Mater. Interfaces* **2018**, *10*, 17512–17518.

(15) Stuart, M. A. C.; Huck, W. T. S.; Genzer, J.; Müller, M.; Ober, C.; Stamm, M.; Sukhorukov, G. B.; Szleifer, I.; Tsukruk, V. V; Urban, M.; et al. Emerging Applications of Stimuli-Responsive Polymer Materials. *Nat. Mater.* **2010**, *9*, 101.